Operando Insights into Size and Shape-controlled Cu-based Nanocatalysts for the Electrochemical Reduction of CO_2 toward C_{2+} Products

vorgelegt von
M. Sc. Antonia Marie Herzog

ORCID: 0000-0002-4402-3007

von der Fakultät II – Mathematik und Naturwissenschaften
der Technischen Universität Berlin
zur Erlangung des akademischen Grades

Doktor der Naturwissenschaften
Dr. rer. nat.

genehmigte Dissertation

Promotionsausschuss:

Vorsitzender: Prof. Dr. Michael Gradzielski
Gutachterin: Prof. Dr. Beatriz Roldán Cuenya
Gutachter: Prof. Dr. Arne Thomas
Gutachter: Dr. Serhiy Cherevko

Tag der wissenschaftlichen Aussprache: 15. Juni 2023

Berlin 2023

“I am the master of my failure…
If I never fail, how will I ever learn.”
C. V. Raman

Acknowledgment

I would like to express my gratitude to the many people who have supported me throughout my doctoral thesis and without whom this work would not have been possible.

First of all, I would like to thank Prof. Dr. Beatriz Roldán Cuenya for taking me into her research group at the Fritz Haber Institute (FHI) and providing me with the opportunity to explore electrocatalysis phenomena using a variety of advanced *in situ*/*operando* methods. Her support and encouragement during my PhD time were invaluable, and she always inspired me to strive for excellence and the highest scientific standards.

I am particularly grateful to Dr. Arno Bergmann, who supervised me from the beginning and later also became my group leader. Throughout my research, he consistently motivated me to learn new techniques and analysis methods while encouraging critical thinking to elucidate scientific phenomena. His mentorship in electrocatalysis was instrumental in my research. He was always available for fruitful scientific discussions and provided invaluable feedback on my publications and presentations.

Furthermore, I would like to thank Dr. Hyo Sang Jeon for his mentorship and supervision in the fascinating field of the electrochemical reduction of CO_2. He was always available to offer expert advice and guidance, motivating me to find innovative solutions.

I also want to thank Prof. Dr. Arne Thomas from the Technische Universität Berlin and Dr. Serhiy Cherevko from the Helmholtz Institute Erlangen-Nürnberg for dedicating their time to review my dissertation. Additionally, I am thankful to have been a part of the SPP2080 priority program of the German Research Foundation (DFG) and the International Max Planck Research School for Elementary Processes in Physical Chemistry (IMPRS-EPPC) at the FHI.

Moreover, I would like to express my biggest appreciation to the whole Interface Science Department at the FHI, which grew up so rapidly during the last four years, making it hard to mention everyone who contributed to this thesis. It was a pleasure to work with so many experts from various fields and enjoy so many fun group activities. My special thanks go to the people in my office A 1.10: Dr. Mauricio L. L., Felix Haase, Eric Liberra, Dr. Inês Jordão Pereira, and Simon Widrinna; thank you for your support and the nice time! I would also like to thank all the other group members of the Dynamics at Electrocatalytic Interfaces group as well as Dr. Janis Timoshenko for showing and teaching me X-ray absorption spectroscopy and Dr.

Mauricio Lopez Luna for his knowledge and introduction to Raman spectroscopy.
I am also grateful to all the people that have not been mentioned yet with whom I shared many hours in the synchrotron facilities around Europe, especially Martina Rüscher, Dr. Uta Hejral, Dr. Andrea Martini, Clara Rettenmaier, Dr. Earl M. Davis, and Dr. Ane Etxebarria.
In addition, I would like to thank all my friends in Berlin, who always believed in me and kept cheering me on (and up) and giving me new energy when I was running low.
Finally, I could not have done this thesis without the support of my family, especially my parents, who fostered my passion for science already as a child, always encouraged me, and made it possible for me to pursue my dreams.

Abstract

In the quest of reducing CO_2 emissions and limiting climate change, the field of electrocatalysis has gained significant interest due to its potential for the sustainable production of energy and chemicals. Inspired by the natural CO_2 metabolism, one promising way for converting intermittent renewable electricity directly into valuable fuels and chemicals is the electrochemical reduction of CO_2 (CO_2RR). Copper catalysts are uniquely capable of converting CO_2 into hydrocarbons and alcohols in significant amounts but suffer from low selectivity and stability. Therefore, nanostructured Cu-based materials with controlled size and shape have been investigated to improve the CO_2RR, *e.g.*, via bimetallic or potential pulse approaches. However, the catalytic properties of these materials are usually only explored with *ex situ* characterization methods resulting in misleading conclusions. This work aims to enhance the current understanding of the catalyst-adsorbate system toward the production of energy-dense C_{2+} products by applying (sub-second) time-resolved *in situ* and *operando* spectroscopic and diffraction techniques during CO_2RR. Here, the implementation of a bimetallic Cu-Ag nanocatalyst enhanced the selectivity of the CO_2RR toward C_{2+} liquid products such as ethanol and acetaldehyde. *Operando* Ag K-edge X-ray absorption spectroscopy (XAS) and surface-enhanced Raman spectroscopy (SERS) revealed the formation of important Ag-Cu binding sites under reaction conditions which altered the CO binding to Cu correlating with the observed selectivity effect. Furthermore, the evolution of characteristic adsorbates, including OH_{ad} and CO_{ad}, was monitored during alternating pulsed potential CO_2RR using time-resolved *operando* SERS. It was found that the oxidative formation of cationic Cu species and an optimized catalyst surface coverage of OH_{ad} and CO_{ad} play a crucial role in enhancing ethanol selectivity. These results were also confirmed by studies of a bimetallic Cu-ZnO nanocatalyst during pulsed CO_2RR, with the selectivities being modulated by changing the anodic potential. Time-resolved *operando* XAS, SERS, and X-ray diffraction uncovered the dynamic interplay between Cu, Zn, and CuZn composition, as well as the adsorption behavior of CO_{ad} and OH_{ad}. These results emphasize the importance of oxides and hydroxide coverage for enhancing the ethanol selectivity, which can be tuned through the oxidation of Cu- or Cu-Zn-based materials using potential pulses. This thesis contributes to the fundamental mechanistic understanding of CO_2RR, which makes a significant contribution to the advancement of the CO_2RR field.

Kurzzusammenfassung

In dem Bestreben die CO_2-Emissionen zu verringern und den Klimawandel zu begrenzen, hat das Gebiet der Elektrokatalyse aufgrund seines Potenzials für die nachhaltige Erzeugung von Energie und Chemikalien stark an Interesse gewonnen. Inspiriert vom natürlichen CO_2-Stoffwechsel ist die elektrochemische Reduktion von CO_2 (CO_2RR) ein vielversprechender Weg, um fluktuierenden erneuerbaren Strom direkt in wertvolle Kraftstoffe und Chemikalien umzuwandeln. Kupferkatalysatoren sind dabei in einzigartiger Weise in der Lage, CO_2 in beträchtlichen Mengen in Kohlenwasserstoffe und Alkohole umzuwandeln, leiden jedoch unter geringer Selektivität und Stabilität. Deswegen wurden nanostrukturierte Cu-basierte Materialien mit kontrollierter Größe und Form untersucht, um die CO_2RR zu verbessern, z. B. durch bimetallische Variationen oder potenzialabhängige Pulse. Das Verständnis der katalytischen Eigenschaften dieser Materialien ist jedoch häufig begrenzt, da ihre Charakterisierung oft nur mit *Ex-situ*-Methoden erfolgt, was zu irreführenden Schlussfolgerungen führt. Diese Arbeit zielt darauf ab, das derzeitige Verständnis des Katalysator-Adsorbat-Systems im Hinblick auf die Bildung von energiedichten C_{2+}-Produkten zu verbessern. Dafür wurden zeitaufgelöste (im Subsekundenbereich) *In-situ*- und *Operando*-Spektroskopie- und Beugungstechniken, während der CO_2RR eingeführt und angewendet. Hierbei verbesserte die Implementierung eines bimetallischen Cu-Ag-Nanokatalysators die Selektivität der CO_2RR für flüssige C_{2+}-Produkte wie Ethanol und Acetaldehyd. *Operando*-Ag-Kanten-Röntgenabsorptionsspektroskopie (XAS) und oberflächenverstärkte Raman-Spektroskopie (SERS) zeigten die Bildung wichtiger Ag-Cu-Bindungsstellen unter Reaktionsbedingungen, die die CO-Bindung an Cu veränderten. Dies korrelierte mit dem beobachteten Selektivitätseffekt. Darüber hinaus wurde die Entwicklung charakteristischer Adsorbate, einschließlich OH_{ad} und CO_{ad}, während Potenzial-gepulster CO_2RR mit zeitaufgelöster *Operando*-SERS beobachtet. Es wurde festgestellt, dass die oxidative Bildung von kationischen Cu-Spezien und eine optimierte Katalysatoroberflächenbedeckung von OH_{ad} und CO_{ad} eine entscheidende Rolle bei der Erhöhung der Ethanol-Selektivität spielen. Diese Ergebnisse wurden auch durch Untersuchungen an einem bimetallischen Cu-ZnO-Nanokatalysator während gepulster CO_2RR bestätigt, wobei die Selektivitäten durch Änderung des anodischen Potenzials moduliert wurden. Zeitaufgelöste *Operando*-XAS, -SERS und -Röntgenbeugung

deckten das dynamische Zusammenspiel zwischen Cu-, Zn- und CuZn-Zusammensetzung sowie das Adsorptionsverhalten von CO_{ad} und OH_{ad} auf. Die Ergebnisse unterstreichen die Bedeutung der Oxide und der Hydroxidbedeckung für die Verbesserung der Ethanol-Selektivität, die durch die Oxidation von Cu- oder Cu-Zn basierten Materialien mit Hilfe von Potenzialpulsen eingestellt werden kann. Diese Arbeit trägt zum grundlegenden mechanistischen Verständnis der CO_2RR bei und leistet damit einen wichtigen Beitrag zur Weiterentwicklung des CO_2RR-Gebiets.

List of Publications

First Author Publications

1. **Operando Investigation of Ag-Decorated Cu_2O Nanocube Catalysts with Enhanced CO_2 Electroreduction toward Liquid Products** Herzog, A.; Bergmann, A.; Jeon, H. S.; Timoshenko, J.; Kühl, S.; Rettenmaier, C.; Lopez Luna, M.; Haase, F. T.; Roldan Cuenya, B. *Angew. Chem. Int. Ed.* **2021**, *60* (13), 7426-7435. DOI: doi.org/10.1002/anie.202017070

2. **Time-resolved Operando Raman Spectroscopy uncovers the crucial Role of Oxides and Hydroxides for the enhanced Ethanol Selectivity in Pulsed CO_2 Electroreduction** Herzog, A.; Lopez Luna, M.; Jeon, H. S.; Bergmann, A.; Roldan Cuenya, B.; *in preparation*.

3. **Time-resolved Operando Insights into Cu-Zn Nanocubes during the Pulsed CO_2 Electroreduction toward Ethanol** Herzog, A.; Jeon, H. S.; Rüscher, M.; Timoshenko, J.; Rettenmaier, C.; Kordus, D.; Hejral, U.; Davis, M. E.; Haase, F. T.; Kühl, S.; Frandsen, W.; Bergmann, A.; Roldan Cuenya, B.; *in preparation*.

Co-Author Publications

4. **Operando Insight into the Correlation between the Structure and Composition of CuZn Nanoparticles and Their Selectivity for the Electrochemical CO_2 Reduction** Jeon, H. S.; Timoshenko, J.; Scholten, F.; Sinev, I.; Herzog, A.; Haase, F. T.; Roldan Cuenya, B. *J. Am. Chem. Soc.* **2019**, *141* (50), 19879-19887. DOI: 10.1021/jacs.9b10709

5. **Linking the evolution of catalytic properties and structural changes in copper–zinc nanocatalysts using operando EXAFS and neural-networks** Timoshenko, J.; Jeon, H. S.; Sinev, I.; Haase, F. T.; Herzog, A.; Roldan Cuenya, B. *Chem. Sci.* **2020**, *11* (14), 3727-3736. DOI: 10.1039/D0SC00382D

6. **Dynamic imaging of nanostructures in an electrolyte with a scanning electron microscope** Yoon, A.; Herzog, A.; Grosse, P.; Hein Alsem, D.; Chee, S. W.; Roldan Cuenya, B. *Microsc. Microanal.* **2021**, *27* (1), 121-128. DOI: 10.1017/S1431927620024769

7. **Selectivity Control of Cu Nanocrystals in a Gas-Fed Flow Cell through CO_2 Pulsed Electroreduction** Jeon, H. S.; Timoshenko, J.; Rettenmaier, C.; Herzog, A.; Yoon, A.;

Chee, S. W.; Oener, S.; Hejral, U.; Haase, F. T.; Roldan Cuenya, B. *J. Am. Chem. Soc.* **2021**, 143 (19), 7578-7587. DOI: 10.1021/jacs.1c03443

8. **Dynamic transformation of cubic copper catalysts during CO_2 electroreduction and its impact on catalytic selectivity** Grosse, P.; Yoon, A.; Rettenmaier, C.; Herzog, A.; Chee, S. W.; Roldan Cuenya, B. *Nat. Commun.* **2021**, *12* (1), 6736-6747. DOI: 10.1038/s41467-021-26743-5

9. **Tracking heterogeneous structural motifs and the redox behaviour of copper–zinc nanocatalysts for the electrocatalytic CO_2 reduction using operando time-resolved spectroscopy and machine learning** Rüscher, M.; Herzog, A.; Timoshenko, J.; Jeon, H. S.; Frandsen, W.; Kühl, S.; Roldan Cuenya, B. *Catal. Sci. Technol.* **2022**, *12* (9), 3028-3043. DOI: 10.1039/D2CY00227B

10. **Steering the structure and selectivity of CO_2 electroreduction catalysts by potential pulses** Timoshenko, J.; Bergmann, A.; Rettenmaier, C.; Herzog, A.; Arán-Ais, R. M.; Jeon, H. S.; Haase, F. T.; Hejral, U.; Grosse, P.; Kühl, S.; Davis, E. M.; Tian, J.; Magnussen, O. M.; Roldan Cuenya, B. *Nat. Catal.* **2022**, *5* (4), 1-9. DOI: 10.1038/s41929-022-00760-z

11. **Role of Nanoscale Inhomogeneities in Co_2FeO_4 Catalysts during the Oxygen Evolution Reaction** Haase, F. T.; Rabe, A.; Schmidt, F.-P.; Herzog, A.; Jeon, H. S.; Frandsen, W.; Narangoda, P. V.; Spanos, I.; Friedel Ortega, K.; Timoshenko, J.; Lunkenbein, T.; Behrens, M.; Bergmann, A.; Schlögl, R.; Roldan Cuenya, B. *J. Am. Chem. Soc.* **2022**, *144* (27), 12007-12019. DOI: 10.1021/jacs.2c00850

12. **Size effects and active state formation of cobalt oxide nanoparticles during the oxygen evolution reaction** Haase, F. T.; Bergmann, A.; Jones, T. E.; Timoshenko, J.; Herzog, A.; Jeon, H. S.; Rettenmaier, C.; Roldan Cuenya, B. *Nat. Energy* **2022**, *7* (8), 765-773. DOI: 10.1038/s41560-022-01083-w

13. **Deciphering the structural and chemical evolution of oxide catalysts during OER using QXAFS and machine learning** Timoshenko, J.; Haase, F. T.; Saddeler, S.; Rüscher, M.; Jeon, H. S.; Herzog, A.; Hejral, U.; Bergmann, A.; Schulz, S.; Roldan Cuenya, B. *J. Am. Chem. Soc.* **2023**, *145* (7), 4065-4080. DOI: 10.1021/jacs.2c11824

14. **Atomic-scale Surface Restructuring of Copper Electrodes Under CO_2 Electroreduction Conditions** Amirbeigiarab, R.; Tian, J.; Herzog, A.; Qiu, C.; Bergmann, A.; Roldan Cuenya, B.; Magnussen, O. M. *under review* **2023**.

15. **Lattice Strain during CO_2 Electroreduction Conditions: An operando time-resolved X-ray Diffraction Study on Oxide-derived Cu Electrocatalysts** Bergmann, A.; Herzog, A.; Jones, T. E.; Qiu, C.; Jing, T.; Amirbeigiarab, R.; Rettenmaier, C.; Arán Ais, R. M.; Kühl, S.; Schlögl, R.; Magnussen, O.; Roldan Cuenya, B. *in preparation*.

16. **Operando Insights correlating the CO-Coverage and the Selectivity of the Electrochemical CO_2 Reduction through Au NP decorated Cu_2O Nanocubes** Rettenmaier, C.; Herzog, A.; Casari, D.; Rüscher, M.; Timoshenko, J.; Jeon, H. S.; Kordus, D.; Lopez Luna, M.; Kühl, S.; Chee, S. W.; Duncan, A.; Bergmann, A.; Roldan Cuenya, B. *in preparation*.

17. **Beyond the Pourbaix diagram: Understanding Redox Stability of Cu Catalysts During Electrochemical Nitrate Reduction** Yoon, A.; Bai, L.; Franco, F.; Zhan, C.; Rüscher, M.; Timoshenko, J.; Jeon, H. S.; Herzog, A.; Hejral, U.; Bergmann, A.; Monteiro, M. C. O.; Chee, S. W.; Roldan Cuenya, B. *in preparation*.

18. **Unveiling the active species and reaction mechanisms of Cu_2O nanocubes for ammonia synthesis from electrocatalytic nitrate and nitrite reduction** Franco, F.; Bai, L.; Timoshenko, J.; Scholten, F.; Jeon, H. S.; Yoon, A.; Rüscher, M.; Herzog, A.; Haase, F. T.; Kühl, S.; Chee, S. W.; Bergmann, A.; Roldan Cuenya, B. *in preparation*.

19. **Reversible evolution of metal-nitrogen-doped carbon catalysts during CO_2 electroreduction: an operando X-ray absorption spectroscopy study** Hursán, D.; Timoshenko, J; Ortega, E.; Jeon, H. S.; Rüscher, M.; Herzog, A.; Rettenmaier, C.; Chee, S. W.; Roldan Cuenya, B. *in preparation*.

20. **Steering the CO_2 reduction selectivity of copper-nitrogen-doped carbon catalysts by pulsed potential electrolysis** Hursán, D.; Timoshenko, J; Jeon, H. S.; Ortega, E; Rüscher, M.; Bergmann, A.; Yoon, A.; Hejral, U.; Herzog, A.; Rettenmaier, C.; Haase, F. H.; Roldan Cuenya, B. *in preparation*.

21. **On the Role of Fe Decoration on the Oxygen Evolving State of Co_3O_4 Nanocatalysts** Haase, F. T.; Ortega, E; Saddeler S.; Schmidt, F.-P.; Cruz, D.; Scholten, F.; Rüscher, M.; Martini, A.; Jeon, H. S.; Herzog, A.; Hejral, U.; Davis, M. E.; Timoshenko, J.; Knop-Gericke, A.; Lunkenbein, T.; Schulz, S.; Bergmann, A.; Roldan Cuenya, B. *in preparation*.

List of Abbreviations

AFM	Atomic Force Microscopy
BF	Brightfield
C_{2+}	Two or more carbon atoms
CA	Chronoamperometry
CCD	Charge-Coupled Device
CCS	Carbon Capture and Storage
CE	Counter Electrode
CO_2RR	Electrochemical Reduction of CO_2
CT	Charge Transfer
CV	Cyclic Voltammetry
DF	Darkfield
DFT	Density Functional Theory
ECSA	Electrochemical Surface Area
EDL	Electrical Double Layer
EDX	Energy-Dispersive X-ray spectroscopy
EM	Electron Microscopy
EXAFS	Extended X-ray Absorption Fine Structure
FCC	Face-Centered Cubic
FE	Faradaic Efficiency
FEP	Fluorinated Ethylene Propylene
FID	Flame Ionization Detector
FT	Fourier Transformed
FWHM	Full Width at Half Maximum
GC	Gas Chromatograph
GI	Grazing Incidence
GRR	Galvanic Replacement Reaction
HAADF	High-Angle Annular Darkfield
HCP	Hexagonal Close-Packed
HER	Hydrogen Evolution Reaction

HE-XRD	High Energy X-Ray Diffraction
HFB	High-Frequency Band
HOPG	Highly Oriented Pyrolytic Graphite
HPLC	High-Pressure Liquid Chromatograph
ICP-MS	Inductively Coupled Plasma-Mass Spectrometry
IR	Infrared Spectroscopy
LCA	Linear Combination Analysis
LFB	Low-Frequency Band
L-GC	Liquid-Gas Chromatograph
LSPR	Localized Surface Plasmon Resonance
LSV	Linear Sweep Voltammetry
ML	Machine Learning
MS	Multiple Scattering
NC	Nanocube
NN	Neural Network
NP	Nanoparticle
OCP	Open Circuit Potential
OER	Oxygen Evolution Reaction
PCA	Principal Component Analysis
PE	Pulsed Electrolysis
PEEK	Polyether Ether Ketone
PEIS	Potentio-Electrochemical Impedance Spectroscopy
PIPS	Passivated Implanted Planar Silicon
PTFE	Polytetrafluoroethylene
QXAFS	Quick scan X-ray Absorption Fine Structure
RDF	Radial Distribution Function
RE	Reference Electrode
RHE	Reversible Hydrogen Electrode
RID	Refractive Index Detector
RSF	Relative Sensitivity Factor
SEIRAS	Surface-Enhanced Infrared Absorption Spectroscopy
SEM	Scanning Electron Microscopy
SERS	Surface-Enhanced Raman Spectroscopy
SHE	Standard Hydrogen Electrode

SS	Single Scattering
STEM	Scanning Transmission Electron Microscopy
TCD	Thermal Conductivity Detector
TEM	Transmission Electron Microscopy
UHV	Ultra-High Vacuum
WE	Working Electrode
XAES	X-ray induced Auger Electron Spectroscopy
XAFS	X-ray Absorption Fine Structure
XANES	X-ray Absorption Near Edge Structure
XAS	X-ray Absorption Spectroscopy
XPS	X-ray Photoelectron Spectroscopy
XRD	X-Ray Diffraction

Table of Contents

1. Introduction and Motivation

Climate change is one of today's most urgent global issues, leading to severe natural and social consequences. It refers to the increase in temperature caused by the accumulation of CO_2 and other greenhouse gas emissions in the atmosphere. Figure 1.1 illustrates the consistent rise in yearly CO_2 emissions over the past 50 years, which resulted mainly from human activities such as burning fossil fuels and deforestation driven by economic expansion and population growth.[1] To combat climate change, countries around the world have set ambitious climate goals to reduce greenhouse gas emissions and limit global temperature rise. The Paris Agreement, signed in 2015 by initially 175 parties, aims to limit global warming to well below 2.0 °C above pre-industrial levels and pursue efforts to limit the temperature increase to 1.5 °C.[2] The reduction in CO_2 emissions required to achieve these temperature increase scenarios is depicted in Figure 1.1. However, despite a 5.4 % decrease in CO_2 emissions in 2020 compared to 2019 due to the Covid-19 pandemic, emissions increased again by 2.0 % to 36.1 gigatons of CO_2 in 2022, setting a new record.[3] The recent 2023 report of the Intergovernmental Panel on Climate

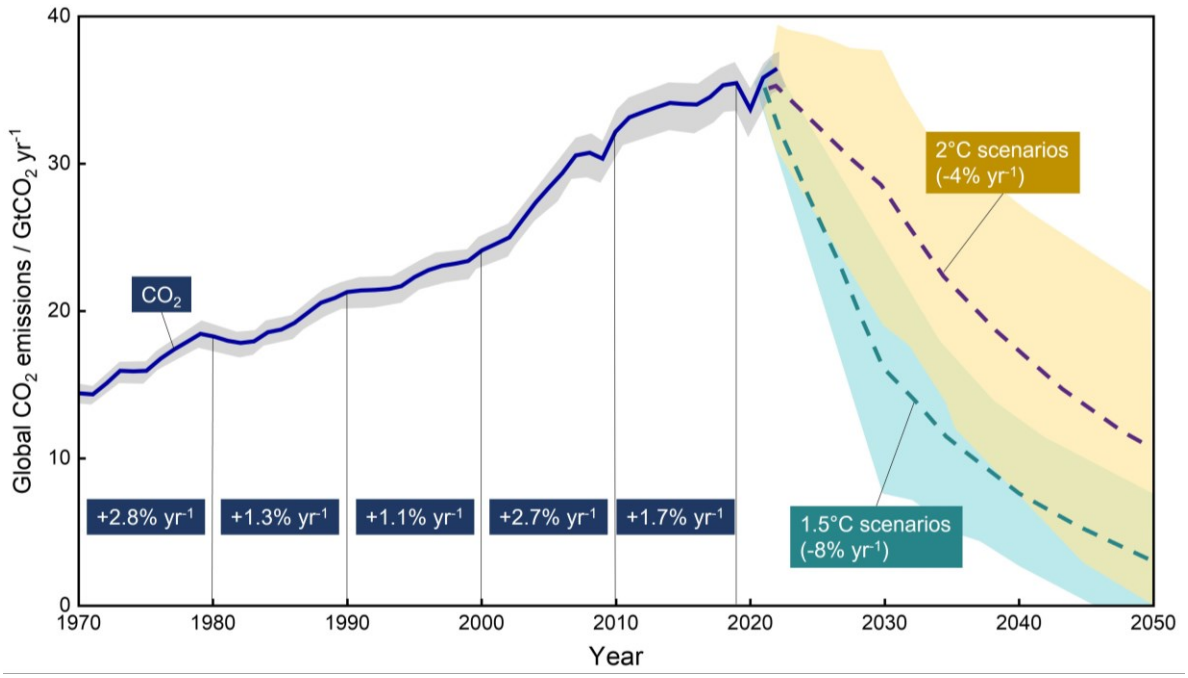

Figure 1.1 Temporal evolution of global CO_2 emissions until 2022 and projected CO_2 mitigation pathways of 2021 redrawn from Liu et al.[3, 4] Solid and dashed lines represent the median, while shading squares represent the corresponding range.

Change (IPCC) also found that we are likely to fall behind on our climate goals and pass the 1.5 °C already in the early 2030s.[5] Without a rapid reduction in CO_2 emissions, the carbon cycle will be disrupted, resulting in irreversible changes in the climate.[1, 3]

Moreover, the war in Ukraine has emphasized the necessity of energy independence from countries that supply fossil fuels to ensure national energy security, especially in the face of the extreme impacts of climate change.

In this regard, renewable energy sources such as wind and solar power offer an attractive way toward achieving net-zero CO_2 emissions; nevertheless, the electricity they produce is intermittent and must be stored for later use. While battery technologies such as lithium-ion batteries possess high energy and power densities, the limited supply of Li, high costs, and safety concerns, as well as reliability issues, make them unsuitable for large-scale energy storage applications.[6] Hydrogen, on the contrary, offers a promising solution as an energy carrier for a clean energy economy if obtained through electrochemical water splitting.[7] However, full decarbonization of the economy is extremely difficult because carbon is used in the production of many key products, such as cement, steel, plastic, fertilizers, and aluminum.[8] Therefore, carbon capture and storage (CCS) solutions can be utilized to reduce the amount of CO_2. Currently, CCS can capture and store 244 million tons of CO_2 from industrial sources per year.[9] Nonetheless, the high energy amount and cost of these solutions are prohibitive, and the risk of CO_2 leakage remains. Additionally, CO_2 utilization technologies, inspired by the natural CO_2 metabolism, present an attractive approach that can convert CO_2 into valuable fuels and chemicals in the presence of a catalyst. In particular, CO_2 can be converted into syngas (a mix of hydrogen and carbon monoxide), methane, formic acid, and various alcohols via thermal catalysis, but harsh reaction conditions need to be applied (*e.g.*, high pressures and high temperatures).[10]

The electrochemical CO_2 reduction reaction (CO_2RR) is an appealing method for converting intermittent renewable electricity directly into valuable fuels and chemicals, thereby creating a net-zero CO_2 cycle.[8] Unlike thermal methods, CO_2RR can be carried out under mild conditions such as moderate temperatures and atmospheric pressure. Since the pioneering work of Y. Hori in the 1980s, a considerable amount of effort has been directed toward enhancing the catalytic performance of CO_2RR, and particularly in the last decade, CO_2RR has been a field of extensive research.[8, 11] There, key areas of focus have been the design of catalyst materials, electrolytes, and electrochemical cell setups.[12, 13]

Copper stands out among the metals as uniquely capable of directly converting CO_2 into significant quantities of hydrocarbons and alcohols.[11, 14] Based on the Sabatier principle, Cu has

an optimal binding energy for crucial reaction intermediates such as *H, *COOH, *CO, and *CHO.[15] However, Cu electrodes yield a broad spectrum of products, including C_1 compounds such as carbon monoxide, formate, and methane, and C_{2+} compounds such as ethylene, ethanol, and propanol.[16] Due to the high separation costs of these products, it is necessary to improve the selectivity with high activity and stability toward a particular product for the economic feasibility of the CO_2RR.[17] Furthermore, it would be especially favorable to tune the selectivity toward important high energy-dense C_{2+} products and fuels, which can be easily stored and transported through the current infrastructure.[8]

Nanostructured Cu-based materials with controlled size and shape, as well as high electrochemical surface area based on the nanoscale effect, offer ideal systems for investigating the electrocatalytic properties of the CO_2RR.[18] It has been observed that catalyst structures with predominantly (100) facets, undercoordinated sites, and defects, as well as Cu(I) and sub-surfaces oxygen, favor the production of C_{2+} products.[12, 18] Another strategy for further improving the C_{2+} selectivity is the incorporation of a second metal in Cu catalysts to tune the chemical and electronic properties of two different metals or to enable bifunctional effects, *e.g.*, with a CO-producing co-catalyst.[19] Additionally, CO_2RR can be applied via alternating potential pulses, which can tune the catalyst and adsorbate structures *in situ* without the need of re-designing the catalytic and electrolyte system.[20] In this way, pulsed CO_2RR can steer the selectivities to different products in dependence on the applied pulse parameters. Nevertheless, there are many contrasting results of CO_2RR product selectivities with similar materials in the literature, and the exact mechanistic pathways toward one specific product are still unknown. This results from the complex nature of the C-C coupling step in CO_2RR and its high sensitivity to the catalyst structure and electrolyte.

While traditional *ex situ* techniques are commonly employed to explore the CO_2RR mechanism by analyzing pre- and post-reaction catalysts, these techniques are limited since the catalyst structure, morphology, as well as intermediate type, and coverage undergo large transformations during the reaction.[19] Moreover, active sites of any catalyst are only formed when the catalyst is exposed to the reactants during the reaction.[21] Therefore, advanced *in situ* and *operando* techniques are crucial to uncover the dynamic evolution of the catalyst, electrolyte, and their interface during reaction conditions.[22] A combination of different *in situ* and *operando* methods, such as vibrational spectroscopy, as well as X-ray-based spectroscopic and diffraction characterization methods, is beneficial due to their varying strengths in surface and bulk sensitivity and their capabilities to monitor the crystallite structures and/or adsorbates on the catalyst surface. Furthermore, a high temporal resolution of these techniques is essential

to capture changes in the sub-second range, especially for the pulsed CO_2RR approach.

The goal of this thesis is to understand the mechanistic pathways of the CO_2RR toward C_{2+} products by utilizing well-defined Cu-based bimetallic nanocatalysts and the pulsed potential CO_2RR approach in conjunction with time-resolved *in situ* and *operando* methods. The findings can be applied to the design of superior CO_2RR catalysts, which is critical for the future efficient and large-scale utilization of these catalysts in CO_2RR applications. The structure of the thesis is as follows:

Chapter 2 provides the theoretical background of the CO_2RR by outlining potential mechanistic pathways and recent advancements in catalyst design, with a particular emphasis on the properties of state-of-the-art Cu-based nanocatalysts for the production of C_{2+} products. This chapter places a significant focus on studies of bimetallic catalysts and the different effects of pulsed potential CO_2RR. The scientific framework helps later to contextualize the results of this thesis.

Chapter 3 gives a description of the electrochemical background for CO_2RR, along with the characterization methods utilized in this study. The chapter places particular emphasis on *in situ* and *operando* techniques, including surface-enhanced Raman spectroscopy (SERS), X-ray absorption spectroscopy (XAS), and X-ray diffraction (XRD). The theoretical principles underlying these techniques are explained, as well as the specific setups and cell designs required for their implementation. Furthermore, the chapter highlights the strategies used to achieve high temporal resolution (in the sub-second range) with these *operando* measurements.

Chapter 4 describes the synthesis procedures to prepare well-defined cubic-shaped Cu oxide and Cu bimetallic nanocatalysts that were developed and employed in this thesis. This chapter highlights the principles underlying the wet-chemical synthesis methods and crucial synthesis steps.

Chapter 5 presents the development of a new cubic-shaped Cu-Ag nanocatalyst that enhances the CO_2RR toward valuable energy-dense liquid products such as ethanol and acetaldehyde. Through the implementation of *operando* Ag K-edge XAS and SERS, the formation of important Ag-Cu binding sites which alter the CO binding configuration could be shown and are discussed. These findings are essential for the observed selectivity effect and have made

significant contributions to the explanation of previous research on bimetallic catalysts for CO_2RR and their further improvement.

Chapter 6 discusses how the catalytic selectivity of an oxide-derived Cu nanocatalyst during pulsed CO_2RR changes in relation to its adsorbate structure and composition. Time-resolved *operando* SERS is used to monitor the evolution of characteristic adsorbates, including OH_{ad} and CO_{ad}, during each pulse. Through testing various pulse length conditions that influence the product formation, it was discovered that the oxidative formation of cationic Cu species played a crucial role, as did optimizing the catalyst surface coverage of the coverage of OH_{ad} and CO_{ad}, in enhancing the ethanol selectivity. This study provides a deeper insight into the reaction mechanism of pulsed CO_2RR and sheds light on the impact of the adsorbate structure on the observed selectivity trends.

Chapter 7 presents the utilization of a cubic-shaped Cu-ZnO nanocatalyst for pulsed CO_2RR, with the selectivity being modulated through changes in the anodic potential. The selectivity and stability of the catalyst were enhanced by pulsing only into the Zn oxidation regime and not into the Cu oxidation regime. Time-resolved *operando* XAS, XRD, and SERS techniques uncovered the dynamic interplay between the content and surface coverage of various Cu, Zn, and CuZn species, as well as the adsorption behavior of CO_{ad} and OH_{ad}. The results highlight the importance of oxides and OH coverage, which can be achieved through the oxidation of Zn by using potential pulses for enhancing the ethanol selectivity.

Chapter 8 concludes the thesis by summarizing the obtained results and drawing overarching conclusions regarding the structure-selectivity relationships established through the bimetallic and pulsed CO_2RR approach. Furthermore, the chapter provides perspectives for future investigations based on the findings of this work and their implementation into state-of-the-art catalysts.

2. Theoretical Background

The aim of this chapter is to give an overview of the electrochemical reduction of CO_2 by reviewing the current literature. It covers the proposed mechanistic pathways that result in different product outcomes and strategies to adjust the selectivity of Cu-based catalysts toward valuable C_{2+} products. The emphasis is on improving the catalyst design, including techniques such as nanostructuring and compositional modifications by changing the oxidation state of Cu or adding a second metal. Additionally, the chapter explores the reaction under pulsed potential conditions by highlighting the crucial effects that enhance the catalytic properties. Finally, several unresolved questions are outlined that will be addressed during the course of this thesis.

2.1 Electrochemical CO_2 Reduction

The electrochemical reduction of carbon dioxide (CO_2RR) is a cathodic reaction that operates together with the oxygen evolution reaction (OER) as the anodic counter reaction to enable the overall electrochemical recycling reaction of CO_2:

Cathode (CO_2RR) $$x\,CO_2 + n\,(H^+ + e^-) \rightarrow Product + y\,H_2O \quad (2.1)$$

Anode (OER) $$\frac{n}{2}\,H_2O \rightarrow O_2 + n\,(H^+ + e^-) \quad (2.2)$$

Overall reaction $$x\,CO_2 + m\,H_2O \rightarrow Product + z\,O_2 \quad (2.3)$$

The CO_2RR half-reaction forms various products, while the OER half-reaction produces oxygen, akin to water electrolysis. In this reaction, water serves as the source of electrons and protons with equivalent stoichiometric coefficients. Table 2.1 presents the standard redox potentials for commonly reported products at the cathode side,[8] which are investigated during this work. These thermodynamic potentials are all very close to 0 V_{RHE} (versus the reversible hydrogen electrode), while the difference between the standard potential of the CO_2RR and the OER ($E°_{OER}$ = 1.23 V_{RHE}) leads to an overall reaction potential above 1.23 V that needs to be applied.[8] However, the OER and CO_2RR require both large overpotentials, which refer to the voltage that is needed on top of the thermodynamically required potential. In the case of the

Table 2.1 Thermodynamical standard redox potentials ($E°$) and aggregate state of typical products at the cathode side with the number of CO_2, electrons (e^-), protons (H^+), and H_2O species involved in the cathode reaction.[8]

Product	$E°$ / V_{RHE}	Aggregate state	CO_2	e^-/H^+	H_2O
Hydrogen, H_2, HER	0.00	Gaseous	0	2	-1
Carbon monoxide, CO	-0.10	Gaseous	1	2	1
Formic acid, HCOOH	-0.12	Liquid	1	2	0
Methane, CH_4	0.17	Gaseous	1	8	2
Acetaldehyde, CH_3CHO	0.06	Liquid	2	10	3
Ethanol, CH_3CH_2OH	0.09	Liquid	2	12	3
Ethylene, C_2H_4	0.08	Gaseous	2	12	4
Propionaldehyde, C_2H_5CHO	0.09	Liquid	3	16	5
n-Propanol, C_3H_7OH	0.10	Liquid	3	18	5

CO_2RR, the high overpotentials result from the slow kinetics due to the multi-electron/proton transfer steps and the high energy barriers involved in the reactions to different products. Meanwhile, the competing hydrogen evolution reaction (HER) occurs at a similar potential but is a kinetically easier reaction. Therefore, the CO_2RR requires efficient catalysts to facilitate the kinetics and to reduce the overpotentials toward a certain product.[8, 23]

The employed catalysts usually consist of metal electrodes. Based on the studies of Y. Hori, metal electrodes can be classified into four groups, as illustrated in Figure 2.1, which primally

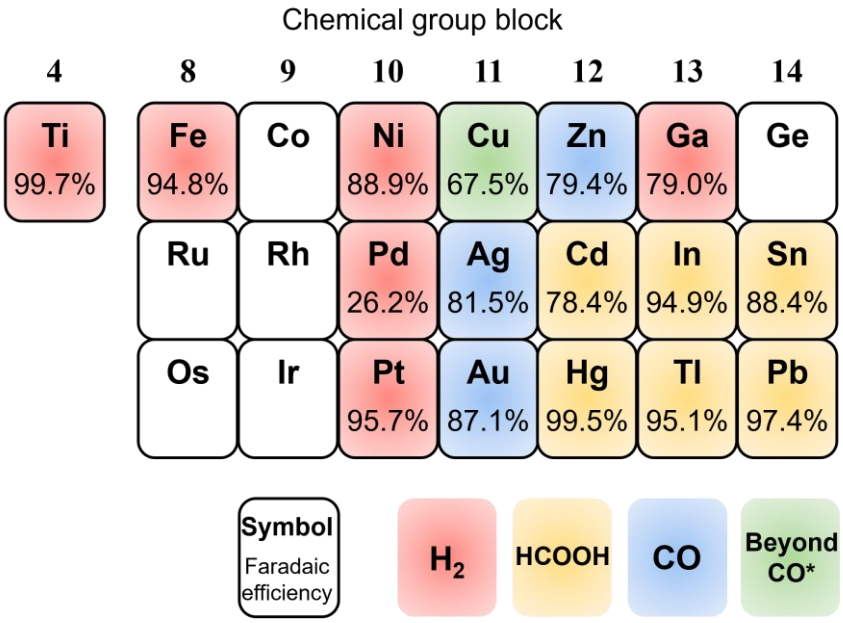

Figure 2.1 Classification of metal electrodes in the periodic table toward their main product selectivity in CO_2RR by measurements of Hori.[14] The Faradaic efficiencies for the main products are indicated. The scheme is redrawn from Bagger et al.[15]

produce formate ($HCOO^-$) and carbon monoxide (CO) or are almost inactive toward CO_2RR and form hydrogen instead. Cu is the only metal that produces products beyond *CO, such as hydrocarbons, aldehydes, and alcohols.[11, 14] This product outcome has been explained by a simple concept based on the adsorption energies for *CO and *H.[15] In the first step of the CO_2RR, it was proposed that CO_2 be reduced to the *COOH intermediate. Metals that bind *COOH and *H very weakly, which refer to a high barrier for the HER, mainly produce $HCOO^-$, such as Sn and In. On other metals, the *COOH intermediate can be further reduced to *CO, which is adsorbed on the metal surface. Metals that bind *CO very strongly produce mainly H_2, such as Pt, since *CO poisons the catalytic surface, and the HER is favored (strong *H binding). On the other hand, metals that bind *CO and *H very weakly produce mainly CO, such as Ag or Zn, since CO is immediately released from the surface and cannot further react. The exceptional behavior of Cu results from an intermediate *CO and low *H binding energy. In this way, *CO can be further reduced, which leads to the formation of products beyond *CO, such as hydrocarbons and alcohols.[23]

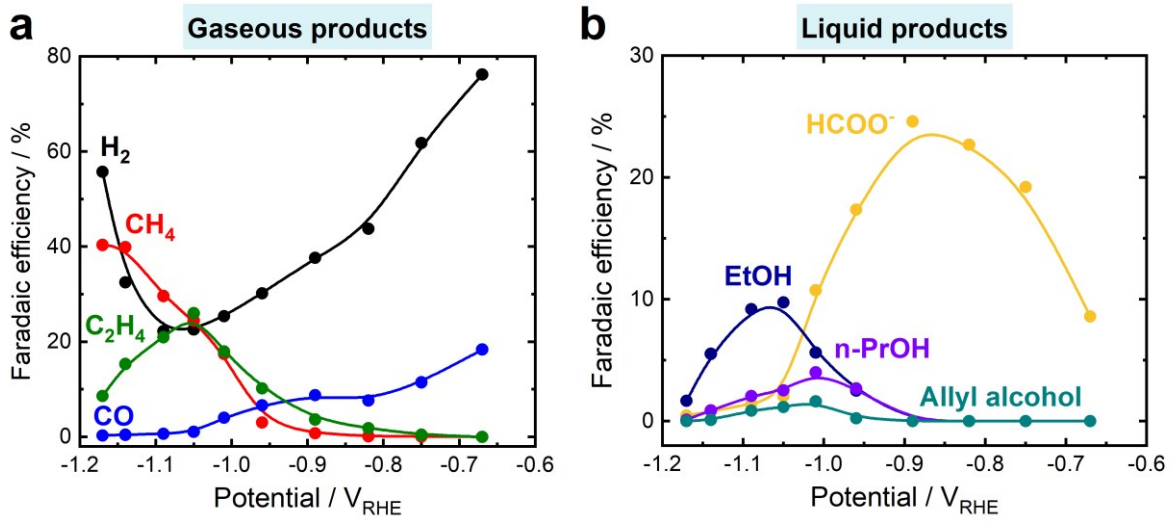

Figure 2.2 Potential-dependent Faradaic efficiencies of a polycrystalline Cu foil during CO_2RR for 1 h in CO_2 saturated $KHCO_3$ with data from Kuhl et al.[16] (a) shows the Faradaic efficiencies for gaseous products and (b) the Faradaic efficiencies for liquid products.

One drawback of Cu electrodes is their poor selectivity toward a particular product. Specifically, Kuhl et al. detected 16 different products during CO_2RR on a polycrystalline Cu foil in 0.1 M potassium bicarbonate in an H-type electrochemical cell. Hereby, the main products are methane, ethylene, hydrogen, formate, and CO with a Faradaic efficiency (FE) above 10 %, while the intermediate products are ethanol, n-propanol, and allyl alcohol with a FE above 1 % (Figure 2.2), and the minor products include products such as acetaldehyde, acetate, propionaldehyde, […] with a FE below 1 % (not displayed in Figure 2.2). The

selectivity trends for the main and intermediate products can also be classified by their aggregate state (gaseous or liquid) and are shown in Figure 2.2.[16] Furthermore, the product selectivity of the Cu foil strongly depends on the applied overpotential. At low overpotentials between -0.6 and -0.9 V_{RHE}, mainly 2e$^-$ products (hydrogen, formate, and CO) are formed. At higher overpotentials, higher e$^-$ products can be formed, and the ideal overpotential for the formation of the desired energy-dense C_{2+} liquid products (ethanol, n-propanol, allyl alcohol, acetaldehyde, propionaldehyde) is around -1.0 V_{RHE}. At even higher overpotentials up to -1.2 V_{RHE}, the methane and hydrogen production increase significantly. In order to further understand this product outcome on Cu electrodes, a deeper look into the mechanistic pathways on Cu that have been postulated in the literature is necessary.

2.2 Proposed Mechanistic Pathways

The reaction mechanisms of the CO_2RR on Cu toward different products have been broadly discussed in the literature.[8, 24, 25] These studies are based on experimental and theoretical data to gain more mechanistic insights to improve the efficiency of the catalyst toward a particular product. However, there is still much disagreement in the proposed mechanisms, and more research needs to be conducted in this field, *e.g.*, by combining density functional theory (DFT) calculations, isotope labeling experiments, and *in situ*/*operando* characterization methods. In the following, some of the main proposed pathways will be described as illustrated in Figure 2.3.

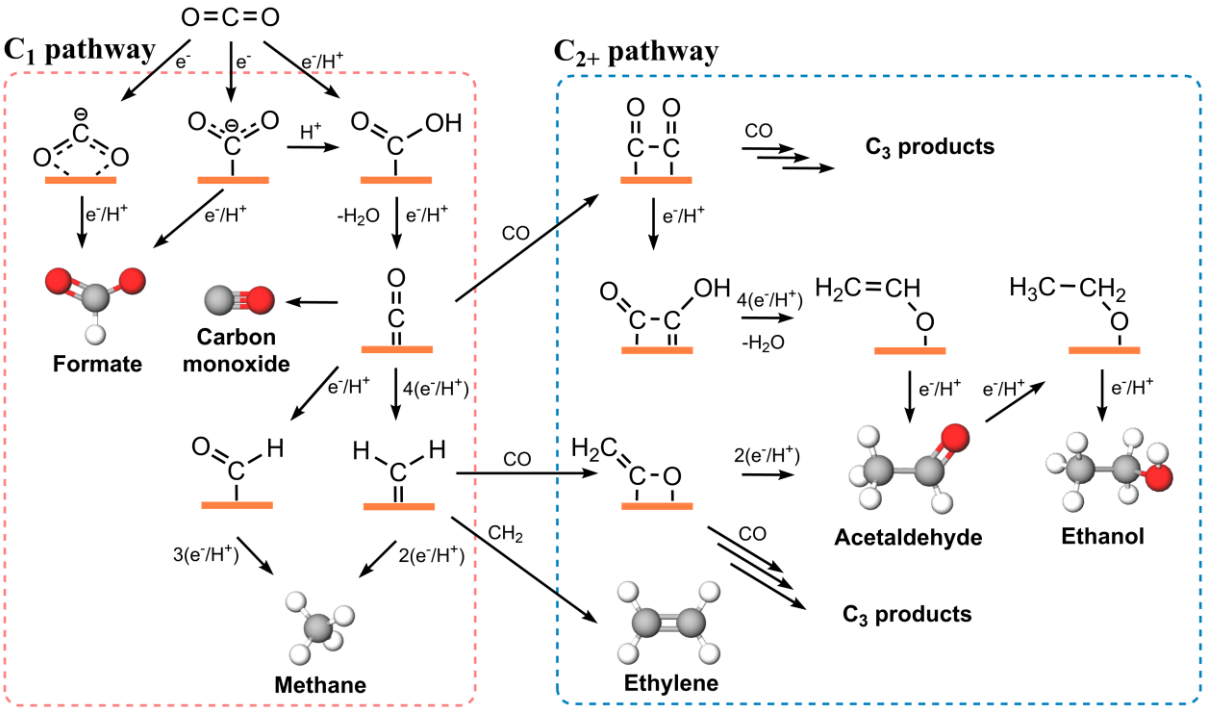

Figure 2.3 Possible mechanistic pathways of the CO_2RR on Cu toward C_1 and C_{2+} products.

2.2.1 Formation of Two-Electron Products

In the first step, CO_2 needs to be activated by a rate-determining step to form $2e^-$ products such as formate or CO. This either occurs by a concerted proton-electron (e^-/H^+) transfer leading directly to the carboxyl intermediate *COOH or a decoupled one electron transfer leading first to the carboxylate anion $*CO_2^-$.[26] For the pathway to formate, a further reduction of $*CO_2^-$ occurs,[27] while several studies also suggest a different binding configuration over the oxygen atoms of this anion based on DFT calculations.[26, 28] For the pathway to CO, the conversion of *COOH to *CO takes place rapidly via a second (e^-/H^+) transfer and the cleavage of water.[29] As already discussed in Section 2.1, the further product outcome strongly depends on the binding strength of the *CO intermediate.[15] The *CO intermediate was already experimentally observed by several techniques such as *operando* surface-enhanced Raman spectroscopy (SERS)[30-32] or *operando* infrared spectroscopy (IR),[33] which allowed insights into the binding behavior and sites of the *CO intermediate.

2.2.2 Beyond *CO Products

One key difference between the selectivities of products beyond *CO lies in their experimentally observed pH dependency.[34, 35] While the C_1 pathway to products such as methane is pH-dependent, the C_{2+} pathway to products such as ethylene is pH-independent.[36] This results in the formation of C_{2+} products at lower onset potentials when the pH values are higher.[37, 38] Thus, it was concluded that the rate-limiting step for the methane pathway would be the formation of the *CHO intermediate via the protonation of *CO,[29, 39] while the rate-limiting step for C_{2+} products would be the formation of the $*C_2O_2$ intermediate via CO dimerization (coupling of two *CO) without any proton transfers.[26, 40] However, the pH independence of the C_{2+} pathway could also arise from several other effects such as field-stabilization of a limiting chemical reaction (*e.g.*, CO dimerization) or an (e^-/H^+) transfer from water to an adsorbate.[8] Another plausible C_1 pathway to methane starting from *CO could involve the formation of a $*CH_2$ intermediate through several (e^-/H^+) transfers.[26, 41] The $*CH_2$ intermediate also opens up two alternate C_{2+} pathways, where one leads to the formation of ethylene over the dimerization of the $*CH_2$ intermediates.[29] The other one involves a CO insertion next to the $*CH_2$ intermediate to form an $*OCCH_2$ intermediate similar to the Fischer-Tropsch mechanism.[42] After the C-C coupling steps, the literature suggests diverse intermediates and pathways since the processes become even more complex.[8, 27 39, 43] The pathways to alcohols such as ethanol often involve the reduction of oxygenated species such as acetaldehyde (and propionaldehyde for n-propanol,…).[8, 44] Additionally, water and $*OH^-$ adsorbates might be crucial for the formation of oxygenated products.[45-47] The further formation

of C_3 products could stem from additional CO insertions next to C_2 intermediates.[27, 48]

2.3 Catalyst and Electrolyte Design

Cu is the only metal capable of producing significant amounts of the desired C_{2+} products, as discussed in Section 2.1. Further enhancement of the electrocatalytic properties of the CO_2RR toward the C-C coupling step with high activity and stability can be achieved through the appropriate design of the catalyst and the electrolyte. The electrolyte plays a crucial role in maintaining the optimal microenvironment, which includes the pH and the (adsorbed) anionic and cationic species. The effects of the electrolyte are extensively discussed in the literature.[8, 12, 19, 49] Usually, CO_2RR is performed at neutral pH in aqueous electrolytes such as potassium bicarbonate solutions since they can increase the CO_2 concentration close to the electrode surface.[50] However, the pH at the electrode interface differs from the bulk pH due consumption of protons or the release of OH^- by the CO_2RR and HER and the low buffer capacity of potassium bicarbonate.[51] This process leads to a concentration gradient of OH^-, resulting in a pH increase near the electrode. Moreover, the reaction rate of the CO_2RR is mass-transport limited due to the low solubility of CO_2 in the aqueous phase (33 mM at 25 °C, 1 atm).[12] The pH can also affect the selectivities, as outlined in Section 2.2.2. In addition, the design of the catalyst significantly affects its catalytic properties. This includes nanostructuring Cu-based catalysts and making compositional and morphological modifications. These effects will be discussed in detail in the following sections.

2.4 Cu Nanoparticles

Cu nanoparticles (NPs, between 1 and 100 nm in diameter) can be used as catalysts for CO_2RR to maximize the surface-to-volume ratio. In this way, the electrochemical surface area (ECSA) of the catalyst increases compared to planar electrodes, which leads to improved utilization of the catalyst material.[8] Another advantage of nanocatalysts is the possibility of implementing them in gas diffusion electrodes (GDEs) and membrane electrode assemblies (MEAs), which are needed for further industrial applications of the CO_2RR at higher current densities.[52] Well-defined nanocatalysts are also ideal model systems to study and understand properties that influence the CO_2RR. By tuning the size, shape, and interparticle distance (or loading of the support) as displayed in Figure 2.4, the catalytic properties of Cu nanocatalyst could be tuned, and the different effects on the CO_2RR properties will be discussed briefly in the following.[8, 18, 19]

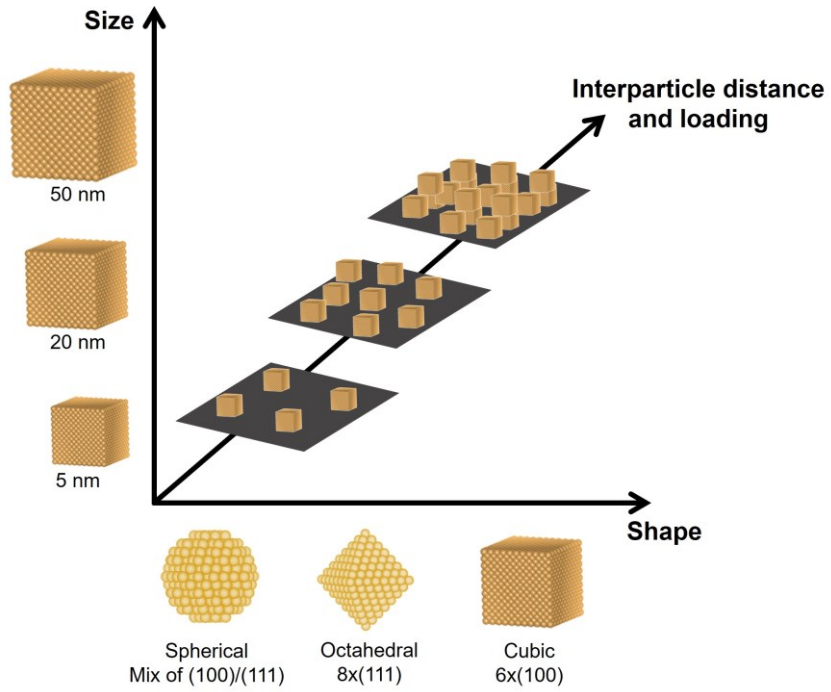

Figure 2.4 Schematic illustration of important nanoparticle properties that influence the electrocatalytic behavior of the CO_2RR.

2.4.1 Shape Effect

Different NP shapes expose different crystallographic facets on the surface. Cu single crystal studies assigned Cu(100) facets active for ethylene and Cu(111) surfaces active for methane production.[53, 54] However, recently, Scholten et al. found that well-oriented ultra-high vacuum (UHV)-prepared Cu single crystals mainly favor the production of H_2.[55] Only the introduction of roughness and surface defects such as steps and kinks led to a significant enhancement of the hydrocarbon production and several studies stated a beneficial effect of (111) and (110) steps in (100) facets for C-C bond formation.[56, 57] On the basis of the single-crystal studies, several shape-controlled metallic Cu nanocatalysts were developed, such as spheres, tetrahedra, octahedra, star-shaped decahedra with mostly (111) facets, nanorods with (111) pentagonal cross-section and (100) side facets, and cubes with mostly (100) facets.[18, 58] These nanocatalysts followed a similar facet-dependent trend as the (rough) single crystals. In particular, octahedral-shaped particles yielded mainly methane,[59] while Cu spheres were not selective for any particular product, similar to the selectivity of polycrystalline Cu foil.[60] On the other hand, cubic-shaped particles with (100) domains combined with steps and edges favored the formation of ethylene, while methane production was suppressed.[61]

Nevertheless, one needs to keep in mind that the initial well-defined structures can significantly alter under CO_2RR conditions. For example, Grosse et al. revealed that Cu oxide cubes lose the cubic structure and decrease in size accompanied by the formation of small NPs as observed by

operando electrochemical atomic force microscopy (AFM) and *operando* electrochemical transmission electron microscopy (TEM).[62, 63] Such transformations can lead to the deactivation of the catalyst or changes in the selectivity behavior.

2.4.2 Size Effect

The smaller the size of the NPs, the higher the density of low-coordinated atoms at the surface.[64] This has a direct impact on the electronic properties of the material and, thus, influences the final product selectivity. For example, small NPs exhibited an induced strain on the surface atoms, which shifted the d-band as shown by DFT and X-ray diffraction (XRD).[65, 66] Reske et al. demonstrated an enhanced catalytic activity of Cu NPs when decreasing the NP size from 15 to 2 nm, which was coupled with a drastic increase in the H_2 and CO selectivity in detriment of the hydrocarbon production.[60] They mainly linked this behavior to the increased population of low-coordinated surface sites on small Cu NPs. A similar trend was also observed for other metal NPs, such as Ag[67] and Zn[68], where the HER was found to increase at a certain point for small particles. Furthermore, in a study by Loiudice et al., Cu cubes with an edge length of 44 nm exhibited an optimized selectivity toward ethylene in comparison to smaller (24 nm) and bigger (63 nm) cubes.[61] This was explained by an optimized face-to-edge ratio, which affects the (100)/(110) ratio. Nevertheless, the different samples investigated in these studies were synthesized following different methods, and the role of possible leftover ligands from the preparation procedure was unclear.

2.4.3 Interparticle Distance and Particle Loading

The number of particles loaded on a support and their distribution can significantly influence the CO_2RR properties. Mistry et al. prepared Cu NPs with a uniform size distribution and arrangement that showed an increasing current density and selectivity toward ethylene and methane as their interparticle distance decreased.[69] They assigned this to the diffusive transfer between neighboring NPs and the re-adsorption of intermediate species. However, changes in the local pH due to the depletion of reactants and intermediates might also play an important role here. Moreover, in a study by Kim et al., densely packed Cu NPs (6.7 nm) on carbon paper underwent structural transformations into more active cubic-like particles, which resulted in a shift of the product selectivity toward C_{2+} products.[70] Recently, Yang et al. could directly track and observe the transformation of these particles with electrochemical liquid-cell scanning TEM.[71]

The dynamic and compositional changes of Cu-based catalysts highlight the importance of advanced *in situ* and *operando* characterization techniques to understand and correlate the relevant parameters that are responsible for enhanced CO_2RR properties.

2.5 Oxide-Derived Cu

The rapid *in situ* removal of oxygen from oxidized Cu electrodes during the reducing potentials of the CO_2RR leads to porous, inhomogeneous surface structures. These oxide-derived Cu catalysts are of high interest since they frequently exhibit improved CO_2RR performance.[8, 19] In particular, oxidized Cu materials can be either synthesized by thermal oxidation,[72, 73] anodic[30, 74] and plasma treatment[75, 76] of metallic Cu structures or by the direct synthesis of Cu(I) oxides via electrodeposition[77, 78] and wet-chemical synthesis procedures.[61, 79] The CO_2RR performance of these materials showed an enhancement of the selectivity toward C-C coupled products, while methane was suppressed and the onset potentials were decreased.[80-82] The improvements were assigned to their rough morphology (leading to a high ECSA with a greater number of surface sites)[8, 80] and their high density of grain boundaries/surface defects (leading to a higher local pH).[79, 83]

In recent years, the role of remaining oxygen in the form of Cu^+ on the surface or residual subsurface oxygen during CO_2RR has developed as a topic of debate. *Ex situ* characterization methods that were used in some studies in the past, such as X-ray photoelectron spectroscopy (XPS) or energy-dispersive X-ray spectroscopy (EDX)-TEM are not accurate to determine the oxidation state due to the fast reoxidation of Cu-based catalysts.[84-86] Instead, *in situ*/*operando* techniques must be implemented.[19] Studies of oxide-derived Cu surfaces using *in situ* Raman spectroscopy[87, 88] and isotopic labeled ^{18}O oxygen[89] revealed that the reduction of Cu_2O to Cu is energetically and kinetically favored compared to the start of the electrocatalytic CO_2RR. On the other hand, *operando* X-ray absorption spectroscopy (XAS) revealed the existence of Cu^+ during reaction conditions of plasma-oxidized Cu catalysts[90] and Cu_2O-derived nanocubes,[79] which correlated with high C_{2+} selectivities. Additionally, theoretical simulations showed an improvement of kinetics and thermodynamics with subsurface oxygen in terms of CO_2 activation and dimerization.[37, 91] Besides, Cu^+ species were also stabilized or regenerated by different approaches such as by adding iodine species[92, 93] or boron dopants[94, 95] or by performing pulsed CO_2RR into the oxidation regime of Cu.[96, 97] Nevertheless, it remains challenging to determine oxygen species at the surface where the CO_2RR takes place.

The applied *operando* techniques can often not exactly determine the position of the detected oxygen in the catalyst or are not sensitive enough.[8] Thus, one needs to combine complementary surface-sensitive *operando* methods to shed more light on the role of oxygen in Cu-based catalysts and link its composition to the catalytic function.

2.6 Bimetallic Effects

Bimetallic Cu-based catalysts have emerged as promising materials for CO_2RR due to their ability to steer the selectivity toward a particular product and improve the activity and stability of the catalyst. There are three major bimetallic systems with distinct selectivity trends following the classification that was previously introduced in Section 2.1.[14, 15] In particular, the combination of Cu with an H_2-producing metal (Fe, Ni, Pt) was found to mainly increase the HER activity and selectivity,[98, 99] while the combination of Cu with an $HCOO^-$ producing metal (In, Sn) led either to an increase in the CO selectivity and HER suppression;[100, 101] or to an increase in the $HCOO^-$ production.[102, 103] Here, the focus lies on the combination of Cu with a CO-producing metal (Ag, Au, Zn), which can lead to the enhancement of the desired C_{2+} products;[104-108] besides an increase in the CO selectivity.[108, 109]

The addition of a second metal to a Cu catalyst can introduce a variety of effects, including electronic, geometric, and tandem effects, that influence the behavior of these systems (Figure 2.5). Since these effects are often intertwined, it can be complex and challenging to disentangle the behavior of these catalysts.

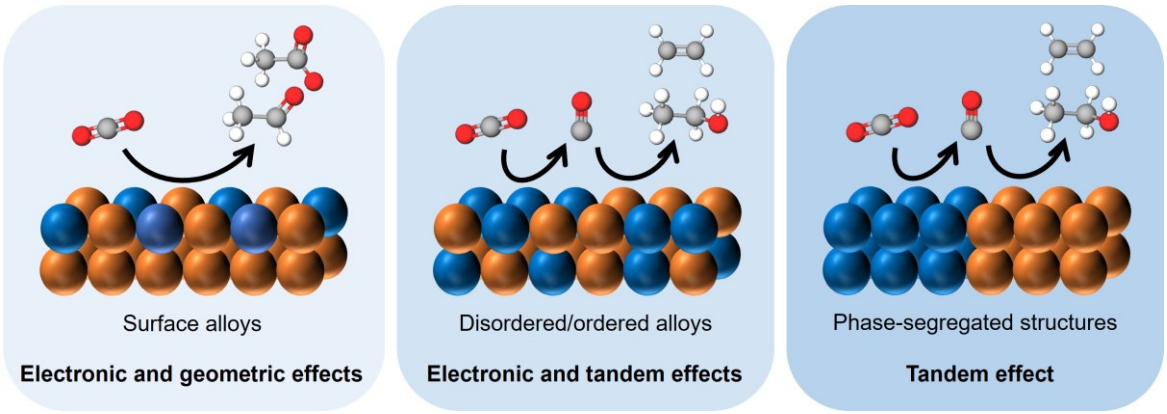

Figure 2.5 Schematic illustration of different bimetallic Cu-based nanostructures and their selectivity trends of the CO_2RR with proposed effects on the catalysis by the introduction of a second CO-producing metal.

2.6.1 Electronic and Geometric Effects

The electronic effect results from the changes in the electronic structure of the Cu catalyst, which alters the binding energies of the reaction intermediates according to the d-band theory. This theory states that the behavior of the occupied d orbitals on the catalyst surface strongly correlates with the local electron transfer and surface chemisorption.[110] On the other hand, the geometric effect alters the atomic arrangement of the active sites, changing the way how the adsorbates interact with the surface and each other. The electronic and geometric effects often play a crucial role in bulk alloys, surface alloys, near-surface alloys, and guest metal-modified

surfaces.[8] For example, Clark et al. prepared CuAg bimetallic electrodes and surface alloys that decreased the competing HER, while C_{2+} oxygenated products, particularly the carbonyl-containing products, were enhanced.[111] This was linked to the formation of a CuAg surface alloy, as shown by *ex situ* XPS, that introduced a compressive strain into the Cu surface, weakening the adsorption energy of *H. The suppressed HER and the reduced oxophilicity of the strained Cu led then to reduced rates of C-O bond scission, resulting in the observed product outcome toward more oxygenated products. Higgins et al. observed a similar trend for CuAg thin films, including the suppression of the HER and the increase of oxygenated C_{2+} products.[112] An increase in the Ag content was also accompanied by an increase in the activity and selectivity toward CO. The significant selectivity improvements were here correlated with the high Ag miscibility in Cu. Moreover, DFT simulations confirmed that Ag doping in Cu weakens the binding energy of *H species, as previously assumed.

Furthermore, Jeon et al. studied the correlation between the selectivities of size-controlled CuZn NPs (~5 nm in diameter) and the initial composition of Cu and Zn, as well as the extent of alloying between Cu and Zn during CO_2RR.[113] Time-dependent *operando* X-ray absorption fine structure (XAFS) data revealed that Cu-ZnO NP structures at the initial stage of the CO_2RR were selective for methane production, while CuZn NPs with a high degree of CuZn alloy (brass), evolving over the course of the CO_2RR, were mainly selective for CO and H_2. The shift of the d-band center of Cu away from the Fermi level due to CuZn alloying was suggested as the reason for this phenomenon, as it weakened the binding strength of *CO. Timoshenko et al. introduced a new artificial neural network (NN) method to further analyze the *operando* extended X-ray absorption fine structure (EXAFS) data of these CuZn NPs during CO_2RR.[114] They demonstrated that the Cu-M interatomic distance, which impacts the geometric effect, could be used as a descriptor for the observed catalytic selectivities. The NPs at the initial stage of CO_2RR (favoring methane) had shorter interatomic distances similar to those of Cu, while the NPs at a later stage of CO_2RR (favoring CO) developed longer Cu-M distances. Rüscher et al. also emphasized the importance of the alloy type (electronic structure) of cubic-shaped ZnO-Cu_2O-derived nanocatalysts by *operando* NN-EXFAS.[115] They observed that Zn-rich hexagonal close-packed-type (hcp) structures favored the formation of H_2 and CO, while diluted Cu-rich face-centered cubic-type (fcc) structures in combination with sub-surface Cu(I) favored C-C coupling toward C_{2+} products.

2.6.2 Tandem Effects

The enhancement in activity and selectivity toward C-C coupled and oxygenated products are also many times attributed to the tandem catalysis phenomenon, where CO is believed to be

transferred from the CO-generating co-catalyst site to the C-C coupling Cu sites through either surface diffusion or an increase in local CO concentration (known as the "CO spillover" effect). This effect is commonly observed in phase-segregated structures but has also been attributed to a beneficial effect in alloy structures.[18] One example is an Ag-covered Cu_2O nanowire catalyst developed by Gao et al., which increased the CO_2RR toward ethylene compared to the bare Cu_2O catalyst.[116] *Operando* SERS revealed the intermediate formation of CO at Ag sites, which were assumed to undergo a subsequent spillover and hydrogenation on the Cu nanowires. In another study, Lee et al. prepared phase-separated and phase-blended Ag-Cu_2O electrodes.[117] Both structures demonstrated an enhancement toward ethanol in comparison to the Cu_2O electrode. Interestingly, the phase-blended Ag-Cu_2O catalyst exhibited a higher ethanol selectivity than the phase-separated Ag-Cu_2O catalyst. They concluded that an optimal distribution and distance between Ag and Cu was important to transfer CO from the Ag to the Cu sites in order to enhance the selectivity toward ethanol.

In the case of Cu-Zn-based catalysts, the changes in the selectivity were frequently assigned to the tandem effect, which might also interplay with electronic effects. A recent study on an alloyed CuZn nanocatalyst by Varandili et al. revealed the importance of the composition and structure for the selectivity trends.[118] In particular, the catalyst with a lower Zn content (5 %) was selective for methane formation, while the catalyst with a higher Zn content (19 %) was more selective toward ethanol. DFT calculations showed that isolated Zn atoms modified the electronic properties of the catalyst in a way that the methane-producing *CHO intermediate was stabilized. In turn, higher amounts of Zn released more CO from the Zn sites, and thus, the CO concentration increased to enhance the C-C coupling via a tandem mechanism. Furthermore, Ren et al. incorporated Zn into Cu using atomic layer deposition, which increased the CO_2RR toward ethanol.[107] CO was again proposed to be produced from the Zn sites, which could facilitate the further reduction on the Cu sites. Additionally, *operando* SERS gave evidence that the CO binding configuration on the Cu sites was altered by the introduction of Zn, which might be important for the efficient formation of ethanol. Feng et al. further prepared a CuZn alloy catalyst, which tuned the selectivity toward ethylene.[119] They explain that the close distance between Cu and Zn atoms on the surface can stabilize the *CO intermediate, which is then transferred from the Zn to the Cu sites, where further dimerization to ethylene occurs.

These examples demonstrate the conflicting trends in the literature, such as the production of hydrocarbons versus oxygenated products, which probably arise from differences in size, morphology, stoichiometry, and arrangement (degree of alloying/segregation) of the bimetallic

systems.[18] Additionally, many studies only involve the characterization of the as-prepared sample and post-mortem *ex situ* characterization, making it difficult to distinguish the effects of bimetallic systems during reaction conditions that are crucial for a rational catalyst design. Therefore, *in situ* and *operando* methods are essential for gaining deeper insights into the interplay between Cu and the second metal, such as the reversible or irreversible formation of bulk or surface alloys during the reaction.

2.7 Pulsed Potential CO_2RR

In the previous sections, so far, the CO_2RR was only considered under a continuously applied static potential. However, an alternative approach to adjust the electrocatalytic properties, particularly the selectivity and stability, is the application of dynamic potential pulse conditions, where the potential is modulated alternatingly. This approach has the benefit of allowing the catalytic properties to be adjusted *in situ* without the need for prior re-designing of the catalyst and electrolyte system. The key parameters that can be manipulated include the applied anodic (E_a) and cathodic (E_c) potential, as well as the duration of the anodic (t_a) and cathodic (t_c) potential pulses (Figure 2.6 a).[20] In the following section, the primary effects of pulsed CO_2RR will be discussed, such as the compositional and morphological changes in the catalyst as well as the modifications in the adsorbate structure and hydrodynamics of the electrical double layer that have been investigated in the literature (Figure 2.6).

2.7.1 Compositional Effect

By applying a positive oxidative potential, the composition of Cu-based catalysts can be altered (Figure 2.6 b). For instance, the oxidation state can be adjusted, and in the case of bimetallic catalysts, the alloy structures may change as well. Figure 2.7 illustrates Pourbaix diagrams of Cu and Zn, which depict the correlation between the applied potential, pH value, and different oxidation states of the metals. For instance, in the case of Cu, transitioning from -1.0 V to 0.2 V_{SHE} (versus the standard hydrogen electrode) at a pH of 8-9 would cause the Cu oxidation state to shift from metallic Cu to Cu_2O. However, it should be noted that Pourbaix diagrams only represent conditions at the equilibrium phase and may not apply to non-equilibrium pulse conditions.[20] Hence, careful determination of the oxidation states under operating conditions is necessary, *e.g.*, by performing cyclic voltammetry (CV) coupled with time-resolved *operando* methods.

As discussed in Section 2.5, the presence and impact of Cu(I) species during static CO_2RR is still a topic of debate. The use of potential pulses can provide better insights into this phenomenon, as Cu(I) can be regenerated during the anodic pulse, which is also

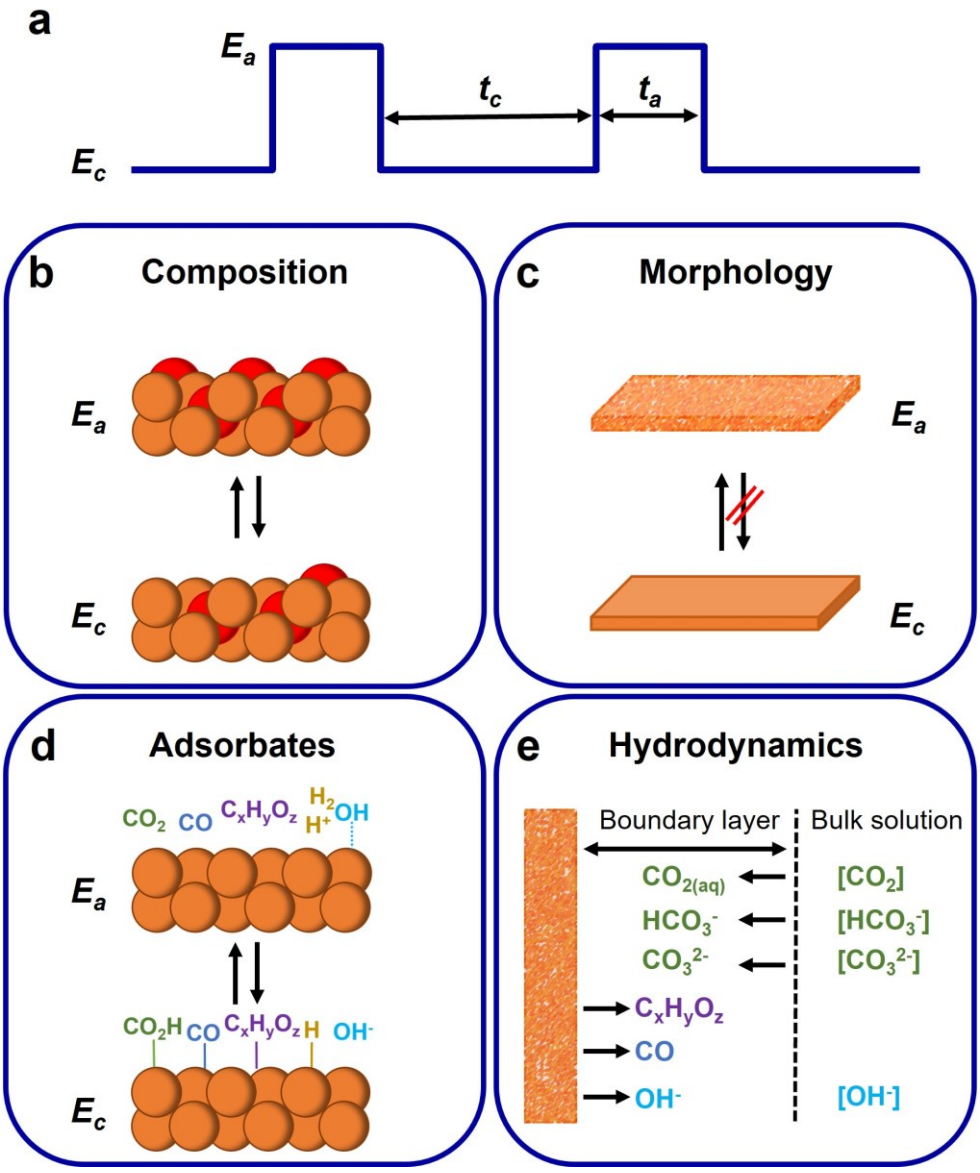

Figure 2.6 Illustration of the main effects that occur reversibly or irreversibly during pulsed potential CO_2RR. (a) Exemplary square-wave potential pulse where pulse parameters are noted. (b-e) Potential pulse effects such as the compositional, morphological, adsorbates, and hydrodynamics effects. (e) is redrawn from Kimura et al.[120]

thermodynamically feasible according to the Pourbaix diagram (Figure 2.7 a). A recent investigation by Arán-Ais et al. of pulsed potential CO_2RR on Cu(100) single crystals (E_c = -1.0 V_{RHE}, E_a = +0.6 V_{RHE}, $t_c = t_a$ = 1 s) suggested that the enhanced ethanol selectivity can be linked to the *in situ* regeneration of Cu(I) species.[96] Moreover, the coexistence of Cu(I) and Cu(0) species was crucial for the observed improvement, which was demonstrated by quasi-*in situ* XPS measurements. Additionally, Lin et al. utilized time-resolved *operando* XAS during pulsed CO_2RR (E_c = -1.0 V_{RHE}, E_a = +0.5 V_{RHE}, $t_c = t_a$ = 10 s) and confirmed the generation of Cu(I) during the anodic pulse, as well as residual Cu(I) during the cathodic pulse.[121]

Furthermore, Tang et al. performed pulsed CO_2RR at lower temperatures between 5 and 15 °C (E_c = -1.0 V_{RHE}, E_a = +0.6 V_{RHE}, t_c = t_a = 1 s), which favored the ethanol over the ethylene selectivity.[122] This was attributed to the slower reduction of Cu(I) to Cu(0) during the cathodic pulse. Thus, Cu(I) likely exerts a positive influence on the C_{2+} selectivity. Timoshenko et al. further performed pulsed CO_2RR with varying pulse duration (E_c = -1.0 V_{RHE}, E_a = +0.6 V_{RHE}, t_c = 0.5-32 s, t_a = 0.5-32 s) on oxide-derived Cu nanocubes to investigate the (reversible) formation of different types of Cu oxides and their catalytic function by the use of time-resolved *operando* XAS.[97] They found that distorted Cu(I)/Cu(II) species formed at short anodic pulses (below 2 s) enhanced the ethanol selectivity, while bulk-like Cu oxides formed at long anodic pulses (especially above 3 s) enhanced the CO selectivity.

However, regarding Cu-based bimetallic systems, there is only one study by Ishimaru et al. on a bimetallic CuAg-alloyed system under pulsed CO_2RR (varied E_c and E_a, t_c = t_a = 5 s), which improved the C_{2+} selectivity. Although the researchers speculated on the effect of CO adsorption from Ag, they did not investigate or consider the compositional changes in the CuAg alloy structure, which could occur under such oxidizing Cu conditions.[105]

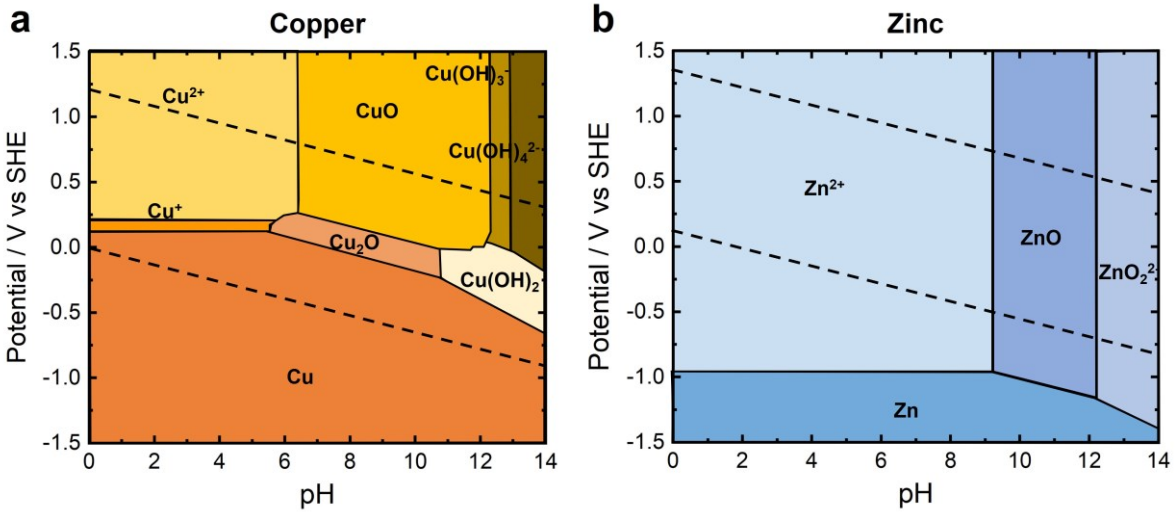

Figure 2.7 Pourbaix diagrams (potential/pH diagrams) of Cu and Zn at 25 °C redrawn from Beverskog et al.[123, 124] The dashed green lines show the stability limits of water in the system.

2.7.2 Morphology Effect

Potential pulses between cathodic and anodic potentials can cause significant modifications in the surface morphology of the catalyst, particularly when oxidative anodic potentials are applied, leading to dispersion/dissolution-redeposition processes of Cu species (Figure 2.6 c). These morphological modifications involve microscopic roughening of the surface, resulting in defective surface structures with larger grain boundaries, as well as crystallographic faceting and reconstruction toward a specific surface orientation. As outlined in Section 2.4.1,

morphological changes can have a noteworthy influence on the catalyst's activity and selectivity toward different products. In one of the first potential pulse studies, Lee et al. showed changes in the surface structure of Cu after pulsed CO_2RR (E_c = -2.1 V_{SCE}, E_a = +0.0 V_{SCE}, t_c = 10 s, t_a = 5 s) based on *ex situ* scanning electron microscope (SEM) images.[125] They concluded that this structural change avoided the adsorption of amorphous graphite on the catalyst' surface, which led to improved long-term stability toward methane. Furthermore, Engelbrecht et al. studied Cu sheet electrodes which demonstrated stable hydrocarbon selectivities and suppression of the HER during long-term pulsed CO_2RR (E_c = -1.5 to -1.8 $V_{Ag/AgCl}$, E_a = -0.88 to +0.15 $V_{Ag/AgCl}$, varied pulse lengths). They observed a modification in the surface structure by *ex situ* SEM, resulting in the reorganization of grain formations at higher anodic potentials.[126] Additionally, Jeon et al. revealed that pulsed CO_2RR (E_c = -0.7 V_{RHE}, E_a = +0.9 V_{RHE}, $t_c = t_a$ = 1 s) led to the introduction of defective interfaces and grain boundaries on the surface of a cubic-shaped Cu nanocatalyst, as observed by *ex situ* microscopy techniques (SEM and TEM).[34] This was found to correlate with the observed increase in the production of C_{2+} products. These three studies highlight the impact of irreversible changes in the catalyst morphology. In the Cu(100) single crystal study by Arán-Ais et al., potential pulses to E_a = +0.6 V_{RHE} created cubic islands as evidenced by *ex situ* AFM.[96] However, the change in faceting could not be solely responsible for the high ethanol yields they achieved, which was instead rather attributed to the formation of Cu(I) species. Additionally, the ECSA in this study remained almost unchanged after pulsed CO_2RR compared to static conditions while surface steps were introduced. From these studies, it appears that the morphology changes during pulsed CO_2RR, such as the introduction of grain boundaries and surface steps, as well as surface faceting, are often intertwined and greatly impact on the catalytic function.

2.7.3 Adsorbate Effect

Besides the modifications in the catalyst structure, potential pulses have a significant impact on the adsorbate coverage and the rearrangement of the electrochemical double layer. Each pulse modulates the electrode polarization, leading to the adsorption and desorption of important adsorbates, including H^+, OH^-, carbonate ions, *CO, and other intermediates of the CO_2RR as well as hydrated cations of the electrolyte (Figure 2.6 d).[20] To explore this phenomenon, various studies have employed non-oxidizing and less morphologically disruptive conditions. Arán-Ais et al. discovered a positive effect on the ethanol formation on Cu(100) single-crystals under non-oxidizing pulsed conditions at E_a = 0.0 V_{RHE}.[96] They speculated that electrode polarization leads to a lower H_{ad} and higher OH_{ad} surface coverage, which enhances the selectivity toward oxygenated products. Other researchers have expressed similar opinions.[127, 128] Kimura et al.

further concluded that OH_{ad} adsorption promotes the favorable CO_{atop} binding, while inhibiting its transformation into the inactive CO_{bridge} species.[129] Moreover, DFT calculations demonstrated that the presence of hydroxides decreases the binding energy of CO while stabilizing the *OCCO intermediate, thus favoring the CO dimerization step.[130] Nevertheless, by going up to oxidizing anodic potential pulses, the change in the Cu oxidation state might also modify the adsorbate configuration. For example, Chou et al. performed time-resolved *in situ* surface-enhanced infrared absorption spectroscopy (SEIRAS) on Cu and experimentally evidenced that Cu oxidation eliminated the poising CO_{bridge} species.[131] De Ruiter et al. further utilized time-resolved *in situ* SERS to understand the observed activation of CO_2 to CO at low cathodic overpotentials during pulsed CO_2RR (E_c = -0.55 V_{RHE}, E_a = +1.0 V_{RHE}, t_c = 150 s, t_a = 10 s).[132] They correlated this behavior to the increase in the *CO vibrations directly after applying an oxidative anodic potential together with the formation of an active copper carbonate hydroxide species during the anodic pulse. Besides, Jeon et al. detected an increase in methane selectivity during pulsed CO_2RR of the cubic-shaped Cu nanocatalyst when the anodic potential was raised up to +1.2 V_{RHE}.[34] They attributed this behavior to the consumption of OH^- due to the regeneration of Cu_2O species during the anodic pulse as demonstrated by *operando* SERS. This resulted in an OH-poor environment and, thus a decrease of the local pH value favoring methane formation. Next to these dynamic effects, potential pulses can also reverse the deactivation of the electrodes from impurities and irreversibly adsorbed intermediates, thereby improving the catalyst's lifetime and performance stability.[125, 126, 133] Altogether, the former studies highlight the dynamic interplay between the different surface adsorbates and give evidence of particular adsorbate motives in pulsed CO_2RR. Nevertheless, obtaining further direct experimental observations of the adsorbate nature and surface coverage is crucial to comprehend how to adjust the product selectivity to achieve the targeted C_{2+} products.

2.7.4 Hydrodynamics and Mass Transfer Effects

Other aspects of any electrochemical process at the solid/liquid interface are the kinetic aspects (*e.g.*, hydrodynamics) and the mass transport limitation effects (Figure 2.6 e). Mass transport of reactants is crucial for CO_2RR, but concentration polarization can limit it as reactants near the electrode surface become depleted, which slows down the reaction rate. In the mass transport limited regime, the overall reaction rate is restricted by the transport (diffusion, migration, and convection) of the reactants through the boundary layer to the active site.[20] This is more important at higher current densities due to the fast consumption of the reactants. In static CO_2RR, CO_2 diffusion can be rate-limiting due to its low solubility in an aqueous electrolyte. The thickness of the boundary layer also plays a significant role in determining the

mass transport rate. Here, pulsed potential CO_2RR offers a strategy to replenish the CO_2 levels within the boundary layer. In order to achieve this, the duration of the anodic pulse must be sufficiently long (typically lasting several seconds), or the boundary layer must be decreased, for instance, through convection.[134, 135] In a study conducted by Kim et al., it was demonstrated that the replenishing effect could increase the selectivity of C_{2+} products during pulsed CO_2RR.[135] Through simulations and estimations of the local CO_2 concentrations, they discovered that there was an elevation in CO_2 concentration at cathodic pulse durations that were sufficiently short (less than 12 s). Besides, Kimura et al. investigated pulsed CO_2RR on a rotating disk electrode with varying pulse durations and compared the results to the static CO_2RR.[120] They found that the improved mass transfer alone could not account for the enhanced selectivities under pulsed conditions at short pulse length in the millisecond range, as the static CO_2RR measurements at elevated convection exhibited significant discrepancies in the catalytic selectivity, despite a similar mass transport of the reactants. In general, it is crucial to comprehend and optimize the transport phenomena, which are especially significant for pulses that last in the range of seconds.

To summarize, pulsed potential CO_2RR is characterized by a complex and dynamic interplay between various interconnected effects. One critical parameter is the applied anodic potential, which can cause changes in the electrical double layer at lower potentials or induce the oxidation/reduction of the catalyst at higher potentials, also leading to morphological changes. The second key parameter is the pulse length, which can be used to adjust the electrocatalytic properties. Short pulses in the millisecond range affect the adsorbate coverage, while longer pulses in the second range cause compositional and roughening changes and increase local CO_2 concentration. However, the rapid transformations involved in pulsed potential CO_2RR make it difficult to fully understand the underlying mechanisms. To gain a complete mechanistic picture, time-resolved *in situ* and *operando* techniques are necessary to track the structural, compositional, and adsorbate alterations that occur during each individual pulse.

2.8 Scientific Objectives

After reviewing the theoretical background of the CO_2RR on Cu-based catalysts under both, static and pulsed potential conditions, several unanswered questions arise. Addressing these questions would aid the catalyst design toward valuable C_{2+} products and provide further mechanistic insights. The open questions are:

1) **How are oxide-derived Cu catalysts modified by the introduction of Ag to enhance the catalytic properties toward C_{2+} liquids?**
   Numerous studies have indicated significant improvements in the catalytic properties of Cu-Ag catalysts for CO_2RR, resulting in the production of valuable products like ethanol or ethylene. However, the current comprehension of the catalyst composition and its influence on the adsorbate structure under operating conditions is still limited, hindering the rational design of bimetallic catalysts toward specific products. To address this knowledge gap, Chapter 5 of this work aims to provide deeper insights into the Cu-Ag catalyst system through the implementation of advanced characterization methods, specifically *operando* Cu and Ag K-edge X-ray absorption spectroscopy and *operando* surface-enhanced Raman spectroscopy.

2) **What adjustments are required in the surface composition and interfacial adsorbate structure of oxide-derived Cu catalysts to improve the selectivity of ethanol?**
   The relationship between the oxidation state of Cu, the adsorbates and their coverage on the electrode surface of oxide-derived Cu catalysts remains insufficiently understood, particularly in the field of (pulsed potential) CO_2RR. Chapter 6 of this work aims to advance the understanding of this intricate interplay, which is crucial for fine-tuning selectivities toward energy-dense products such as ethanol. To accomplish this, a state-of-the-art sub-second time-resolved *operando* surface-enhanced Raman spectroscopy technique will be employed, which enables, for the first time, the direct observation of essential *CO and $*OH^-$ adsorbates, as well as the introduction of surface oxygen during the oxidative pulse in pulsed CO_2RR.

3) **How does a bimetallic Cu-Zn catalyst react under pulsed potential CO_2RR conditions?**
   The implementation of pulsed potential CO_2RR conditions has demonstrated remarkable potential for controlling the selectivities of Cu catalysts. Nonetheless, the investigation of bimetallic Cu-based systems during these conditions is rarely explored, despite their

potentially fascinating properties since the redox characteristics of the two metals can be adjusted. Chapter 7 of this thesis will investigate a Cu-Zn system, which exhibits distinctly different redox properties as predicted by the Cu and Zn Pourbaix diagrams (Figure 2.7). Depending on the anodic potential, the selectivities will be tuned to different products, including ethanol. To gain deeper insight into this behavior, highly advanced sub-second time-resolved techniques such as *operando* Cu and Zn K-edge X-ray absorption spectroscopy, *operando* X-ray diffraction, and *operando* surface-enhanced Raman spectroscopy will be employed. The synergistic combination of these techniques will lead to the establishment of significant structure-selectivity correlations, encompassing various aspects such as the composition of the catalyst, its crystalline structure, and adsorbate structure.

Additionally, Chapter 3 will provide a detailed description of the methodology employed in this thesis, including various *ex situ*, *in situ*, and *operando* techniques, along with their theoretical basis and experimental setups. Furthermore, Chapter 4 will outline the synthesis procedures that were developed to prepare well-controlled and defined nanoparticle catalysts. Finally, Chapter 8 will provide a summary of the key findings obtained by the studies in this thesis and will present further perspectives.

3. Experimental Methods

This chapter aims to provide a comprehensive overview of the fundamental principles and techniques of electrochemistry, which form the foundation for the electrochemical reduction of CO_2, followed by a detailed description of the employed *ex situ*, *in situ,* and *operando* characterization techniques and their fundamental underlying principles.

3.1 Electrochemistry

Electrochemistry is a branch of chemistry that deals with the flow of electrons or ions at the interface between an electron conductor and an ion conductor. This encompasses a broad range of phenomena and technologies, such as corrosion, batteries, electrolysis, and electroplating. Here, the focus is centered on heterogeneous electrochemical systems with a solid-liquid interface, where the electrical charge is transported across the interface through the movement of electrons (and holes) between a solid electronic conductor (electrode) and a liquid ionic conductor (electrolyte). Experimentally, it is not possible to work with a single interface, and instead, electrochemical cells must be used.[136-139]

3.1.1 Electrochemical Cells

Electrochemical cells are composed of two half-cells, each consisting of an anode and cathode electrode. The anode electrode acts as the side of oxidation (loss of electrons), while the cathode electrode serves as the side of reduction (gain of electrons). The electrodes are placed in an electrolyte, where the ions can freely move in. When a potential E is applied between the electrodes, different processes can occur, *e.g.*, a chemical reaction that results in the transfer of electrons across the electrode/electrolyte interface, leading to a current flow I in the external circuit. This transfer of electrons is represented by the total charge Q and is referred to as a Faradaic process. Thereby, Faraday's law describes the proportionality between Q and the amount of the generated product. On the other hand, non-Faradaic processes do not involve charge-transfer reactions but instead involve adsorption, desorption, and charging processes that can also lead to a current flow.[136-139]

When studying an electrochemical reaction of interest, the focus is usually only on one half-side of the electrochemical cell, with the electrode being referred to as the working electrode

(WE). The other half of the cell is known as the counter electrode (CE), and together they built up a simple two-electrode setup. However, in order to define and control the potential of the WE to a reference point, a three-electrode setup must be implemented. This setup includes a third electrode, referred to as the reference electrode (RE), which is placed close to the WE. In this work, all recorded potentials are referenced with respect to the reversible hydrogen electrode (RHE), which correlates with the pH value under standard conditions (25 °C and 1 atm) as derived from the Nernst equation:

$$E_{RHE} = E_0 - 0.059 \cdot pH \tag{3.1}$$

where E_{RHE} is the electrode potential versus RHE, and E_0 is the standard reduction potential (which is 0 V for the hydrogen and 0.205 V for the Ag/AgCl in 3.5 mol/L KCl).

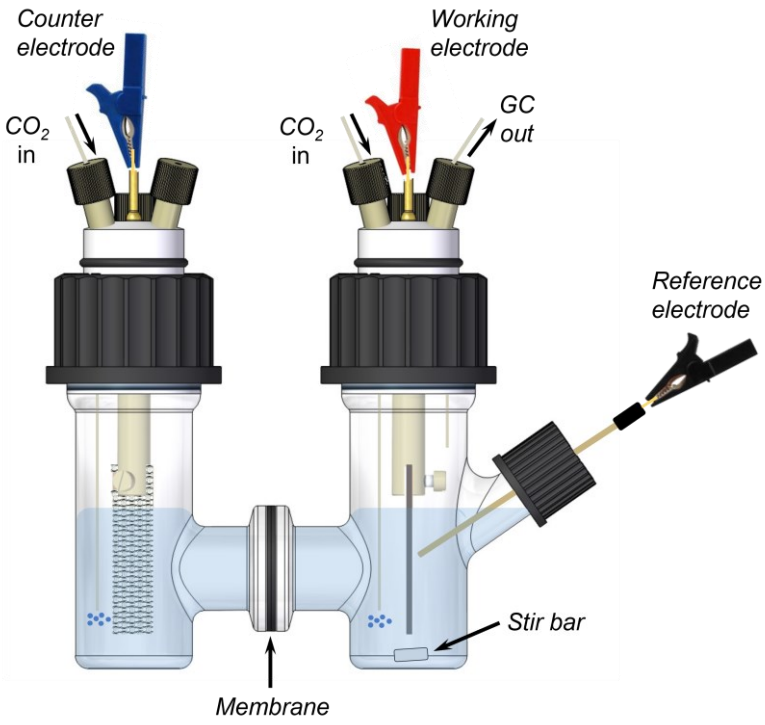

Figure 3.1 Scheme of the electrochemical H-type three-electrode cell setup used for the CO_2RR measurements.

For the CO_2RR measurements, an electrochemical H-type glass cell (three-electrode setup) is utilized, as schematically shown in Figure 3.1. This cell is composed of two separate compartments: the WE (cathode) side, where the CO_2RR and the competing hydrogen evolution reaction (HER) take place, and the CE (anode) side, where the counter reaction, in this case, the oxygen evolution reaction (OER), occurs. The WE consists of one of the Cu-based electrocatalysts developed in this work, while the RE is either a commercial RHE or a leak-free Ag/AgCl electrode. The CE is made up of a high surface-area Pt gauze mesh. Both

compartments are filled with 0.1 M potassium bicarbonate solution ($KHCO_3$), which is continuously saturated with CO_2 with a flow rate of 20 mL min^{-1}. The two compartments are air-tight and separated by an anion exchange membrane (Selemion^{TM}) to prevent the diffusion of reaction products to the CE. Additionally, the WE side is directly connected to a gas chromatograph (GC) for online measurements of the gaseous products.

3.1.2 Electrochemical Techniques

In the following section, the electrochemical techniques that are used in this thesis will be shortly introduced.

Chronoamperometry

Chronoamperometry (CA) is one of the most common techniques in electrocatalysis. In a CA, a constant potential E_i is applied at the WE, and the resulting current response is recorded as a function of time commonly in an *I-t* curve (Figure 3.2). During the first few seconds of a CA, high charging currents I_c are generated, which decay exponentially. These are followed by the generation of Faradaic currents I_F from reduction or oxidation processes, which usually decay much slower, as described in the Cottrell equation (which describes the current response of planar electrodes in a reversible redox reaction). One application of CA is the potential-controlled electrolysis, such as the CO_2RR experiments conducted in this work, where CA is coupled with measurements of the resulting products to determine the Faradaic efficiencies (FE). A CA can also be conducted over a longer time range to obtain information about the activation/deactivation behavior and stability of the catalyst.

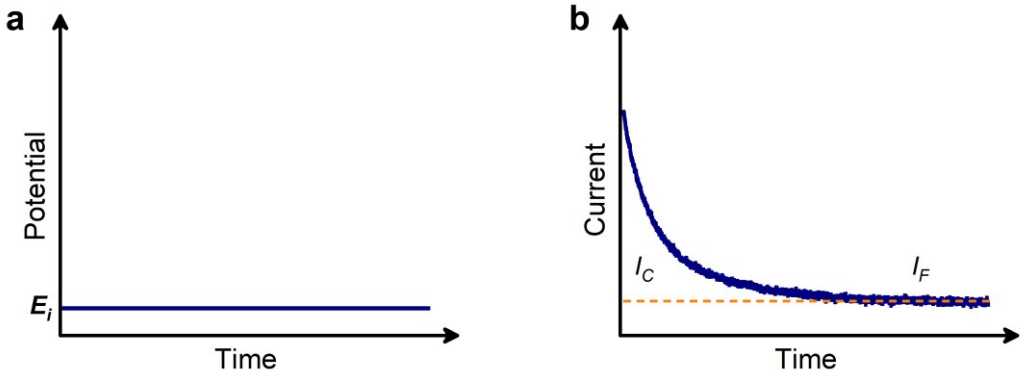

Figure 3.2 Exemplary chronoamperometry. (a) Applied potential over time. (b) Measured current over time (*I-t* curve) with charging current I_C and Faradaic current I_F region.

Pulsed Electrolysis

In pulsed electrolysis (PE), the applied potential or current is sequentially altered between two values. Here, the focus is centered on the potential-controlled PE experiments, where the

response of the applied potential is measured by the current similar to a CA. The simplest shape of a pulsed potential is the square wave profile, as shown in Figure 3.3 a, together with the key control parameters such as the electrocatalytic cathodic potential E_c and the anodic potential E_a as well as the respective pulse lengths t_c and t_a. The value of E_a is especially important to either change the redox state of the catalyst or rather clean the catalyst surface from its adsorbates, as explained in Chapter 2.7. Similar to a static CA, the current profile of a cathodic pulse (shown in Figure 3.3 b) can be classified into three regions (I-III). However, in the potential pulse case, regions (I) and (II) carry greater significance and are influenced by the preceding application of an anodic pulse, whereas in the static CA case, region (III) is the primary contributor. (I) results from the charging current I_C and decays exponentially, (II) reflects the Faradaic current I_F, and (III) only occurs if the cathodic pulse length lasts for several seconds to hours, where the current decreases due to degradation or deactivation of the catalyst (fragmentation, Ostwald ripening, dissolution, detachment, agglomeration, reshaping, or poisoning).[20]

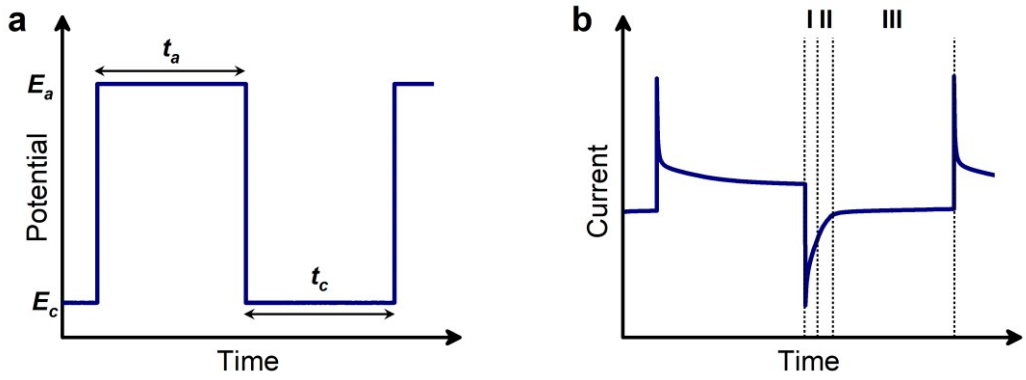

Figure 3.3 Exemplary pulsed electrolysis. (a) Applied potential over time. (b) Measured current over time.

Linear Sweep Voltammetry

Linear sweep voltammetry (LSV) is a basic potential sweep method. In this case, the potential is swept linearly in time with a fixed scan rate v (voltage/time rate) from the initial potential E_1 in one direction until the final potential E_2, while the current at the working electrode is measured (Figure 3.4 a). Usually, the current is plotted against the changes in the potential (Figure 3.4 b). Here, this technique is used to sweep the potential slowly from the open circuit potential to the CO_2RR reduction potential region to avoid a rapid change in the potential for the catalyst. Additionally, an LSV reveals redox transitions, such as the reduction peak at E_R and the onset of the catalytic region, as indicated by a significant decrease in the current.

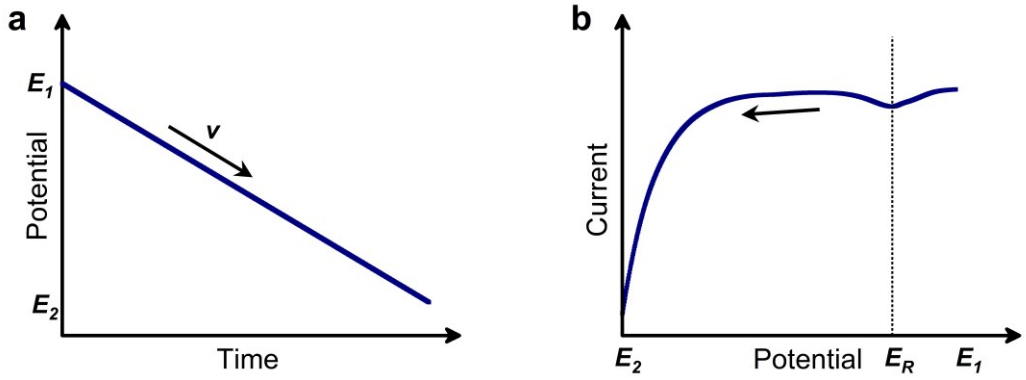

Figure 3.4 Exemplary linear sweep voltammetry. (a) Applied potential over time. (b) Measured current against the applied potential.

Cyclic Voltammetry

Cyclic voltammetry (CV) is similar to LSV, but after reaching a vertex potential E_2 the working electrode's potential is linearly swept back with the same scan rate v in the opposite direction to its initial potential E_1 (Figure 3.5 a). These cycles of potential may be repeated many times either for the activation of the electrodes or to study the chemical and electrochemical reversibility of the electrode processes. Also, here, the current usually is plotted against the applied potential (Figure 3.5 b). CVs are a powerful tool in electrocatalysis to understand the electrochemical properties of a system. In particular, they can reveal information about reversible or irreversible Faradaic processes at the electrode surface, adsorption/desorption processes, and charging. Additionally, the electrochemically active surface area (ECSA) can be estimated by the determination of the double layer capacitance C_{DL}, which results from the non-Faradaic processes in the electrical double layer (EDL) region of a CV. The EDL is a region of charged particles that forms at the interface between an electrode and an electrolyte and plays a crucial role in controlling the kinetics and thermodynamics of both electron-transfer and ion-

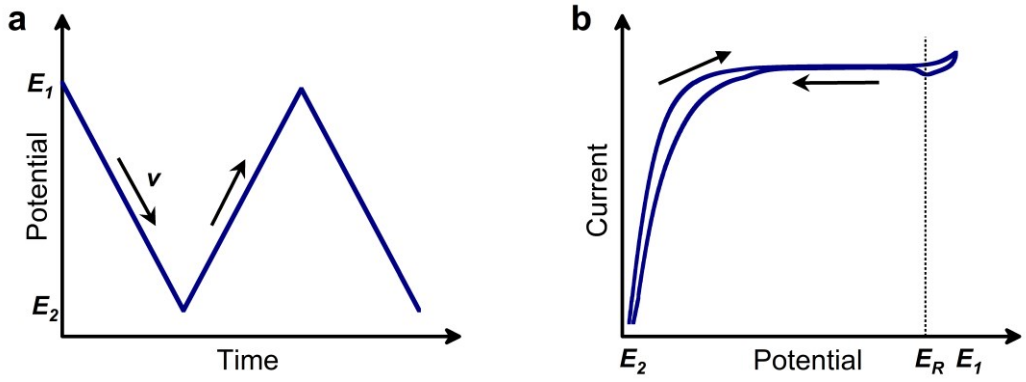

Figure 3.5 Exemplary cyclic voltammetry. (a) Applied potential over time. (b) Measured current against the applied potential.

transfer reactions at the interface.[140] Since the charging current I_C in the double layer region of a CV scales linearly with the scan rate v, C_{DL} can be extracted from the slope.

$$I_C = vC_{DL} \tag{3.2}$$

The ECSA can be subsequently determined by the obtained C_{DL} and the specific capacitance C_S of any investigated electrode and electrolyte material.[141]

$$ECSA = \frac{C_{DL}}{C_S} \tag{3.3}$$

Potentio-Electrochemical Impedance Spectroscopy

PEIS is a sensitive technique that can analyze transport processes at the solid/liquid interface in relation to contributions from diffusion and kinetics. In PEIS, a sine wave potential with a small set amplitude is applied to the WE for a wide range of frequencies, and the current response is measured as illustrated in Figure 3.9 a. One requirement of PEIS is that the potential and current need to be in a steady state. The electrochemical impedance Z follows Ohm's law and can be expressed as a complex function with a frequency-dependent resistance real part Z_{Re} and a frequency-dependent reactance imaginary part Z_{Im}:

$$Z(\omega) = \frac{\tilde{E}(\omega)}{\tilde{I}(\omega)} = Z_{Re} - jZ_{Im} \tag{3.4}$$

where ω is the angular frequency related to the applied frequency $\omega = 2\pi f$, $\tilde{E}(\omega)$ and $\tilde{I}(\omega)$ are phasors that account for the amplitude and phase ϕ of the sinusoidal function, and $j = \sqrt{-1}$

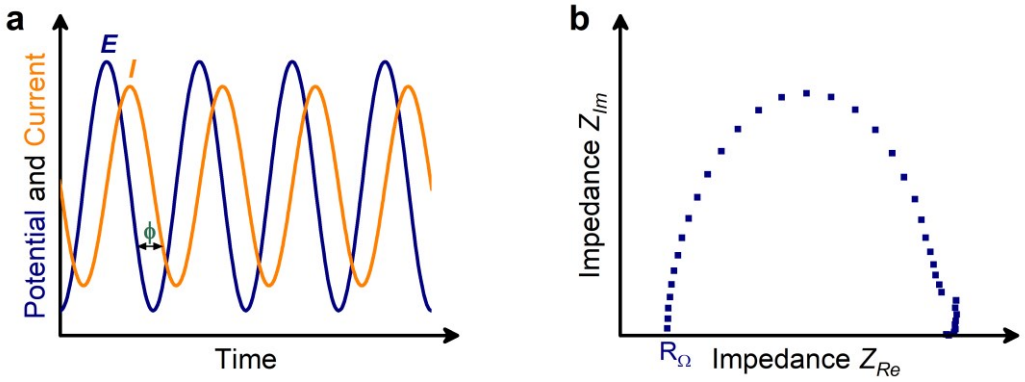

Figure 3.6 Exemplary impedance spectroscopy. (a) Applied sinus-wave potential $E = Asin\omega t$ and the current response I, which is shifted by the amplitude A and a phase-shift of ϕ in dependence of the time t at a set angular frequency ω. (b) Nyquist plot at high frequencies with kinetic control, where the imaginary part of the impedance Z_{Im} is plotted as a function of the real part Z_{Re} with the electrochemical resistance R_Ω.

is an imaginary number. The relationship between the impedance and the frequency is either displayed as a Bode plot, where log $|Z|$ and ϕ are both plotted against log ω or as a Nyquist plot, where Z_{Im} is plotted against Z_{Re}. Figure 3.9 b shows an example of a Nyquist plot of one of the electrocatalysts used in this thesis, from which the electrochemical solution resistance R_Ω could be determined. Beyond this, the data points in a Nyquist plot can also be fitted with a suitable model that provides information about the capacitive charge-transfer resistance at high-frequencies and the Warburg impedance for mass transfer processes at low frequencies.[142]
In this work, PEIS was applied only for the determination of R_Ω, which occurs due to the ohmic losses between the applied potential at the WE and the RE. Since ohmic losses are proportional to the thickness of the electrolyte layer, the RE is mounted as close as possible to the WE. However, an ohmic resistance will still occur, and the applied potential $E_{applied}$ needs to be compensated (iR corrected) with the loss of potential E_{iR} as follows:

$$E = E_{applied} - E_{iR} \qquad with\ E_{iR} = R_\Omega \cdot J \tag{3.5}$$

3.1.3 Electrocatalytic Parameters

In order to compare the electrocatalytic properties of different catalysts to each other, certain representative parameters need to be introduced. The Faradaic efficiency (FE) gives insights into the selectivity behavior of the catalyst and can be determined for the gaseous and liquid products. It describes the fraction of electrons that are transferred for an electrochemical reaction to a certain product. Beforehand, the gaseous products (such as H_2, CO, CH_4, C_2H_4, C_2H_6) are detected online during the reaction every 15 min by a gas chromatograph (GC), which is equipped with a thermal conductivity detector (TCD) and a flame ionization detector (FID). The FE_x of a gaseous product can be then calculated by the following equation:

$$FE_x = \frac{\dot{V}\, C_x\, z_x\, F}{V_M\, j_{total}\, t} \cdot 100\ \% \tag{3.6}$$

where $\dot{V}$ is the flow rate, C_x is the volume-fraction of the product detected by the GC, z_x is the number of electrons transferred for reduction to the product, F is the Faradaic constant, V_M is the molar volume, and j_{total} is the total current density during CO_2 electrolysis (in the cathodic part). Thereby, t is 1 for static CO_2RR conditions and $t = \frac{t_c}{t_c + t_a}$ for pulsed CO_2RR conditions with the duration of the cathodic pulse, t_c, and of the duration of the anodic pulse, t_a.
The liquid products are detected after the reaction by a liquid GC (L-GC) and a high-pressure liquid chromatograph (HPLC), and the FE_x for a liquid product is calculated as:

$$\mathrm{FE_x} = \frac{V\, \Delta C_x\, z_x\, F}{\Delta Q} \cdot 100\ \% \tag{3.7}$$

where V is the volume of the electrolyte, ΔC_x is the accumulated concentration of product x detected by HPLC or L-GC, and ΔQ is the total charge transferred during the electrolysis, which can be obtained by the integration of the cathodic current and subtraction of the charging current. The sum of all FE_x needs to be 100 %.

Additionally, the catalytic activity for certain products can be compared by the partial current density J. J_x for the product x can be derived from the FE:

$$J_x = \frac{\mathrm{FE_x}\, j_{total}}{A} \cdot \frac{1}{100\ \%} \tag{3.8}$$

where A is the geometric area of the electrode.

3.2 *Ex Situ*, *In Situ*, and *Operando* Characterization

Characterization plays a key role in the field of catalysis. It provides knowledge of the physical and chemical properties of the catalyst and helps to uncover the structure-reactivity or selectivity relationships of a catalytic system. The catalytic system is not static but instead can change reversibly or irreversibly during the catalytic reaction, and the active sites of the catalyst only evolve under reaction conditions.[21] This includes changes in morphology, chemical state, surface reconstructing, alloying, and segregation. There are three different terms to describe the conditions under which the employed characterization methods are performed.

Ex situ is the simplest way to analyze a catalyst. Here, the catalyst is characterized without applying any catalytic condition. It is frequently used to analyze the catalyst after the synthesis procedure in the as-prepared state and can also monitor irreversible changes in the catalyst after applying the catalytic conditions. However, *ex situ* measurements may give misleading conclusions since the catalyst might have transformed another time once the catalytic reaction was stopped (*e.g.*, reoxidation of a Cu-based system in air).

Therefore, *in situ* measurements can give more insights into the active center of a catalyst during the reaction. *In situ* measurements are conducted in the reaction environment but not under the optimal catalytic conditions. This means that the experimental setups, *e.g.*, the electrochemical cells or substrates, differ from the ones used for the real catalytic testing so that the catalytic turnover is not reached.

The ultimate goal in catalysis research is to perform *operando* measurements, where the characterization method during a catalytic reaction is coupled simultaneously with the measurement of catalytic activity and selectivity. In this way, structure-reactivity/selectivity relationships of catalysts can be established. Thereby, the active catalytic center can be determined to uncover the mechanism of the reaction. Additionally, time-resolved *operando*

measurements help to follow the dynamic changes of the catalyst in real-time, *e.g.*, to understand the changes of the selectivity over time or to follow induced dynamic changes in a pulsed potential experiment. In this thesis, *operando* investigations are extensively used to understand the behavior of the catalyst.

Table 3.1 presents the assignment of the employed techniques to the just introduced terms. These techniques will be introduced in the following sections.

Table 3.1 Assignment of employed techniques in this thesis to the *ex situ*, *in situ*, *operando* methodology.

Method	*Ex situ*	*In situ*	*Operando*
SEM, TEM	x		
SERS		x	x
XAS		x	x
XPS	x	x	
XRD	x	x	x

3.3 Electron Microscopy

Electron microscopy (EM) is a straightforward and commonly used technique for the investigation of nanomaterials providing structural and chemical information down to the level of atomic dimensions. Whereas the resolution of an optical microscope is limited by the wavelength of the visible light (Abbe limit), the resolution can be enormously improved by using an electron beam with a wavelength of less than one Angstrom (10^{-10} m), enabling almost atomic resolution. There are two principal electron-based microscopy techniques, namely transmission and scanning electron microscopy (TEM and SEM), which differ in how the images are generated.[143]

A TEM operates similarly to an optical microscope, where the optical lenses are replaced by electromagnetic lenses. In TEM, a primary electron beam passes through a condenser system, which produces parallel rays down to a certain spot. The objective lens forms an image from beams that have been either transmitted (bright-field image) or diffracted (dark-field image) when passing through the sample. Another type of TEM is scanning transmission electron microscopy (STEM), where the electron beam is focused on a fine sub-nanometer spot and scanned across the sample. Depending on the acceleration voltage (100-200 keV), modern TEM instruments can reach a resolution of 0.1-0.5 nm.

In SEM, a focused electron beam is scanned over the sample surface, and the yield of the

secondary or the backscattered electrons is detected as a function of the position of the primary beam. The contrast is caused due to the topology and composition of the surface. Modern SEM instruments reach a resolution of about 5 nm. Whereas TEM requires thin samples, even bulk samples can be measured in SEM if fitting into the microscope chamber.

Additionally, electron microscopes can be equipped with an energy-dispersive X-ray (EDX) detector. Since the energy of the emitted X-rays and their corresponding intensity are characteristic of certain elements, they allow their appropriate identification, quantification, and localization in the sample being investigated.[144, 145]

Overall, EM offers great possibilities to determine particle sizes and their distribution. However, EM gives only local information of a certain sample spot, and the sample characterization should be thus combined with other more averaging methods (*e.g.,* XRD). In general, EM experiments need to be performed in a vacuum, which makes *in situ* and *operando* experiments challenging even though *in situ* TEM shows promising advances.[146] In this thesis, *ex situ* TEM and SEM are utilized to compare the catalyst structure before and after the reaction.

3.4 Surface-Enhanced Raman Spectroscopy

Surface-enhanced Raman spectroscopy (SERS) has recently gained strong relevance as a spectroscopic tool in the field of electrocatalysis. SERS is a surface-sensitive non-destructive technique that enhances the Raman scattering of molecules supported by plasmonic materials. Its ultra-high sensitivity and selectivity make it an ideal versatile method for *in situ* and *operando* studies to determine not only the chemical identity of the active catalytic species but also the surface species and reaction intermediates. In this way, mechanistic insights underlying the catalytic reaction can be attained. Additionally, the acquisition times of the spectra can be reduced down to the millisecond range due to the high signal intensities of SERS and improvements in optics, detectors as well as data processing, which enable to track the dynamic rearrangement of the surface species during the electrocatalytic reaction.[30, 147, 148]

3.4.1 Fundamentals of Raman Spectroscopy

SERS results from the enhancement of Raman scattering, and it is, therefore, crucial to introduce the fundamentals of Raman spectroscopy. Raman scattering, or the Raman effect, was first reported in 1928 by the Indian scientists C. V. Raman and K. S. Krishnan.[149] It is based on the scattering of photons from a molecule when electromagnetic radiation interacts with matter. The scattered photons can then be observed by their collection at an angle to the incident light.

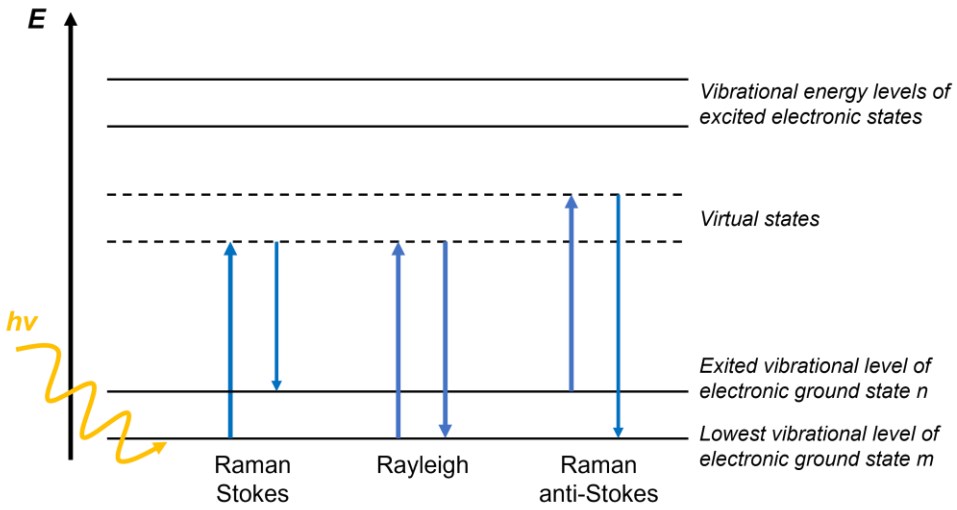

Figure 3.7 Rayleigh and Raman scattering. Rayleigh scattering occurs if the incident and scattered photons (of an energy $E = h\nu$) have the same energy. Stokes Raman scattering occurs if the atom/molecule absorbs energy, and the scattered photon has less energy. Anti-Stokes Raman scattering occurs if the atom/molecule loses energy, and the scattered photon has more energy than the incident photon. Rayleigh scattering can also occur from excited vibrational ground states. The schematic is adapted from Smith and Dent.[150]

In general, electromagnetic radiation can be characterized by its wavelength λ:

$$\lambda = \frac{c}{\nu} \tag{3.9}$$

where c is the speed of light and ν is the frequency of the light. In Raman spectroscopy, usually, frequency ν or wavenumber $\tilde{\nu}$ scales are used since they are directly proportional to the energy of the incident light ΔE:

$$\nu = \frac{\Delta E}{h} \tag{3.10}$$

and

$$\tilde{\nu} = \frac{\nu}{c} = \frac{1}{\lambda} \tag{3.11}$$

where h is the Planck constant. If a sample is now irradiated with a single-frequency radiation source, the scattered radiation from the molecule differing by one vibrational unit compared to the incident beam can be detected. This is in contrast to infrared (IR) spectroscopy, where the incident radiation covering a range of infrared frequencies needs to match the energy difference between the excited and the ground state of a molecule.

There are three different ways that are relevant for Raman spectroscopy, how the light can scatter by a material, as illustrated in Figure 3.7. When a monochromatic light source (usually

a laser) interacts with the molecule, the electrons are excited, and so-called virtual states with short live times are created. These states are not stable, and photons can be elastically and inelastically scattered. If the scattered photons have the same energy as the incident photons, they are elastically scattered, which is called Rayleigh scattering. This is the most intense process. However, if nuclear motion is induced during the scattering process, the light scatters inelastically, which is called Raman scattering. Stokes Raman scattering occurs if the molecule is excited from the lowest vibrational level of the electronic ground state *m* to a higher energy excited vibrational level of the electronic ground state *n,* and the scattered photon loses energy. Inversely, anti-Stokes Raman scattering occurs if the molecule loses energy by relaxing from a higher energy excited vibrational level of the electronic ground state *n* to a lower vibrational level of the electronic ground state *m,* and the scattered photon gains the corresponding energy. Raman scattering is a weak process, and therefore, modern lasers and optics with very high-power densities are needed to gain sufficient signal. Commonly, only Stokes Raman scattering is recorded, which has higher signal intensities due to the higher population of the lower states at room temperature.[150, 151]

Raman spectra result from electronic transitions, which are related to the vibrational and rotational states of a molecule. Figure 3.8 shows the electronic ground state of a diatomic molecule for one vibrational level without rotational levels, known as the Morse potential curve.

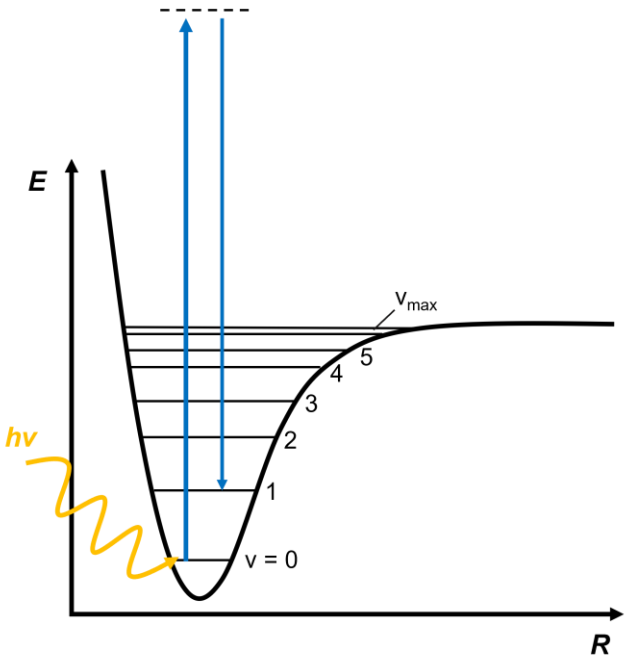

Figure 3.8 A typical Morse potential energy curve. The minimum of the curve equals the internuclear separation *R* with the lowest potential energy *E*. The horizontal lines represent the fundamental and overtone levels of one vibration *v*. Stokes Raman scattering of the incident photons of an energy *hv* is indicated with blue arrows. The schematic is adapted from Smith and Dent.[150]

This curve represents the electronic state, where the vibrational energies are quantized. Hooke's law describes the Morse curve with a harmonic approximation:

$$\nu = \frac{1}{2\pi c}\sqrt{\frac{K}{\mu}} \tag{3.12}$$

where c is the speed of light, K is the force constant of the bond between atoms A and B, and μ is the reduced mass of the molecule. μ can be calculated by the following equation:

$$\mu = \frac{M_A M_B}{M_A + M_B} \tag{3.13}$$

where M_A and M_B are the masses of atoms A and B. Therefore, the lighter elements show specific vibrations at higher wavenumbers. For example, the C-H vibrations are situated around 3000 cm^{-1}, the C-O vibration around 2000 cm^{-1}, and the Cu-C vibration around 300 cm^{-1}. It should be noted that the harmonic model is only a simple approximation, where the overtones (the higher vibrational states) of a molecule are equally spaced, even though the energy separations between the levels are decreasing in a real system (Figure 3.8).[150, 151]

Raman selection rules require a change in the polarizability of the molecule, where symmetric vibrations are the most intense. In contrast, IR results from a dipole change in the molecule, where asymmetric vibrations are more intense. Both techniques have the same selection rule $\Delta\omega = 1$, which applies stricter on Raman, where usually no overtones are observed. For example, the linear CO_2 molecule has four modes of vibration according to the $3N$-5 rules (which is $3N$-6 for non-linear molecules, where N is the number of atoms). The normal vibrational modes of CO_2 are displayed in Figure 3.9. The symmetric stretching mode causes a change in polarization but no change in the dipole. Therefore, this mode is only Raman active

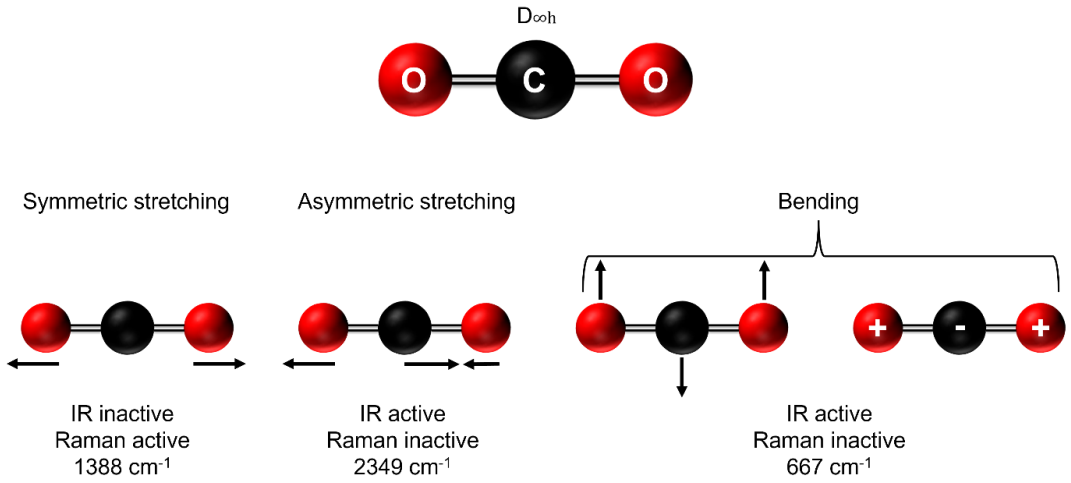

Figure 3.9 Vibrational normal modes of the linear CO_2 molecule, which belongs to the $D_{\infty h}$ point group.

with a band at around 1388 cm^{-1}. The asymmetric stretching and bending modes show no change in polarization, while the dipole is changing. Thus, these modes are only IR active with bands at 2349 and 667 cm^{-1}. However, in real Raman spectra, another band at 1286 cm^{-1} appears due to the second harmonic of the bending vibration.[150, 152]

3.4.2 Fundamentals of SERS

Even though Raman spectroscopy is an attractive method, the low signal intensities limit its practical use, especially for *in situ*/*operando* studies. The discovery of SERS by Fleischmann et al. in 1973 greatly improved the signal intensities by an enhancement factor of up to 10 to 11 orders of magnitude.[153, 154] Practically, a SERS spectrum can be easily obtained from a suitable analyte such as roughened surfaces or nanostructures (mainly Cu-, Ag-, Au-based).

Two different theories of the surface enhancement mechanism have been established, namely the electromagnetic and the chemical enhancement theory. In the electromagnetic theory, localized surface plasmons are excited when the incident light hits (nano)particles that are much smaller than the incident wavelength. When the frequency of the induced oscillation of the electrons matches the light frequency, localized surface plasmon resonance (LSPR) occurs, which enhances the electric field near the particle surface. As a result, the Raman scattering of adsorbates within that electromagnetic field is enhanced. Thus, SERS can occur even when the molecule is relatively far from the nanoparticles that induce the surface plasmons. The SERS enhancement strongly depends on the properties of the nanoparticles, such as their size, shape, and morphology.

In the chemical enhancement theory, charge transfer (CT) leads to the SERS enhancement, where the adsorbate needs to be chemically bonded to the surface. The incident radiation is absorbed by the metal that creates a hole pair. The energy is then transferred from the hole pair to the molecule to cause the Raman process, and the reduced energy is returned back to the metal before scattering from it, which causes the enhancement. The CT enhancement only occurs from the first layer of the analyte attached to the surface since the adsorbate needs to be bound to the metal. Nowadays, it is believed that both mechanisms contribute together to the overall SERS signal, where the electromagnetic mechanism is the more dominant process.[147, 150]

Frequently, the selection rules of SERS change compared to the ones of Raman spectroscopy as introduced in Section 3.4.1. This arises from the fact that the symmetry of the molecules changes when there are adsorbed onto a surface. As a result, new bands, which are inactive for Raman, can be active for SERS and vice-versa, and also, the band intensity ratios might change in comparison to a conventional Raman experiment.[150, 155]

3.4.3 *Operando* SERS

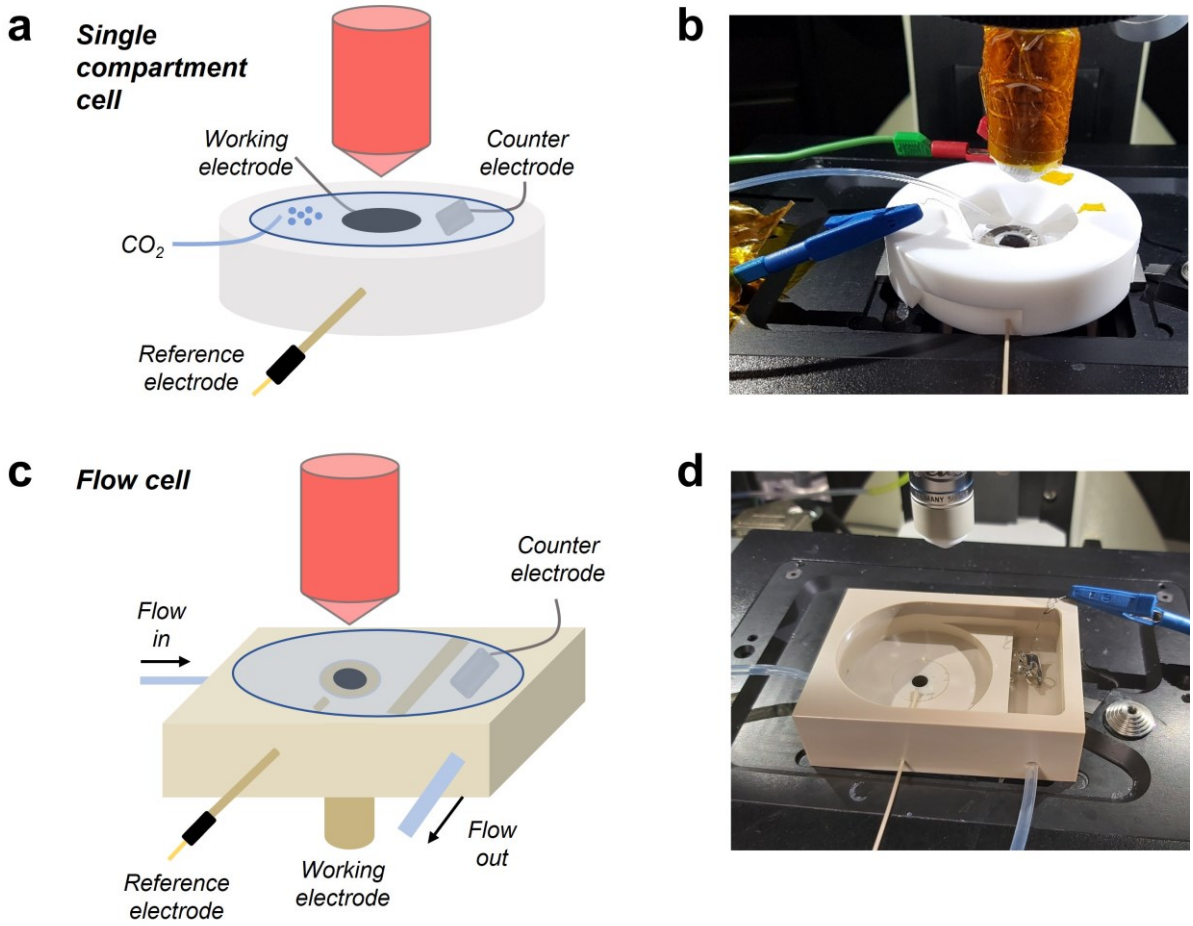

Figure 3.10 *Operando* SERS spectro-electrochemical cells (a) Scheme and (b) image of the custom-made *operando* single-compartment electrochemical SERS cell made of Teflon with water immersion objective. (c) Scheme and (d) image of the custom-made *operando* flow electrochemical SERS cell made of PEEK together with the water immersion objective. The flow is controlled via a peristaltic pump outside of the Raman system and cycled through the cell over an electrolyte reservoir, where the electrolyte is saturated with CO_2.

For the *operando* measurements, two different spectro-electrochemical cells were designed, which are displayed in Figure 3.10. The single-compartment cell consists of a platinum mesh as the counter electrode and of an Ag/AgCl electrode as the reference electrode. The sample is drop-casted on a glassy carbon plate, which is taped onto the bottom of the cell and serves as the working electrode. The electrolyte is permanently purged with CO_2. The main drawback of this cell is the bubble formation during CO_2RR on the working electrode, which can lead to an immense decrease in the SERS signal intensity.

Therefore, a new cell was designed, which works with an electrolyte flow over the working electrode. Here, the working electrode is mounted in a sample holder and drilled from the bottom into the cell. The reference electrode is placed next to the working electrode, while the

counter electrode (a Pt gauze) is in the outlet of the cell to avoid Pt contamination of the working electrode. The flow is induced with a peristaltic pump over an electrolyte reservoir (V = 50 mL), which is constantly saturated with CO_2.

When Raman spectroscopy was invented, it relied on a low-pressure mercury arc as its excitation light source. However, the development of lasers (Light amplifier by stimulated emission of radiation), which provide strong, coherent, and monochromatic light, greatly enhanced the signal intensities of Raman scattering.[150] In this thesis, both a near-infrared laser (λ = 785 nm) and a HeNe laser (λ = 633 nm) were utilized as excitation sources. A water immersion objective (63x, numerical aperture of 0.9), protected from the electrolyte by a Teflon (FEP) film, was employed to focus the laser onto the sample. Backscattered light was then Rayleigh-filtered, and the Raman scattering light was diffracted by a grating and directed toward a CCD detector, which recorded the SERS signal.

In summary, SERS is a powerful lab-based surface-sensitive tool in electrocatalysis for *in situ* and *operando* studies to identify the composition of the catalyst and important intermediates with great sensitivity. However, the enhancement effect strongly depends on the implemented materials, and the interpretation of SERS spectra is often not straightforward since the selection rules change in comparison to conventional Raman scattering. Here, the employed Cu-based nanocatalysts offer an applicable system for SERS measurements with sub-second time resolution.

3.5 X-Ray Absorption Spectroscopy

X-ray absorption spectroscopy (XAS) is a strong tool in catalysis research and is especially attractive for *in situ* and *operando* studies due to the high penetration depth of X-rays. This element-specific technique can uncover active sites in multielement systems and gives diverse structural and electronic information about a studied sample under different electrochemical reaction conditions. XAS experiments usually require a bright and tunable X-ray source (up to several tens of keV), which is provided by synchrotron radiation facilities. Recent developments in XAS even enable acquisition times in the millisecond range, which is key for the direct observations of fast transitions in the catalyst to uncover the reaction mechanism.[144, 156]

3.5.1 Fundamentals of XAS

XAS is based on the absorption of X-rays in a material, which is for all types of electromagnetic radiation described by the Beer-Lambert law. The letter states that the transmitted radiation intensity I_T after the sample is exponentially reduced compared to the incident radiation

intensity I_0 depending on the sample thickness d and the energy-dependent X-ray absorption coefficient $\mu(E)$ as the photons pass through the material:

$$I_T = I_0 e^{-\mu(E)d} \tag{3.14}$$

Over a wide energy range, $\mu(E)$ is a smooth function of the photon energy and decreases with increasing photon energy. However, if the photon energy matches the binding energy of a core electron, the electron leaves the atom by creating a photoelectron and a core hole. This leads to a sharp increase of $\mu(E)$, which is usually called the absorption edge or absorption jump.[157] For example, Figure 3.11 illustrates the absorption edge of Cu at ~9 keV in a Cu_2O nanocatalyst sample.[158]

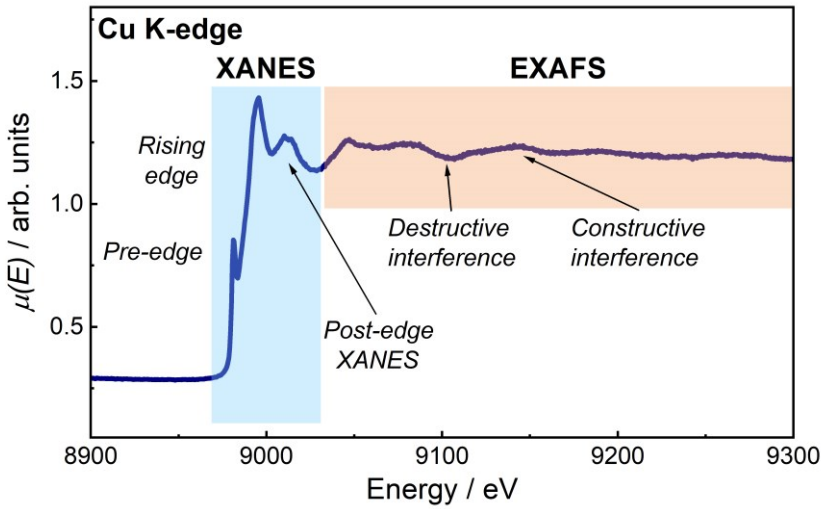

Figure 3.11 Cu K-edge XAS spectrum of a Cu_2O nanocatalyst sample acquired at the SOLEIL SAMBA beamline. Characteristic regions of the spectrum are highlighted.

Here, the 1s core electrons (K-shell) of Cu are excited to unoccupied states in the valence bands, to quasi-bound states, or to the continuum by the absorbed X-rays, which results in the so-called Cu K-edge. The fact that every element has a different energy of the absorption edge scaling with $\sim Z^2$ makes XAS element specific. Typically, only 1s or 2p core electrons are excited, which are referred to K- and L-edge, respectively. Above the absorption edge, the difference of the photon energy and the binding energy is converted into the kinetic energy of the photoelectron, while $\mu(E)$ decreases with increasing photon energy. The modulations of $\mu(E)$ directly below and above the absorption edge create the X-ray absorption fine structure (XAFS). XAFS is sensitive to the chemical state and local atomic structure. The XAFS spectrum is typically separated into two regions, namely the X-ray absorption near edge structure (XANES) close to the absorption edge, and the extended X-ray absorption fine structure (EXAFS) region, which extends at photon energies higher than ~30 eV above the edge.[157, 159]

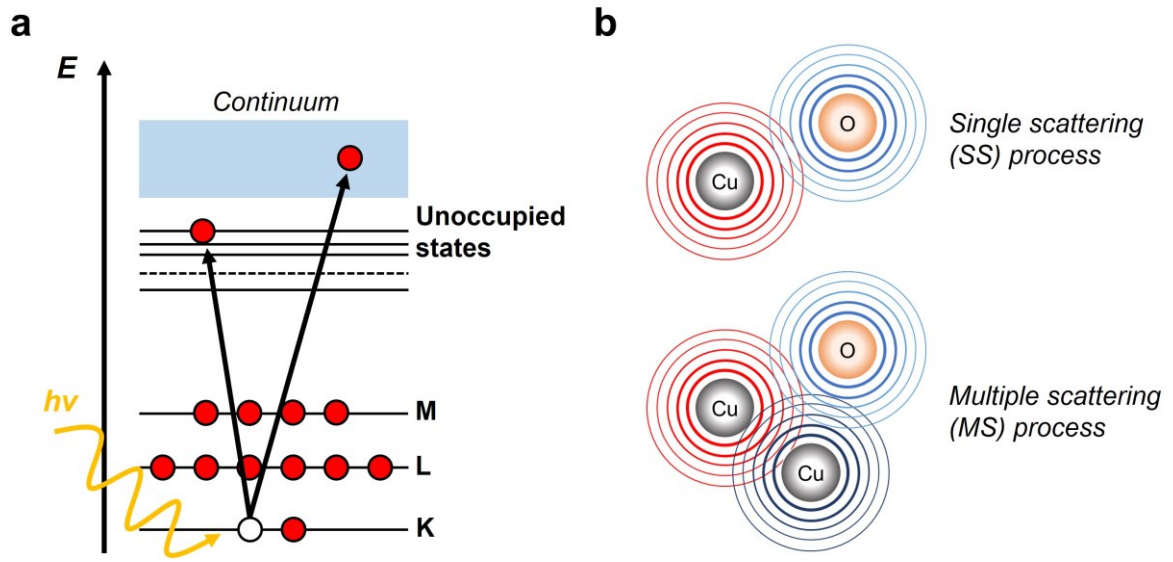

Figure 3.12 (a) Schematics of the absorption process of core level K-shell electrons by incident X-rays of an energy *hv* to unoccupied states or the continuum. (b) Schematics of the outgoing photoelectron waves of the absorbing atom (Cu atom on the left side, red waves) and the reflected photoelectron waves of its nearest neighbors (Cu an O atom, blue waves), which creates an interference pattern either from a single scattering (SS) or multiple scattering (MS) paths. The schematics are adapted from Schnohr and Ridgway.[159]

XANES results from transitions of the photoelectron to unoccupied bound states or to the continuum (Figure 3.12 a). The XANES region consists of the pre-edge, the absorption edge, and the post-edge region. The position of the absorption edge shifts to higher energies at higher oxidation states and can be thus used to determine the chemical state of the absorbing atom.[160] The region also provides information about the local symmetry and chemical bonding of the absorbing atom.[161] Additionally, the post-edge XANES feature (30-50 eV above the edge) is influenced by strong multiple scattering (MS) effects, which arise from the scattering of the ejected photoelectrons with neighboring atoms around the absorbing atom due to the long mean free path of these low energy electrons (Figure 3.12 b).[161] These multiple scattering effects depend on the three-dimensional geometry of the crystal structure but are challenging to interpret.[162] As a consequence, XANES spectra are mainly qualitatively interpreted with empirical knowledge derived from reference spectra, *e.g.,* by the implementation of linear combination analysis (LCA). LCA can be performed if the obtained XAS signal $\mu_i(E)$ is described as the sum of the reference spectra for the pure compounds $s_j(E)$ weighted by the concentration of the specific species w_{ij}:[161]

$$\mu_i(E) = \sum_j^N w_{ij}\, s_j(E) \tag{3.15}$$

LCA then optimizes the parameters w_{ij} to complement the measured spectrum with the linear combination of $s_j(E)$. This method is an easy way to determine the oxidation state of a sample and track its changes under applied reaction conditions. Alternatively, linear algebra techniques such as principal component analysis (PCA) and factor analysis can also be performed to analyze the XANES part.[157, 161]

The XANES region is followed by the EXAFS region at higher photon energies. Since the photoelectron is excited to a free or continuum state, EXAFS is not dependent on the chemical bonding but is sensitive to probe the spatial arrangement of the nearest neighbors around the absorbing atom. When a photoelectron meets the neighboring atoms, it is scattered elastically and changes its wavefunction by constructive and destructive interference (Figure 3.11 b).[160] Due to the small effective mean-free path for the excited electrons at these large photoelectron energies, the sensitivity of EXAFS spectra is limited to interactions with only a few nearest neighbors.[160] Therefore, in contrast to the XANES post-edge region, EXAFS is dominated by single scattering (SS) events (Figure 3.12 b), which makes it a very local method.[157, 163]

For analysis, the EXAFS component $\chi(E)$ needs to be normalized by subtracting a smooth background function $\mu_0(E)$ from the measured spectrum $\mu(E)$ followed by the division with the absorption edge value $\Delta\mu_0(E_0)$ at the reference energy value E_0:

$$\chi(E) = \frac{\mu(E) - \mu_0(E)}{\Delta\mu_0(E_0)} \tag{3.16}$$

Then, the EXAFS signal is transformed from the energy space to the photoelectron wavenumber k-space:

$$k = \sqrt{\frac{2m_e}{\hbar^2}(E - E_0)} \tag{3.17}$$

where m_e is the electron mass and $\hbar$ is the Planck's constant. An example of the Cu K-edge EXAFS in the k-space of the Cu_2O nanocatalyst sample is displayed in Figure 3.13 a. The different frequencies in the oscillations of $\chi(k)$ depend on the distance of the absorbing and back-scattered atoms (extracted from the magnitude of the Fourier transform) and the number of atoms surrounding it (directly proportional to the amplitude), which can be described by the EXAFS equation:[157, 163]

$$\chi(k) = \sum_p \frac{C_p\, S_0^2}{k\, R_p^2} F_p\big(k, R_p\big) e^{-\frac{2R_p}{\lambda(k)}}\, e^{-2\sigma_p^2 k^2} \sin\Big(2kR_p + \Phi_P\big(k, R_p\big)\Big) \tag{3.18}$$

where p is the coordination shell, C_p is the coordination number, R_p is the average interatomic distance, and σ_p^2 is the disorder factor or Debye-Waller factor accounting for thermal and static

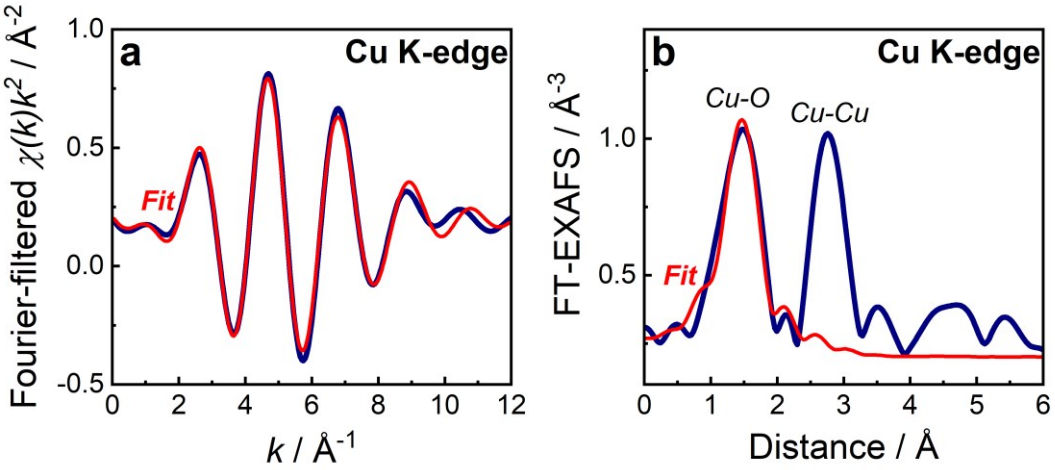

Figure 3.13 Cu K-edge (a) Fourier-filtered k^2-weighted $\chi(k)$ and (b) Modulus of the Fourier-transformed (FT) (phase uncorrected) EXAFS data with the corresponding fits (single shell fit involving only the Cu-O SS contribution) as extracted from the XAS spectrum in Figure 3.11.

disorder in the material. This equation is written for the SS approximation, while MS effects can be included if the index p runs over all possible SS and MS pathways without using the coordination number.[160] The structural parameters can be derived from nonlinear least-squares fitting of the experimental EXAFS data, while the nonstructural parameters E_0 and S_0^2 can be determined from the analysis of EXAFS spectra with reference materials or fitting. Thereby, S_0^2 describes the reduction of the EXAFS amplitude due to many-electron effects. The functions F_p, Φ_p, and λ_p are usually calculated theoretically through different *ab initio* codes (*e.g.*, the FEFF code).[164] Figure 3.13 b illustrates the total Fourier-transformed (FT) EXAFs (R-space) of the Cu_2O nanocatalyst sample, which shows the Cu-O and Cu-Cu distances at ~1.5 and 2.7 Å together with an exemplary single-shell fit involving only the Cu-O SS contribution of the EXAFS spectrum.

In some cases, it is challenging to determine the concentrations of different species from LCA-XANES analysis, *e.g.*, for certain alloy phases, since appropriate reference materials are missing. Therefore, a new approach can be used, where an artificial neural network (NN) "inverts" the EXAFS spectrum and serves to extract the radial distribution functions (RDFs) of neighboring atoms.[115, 156, 165] The total EXAFS spectrum $\chi(k)$ consists of the sum of the different weighted contributions of the different species:

$$\chi(k) = \sum_s w_s \chi_s(k) \tag{3.19}$$

where w_s is the concentration of the species, and $\chi_s(k)$ is the partial EXAFS spectrum.

The single-scattering path contributions $\chi_s(k)$ can be described as the following:[156]

$$\chi_s(k) = S_0^2 \sum_p \int_0^{+\infty} A_{sp}(k)\, g_{sp}(R) \sin\left(2kR + \Phi_{sp}(k)\right) \frac{dR}{R^2} \tag{3.20}$$

where S_0^2 describes the reduction of the EXAFS amplitude due to many-electron effects, $g_{sp}(R)$ is the radial distribution function attributed to the probability density to find an atom at a distance R, $A_{sp}(k)$, and $\Phi_{sp}(k)$ are the changes in the photoelectron wave amplitude and phase depending on the type of the neighboring atom. The $g_{sp}(R)$ functions can then be obtained from the EXAFS spectrum by machine learning (ML). Finally, an artificial NN is constructed and trained to find the weighted RDFs for the different spectroscopic phases.[115, 156]

Conventional Cu K-edge XAS data collection of our nanocatalyst samples usually required ~10 minutes for the acquisition of one spectrum. Quick scans XAFS (QXAFS) enable the possibility to measure XAS in a time-resolved way in the millisecond range. The high time resolution can be achieved by using continuously oscillating monochromators together with rapid data acquisition, whereas in conventional XAS, each energy point is measured.[166]

3.5.2 *Operando* XAS

For the *operando* investigations, a custom-made three-electrode electrochemical cell, as shown in Figure 3.14, was used. There, the working electrode consists of a thin carbon paper electrode on which the catalyst was either drop-casted or spray-coated onto the side-mounted toward the cell inside. Additionally, a platinum gauze serves as the counter electrode and an Ag/AgCl electrode as the reference electrode. The electrolyte is constantly purged with CO_2 and exchanged by pumping it with an electrolyte reservoir. Due to the absorbing character of the aqueous electrolyte, the intensity of the transmitted X-rays is very low. Thus, the measurements are conducted in fluorescence mode, where the X-rays incident the cell from the back of the

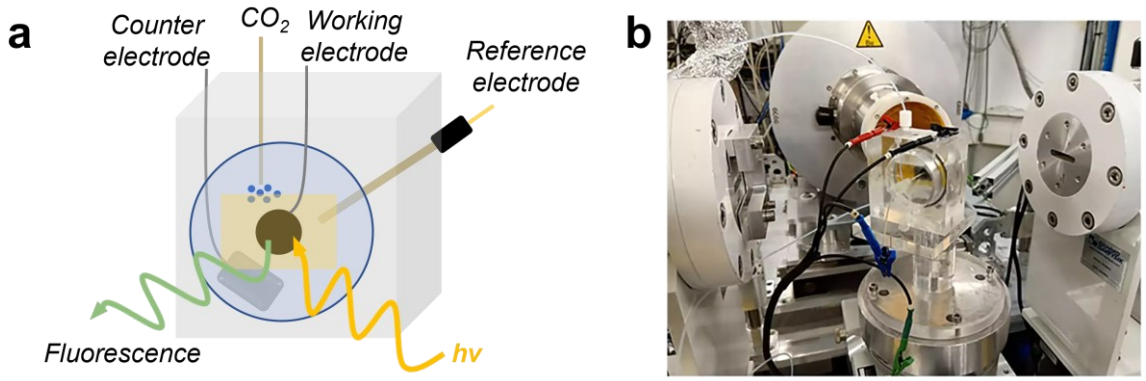

Figure 3.14 (a) Schematics of the custom-made *operando* XAS electrochemical cell with the incident X-rays of an energy *hv* and the outgoing perpendicular fluorescence signal. (b) Picture of the cell under operation at the SOLEIL SAMBA beamline.

sample, and the emitted fluorescence signal is detected by a passivated implanted planar silicon (PIPS) or a germanium detector. The emittance of X-ray fluorescence results from the eventual filling of hole electrons in the core states with electrons with high energy from the excites states. In order to prevent self-absorption, where the secondary photons are reabsorbed and scattered within the material itself, sufficiently thin samples (below ~5 µm) and an optimized sample loading (*e.g.,* ~0.5 mg_{Cu} cm^{-2} for Cu) were used for the conducted experiments.[156]

An important requirement for the collection of XAS data on catalysts is that the particles are monodisperse since XAS is a sample averaging technique, where the signal comes from the whole sample. This also means that the method is not surface-sensitive unless the particle size is very small (< 3 nm). However, XAS of optimized monodisperse catalysts reveals unique information on its local environment and its structure.[144]

3.6 X-Ray Photoelectron Spectroscopy

X-ray photoelectron spectroscopy (XPS) is one of the most frequently used techniques in materials characterization. It is a surface-sensitive non-destructive spectroscopic method that provides information about the elemental composition as well as the chemical state of a given surface. XPS usually requires high vacuum (p ~10^{-6} Pa) or ultra-high vacuum (UHV, p < 10^{-7} Pa) conditions even though they are also current developments in ambient-pressure XPS with pressures p of up to 2.5 bar.[167]

XPS is based on the photoelectric effect, which was described by Einstein in 1905. There, an atom absorbs a photon of an energy $h\nu$ in a way that a core electron with the binding energy E_b is ejected, and its kinetic energy E_k can be measured (Figure 3.15 a):[168]

$$E_k = h\nu - E_b - \varphi \tag{3.21}$$

where h is the Planck's constant, ν is the frequency of the exciting radiation, and φ is the work function for the specific surface of a material, which is the energy difference between the Fermi level and the vacuum level. XPS plots the number of photoelectrons as a function of their kinetic energy. By using Equation 3.21, the kinetic energy is commonly converted into the binding energy, which is element specific. Moreover, chemical information can be extracted from the chemical shift of the XPS peaks since the energy levels of the core electrons are also dependent on the oxidation state of the atom. For example, the weaker shielding of the Cu atom in positively charged Cu, as in CuO compounds, results in a lower kinetic energy of the photoelectrons and, therefore, in a higher binding energy compared to metallic Cu.[169]

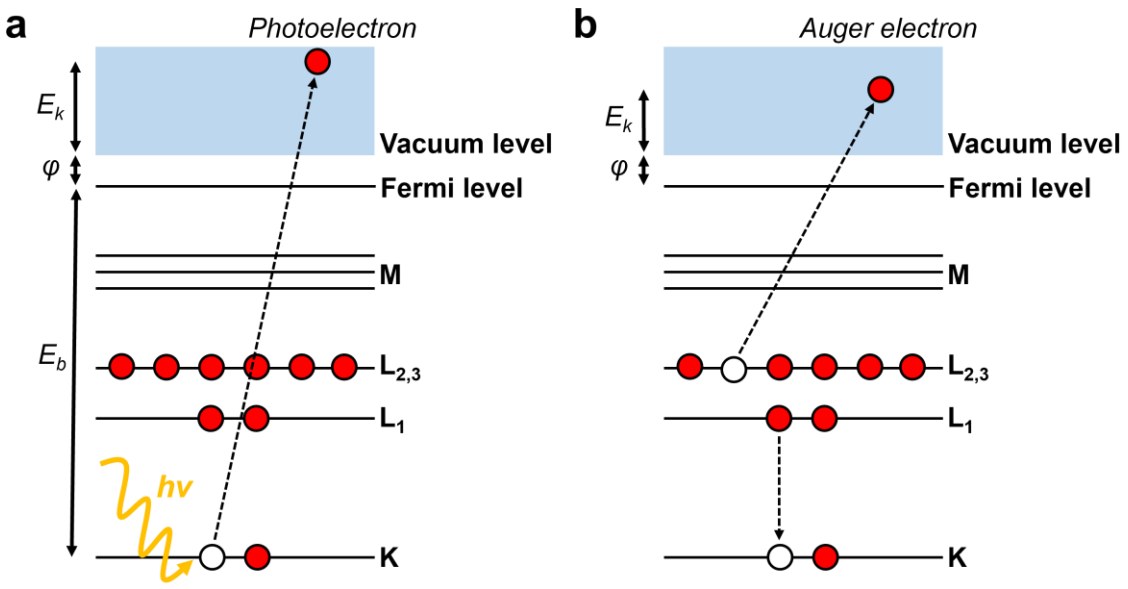

Figure 3.15 Schematics of the photoelectron and Auger process. (a) An incident X-ray photon is absorbed from the K-shell, and a photoelectron is generated and ejected. (b) The vacancy in the K-shell is filled by an electron from the higher L-shell. The energy released from this process excites another electron from the L-shell, the so-called Auger electron. The schematics are adapted from Holland.[170]

The sample is irradiated with soft X-rays, where usually Mg K_α ($h\nu$ = 1253.6 eV) and Al K_α ($h\nu$ = 1486.3 eV) anodes of 0-1 keV serve as X-ray sources for lab-based XPS. This leads to kinetic energies of the photoelectrons up to the energies of the incident X-rays, and the electrons can only travel a few nanometers through the material, which makes XPS surface-sensitive.[144] The measured XPS spectrum does not only contain the expected photoelectron peaks but also exhibits additional peaks. Among these peaks, some arise from secondary processes since the atom which the photoelectron left possesses a hole in its inner shell. This hole is filled by an electron from a higher shell, and the resulting excess energy can then be released by the emission of an electron from a higher shell if the transferred energy is greater than the orbital binding energy (Figure 3.15 b). These emitted electrons are called Auger electrons. Therefore, Auger electrons have fixed kinetic energies independent of the incident X-ray photon energy. Auger peaks can be identified by recording the spectrum at two different X-ray energies, where Auger peaks shift depending on the binding energy scale in contrast to the XPS peaks. Auger peaks contain information about the chemical state and the binding environment since Auger electrons usually originate from the outer shells of the atoms. For example, the Auger peaks of Cu can give detailed information about the contribution of different Cu oxidation states on the surface of the catalyst by comparison with reference spectra.[169, 170]

Since XPS needs to be performed under UHV conditions, it is challenging to implement *operando* electrochemical cell setups, which usually contain liquids. Therefore, the most

accessible method remains quasi-*in situ* XPS where an electrochemical cell is directly attached to a UHV system, and the XPS measurements are performed directly before and after the electrochemical measurements. In this way, the sample is never exposed to air (but only to Argon and vacuum), and the oxidation state of the catalyst can be tracked, which would be otherwise chemically affected by the ambient conditions (*e.g.*, re-oxidization in air). More details about the custom-made quasi-*in situ* XPS electrochemical cell setup that was used for this thesis can be found in the literature.[76]

In conclusion, XPS is a great surface-sensitive method to complement the previously introduced bulk-sensitive X-ray-based techniques (XAS and XRD). However, since it is not performed *operando* in this thesis, it can only give extracts of the catalyst surface behavior.

3.7 X-Ray Diffraction

X-ray diffraction (XRD) is one of the most commonly used and oldest non-destructive techniques for catalyst characterization. It is used for the identification of the crystalline phases of a sample in terms of the lattice structural parameters and to obtain information about the particle size. While lab-based XRD is a good way to study *ex situ* samples, XRD also offers great *in situ* and *operando* methods, especially if coupled with synchrotron radiation.[144]

3.7.1 Fundamentals of XRD

XRD relies on the elastic scattering of X-ray photons by atoms in a periodic lattice. In a material with an ordered crystal structure, different X-ray photons will scatter on different layers of the crystal lattice, as illustrated in Figure 3.16. Constructive interference of the scattered X-rays occurs when the path difference is a multiple of the wavelength in dependence on the lattice spacings. This is mathematically described by Bragg's law:

$$n\lambda = 2d\ sin\theta \tag{3.22}$$

where n is an integer number called the reflection order, λ is the wavelength of the X-rays, d is the distance between two lattice planes, and θ is the incident angle of the X-rays. By knowing λ and measuring the angles 2θ, an intensity pattern known as a diffraction pattern can be obtained. From these patterns, different phases of a crystalline sample can be identified by the comparison of the line positions and the intensity distributions of a set of reflections with a reference diffraction pattern.[171, 172]

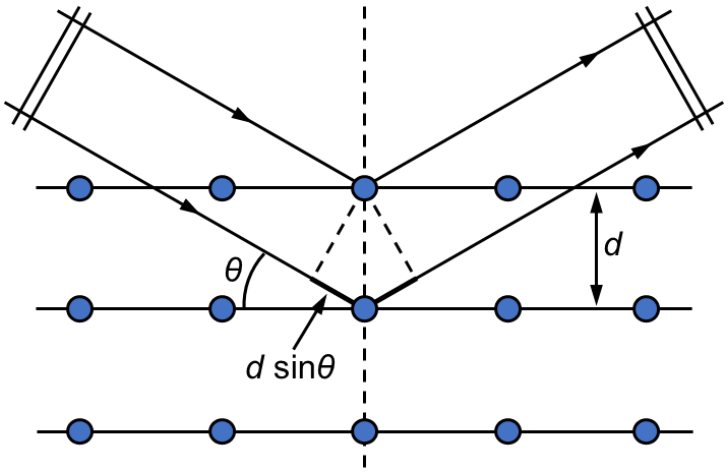

Figure 3.16 X-rays scattered by atoms in an ordered lattice exhibit constructive interference as given by Bragg's law.

Moreover, Bragg's law can be used to obtain the lattice parameter of the unit cell (*e.g.*, *a*) of a particular cubic crystal system, such as Cu, from a diffraction experiment via the following relation:

$$a = d_{hkl}\sqrt{h^2 + k^2 + l^2} \tag{3.23}$$

where *h*, *k*, and *l* are the Miller indices of the Bragg plane.

While diffraction lines from ideal crystals are very narrow, line broadening (instrumental and spectral broadening) occurs for crystallite sizes below 100 nm due to incomplete destructive interference in scattering directions where the X-rays are out of phase. The peak width of diffraction peaks can be used to determine the dimensions of the reflecting planes. Therefore, the Scherrer formula estimates the mean size of the ordered (crystalline) domains *L* assuming quasi-spherical, monodisperse nanoparticles free of lattice strain:[173]

$$L = \frac{K\,\lambda}{\beta\,cos\theta} \tag{3.24}$$

where *K* is the shape factor whose value is 0.89 for spherical particles, λ is the wavelength of the used X-rays, β is the peak width in radians, and θ is the Bragg angle at the position of the peak maximum. This equation provides a quick but not always reliable estimation of the particle size since several factors must be examined that can contribute to line broadening too. Besides crystallite size and instrumental effects, the most important of these are inhomogeneous strain and crystal lattice imperfections.[174]

Better analysis models such as Rietveld refinement allow modeling the full powder diffraction profile based on the crystal structure data, specimen, and instrument effects. In this way, the phase composition, as well as structural parameters like crystallite sizes and lattice parameters,

can be obtained.[175, 176]

Besides, XRD gives mainly information about the bulk sample since X-rays can penetrate several micrometers into the sample. However, the surface sensitivity can be improved by performing grazing incidence XRD (GIXRD), where the measurements take place at angles θ below the critical angle of the corresponding material. Then, the X-rays are reflected by total external reflection, and it is only an evanescent wave that probes the surface layers.[177]

3.7.2 Synchrotron High Energy XRD

The use of synchrotron radiation as a source for XRD offers better sensitivity and resolution of diffraction peaks than the conventional laboratory XRD due to the high-flux, high energy, well-defined tunable wavelength, and better collimation of synchrotron X-rays. Especially, high energy X-rays between 70 and 300 keV for high energy XRD (HE-XRD) offer advantages compared to the conventional hard X-rays between 5-20 keV, namely their high penetration depth leading to simple diffraction setups with operation in air, their diffraction in the forward direction for easy registration with 2D detectors, and no radiation damage. This also enables great opportunities to study the catalyst under *in situ* and *operando* conditions to track, *e.g.*, its reduction behavior and the evolution of the crystallite parameters as the crystallite sizes. Additionally, new detector technologies allow the fast collection of data in the millisecond time range. In this thesis, the diffraction images were recorded with a large-area detector Dectris

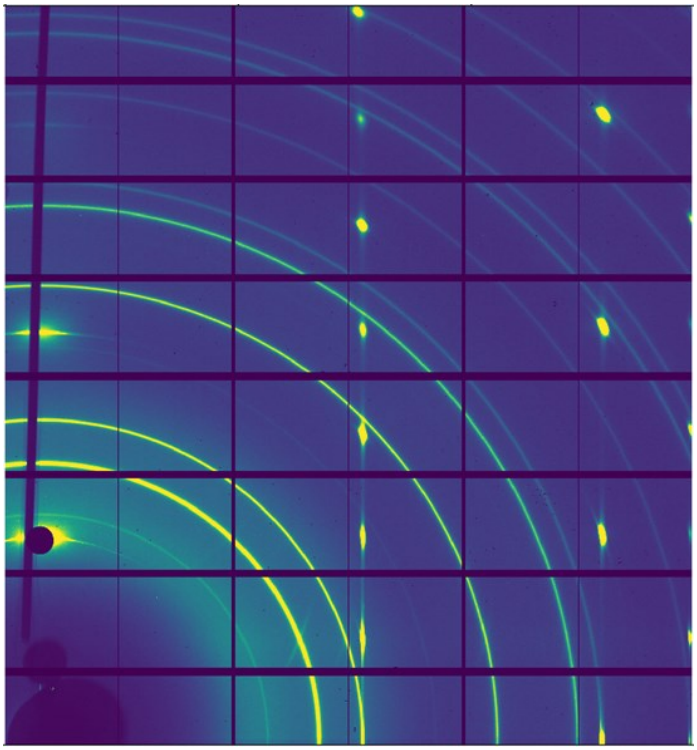

Figure 3.17 Detector image of the Pilatus X-ray detector from the diffraction of a ZnO-Cu_2O nanocatalyst sample in a CO_2-saturated 0.1 M $KHCO_3$ electrolyte.

Pilatus X CdTe 2M at energies around 70 keV. This detector offers the advantage that it can principally measure every single diffracted photon due to its high dynamic range, which leads to high signal intensities, even for weak diffraction signals. An example of a typical detector image of the diffraction from a ZnO-decorated Cu_2O nanocatalyst in an aqueous electrolyte is shown in Figure 3.17, which indicates the prominent powder diffraction rings of Cu_2O. The dark area on the left bottom is caused by the beam stop blocking the part of the incoming radiation, which would damage otherwise the detector with its high energy. The Bragg peaks result from the highly oriented pyrolytic graphite (HOPG) support under the sample. The detector images are then further processed by implementing the software package pyFAI,[178] which includes the calibration, masking of features that do not correspond to the catalyst sample (*e.g.*, the HOPG peaks), and the detector image integration. As a result, the corresponding diffraction pattern is obtained as a function of 2θ, which is given in Figure 3.18. Here, the peaks are marked with the Miller indices (*hkl*) together with the diffraction peaks of a Cu_2O reference (ICSD #26963).

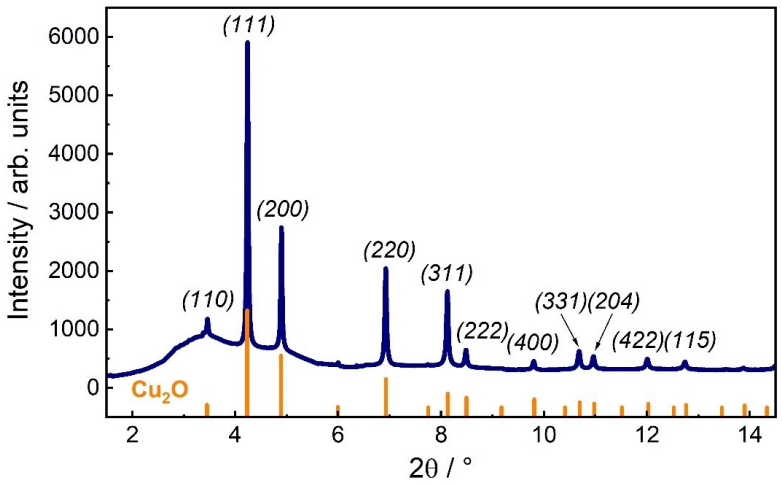

Figure 3.18 HE-XRD pattern of the ZnO-Cu_2O nanocatalyst sample with Miller indices of the peaks and Cu_2O reference peaks.

3.7.3 *Operando* HE-XRD

To perform *operando* HE-XRD measurements, a custom-made electrochemical flow cell setup, which is illustrated schematically and pictured in Figure 3.19, was used. The working electrode is mounted from the bottom of the cell so that the sample is horizontally placed. The sample consists of nanoparticles drop-casted on a HOPG substrate. On top of the sample flows a small volume of electrolyte to minimize the path length of the X-ray beam through the electrolyte. The electrolyte is covered with an X-ray-transparent and optically thin PEEK foil window and constantly pumped through the cell as well as an electrolyte reservoir via a peristaltic pump.

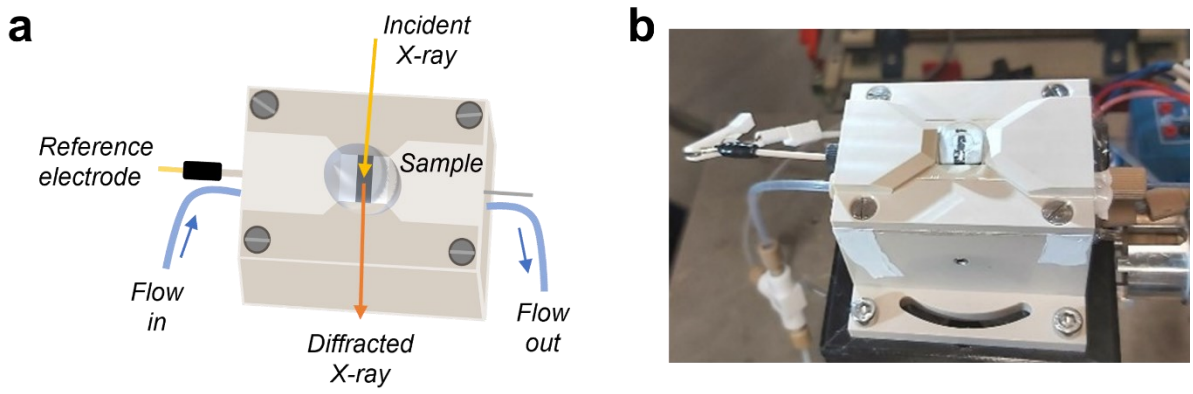

Figure 3.19 (a) Scheme of the custom-made *operando* XRD electrochemical flow cell setup with the incident and diffracted X-rays on the sample. (b) Picture of the cell under operation at the ESRF ID31 beamline.

Additionally, the electrolyte reservoir is purged with CO_2. The electrolyte flow is needed to avoid product accumulation and mitigate bubble formation at high overpotentials. A leak-free Ag/AgCl electrode positioned in the inlet of the flow channel serves as the reference electrode, while a Pt wire positioned in the outlet of the flow channel serves as the counter electrode.

Even though XRD is a powerful tool in catalyst characterization, an important limitation of XRD is that it cannot detect small or amorphous particles. This is also shown in an example of a ZnO-Cu_2O nanocatalyst used in this thesis from Figure 3.18 and 3.19, where the Cu_2O phase can be clearly observed, while there is no indication of the ZnO phase inside the catalyst, probably due to its amorphous character. Thus, one cannot be sure about the number of phases present in a catalyst only by performing XRD measurements. Moreover, XRD is a bulk-sensitive technique, which gives only limited information about the active catalytic surface. Nevertheless, XRD gives useful insights into the crystalline phases in terms of crystallite size or strain inside a particle under working conditions.[144]

4. Catalyst Synthesis

In this chapter, the synthesis procedures employed to prepare the catalyst materials for this thesis are described. The first section covers different wet-chemical synthesis methods to produce cubic-shaped and size-selective Cu oxide nanocatalysts. The subsequent sections describe the synthesis procedures utilized to uniformly decorate these nanocubes with a secondary metal (oxide), namely silver and zinc oxide.

4.1 Catalyst of Choice

The synthesis of highly active, selective, and stable catalysts is crucial for heterogeneous electrocatalysis. In the case of CO_2RR, the catalytic properties of the cathode side, where the reaction takes place, need to be optimized and tailored. Well-defined shape- and size-selective nanoparticles (NPs) can serve as a catalytic model system to study the electrocatalytic properties in a systemic and controlled way. The choice of the catalytic system was based on the properties of Cu-based nanomaterials that are promising candidates for CO_2RR catalysts, as discussed in Chapter 2. Specifically, going from well-defined single crystals to NP catalysts allows for testing under relevant industrial conditions while still exposing specific catalytic active facets.[52] Cubic-shaped NPs have been shown to be particularly promising, as the surface preferentially consists of (100) facets, which were originally thought to favor C_{2+} products.[61] Additionally, an optimal size of NPs for CO_2RR has been observed to be within the range of 20-40 nm.[60] Oxide-derived Cu catalysts are also preferred due to their porous structures and residual oxygen species that might be retained during catalytic conditions.[179] For these reasons, size-controlled cuprous oxide (Cu_2O) nanocubes (NCs) are chosen as an ideal system to study for the CO_2RR in this thesis as they possess all the favorable properties. Furthermore, the controlled addition of a second metal can be used to create well-defined bimetallic catalysts and study the bifunctional effect of the CO_2RR.

4.2 Synthesis of Cu_2O Nanocubes

For the synthesis of NPs, the bottom-up approach offers a strategy to control important physical properties of the NPs, such as size, shape, and composition. Following this approach, well-defined and uniform Cu_2O NCs can be obtained via a one-pot wet-chemical synthesis procedure

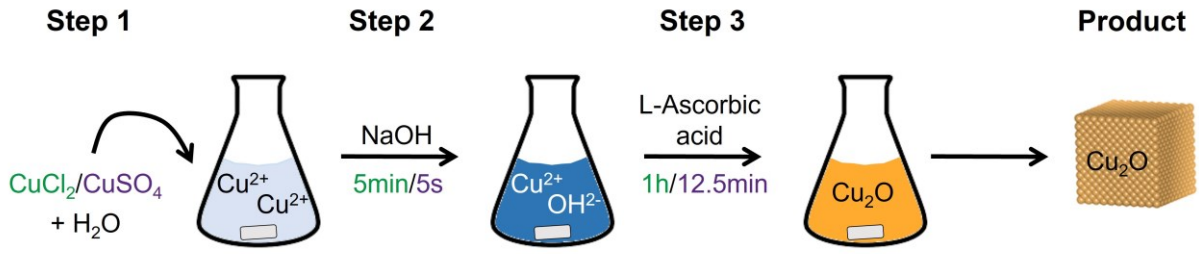

Figure 4.1 Schematic illustration of the synthesis procedure for Cu_2O nanocube catalysts.

at ambient conditions based on the studies of Liu and Ke et al.[180, 181] One main advantage of this synthesis method is that it works without adding any surfactant, enabling a clean surface for CO_2RR.

Figure 4.1 depicts the main steps involved in the synthesis of Cu_2O NCs that are well-controlled in shape and size. First, a copper precursor, which is typically a Cu(II) salt such as $CuCl_2$ or $CuSO_4$, is dissolved in ultrapure water under stirring. In the second step, an aqueous solution of sodium hydroxide is added to the reaction mixture and stirred for a specific time. This results in a color change from transparent to light blue, which was assigned to the formation of a $Cu(OH)_2$ precipitate.[181-183] In the third step, an aqueous solution of L-ascorbic acid (Vitamin-C) is introduced to the reaction mixture, causing a slow color change of the solution from blue over green to yellow/orange. L-ascorbic acid acts here as a mild reducing agent that reduces $Cu(OH)_2$, leading to the formation of Cu seeds that nucleate to form solid Cu_2O NCs.[181-183] Ke et al. found that with an increasing amount of the sodium hydroxide solution, the final size of the NCs significantly increased, resulting in a size tunability of the NCs from 9 to 87 nm in edge length.[181] They linked this to an increase in the solution pH, which leads to a rapid production of $Cu(OH)_2$, while the rapid reduction of $Cu(OH)_2$ can cause the formation of larger particles.

In this work, two slightly different synthesis approaches were employed that differ primarily in the Cu precursor (either $CuCl_2$ or $CuSO_4$) and the reaction times, as indicated in Figure 4.1.[180, 181] The $CuCl_2$-based approach led to bigger sizes (around 35 nm) of the NCs and was employed for the further modification with silver (Chapter 5) and for the bare Cu_2O NC study (Chapter 6). On the other hand, the $CuSO_4$-based approach resulted in smaller particle sizes (around 20 nm) of the NCs and was used for further modification with zinc oxide (Chapter 7).

4.3 Synthesis of Ag-Decorated Cu_2O Nanocubes

Various techniques have been applied to introduce a second metal into or onto Cu oxide-based materials, including impregnation, sol-gel, sputtering, and thermal evaporation.[180] The modification of Cu_2O materials with noble metals, such as Ag, is also commonly achieved via

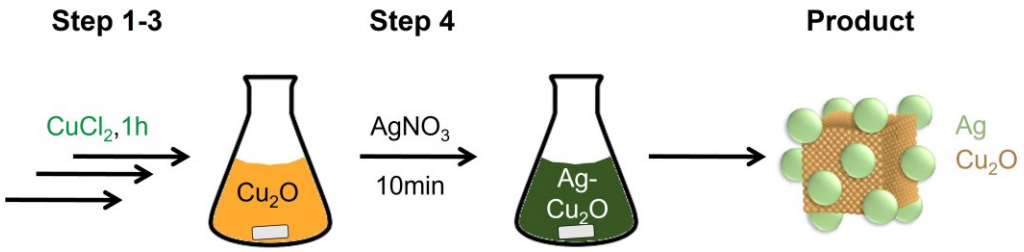

Figure 4.2 Schematic illustration of the synthesis procedure for Ag nanoparticle decorated Cu_2O nanocubes.

the galvanic replacement reaction (GRR) approach.[184] There, the cationic Ag(I) precursor can be reduced by the Cu_2O materials due to the lower reduction potential of Cu(I) compared to Ag(I).[185] A GRR-based approach was implemented to decorate Cu_2O NCs with Ag NPs.

Figure 4.2 illustrates the key steps for the preparation of the Ag NP-decorated Cu_2O NCs with a homogenous distribution and well-controlled shape/size of the Ag NPs. The first three steps are identical to those used in the $CuCl_2$-based Cu_2O NC synthesis outlined in Section 4.2. In order to introduce Ag to Cu_2O, the reaction is not stopped after stirring the solution with L-ascorbic acid in step three. Instead, step four is initiated, whereby an aqueous Ag(I) precursor solution (typically $AgNO_3$) is gradually added to the reaction solution. In this way, Ag^+ is immediately reduced by Cu(I) onto the surface of the NCs, resulting in the formation of Cu(II) species which likely dissolve in the reaction solution. The reduction of Ag^+ could be further supported by the remaining reducing L-ascorbic acid in the reaction solution. The metallic Ag seeds grow then to form NPs, which is driven by the reduction of the surface energy in the reaction system. The final product comprises Ag NPs on top of the Cu_2O NCs. By increasing the amount of the $AgNO_3$ solution, the size of the Ag NPs could be adjusted from 4.6 nm with 3 at% of Ag to 6 nm with 5 at% of Ag, while larger Ag amounts resulted in Ag agglomeration. During the establishment of this synthesis method, several challenges had to be addressed. One was the choice of the Cu(II) precursor, which turned out to be essential. Specifically, the $CuSO_4$-based approach combined with Ag led to rounded edges of the NCs, which may have been caused by the addition of $AgNO_3$. The use of the $CuCl_2$-based approach did not result in this effect, and sharp edges of the NCs were preserved, potentially due to the stabilizing effect of Cl^- ions. Additionally, no formation of AgCl was observed in the $CuCl_2$-based approach due to the fast nucleation of Ag^+ to Ag NPs. Another important aspect of the synthesis is the addition of $AgNO_3$. Particularly, for achieving a homogeneous distribution of the Ag NPs, it was crucial to add a very diluted aqueous solution of $AgNO_3$ slowly and in a controlled way to the reaction solution under vigorous stirring to avoid the agglomeration of Ag.

Finally, the one-pot synthesis method developed here has the benefit of not needing any extra reducing agents or surfactants/ligands. Moreover, the synthesis takes place under gentle conditions (at room temperature and without any pressure). Overall, this synthesis method provides a straightforward approach for producing well-defined Ag NP-decorated Cu_2O NCs, which are used in Chapter 5 for static CO_2RR applications.

4.4 Synthesis of ZnO-Decorated Cu_2O Nanocubes

The introduction of less noble metals and metal oxides such as ZnO into/onto a Cu_2O system is not feasible via GRR due to the lower reduction potential of Zn(II) compared to Ag(I). Therefore, an additional stabilization agent was employed to directly produce ZnO nanostructures on top of Cu_2O NCs via a precipitation method in a one-pot synthesis approach based on the master thesis of S. Widrinna.[186]

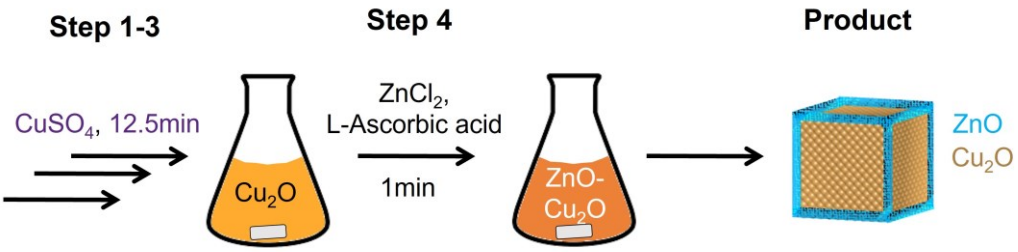

Figure 4.3 Schematic illustration of the synthesis procedure for ZnO-shell-covered Cu_2O nanocubes.

Figure 4.3 highlights the primary steps involved in creating ZnO-shell-covered Cu_2O NCs. The initial three steps are identical to those used in the $CuSO_4$-based Cu_2O NC synthesis, as described in Section 4.2. To introduce ZnO to Cu_2O, the reaction is not stopped after stirring the solution with L-ascorbic acid in step three. Instead, in step four, an aqueous solution of a Zn(II) precursor, here $ZnCl_2$, is mixed with L-ascorbic acid (by shaking) and then added to the reaction solution. This allows the Zn to distribute onto the surface of the NCs. Furthermore, the Cu:Zn composition could be adjusted from 3 at% to 10 at% of Zn by varying the amount of the Zn(II) precursor.[115] At lower Zn amounts, mainly the corners of the NCs were covered with ZnO, while at higher Zn amounts, the edges were covered as well.[186] However, very high Zn amounts (> 15 at%) result in the formation of a ZnO network between the Cu_2O NCs as well as ZnO agglomerations.

Finally, Cu_2O systems can be easily modified with ZnO in a one-pot synthesis approach by employing the same reducing agent (L-ascorbic acid) for both metal(II) precursors. These cage-like ZnO-decorated Cu_2O NCs with 6 at% of Zn were used for the studies in Chapter 7 under pulsed CO_2RR conditions.

5. *Operando* Investigation of Ag-Decorated Cu_2O Nanocube Catalysts with Enhanced CO_2 Electroreduction toward Liquid Products

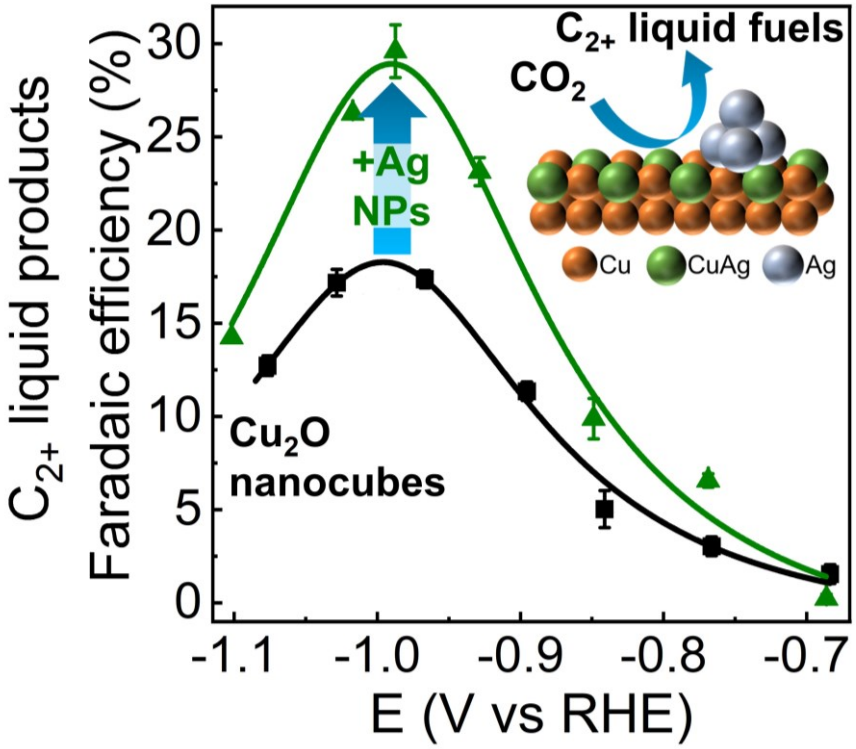

This chapter presents the work of my publication "*Operando* Investigation of Ag-Decorated Cu_2O Nanocube Catalysts with Enhanced CO_2 Electroreduction toward Liquid Products" (https://doi.org/10.1002/anie.202017070) and is reproduced from reference [158]. I have planned and analyzed all experiments shown in this chapter and wrote the publication under the supervision of Dr. A. Bergmann and Prof. Dr. B. Roldán Cuenya. I synthesized the samples and performed the CO_2RR testing as well as the XRD, XPS, XAS, and SERS measurements. Dr. A. Bergmann carried out the Rietveld refinement of the XRD data. Dr. H. S. Jeon, Dr. J. Timoshenko, and F. T. Haase were involved in the XAS measurements and contributed to its data analysis. S. Kühl carried out the ICP-MS and STEM/-EDX measurements, C. Rettenmaier performed a part of the XPS measurements, and M. Lopez Luna contributed to the acquisition of the SERS data.

"Direct conversion of carbon dioxide into multicarbon liquid fuels by the CO_2 electrochemical reduction reaction (CO_2RR) can contribute to the decarbonization of the global economy. Here, well-defined Cu_2O nanocubes (NCs, 35 nm) uniformly covered with Ag nanoparticles (5 nm) were synthesized. When compared to bare Cu_2O NCs, the catalyst with 5 at% Ag on Cu_2O NCs displayed a two-fold increase in the Faradaic efficiency for C_{2+} liquid products (30 % at -1.0 V_{RHE}), including ethanol, 1-propanol, and acetaldehyde, while formate and hydrogen were suppressed. *Operando* X-ray absorption spectroscopy revealed the partial reduction of Cu_2O during CO_2RR, accompanied by a reaction-driven redispersion of Ag on the CuO_x NCs. Data from *operando* surface-enhanced Raman spectroscopy further uncovered significant variations in the CO binding to Cu, which were assigned to Ag-Cu sites formed during CO_2RR that appear crucial for the C-C coupling and the enhanced yield of liquid products.

5.1 Introduction

In the quest for developing a sustainable energy economy, the electrochemical reduction of carbon dioxide (CO_2RR) into value-added chemicals and fuels offers the potential to close the anthropogenic carbon cycle and store renewable (wind, solar, hydro) energy into chemical bonds.[187, 188] It has been therefore of particular interest to develop efficient and selective electrocatalysts, which reduce the reaction overpotential and steer the reaction toward hydrocarbons and multicarbon oxygenates (C_{2+}). The selective generation of liquid products such as ethanol, 1-propanol, and acetaldehyde is highly desirable due to their high energy densities and advantages for storage/transport as compared to gaseous products.[189, 190]

A variety of metal electrodes can be used to catalyze CO_2RR as demonstrated in the pioneering work by Hori.[11] While some metals primarily reduce CO_2 to CO (Ag, Au, Zn) or formate (Sn, In, Bi), copper is the only metal yielding products such as methane, ethylene, and ethanol in considerable amounts.[14] However, the selective conversion to C_{2+} products in the form of liquids (alcohols and carbonyls) still requires high overpotentials, suffers from low current densities that can be achieved, and the generation of parasitic hydrogen through the competing hydrogen evolution reaction (HER). Various strategies have been developed to enhance the performance of Cu-based catalysts, including nanostructuring Cu (control of exposed facets, defects, and low-coordinated sites),[60, 61, 68, 191-193] engineering the Cu-electrolyte interface (change of local pH),[194-198] and adjusting the Cu oxidation state (compositional change).[90, 96, 199, 200] For example, Cu_2O nanocubes (NCs) with well-ordered (100) facets have been shown to lead to an increase in the selectivity toward ethylene, while suppressing methane production.[61,

62, 75

A promising way to further improve the catalyst's performance and selectivity is the introduction of a secondary metal.[108, 113, 201, 202] Recent studies of Cu-Ag bimetallic systems showed enhanced selectivity for C_{2+} products. In particular, a phase-blended Ag-Cu_2O catalyst had a three times higher Faradaic efficiency (FE) toward ethanol than Ag-free Cu_2O, but suffered from low activity ($|j_{ethanol}| < 1$ mA).[117] Additionally, Ag-covered Cu_2O nanowires prepared via a galvanic replacement reaction enabled a 1.4 times higher current density toward ethylene production as compared to pure Cu_2O nanowires.[116] Furthermore, CuAg surface alloys have been found to be more selective for the formation of multi-carbon products than pure copper.[104, 112] The facilitated yield of C_{2+} products in the bimetallic system is usually linked to the suppression of HER due to the enhanced coverage of *CO adsorbates as compared to *H,[104] and the diffusion of CO from Ag sites to Cu sites that enables C-C coupling (CO spillover).[116, 117] Note here that a short diffusion path of CO and therefore a homogeneous distribution of Cu and Ag at the surface of the catalyst is essential for an effective CO spillover.[104, 117] Nonetheless, although the spatial arrangement of Cu and Ag in these studies seems to play a key role for the different CO_2RR selectivity trends obtained, the key parameters for achieving an optimal synergy in Cu-Ag bimetallic systems are still unknown. In particular, open questions still remain on the composition and structure of the most active and C_{2+}-selective systems under *operando* CO_2RR conditions, including the stability of Cu_2O, which might be modified by introducing Ag.[203]

Herein, we prepared well-defined Cu_2O NCs (35 nm) uniformly covered with Ag nanoparticles (NPs, 5 nm) by a facile wet-chemical ligand-free synthesis. Employing *ex situ*, *in situ*, and *operando* characterization techniques, we gained insights into the morphology, chemical state, composition, and adsorbates of the Cu-Ag catalyst under CO_2RR conditions. In particular, we discuss reaction-induced Ag redispersion, Cu-Ag surface alloy formation, the influence of Ag on the reduction of Cu_2O, the adsorption of CO on Cu and Ag, and the effect of the former parameters in the CO_2RR activity and selectivity.

5.2 Experimental Details

5.2.1 Synthesis of Catalysts and Preparation of Electrodes

Cu_2O NCs were prepared by a ligand-free method similar to that used in a prior work[180] and subsequently decorated with Ag NPs. All reagents were purchased from Sigma-Aldrich in ACS grade and used without further purification. In a typical synthesis, an alkaline diluted solution of $CuCl_2$ was-prepared by adding 5 mL of a $CuCl_2$ * 2 H_2O solution (0.1 M) and 15 mL of a

NaOH solution (0.2 M) to 200 mL of ultrapure water (> 18 MΩ cm) at room temperature. After stirring for 5 min, 10 mL of a L-ascorbic acid solution (0.1 M) were added to the mixture. The solution was further stirred for 1 h. Then, 6 or 10 mL of an $AgNO_3$ solution (0.0025 M) were slowly added to the reaction solution under vigorous stirring and were further stirred for 10 min to obtain 3 and 5 at% Ag/Cu_2O NCs (denoted as 3-Ag/Cu_2O and 5-Ag/Cu_2O), respectively. The solution was centrifuged and washed three times, twice with an ethanol-water mixture (1:1) and once with pure ethanol. The final product was dispersed in 10 mL of ethanol to reach a Cu loading of 2 mg mL^{-1}. The solutions were stored in the fridge.

To prepare the electrode, 475 µL of the catalyst dispersion with a Cu loading of 2 mg mL^{-1} were mixed with 25 µL of a Nafion solution (Sigma-Aldrich, ~5 wt% in a mixture of alcohols and water) and then ultrasonicated for 5 min. Then, 37 µL of the catalyst mixture were slowly drop-casted on each side of a 0.5 x 2 cm carbon paper sheet (Alfa Aesar, Toray Carbon Paper, TGP-H-60) to obtain a Cu loading of 70 µg cm^{-2}. After drying, the electrode was ready to use in an H-type electrochemical cell for CO_2RR.

The reference sample Cu_2O/Ag was prepared by drop-casting the Cu_2O NCs on a mechanically polished Ag foil (Alfa Aesar, 0.1 mm thick, 99.998 %) to obtain a Cu loading of 70 µg cm^{-2}.

5.2.2 Electrochemical Characterization

Electrochemical CO_2RR experiments were performed with a Biologic SP-300 potentiostat in a gas-tight custom-made H-type cell. The cathodic and anodic compartments were separated by an anion exchange membrane (Selemion AMV, AGC Inc.). We used a platinum gauze (MaTecK, 3600 mesh cm^{-2}) as the counter electrode and a reversible hydrogen electrode (RHE, HydroFlex, Gaskatel) as the reference electrode. Both compartments were filled with a 0.1 M $KHCO_3$ solution (Sigma-Aldrich, 99.7 %). The electrolyte was previously purified from trace metal ion impurities by a cation-exchange resin (Chelex 100 Resin, Bio-Rad) followed by saturation with CO_2 (99.995 %) for 30 min until a pH of 6.8 was reached. The electrochemical protocol consisted of a linear sweep voltammogram (LSV) from the open circuit potential to the cathodic potential, followed by chronoamperometry (CA) at this potential for 2 h. All potentials are given versus the RHE scale and were corrected for the iR drop. Each presented data point at one potential corresponds to an average of at least three different measurements collected with an identical freshly prepared sample under the same experimental conditions, and the error bars represent the standard deviation.

The gas products were measured every 15 min and quantified by online gas chromatography (GC, Agilent 7890B) equipped with a thermal conductivity detector (TCD) and a flame ionization detector (FID). During the measurements, CO_2 gas was constantly bubbled through

the electrolyte with a flow rate of 20 mL min^{-1}. Carboxylates were analyzed with a high-performance liquid chromatograph (HPLC, Shimadzu Prominence) equipped with a NUCLEOGEL SUGAR 810 column and a refractive index detector (RID). Alcohols were quantified with a liquid GC (L-GC, Shimadzu 2010 plus) equipped with a fused silica capillary column and an FID detector. An aliquot of the electrolyte was collected after each measurement and directly analyzed by the HPLC and L-GC.

The catalyst surface roughness factors were estimated by measuring the double layer capacitance with cyclic voltammetry in a non-Faradaic potential range from +0.10 to +0.25 V_{RHE} at scan rates of 20, 40, 60, 80, and 100 mV s^{-1} in a CO_2-saturated 0.1 M $KHCO_3$ solution after 2 h of electrochemical reaction at -1.0 V_{RHE}.[90]

5.2.3 *Ex Situ* Characterization

The morphology and elemental distribution of the samples were determined by scanning transmission electron microscopy (STEM, FEI Talos F200X microscope, Thermo Fisher Scientific) and energy dispersive spectroscopy (EDX, SuperX 4 SDD EDX detector) maps. The STEM was equipped with an XFEG field emission gun (200 kV) and with brightfield (BF), darkfield (DF), and high-angle annular darkfield (HAADF) detectors. Samples were prepared by coating a nickel grid (400 mesh with lacey carbon film, PLANO GmbH) with the catalyst dispersed in EtOH:H_2O (1:1) before and after CO_2RR.

The crystal structure of the catalysts was analyzed *ex situ* with an X-ray diffractometer (XRD, Bruker D8 Advance) equipped with an energy-dispersive position-sensitive LynxEye detector and Cu X-ray tube. Measurements of the as-prepared samples deposited on a low-background Si substrate were performed in a 2θ range of 10-90° with a step size of 0.03° and a collection time of 5 s per step in the Bragg-Brentano geometry. Grazing incident (GI) XRD measurements of the samples deposited on carbon paper before and after CO_2RR were performed in a 2θ range of 10-87° with a step size of 0.04°, a collection time of 26 s per step and an incident angle of 0.2°. For the grazing-incidence measurements, the XRD was equipped with a Goebel mirror parallelizing the X-ray beam, an equatorial Soller slit (0.3°), and the LynxEye detector in 0D mode. Rietveld refinement was applied to analyze the XRD pattern using the TOPAS® software package. Instrumental broadening and zero error were considered.

The bulk composition and amount of Cu and Ag in the catalyst dispersions and in the catalysts on carbon paper in the as-prepared samples and after CO_2RR were determined by inductively coupled plasma-mass spectrometry (ICP-MS, iCAP RQ, Thermo Fisher Scientific). Samples were digested in a mixture of concentrated acids (HNO_3:H_2SO_4:HCl in a 1:1:3 ratio) and heated using microwave irradiation at 180 °C for 20 min, with a ramping step of 10 min (Multiwave

GO, Anton Paar). The samples were diluted with ultrapure water (> 18 MΩ cm) to reach the appropriate concentrations.

The surface composition of the catalysts was characterized by quasi-*in situ* X-ray photoelectron spectroscopy (XPS) before and directly after CO_2RR without exposure to air. For this purpose, an electrochemical cell was directly connected to an ultra-high vacuum system equipped with a hemispherical electron analyzer (Phoibos 100, SPECS GmbH, E_{pass} = 20 eV) and an X-ray source (XR 50, SPECS GmbH) with a Magnesium anode (1253.6 keV, 250 W). All spectra were aligned to the Cu $2p_{3/2}$ peak (E_{bin} = 932.7 eV). Linear combination fitting of the Cu LMM Auger profiles using reference spectra was performed to distinguish the different copper oxidation states. The Cu, Cu_2O, and CuO amounts were estimated from the integrated areas of the fit with the corresponding reference spectra. These reference spectra were acquired on an *in situ* annealed and sputtered Cu foil (metallic reference) and a plasma oxidized CuO sample, while the reference spectrum of Cu_2O was taken from the literature.[169] The Cu to Ag ratio was determined from the Ag $3d_{5/2}$ to Cu $2p_{3/2}$ regions and calculated considering the relative sensitivity factors (RSF) of the metals (Ag $3d_{5/2}$: 18.04; Cu $2p_{3/2}$: 15.9). The electrochemical measurements were performed using a Metrohm Autolab potentiostat (PGSTAT 302 N) with a platinum mesh as counter electrode and a leak-free Ag/AgCl as the reference electrode.

5.2.4 *Operando* Characterization

Operando X-ray absorption spectroscopy (XAS) measurements were performed at the SAMBA beamline at SOLEIL synchrotron in France (for Cu_2O NCs), and at the Claess beamline at ALBA synchrotron in Spain (for 3-Ag/Cu_2O and 5-Ag/Cu_2O samples). More details on the XAS data collection and EXAFS data fitting can be found in Section 5.2.5.

Operando surface-enhanced Raman spectroscopy (SERS) was carried out with a Raman spectrometer (Renishaw, InVia Reflex) coupled with an optical microscope (Leica Microsystems, DM2500M) together with a motorized stage for sample tracking (Renishaw, MS300 encoded stage). Calibration of the system was performed using a Si(100) wafer (520.5 cm^{-1}). A near-infrared laser (Renishaw, RL785, λ = 785 nm, P_{max} = 500 mW) served as the excitation source. Backscattered light was Rayleigh-filtered, and the Raman scattering was collected in the range of 100-3200 cm^{-1} with a grating of 1200 lines mm^{-1} and directed to a CCD detector (Renishaw, Centrus). For the *operando* measurements, the excitation source was focused on the surface of the sample, and Raman scattering signals were collected with a water immersion objective (Leica microsystems, 63x, numerical aperture of 0.9). The water immersion objective was protected from the electrolyte by a Teflon film (DuPont, film thickness of 0.013 mm) wrapped around the objective. The electrochemical measurements were

performed in a home-built spectro-electrochemical cell made of PTFE and controlled by a Biologic SP-240 potentiostat. The cell was equipped with a leak-free Ag/AgCl reference electrode and a Pt counter electrode, while the working electrode with the catalyst was drop-casted on glassy carbon. A CO_2-saturated 0.1 M $KHCO_3$ solution was used as the electrolyte. Each potential was applied for at least 10 min before collecting the spectra to ensure steady-state conditions at the surface of the catalyst. The collection of each spectrum was performed with 10 s of exposure time. Depth scans were performed to optimize the focus in order to increase the Raman signal of the species studied. Bands at higher wavenumbers (~3000 cm^{-1}) typical for hydrocarbons were not accessible under infrared laser excitation. The Raman data were processed using the Renishaw WiRE 5.2 software. The spectra were baseline-subtracted using the intelligent spline feature (polynomial order 8), and cosmic rays were removed.

5.2.5 Details of XAS Data Collection and Analysis

Operando Cu K-edge XAS measurements of Cu_2O NCs were measured using a Si(220) monochromator for energy selection. Higher harmonics were rejected using a Pd-coated mirror. The beam size was 1 x 0.5 mm. Measurements were performed in fluorescence mode using a 13-channel Ge detector. The intensity of the incident radiation was measured with an ionization chamber (I_0) filled with an N_2(500 mbar)/He(500 mbar) mixture. Two additional ionization chambers filled with 1700 mbar N_2 (in I_1 chamber) and an Ar (150 mbar)/N_2 (850 mbar) mixture (in I_2 chamber) were used for measurements in transmission mode for reference samples.

Operando XAS measurements for 3-Ag/Cu_2O and 5-Ag/Cu_2O were performed in a similar manner using a 6-channel Si drift detector for fluorescence data collection. A Si(111) monochromator was used for measurements at the Cu K-edge and a Si(311) monochromator for measurements at the Ag K-edge. In the latter case, the I_0 chamber was filled with 93:7 Kr to N_2 mixture. For bimetallic samples, XAS spectra for the Cu K-edge (E_0 = 8979 eV) and Ag K-edge (E_0 = 25514 eV) were collected in fluorescence mode separately, using two fresh samples with different sample loadings to ensure reasonable XAS data quality for more diluted Ag but avoiding self-absorption effects in the Cu K-edge spectra.

A custom-built electrochemical cell was used for *operando* XAS measurements. The applied potential was controlled by a PalmSens potentiostat (MultiEmStat). A platinum mesh and leak-free Ag/AgCl electrode were used as counter and reference electrodes, respectively. For the XAS studies, a sample was drop-casted onto one side of a carbon paper (Sigracet 29 BC, SGL Carbon) substrate (with a loading of 0.5 mg cm^{-2} for the Cu K-edge measurements and 3 mg cm^{-2} for Ag K-edge measurements), while the other side of the carbon paper was covered with Kapton tape. Subsequently, the sample was mounted in the *operando* cell with the Kapton

side facing out of the cell and acting as a window, while the side coated with the catalyst was in contact with the electrolyte. The electrolyte (0.1 M $KHCO_3$) was circulated between the cell and a reservoir using a peristaltic pump. The cell was continuously purged with CO_2 during the measurements. All measurements were performed under a constant potential of -1.0 V_{RHE}.

Time-resolved spectra under CO_2RR conditions were acquired with 9-12 min acquisition time per spectrum until no further changes were observed. For all samples, several hours were needed to achieve a steady-state structure and composition. Analysis of the time-dependent X-ray absorption near edge structure (XANES) and extended X-ray absorption fine structure (EXAFS) spectroscopy data was used then to follow the evolution of the chemical composition and the sample structure at the Cu K-edge. At the Ag K-edge, the analysis of individual XAS spectra collected *operando* under CO_2RR conditions was not possible due to the low concentration of Ag. Therefore, the Ag K-edge XAS spectra obtained during the first 2 h under CO_2RR conditions were merged together and compared with those for the as-prepared sample in air. Linear combination analysis (LCA) was applied to process the XANES data. Moreover, Cu- and Ag K-edge EXAFS data fitting was performed to gain quantitative information about the bond lengths and coordination numbers.

Data alignment and normalization of the XANES data were carried out using the conventional approach implemented in the Athena software.[204] For quantitative EXAFS analysis, conventional least-square fitting to theoretical standards, as implemented in the FEFFIT code[204] was applied. Theoretical phases and amplitudes were obtained in self-consistent ab-initio calculations with the FEFF8.5 code.[205] The complex exchange-correlation Hedin-Lundqvist potential and default values of muffin-tin radii as provided within the FEFF8.5 code were employed. Fitting of the Cu K-edge EXAFS spectra $\chi(k)k^2$ of the as-prepared catalysts was carried out in *R*-space in the range from R_{min} = 1 Å up to R_{max} = 2.1 Å, while for the catalysts in the reduced state, R_{min} = 1.0 Å to R_{max} = 3.0 Å were used. The Fourier transforms were carried out in the *k*-range from 3.0 $Å^{-1}$ to 10.0 $Å^{-1}$ with a *k*-weighting of 1, 2, and 3. Fitting of Ag K-edge EXAFS spectra of the as-prepared catalysts and the catalysts during CO_2RR was carried out in *R*-space in the range from R_{min} = 1.4 Å up to R_{max} = 3.2 Å. The Fourier transforms were carried out in the *k*-range from 3.0 $Å^{-1}$ up to 8.0 $Å^{-1}$ with a *k*-weighting of 1,2 and 3. Fitting parameters were the coordination numbers *N*, interatomic distances *R*, disorder factors σ^2 for Cu-O, Cu-Cu, Ag-Ag and Ag-Cu paths, as well as the corrections to the photoelectron reference energies ΔE_0. The S_0^2 factors were obtained from the EXAFS fit data of the references, which were 0.87 ± 0.02 for Cu foil, 0.32 ± 0.01 for Cu_2O, and 0.92 ± 0.02 for Ag foil.

5.3 Results and Discussion

5.3.1 *Ex Situ* and Quasi-*In Situ* Characterization

Figure 5.1 shows STEM-HAADF and STEM-EDX maps of pure and Ag NP-decorated Cu_2O NCs. The as-prepared Cu_2O NCs have an edge length of 35 ± 7 nm (Figure 5.1 a). The STEM-EDX data (Figure 5.1 b, Figure A5.1, Table 5.1) reveal an average Cu:O at% ratio of 66:34, which corresponds to the composition of Cu_2O. In the following, the Cu_2O NCs decorated with 3 and 5 at% of Ag will be denoted 3-Ag/Cu_2O and 5-Ag/Cu_2O. The Ag NPs with a diameter of 4.6 ± 1.1 nm (3-Ag/Cu_2O, Figure 5.1 e, Figure A5.2) and of 6.0 ± 2.1 nm (5-Ag/Cu_2O, Figure 5.1 i, Figure A5.3) appear to be uniformly distributed on the surface of the Cu_2O NCs. The STEM-EDX maps of the as-prepared 3- and 5-Ag/Cu_2O catalysts (Figure 5.1 f,j) indicate a clear phase separation between the Ag NPs and the Cu_2O NCs. After 2 h of CO_2RR at -1.0 V_{RHE} in 0.1 M $KHCO_3$, the cubic morphology appeared less pronounced and hollow structures

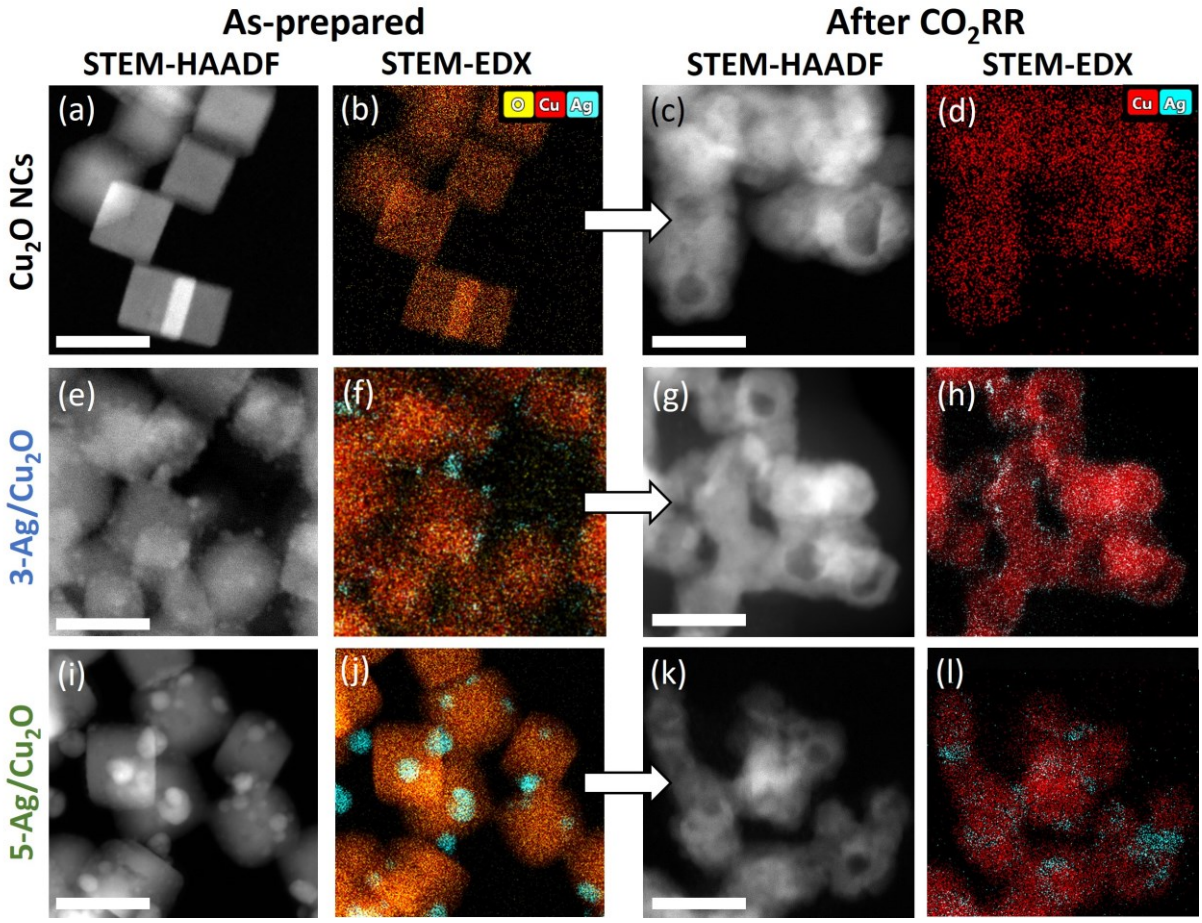

Figure 5.1 STEM-HAADF images with corresponding EDX maps of Cu_2O NCs, 3-Ag/Cu_2O, and 5-Ag/Cu_2O in the upper, middle, and lower panels, respectively. As-prepared samples are shown on the left (a,e,i) with EDX maps in (b,f,j) and samples after 2 h of CO_2RR at -1.0 V_{RHE} on the right (c,g,k) with EDX maps in (d,h,l). The scale bars correspond to 50 nm.

Table 5.1 Edge lengths of Cu_2O NCs and diameters of Ag NPs with the corresponding size distribution obtained from the analysis of STEM-HAADF images of Cu_2O NCs, 3-Ag/Cu_2O, and 5-Ag/Cu_2O in the as-prepared state and after 2 h of CO_2RR at -1.0 V_{RHE}. The decrease in the edge length after CO_2RR was slightly enhanced when the Cu_2O NCs were decorated with Ag NPs.

Sample	As-prepared		After CO_2RR	
	Cu_2O NCs [nm]	**Ag NPs [nm]**	**Cu_2O NCs [nm]**	**Ag NPs [nm]**
Cu_2O NCs	34.8 ± 6.6	-	32.5 ± 9.6	-
3-Ag/Cu_2O	37.0 ± 8.3	4.6 ± 1.1	32.8 ± 10.5	6.3 ± 1.6
5-Ag/Cu_2O	27.6 ± 4.2	6.0 ± 2.1	24.2 ± 7.4	9.5 ± 2.5

Table 5.2 Elemental quantification of Cu, O, and Ag extracted from the STEM-EDX images of Figure 5.1 of Cu_2O NCs, 3-Ag/Cu_2O, and 5-Ag/Cu_2O.

Sample	As-prepared			After CO_2RR		
	Cu [%]	**O [%]**	**Ag [%]**	**Cu [%]**	**O [%]**	**Ag [%]**
Cu_2O NCs	66(15)	34(6)	-	79(19)	21(4)	-
3-Ag/Cu_2O	59(13)	40(7)	1.4(3)	76(18)	23(5)	0.6(1)
5-Ag/Cu_2O	61(13)	36(6)	3.4(7)	65(14)	31(6)	3.9(8)

formed in all cases (Figure 5.1 c,g,k). Simultaneously, the edge length of the NCs decreased in average by 3 nm (Table 5.1) and the size distribution broadened, as reported in the literature for pure Cu_2O NCs after CO_2RR.[62, 75] STEM-EDX maps after reaction (Figure 5.1 d,h,l) reveal that Cu_2O is partially reduced to metallic Cu (Table 5.2) and that the clear phase separation between Ag and Cu is lost. Instead, small Ag clusters are dispersed on the Cu surface. In addition, some Ag-rich areas with sizes of 6.3 ± 1.6 nm (3-Ag/Cu_2O) and 9.5 ± 2.5 nm (5-Ag/Cu_2O) were also found (Table 5.1).

XRD was applied to confirm the phase purity of the catalysts and to track the evolution of the crystal structure after CO_2RR. Figure 5.2 shows the XRD pattern of the as-prepared Cu_2O NCs and Ag/Cu_2O with the main Cu_2O reflections assigned to (111) at 36.4° and (200) at 42.3°. The presence of metallic Ag can be seen by the Ag(111) at 38.2° and Ag(200) at 44.5° for the Ag/Cu_2O. The low intensity of the fcc Ag reflections can be attributed to the low Ag loading and XRD peak broadening due to small particle sizes.

Table 5.3 shows the as-prepared composition and coherence length derived from Rietveld refinement of the XRD patterns. The coherence length of the Cu_2O agrees well with the size distribution obtained by STEM analysis, although it is slightly smaller than the mean NC edge length. The atomic fractions of metallic Ag in the as-prepared Ag/Cu_2O agree well with the Cu:Ag composition obtained by ICP-MS (Table 5.4). This confirms that the majority of the

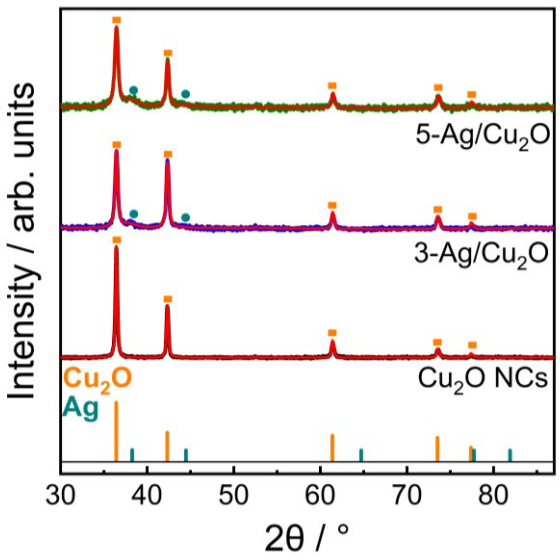

Figure 5.2 *Ex situ* XRD pattern of as-prepared Cu_2O NCs (black), 3-Ag/Cu_2O (blue), and 5-Ag/Cu_2O (green) samples on a Si substrate with corresponding Rietveld fits (red). The intensity ratio of the fcc Cu(111) and (200) reflections vary, most likely due to a preferred orientation of the Cu_2O NCs on the Si substrate. No further reflections, *e.g.,* from CuO, metallic Cu, AgCl or Ag_2O can be found in the as-prepared state, confirming the phase purity of the catalysts.

added Ag from the $AgNO_3$ solution was incorporated in the Ag NPs, and that the initial ratios of the metal salts utilized were maintained.

The structural evolution of the 5-Ag/Cu_2O catalyst was investigated before and after 2 h of CO_2RR using *ex situ* grazing incidence (GI) XRD (Figure 5.3, Table 5.3) and shows the reduction of Cu_2O to metallic Cu as prominently seen in the Cu(111) reflection at 43.2°. The background arises from the carbon paper support (Figure A5.4). Rietveld refinement of 5-Ag/

Table 5.3 Atomic fraction and structural coherence length of Cu_2O and metallic Cu and Ag phases derived from Rietveld refinement of *ex situ* XRD patterns of as-prepared Cu_2O NCs, 3-Ag/Cu_2O, and 5-Ag/Cu_2O, and of 5-Ag/Cu_2O deposited on carbon paper after 2 h of CO_2RR at -1.0 V_{RHE}.

Sample	Atomic fraction [at%]			Structural coherence length [nm]		
	Cu_2O	**fcc Cu**	**fcc Ag**	**Cu_2O**	**fcc Cu**	**fcc Ag**
As-prepared						
Cu_2O NC	100	-	-	32.6(3)	-	-
3-Ag/Cu_2O	97.55(9)	-	2.45(6)	32.3(7)	-	5.9(7)
5-Ag/Cu_2O	95.1(7)	-	4.9(5)	23.1(3)	-	6(2)
After CO_2RR						
5-Ag/Cu_2O	56(16)	24(9)	20(7)	6.8(3)	9(2)	4.4(5)

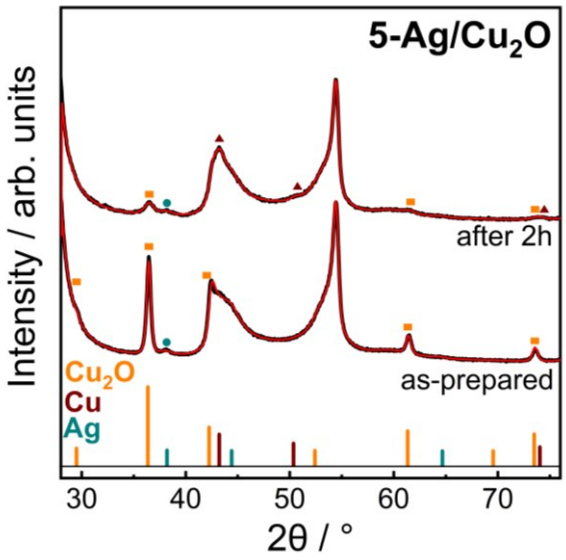

Figure 5.3 *Ex situ* XRD pattern of 5-Ag/Cu_2O deposited on carbon in the as-prepared state and after 2 h of CO_2RR at -1.0 V_{RHE}. Red lines correspond to Rietveld fits.

Cu_2O after CO_2RR suggests a mixture of Cu_2O and metallic Cu and a significantly increased Ag fraction, while ICP-MS did not show changes in the catalyst composition (Table 5.5). Thus, we are missing a considerable fraction of Cu/CuO_x after the reaction by XRD. This suggests that Cu might be present in non-crystalline domains, resulting in an increased Ag:Cu ratio. Additionally, there is a slight contraction of the Ag lattice (4.092 ± 0.003 to 4.088 ± 0.003 Å), which could be explained by the incorporation of Cu into the Ag lattice (Table A5.2). Notably, the coherence length of Cu_2O decreased strongly from 23.1 nm (as-prepared) to 6.8 nm (after

Table 5.4 Cu and Ag composition of as-prepared Cu_2O NCs, 3-Ag/Cu_2O, and 5-Ag/Cu_2O dispersions obtained by ICP-MS.

Sample	Cu [at%]	Ag [at%]
Cu_2O NCs	100	-
3-Ag/Cu_2O	97.75(1)	2.25(1)
5-Ag/Cu_2O	95.07(3)	4.93(3)

Table 5.5 Cu and Ag mass and composition of Cu_2O NCs, 3-Ag/Cu_2O, and 5-Ag/Cu_2O on carbon paper (2 cm^2) obtained by ICP-MS in as-prepared state and after 2 h of CO_2RR at -1.0 V_{RHE}.

Sample	As-prepared				After CO_2RR			
	Cu [µg]	Ag [µg]	Cu [at%]	Ag [at%]	Cu [µg]	Ag [µg]	Cu [at%]	Ag [at%]
Cu_2O NCs	139(32)	-	100	-	134(7)	-	100	-
5-Ag/Cu_2O	146(14)	12(1)	95.3(2)	4.7(2)	149(17)	12(2)	95.3(2)	4.7(2)

CO_2RR), reaching a similar value to the coherence length of the metallic Cu phase (9 nm). We conclude that the hollow structures after CO_2RR (Figure 5.1) might consist of a mixture of Cu_2O and Cu crystallites as seen in XRD. The coherence length of the metallic Ag phase is on average slightly decreased after CO_2RR, which agrees with the partial redispersion of Ag on the Cu surface and the Ag-rich domains likely being formed from multiple Ag NPs.

Quasi-*in situ* XPS measurements were performed to gain deeper insight into the surface composition and chemical state of the Ag NP-decorated and pure Cu_2O NCs before and after 2 h of CO_2RR. Figure 5.4 presents the Ag 3d and Cu Auger LMM spectra, while Figure 5.5 shows the Cu 2p spectra. The Ag 3d core level regions of 3- and 5-Ag/Cu_2O (Figure 5.4 a,b) reveal that Ag is in the metallic state before and after CO_2RR, which is also consistent with the XRD results. The Ag:Cu surface composition ratios were determined by integrating the peak areas of Ag $3d_{5/2}$ and Cu $2p_{3/2}$. As expected for Ag NPs decorating the surface of Cu_2O NCs, the Ag:Cu ratio extracted from the more surface-sensitive XPS technique was higher than the

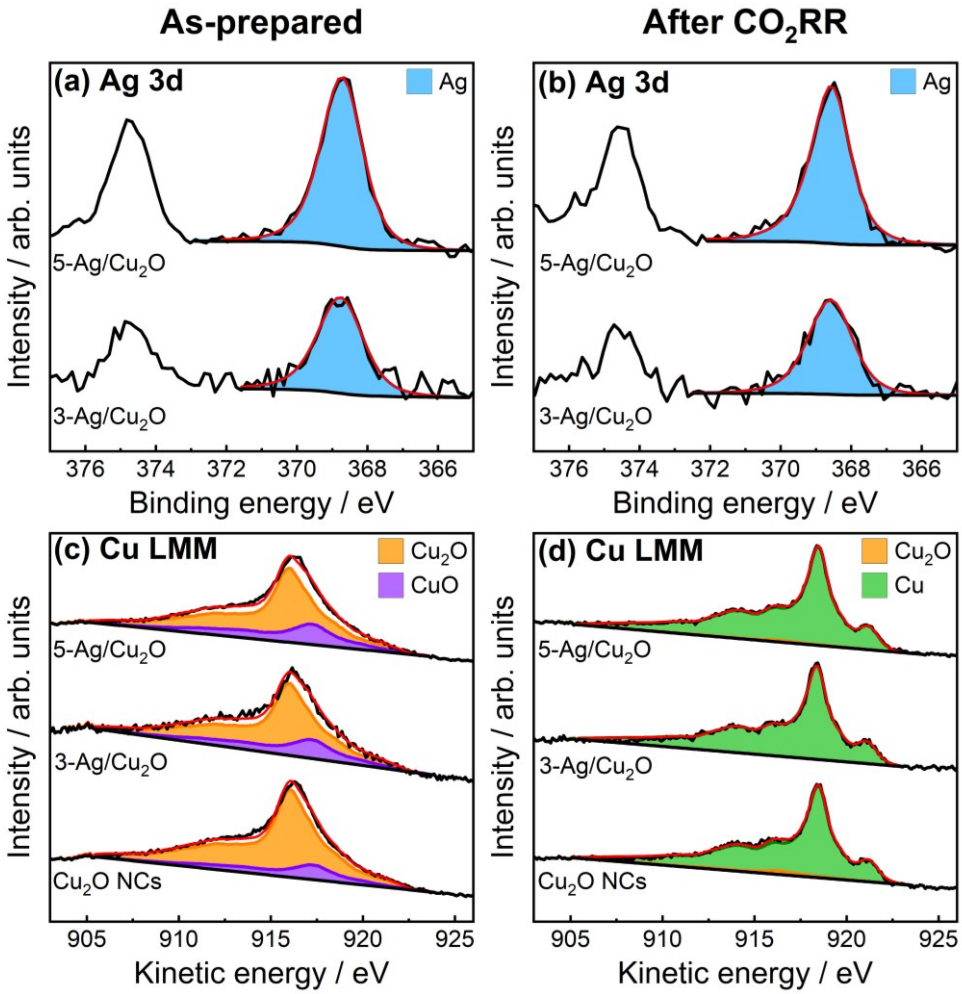

Figure 5.4 Quasi-*in situ* Ag 3d and Cu LMM XAES spectra of Cu_2O NCs, 3-Ag/Cu_2O and 5-Ag/Cu_2O (a,c) in the as-prepared state and (b,d) after 2 h of CO_2RR at -1.0 V_{RHE} (without air exposure) with the corresponding fits (red line) and reference spectra.

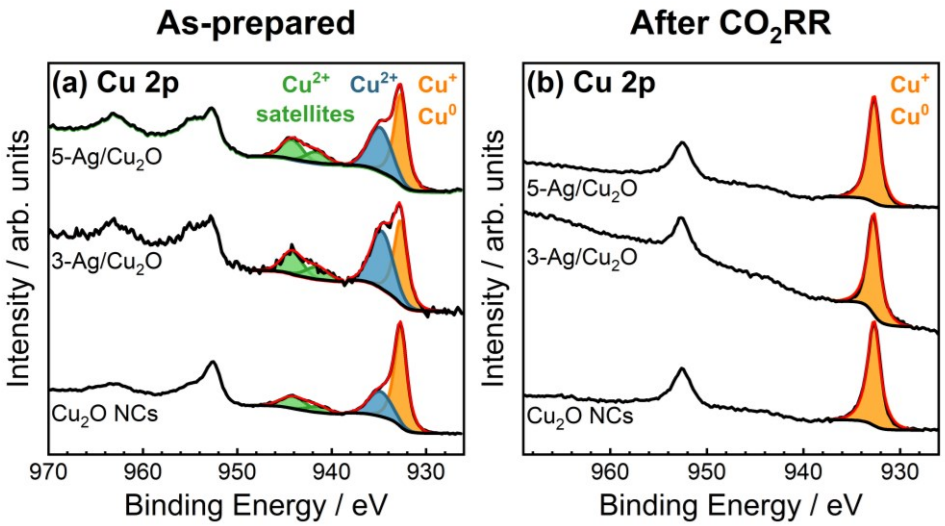

Figure 5.5 Quasi-*in situ* Cu 2p core level regions of Cu_2O NCs, 3-Ag/Cu_2O and 5-Ag/Cu_2O (a) in the as-prepared state and (b) after 2 h of CO_2RR at -1.0 V_{RHE} (without air exposure) with the corresponding fits (red line). The Cu 2p core level regions of the as-prepared samples show the presence of Cu(0)/Cu(I) and a shake-up satellite corresponding to Cu(II).

bulk composition obtained from the XRD and ICP-MS analysis. After CO_2RR, the Ag:Cu XPS ratios further increased from 4:96 to 7:93 at% in 3-Ag/Cu_2O and from 9:91 to 11:89 in 5-Ag/Cu_2O. Thus, we conclude that a more homogenous distribution of Ag (redispersion) on the Cu_2O surface takes place during CO_2RR. Furthermore, we can exclude significant preferential dissolution of Cu during CO_2RR due to the constant bulk Ag:Cu ratio before and after CO_2RR as demonstrated by ICP-MS (Table 5.5). The higher Ag signal observed after CO_2RR agrees with the formation of smaller Ag NPs and clusters and an enhanced Ag dispersion, as also revealed by the STEM and XRD data. Additionally, deconvolution of the Cu LMM spectra (Figure 5.4 c,d, Table 5.6) was carried out to distinguish Cu(0), Cu(I), and Cu(II) near-surface

Table 5.6 Kinetic energies and composition of Cu_2O, CuO, and Cu for Cu_2O NCs, 3-Ag/Cu_2O, and 5-Ag/Cu_2O in as-prepared state and after 2 h CO_2RR obtained by integration of the Cu LMM quasi-*in situ* XAES spectra shown in Figure 5.4 c,d. The presence of surface CuO can explain the discrepancy between STEM and XRD particle sizes because of the possible amorphous character of CuO.

Sample	**As-prepared**				**After CO_2RR**			
	Cu_2O		**CuO**		**Cu_2O**		**Cu**	
	Peak [eV]	**Fraction [at%]**	**Peak [eV]**	**Fraction [at%]**	**Peak [eV]**	**Fraction [at%]**	**Peak [eV]**	**Fraction [at%]**
Cu_2O NCs	916.1	84	917.2	16	916.4	5	918.5	95
3-Ag/Cu_2O	916.1	77	917.2	23	916.4	0	9.18.5	100
5-Ag/Cu_2O	916.1	77	917.2	23	916.4	2	918.5	98

species. In the as-prepared state, the samples consisted mainly of Cu_2O with a contribution of CuO. After 2 h of CO_2RR, the near-surface of the Cu_2O NCs and Ag/Cu_2O samples were fully reduced to metallic Cu within the error margin. In contrast to prior studies, our samples were not exposed to air after CO_2RR, since our electrochemical cell is directly connected to the XPS chamber. Thus, even though no potential is applied during the XPS measurement, re-oxidation in air can be excluded.

5.3.2 Electrocatalytic Performance

The electrocatalytic performance of Ag NP-decorated and pure Cu_2O NCs deposited on carbon paper was evaluated by CA measurements for 2 h at potentials between -0.7 and -1.1 V_{RHE} in a CO_2-saturated 0.1 M $KHCO_3$ electrolyte (Figure 5.6-5.9, Figure A5.5, Figure A5.6, Table A5.3). Figure 5.6 displays the FEs of the main C_2 and C_3 products, namely, ethanol, 1-propanol, and ethylene, as well as the combined FEs of all C_{2+} products, of the C_{2+} liquid products, and of the C_{2+} carbonyl products; see also Figure 5.7 (C_1 products), Figure 5.8 (minor C_{2+} products), Figure 5.9 (sum of all liquid products), and Figure A5.6 (geometric and mass current densities).

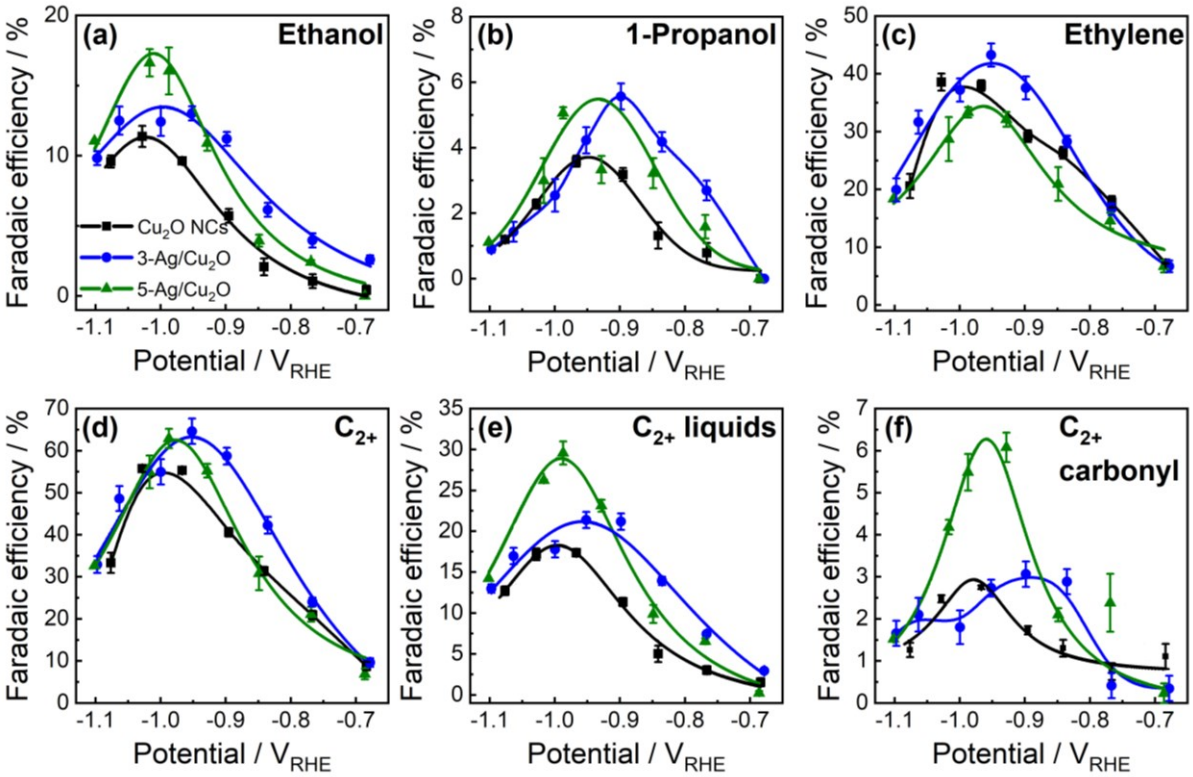

Figure 5.6 Potential-dependent Faradaic efficiencies of (a) ethanol, (b) 1-propanol, (c) ethylene, (d) C_2 + C_3 products (C_{2+}), (e) C_{2+} liquid products and (f) C_{2+} carbonyl products of Cu_2O NCs (black), 3-Ag/Cu_2O (blue), and 5-Ag/Cu_2O (green) after 2 h of electrolysis in CO_2-saturated 0.1 M $KHCO_3$. Solid lines are a guide for the eye.

The production of ethanol at -1.0 V_{RHE} increases significantly with the amount of Ag. Cu_2O NCs, 3-, and 5-Ag/Cu2O reach 10 %, 13 %, and 17 % FE for ethanol at -1.0 V_{RHE}, respectively (Figure 5.6 a, Figure A5.5). Thus, $FE_{ethanol}$ increased 1.5 times by the addition of 5 at% of Ag to Cu_2O NCs. Additionally, the production of 1-propanol is doubled in the Ag/Cu_2O samples with FE of 5-6 % at -0.9 V_{RHE} compared to 3 % for the Cu_2O NCs (Figure 5.6 b). This increase in alcohol yield has been previously linked to CO spillover from Ag to Cu, since the weaker binding between Ag and the *CO intermediate is considered to facilitate CO production as compared to the moderate binding energy between Cu and the *CO intermediate leading to the formation of hydrocarbons.[14, 117] Also in our case, the Ag/Cu_2O samples show higher FEs for CO at low overpotentials, with almost 40 % FE at -0.7 V_{RHE} in comparison to 20 % FE for the pure Cu_2O NCs (Figure 5.7 b). At higher overpotentials, the FE_{CO} decreases for all catalysts, and starting from -1.0 V_{RHE} the selectivity for CO of the Ag/Cu_2O is even similar to that of the bare Cu_2O NCs (FE_{CO} = 3-5 %). We note that 3-Ag/Cu_2O shows a better ability to transform CO_2 into C_{2+} products at lower overpotentials than 5-Ag/Cu_2O, which is also related to a lower

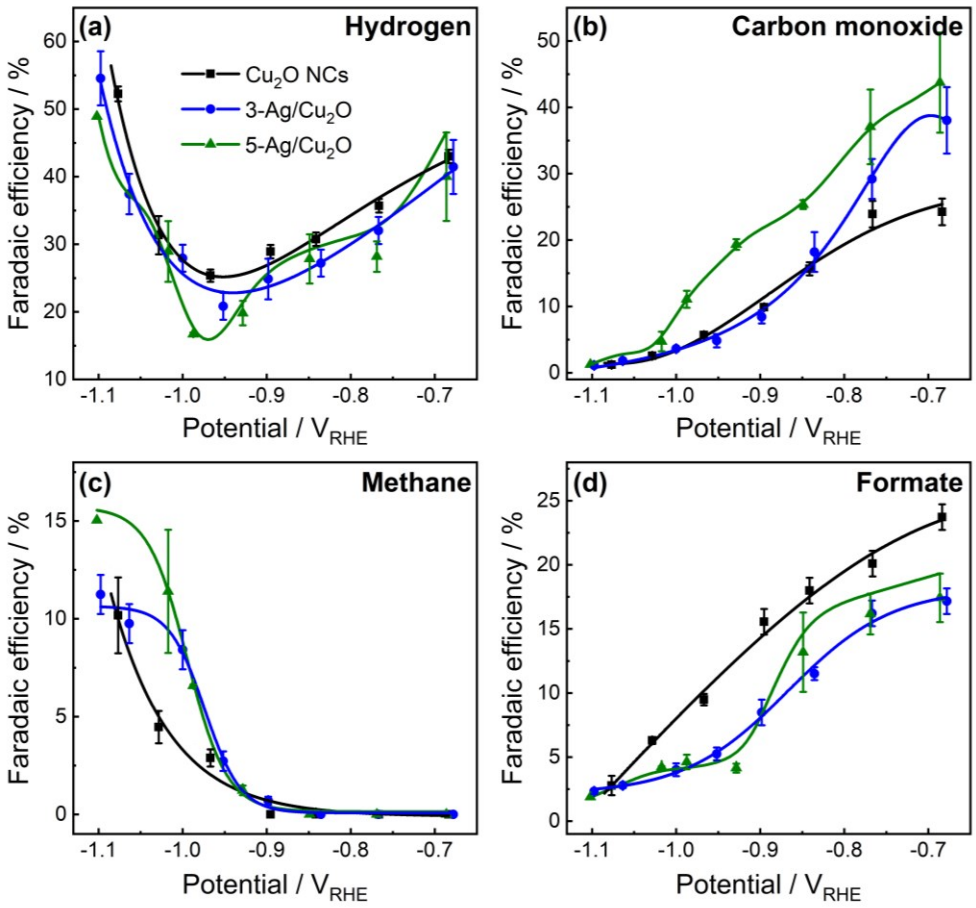

Figure 5.7 Potential-dependent Faradaic efficiencies of the major C_1 products (a) hydrogen, (b) carbon monoxide, (c) methane, and (d) formate of Cu_2O NCs (black), 3-Ag/Cu_2O (blue) and 5-Ag/Cu_2O (green) samples after 2 h of electrolysis in CO_2-saturated 0.1 M $KHCO_3$. Solid lines are a guide for the eye.

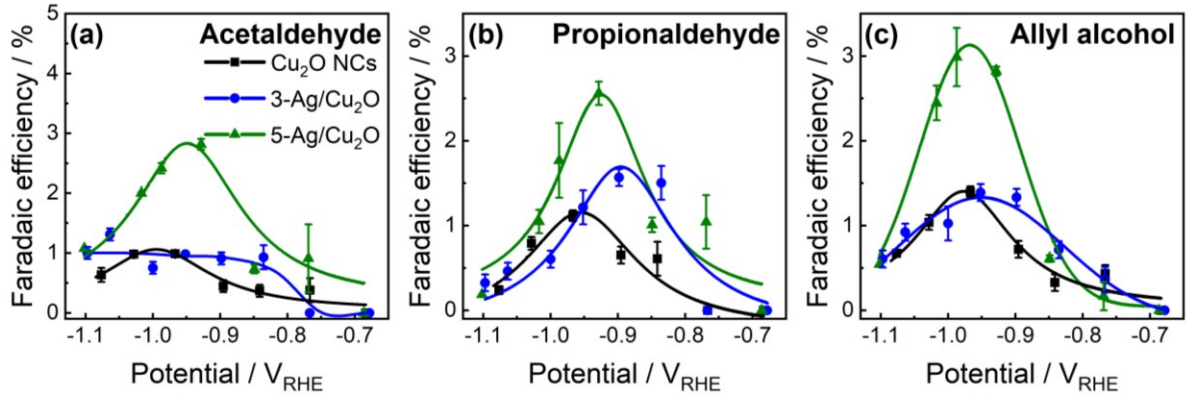

Figure 5.8 Potential-dependent Faradaic efficiencies of the minor C_{2+} products (a) acetaldehyde, (b) propionaldehyde, and (c) allyl alcohol of Cu_2O NCs (black), 3-Ag/Cu_2O (blue) and 5-Ag/Cu_2O (green) after 2 h of electrolysis in CO_2-saturated 0.1 M $KHCO_3$. Solid lines are a guide for the eye.

FE of CO starting from -0.83 V_{RHE} (Figure 5.7 b). These differences might originate from the different sizes of the Ag NPs in the two samples as extracted by STEM analysis (Table 5.1), which can affect the electrocatalytic reduction of CO_2 to CO as well as the CO spillover to the Ag/Cu interface.

The production of ethylene on the Cu_2O NCs peaks at -0.95 V_{RHE} with 40 % FE (Figure 5.6 c, Figure A5.5 c), while for the 3-Ag/Cu_2O the FE is slightly larger (45 %). In contrast, 5-Ag/Cu_2O shows a lower $FE_{ethylene}$ (34 %), paralleled by an enhancement in ethanol production. Consequently, the $FE_{ethanol}$:$FE_{ethylene}$ ratio at -1.0 V_{RHE} increases with Ag loading from 0.28 for Cu_2O NCs, 0.33 for 3-Ag/Cu_2O, to 0.49 for 5-Ag/Cu_2O. The C_{2+} selectivity is the highest for the two Ag/Cu_2O samples with a FE of 65 % at -0.98 V_{RHE}, which is an increase of 10 % compared to pure Cu_2O NCs (Figure 5.6 d, Figure A5.5 d).

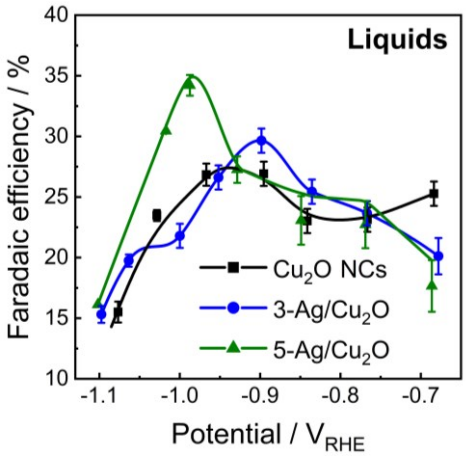

Figure 5.9 Potential-dependent combined Faradaic efficiency of the sum of the liquid products (including formate, acetate, acetaldehyde, propionaldehyde, acetone, ethanol, 1-propanol, and allyl alcohol) of Cu_2O NCs (black), 3-Ag/Cu_2O (blue) and 5-Ag/Cu_2O (green) after 2 h of electrolysis in CO_2-saturated 0.1 M $KHCO_3$. Solid lines are a guide for the eye.

Furthermore, the parasitic HER (Figure 5.7 a) and the production of formate (the only C_1 liquid, Figure 5.7 d) were (slightly) suppressed. The latter has also been recently observed for AgCu foam catalysts as compared to pure Cu foams.[206, 207] In contrast, the formation of acetaldehyde (Figure 5.8 a) and propionaldehyde (Figure 5.8 b) significantly increased for the 5-Ag/Cu_2O, which results in an enhancement of the carbonyl C_{2+} products by a factor of three (Figure 5.6 f, Figure A5.5 f). Overall, introducing Ag increases the FE of the desired C_{2+} liquid products (Figure 5.6 e, Figure A5.5 e) for 5-Ag/Cu_2O by 15 % in comparison to Cu_2O NCs at -1.0 V_{RHE}. This is assigned to the enhanced production of ethanol, 1-propanol, allyl alcohol, and carbonyl C_{2+} products (Figure 5.6 a,b,f, Figure 5.8 c).

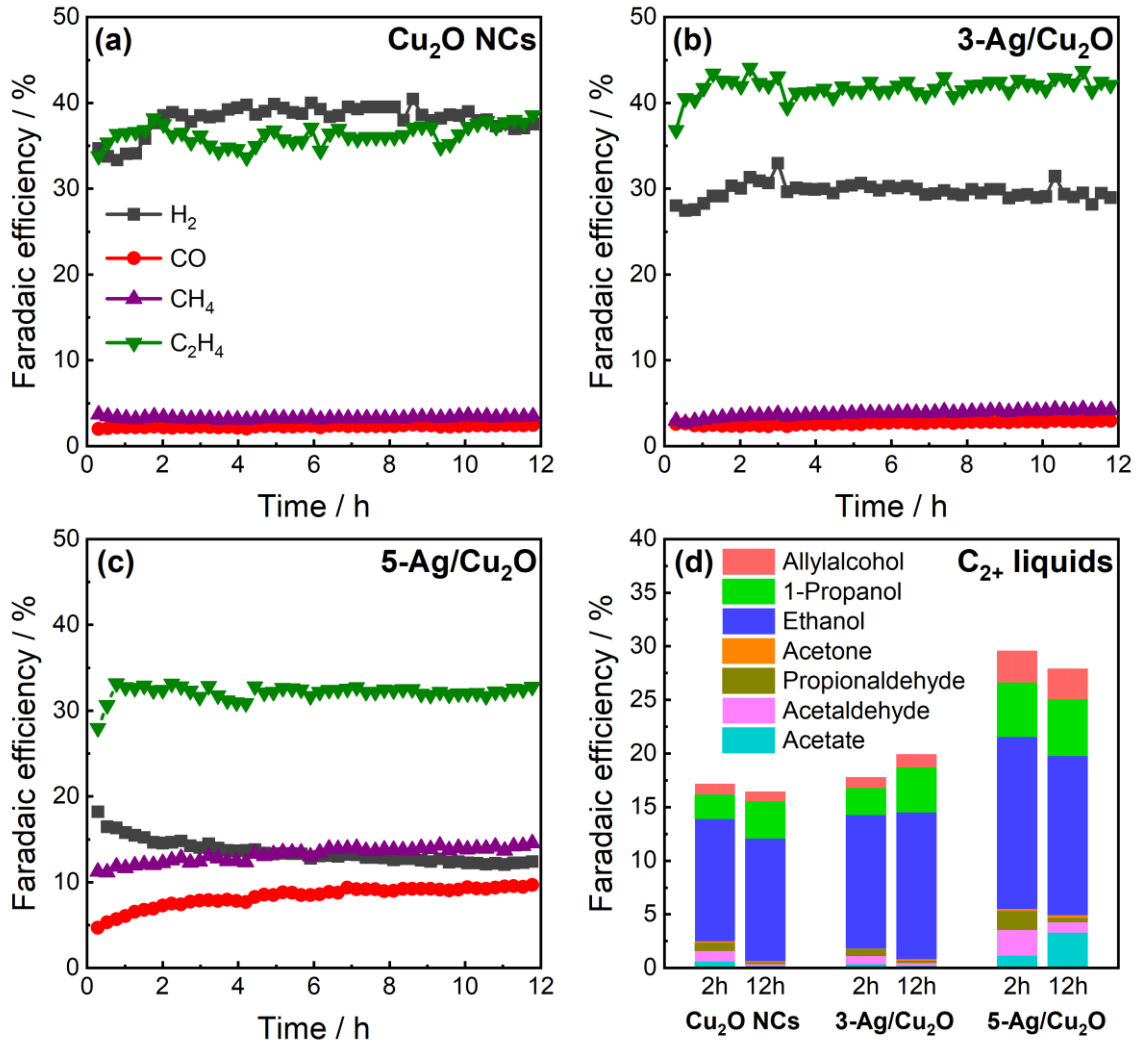

Figure 5.10 Stability measurements during 12 h of CO_2RR at -1.0 V_{RHE} in CO_2-saturated 0.1 M $KHCO_3$. Time-dependent Faradaic efficiencies of the gaseous products of (a) Cu_2O NCs, (b) 3-Ag/Cu_2O, and (c) 5-Ag/Cu_2O. (d) Corresponding evolution of the C_{2+} liquid products after 2 h and after 12 h of CO_2RR of the different samples. For the Ag/Cu_2O samples, the production of CO and CH_4 rises, while H_2 is further suppressed. The amount of C_{2+} liquid products over time remains stable. It should be noted that the liquid products could not be measured online, and therefore, only data after 2 h and 12 h are available.

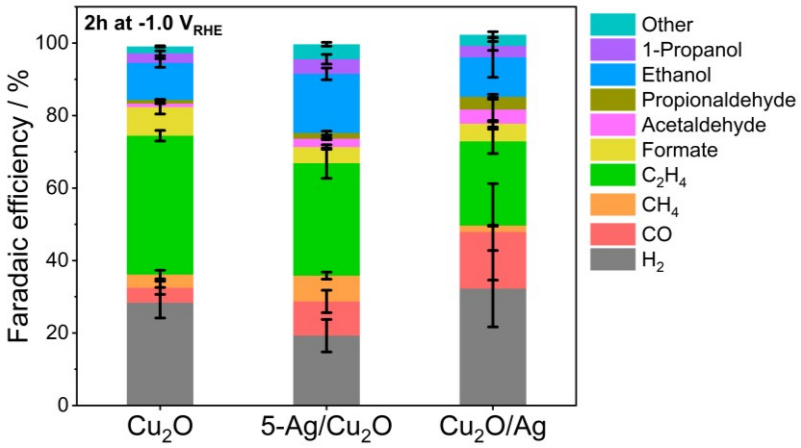

Figure 5.11 Faradaic efficiencies of Cu_2O NCs, 5-Ag/Cu_2O (5 at% Ag NPs-decorated Cu_2O NCs), and Cu_2O/Ag (Cu_2O NCs drop-casted on an Ag foil) after 2 h of CO_2RR at -1.0 V_{RHE} in CO_2-saturated 0.1 M $KHCO_3$. Products indicated as 'Other' are acetate, acetone, 2-propanol, and allyl alcohol.

We additionally performed long-term CO_2RR measurements for 12 h at -1.0 V_{RHE} to track the stability of the catalytic performance (Figure 5.10) and found good stability for all catalysts. For the Ag/Cu_2O samples, the amount of C_{2+} liquid products remains stable over time with a decrease of the aldehydes and an increase of 1-propanol as well as acetate for the 5-Ag/Cu_2O catalyst.

In order to further examine the Cu-Ag interaction and its role in the CO_2RR selectivity, we also investigated the catalytic performance of the pure Cu_2O NCs deposited on a polished Ag foil (Cu_2O/Ag). In this configuration (Figure 5.11), the production of C_{2+} liquids is also enhanced on the Cu_2O/Ag sample at -1.0 V_{RHE}, indicating again the importance of the CO generated at the Ag sites on the further hydrogenation of the C-C products generated on the Cu sites. However, the Cu_2O/Ag sample shows a drastic increase of HER as compared to the 5-Ag/Cu_2O, namely from 20 to 40 % FE, and a suppression of the ethylene FE from 30 to 20 %. This might be correlated to the decrease in the total area of the Ag/Cu interface, which decreases the atomic interaction and synergy between Ag and Cu. Consequently, the well-distributed Ag NPs, which redispersed on the surface of our Cu_2O NCs, appear to play a significant role in the observed synergistic effect and the C-C coupling mechanism.

5.3.3 *Operando* Characterization

Further insight into the Ag-Cu interaction can be extracted from *operando* XAS data. Figure 5.12 depicts the normalized Cu K-edge and Ag K-edge XANES spectra of the Ag NP-decorated and pure Cu_2O NCs in their as-prepared state (Figure 5.12 a,c) and during CO_2RR in a steady-state after 5 h of the reaction (Figure 5.12 b,d). The position of the absorption edge in the Cu K-edge XANES spectra of the as-prepared Cu_2O NCs compared to the reference spectra show

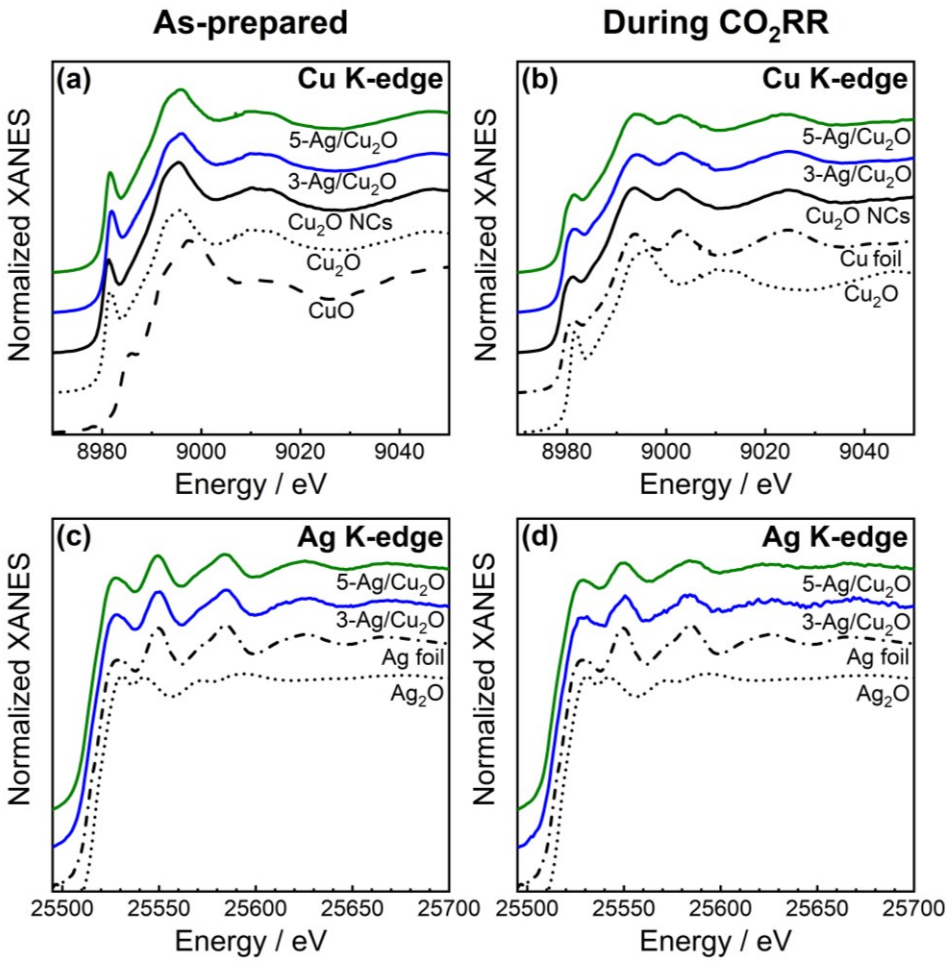

Figure 5.12 Normalized Cu and Ag K-edge XANES spectra of Cu_2O NCs (black), 3-Ag/Cu_2O (blue), and 5-Ag/Cu_2O (green) in as-prepared state (a,c) and in the final state under CO_2RR at -1.0 V_{RHE} (b,d). Reference spectra of Cu_2O, CuO, Cu foil, Ag_2O, and Ag foil are shown for comparison.

that the NCs exhibit mainly a Cu(I) oxidation state, with the characteristic pre-edge feature at 8981 eV. Linear combination analysis (LCA) of Cu K-edge XANES data revealed the presence of Cu(I) and Cu(II) species (Figure 5.13), as already seen in the more surface-sensitive XPS analysis. The decoration with the Ag NPs does not change the Cu XANES spectra (Figure 5.12 c). Ag K-edge XANES spectra, in turn, confirm the metallic state of Ag with all XANES features resembling those of the Ag foil. These findings are consistent with the STEM, XRD, and XPS results, emphasizing the lack of significant interaction between the Cu_2O and Ag species in the as-prepared state.

The reduction of the Cu_2O NCs was investigated during CO_2RR at -1.0 V_{RHE} for 5 h (Figure 5.13). In the final state, the Cu K-edge XANES spectrum resembles that of the metallic Cu foil reference (Figure 5.12 b). We tracked the evolution of the Cu(0):Cu(I):Cu(II) ratios by LCA (Figure 5.13 b,c) and our analysis revealed that a significant fraction of Cu(I) was preserved under CO_2RR reaction conditions with 15-25 % of Cu(I) present in all samples. Figure 5.12 d

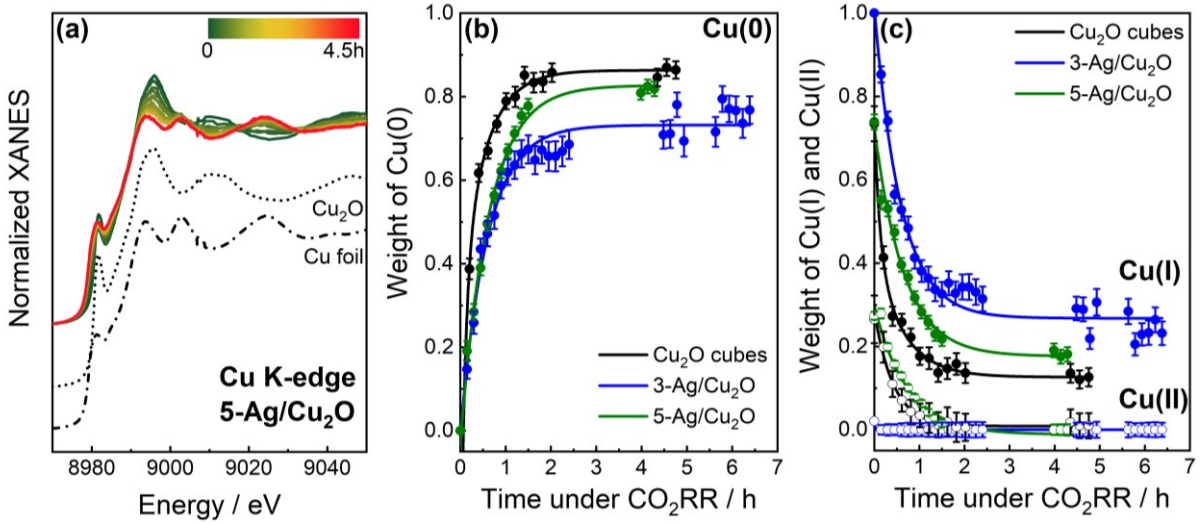

Figure 5.13 Temporal evolution of (a) the normalized Cu K-edge XANES spectra of 5-Ag/Cu_2O and of the weights of (b) Cu(0) and (c) Cu(I) (filled circles) and Cu(II) (open circles) contributions to the Cu K-edge XANES spectra of Cu_2O NCs (black), 3-Ag/Cu_2O (blue), and 5-Ag/Cu_2O (green) during CO_2RR at -1.0 V_{RHE}, as obtained from linear combination fits. The differences in Cu(II) content of the different catalysts could be related to an aging effect of the samples.

shows the Ag K-edge XANES spectra under CO_2RR conditions at -1.0 V_{RHE} after reaching stationary conditions. Ag remained metallic, but an attenuation of the post-edge oscillations is visible during CO_2RR, explainable by a decrease in the size of the Ag NPs due to their redispersion on the Cu_2O NC surface.[208]

To achieve a deeper understanding of the local atomic structure, Fourier transformed- (FT-) EXAFS spectra of the Ag NP-decorated and pure Cu_2O NCs are shown in Figure 5.14 with the corresponding Fourier-filtered EXAFS spectra in Figure 5.15. The peaks at 1.5 Å and 2.8 Å (phase uncorrected) in Cu K-edge FT-EXAFS and at 2.8 Å in Ag K-edge FT-EXAFS for the as-prepared samples indicate the presence of Cu-O and Cu-Cu bonds (typical for Cu_2O) and Ag-M bonds (here, M is Ag or Cu), respectively, in agreement with the XANES analysis.

Under CO_2RR conditions at -1.0 V_{RHE}, a strong peak at 2.2 Å (phase uncorrected) appeared in the Cu K-edge FT-EXAFS, which can be attributed to the Cu-Cu contribution in metallic Cu. The Ag-M peak position at 2.8 Å in Ag K-edge FT-EXAFS did not change significantly, and no additional peaks appeared. Nonetheless, the comparison of the FT-EXAFS before and during CO_2RR shows a decrease in the Ag-M peak intensities. Moreover, the intensity of both the Cu-Cu and Ag-M peaks decreases with an increase in Ag loading (Figure 5.14). These differences suggest structural changes in the Ag and Cu atomic environment under CO_2RR conditions, which we further investigated using quantitative fitting of the EXAFS spectra to obtain the structural parameters presented in Table 5.7, Table A5.5. For the as-prepared state, we obtained

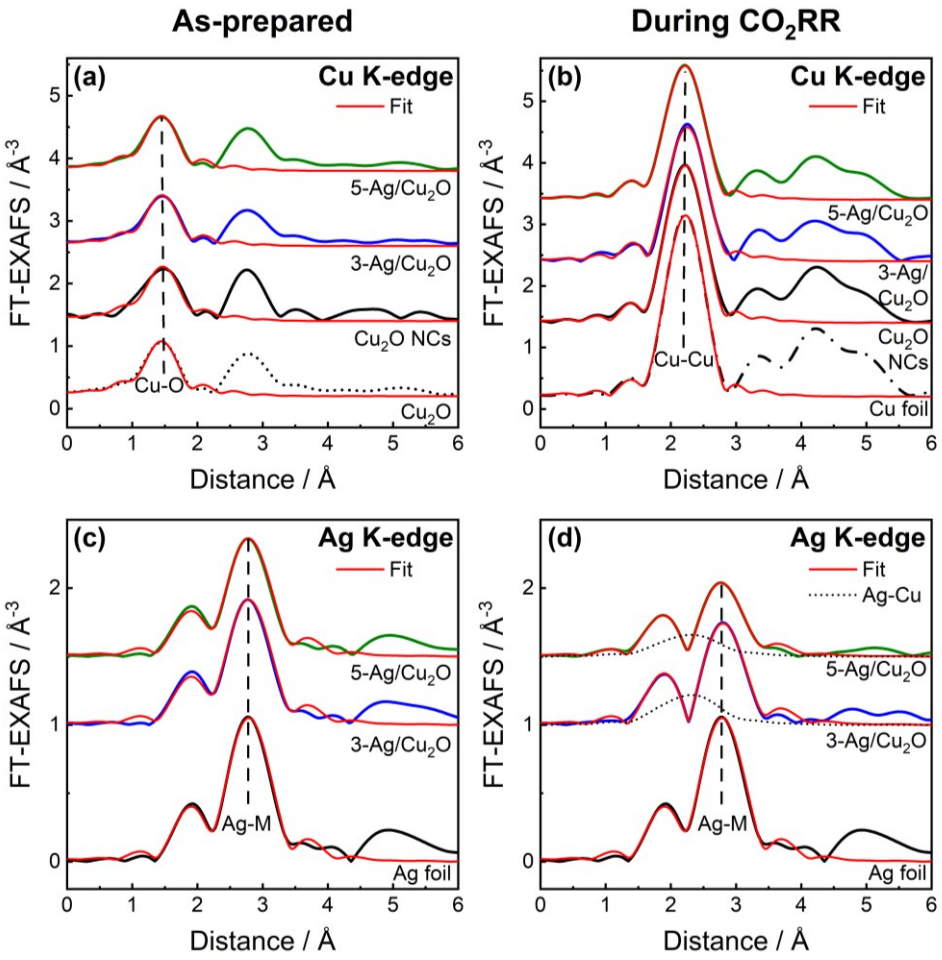

Figure 5.14 Moduli of Fourier-transformed Cu and Ag K-edge EXAFS spectra of Cu_2O NCs (black), 3-Ag/Cu_2O (blue), and 5-Ag/Cu_2O (green) in the as-prepared state (a,c) and in the final state under *operando* CO_2 reduction conditions at -1.0 V_{RHE} (b,d) with corresponding fits (red). Partial contribution of Ag-Cu bonds, as obtained from EXAFS data fitting, is also shown in (d) with dotted lines. Reference spectra of Cu_2O, Cu and Ag foils are shown for comparison.

a Cu-O coordination number ($N_{Cu\text{-}O}$) of ~2 and a Cu-O distance ($R_{Cu\text{-}O}$) of ~1.87 Å, which agree with the values of these parameters in bulk Cu_2O. Furthermore, in the as-prepared samples, the $N_{Ag\text{-}Ag}$ decreased from 12 in the Ag foil over 11.4 ± 0.4 in 3-Ag/Cu_2O to 10.5 ± 0.3 in 5-Ag/Cu_2O, indicating an enhanced disorder within the Ag NPs. However, the $R_{Ag\text{-}Ag}$ distances in all samples are comparable to that of the Ag foil, 2.833 ± 0.003 Å, which means that there is no significant lattice contraction due to alloying in the as-prepared state.

Under stationary CO_2RR conditions, the Cu-Cu coordination number of ~9 is lower than that of the Cu foil reference (12). We also observe Cu-O bonds with $N_{Cu\text{-}O}$ ~0.3. The Cu-Cu distance ($R_{Cu\text{-}Cu}$) during CO_2RR, 2.524 ± 0.003 Å, is comparable to that in the bulk Cu foil reference (2.527 ± 0.002 Å). The Cu(0) to Cu(I) ratio under CO_2RR, as obtained from the EXAFS analysis, agrees well with the XANES data (Table A5.4), showing the partial reduction of the Cu_2O to metallic Cu under CO_2RR conditions. Our primary finding from the Cu K-edge is the

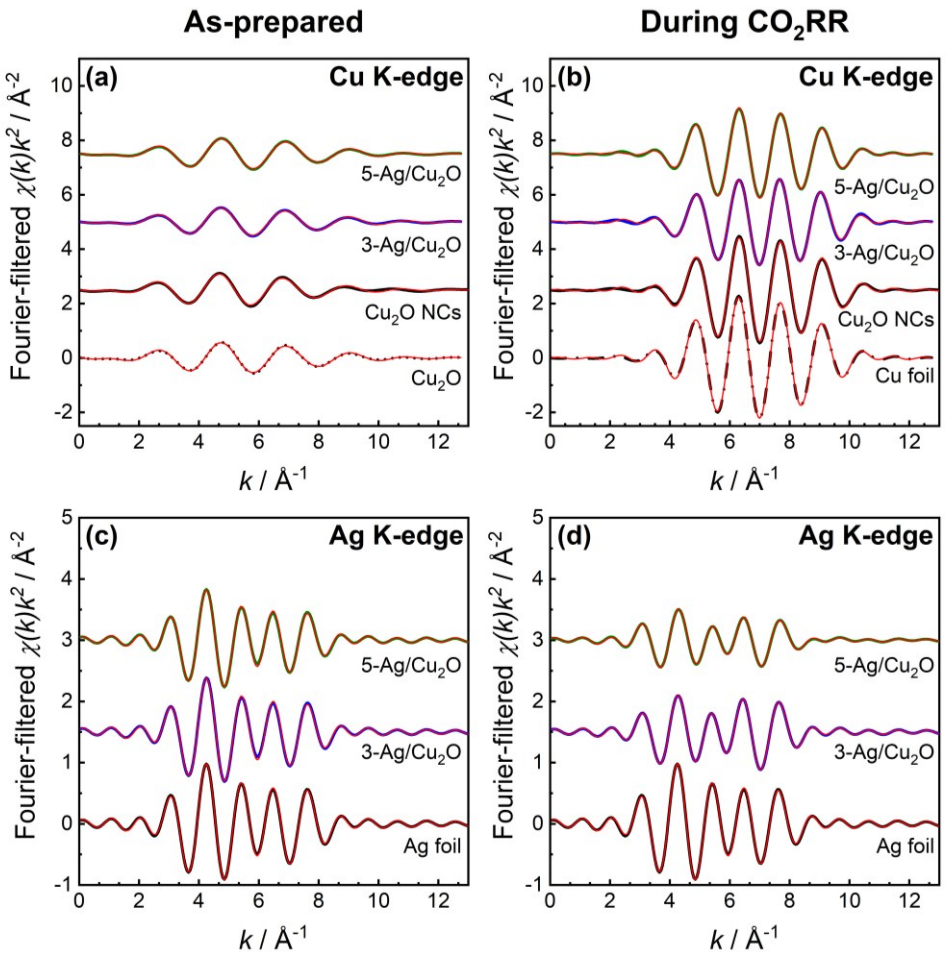

Figure 5.15 Fourier-filtered Cu and Ag K-edge EXAFS spectra in k-space of Cu_2O NCs (black), 3-Ag/Cu_2O (blue), and 5-Ag/Cu_2O (green) in the as-prepared state (a,c) and the final state under *operando* CO_2 reduction conditions at -1.0 V_{RHE} (b,d) with corresponding fits (red). Reference spectra of Cu_2O, Cu, and Ag foils are shown for comparison.

increasing disorder of the Cu-Cu bonds with higher Ag loading and thus reveals the decoration of the Cu_2O NCs with Ag NPs during CO_2RR, but one cannot exclude that this could also be a result of incomplete CuO_x reduction.

One of the main goals of this study is to explore the interaction between Cu and Ag at the atomic scale under CO_2RR conditions. Due to the low concentration of Ag as compared to Cu, information on the interplay between Ag and Cu atoms can be best extracted from the analysis of Ag EXAFS data (Figure 5.14 c,d, Figure 5.16). During CO_2RR, we identified an additional contribution of Ag-Cu bonds with $R_{Ag\text{-}Cu}$ of 2.623 ± 0.005 Å (3-Ag/Cu_2O) and 2.596 ± 0.008 Å (5-Ag/Cu_2O), while the bond-lengths in the more prominent Ag-Ag component did not contract significantly for the 3-Ag/Cu_2O (2.840 ± 0.005 Å), but did so for 5-Ag/Cu_2O (2.787 ± 0.007 Å). The Ag-Ag coordination number decreased from 12 (bulk) to 9, and an Ag-Cu coordination number ($N_{Ag\text{-}Cu}$) of up to 1 was obtained under CO_2RR conditions, being larger for the 3-Ag/Cu_2O sample than for 5-Ag/Cu_2O. The obtained Ag-Cu bond-length is in between

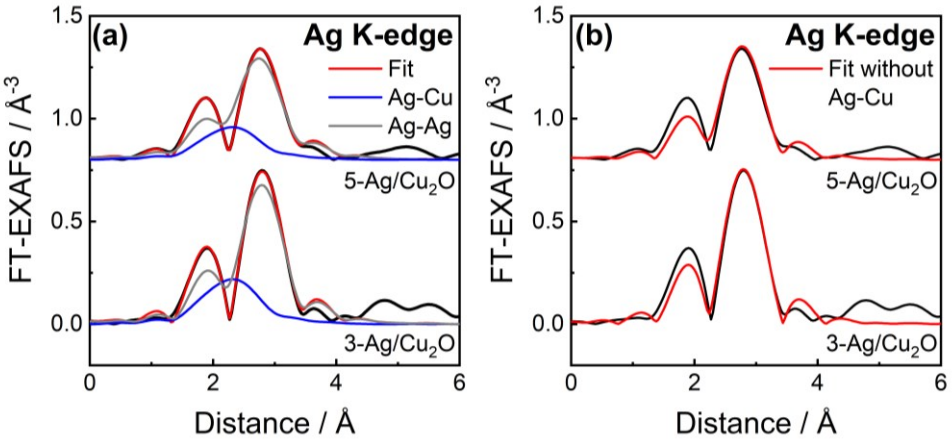

Figure 5.16 Moduli of the Fourier-transformed Ag K-edge EXAFS spectra of 3-Ag/Cu_2O and 5-Ag/Cu_2O in the final state under *operando* CO_2 reduction conditions at -1.0 V_{RHE}: (a) fits including an Ag-Cu contribution (red). The partial contribution of Ag-Ag (gray) and Ag-Cu bonds (blue) is also shown. Analogous fits without the Ag-Cu contribution (red) are shown in (b).

the values for Cu-Cu distance in bulk Cu (2.527 ± 0.002 Å) and the Ag-Ag distance in bulk Ag (2.833 ± 0.003 Å). The Ag-Cu bond lengths, as well as the coordination numbers suggest the partial incorporation of Ag into Cu-rich domains either as an AgCu phase or as dispersed particles or clusters on the Cu surface under CO_2RR conditions. Furthermore, the reduced total Ag-M coordination numbers with respect to those in the as-prepared samples suggest an increase in the disorder in the Ag-Ag component during CO_2RR, which agrees well with a smaller particle size and/or Ag redispersion during CO_2RR, as shown by the STEM results.

Table 5.7 Structural parameters (coordination numbers *N*, interatomic distances *R,* and disorder factors σ^2) obtained from the fit of experimental Ag K-edge EXAFS data collected before and during CO_2RR at -1.0 V_{RHE}, as well as corrections to photoelectron reference energies ΔE_0.

Sample	$N_{Ag\text{-}Ag}$	$R_{Ag\text{-}Ag}$ [Å]	$\sigma^2_{Ag\text{-}Ag}$ [Å²]	$N_{Ag\text{-}Cu}$	$R_{Ag\text{-}Cu}$ [Å]	$\sigma^2_{Ag\text{-}Cu}$ [Å²]	ΔE_0 [eV]	*R*-factor [%]
Ag foil (Ref)	12	2.833(3)	0.0116(4)	0	-	-	1.4(2)	0.17
3-Ag/Cu_2O (as-prep)	11.4(4)	2.829(3)	0.0130(5)	0	-	-	1.4(2)	0.33
5-Ag/Cu_2O (as-prep)	10.5(3)	2.831(3)	0.0126(5)	0	-	-	1.3(2)	0.35
3-Ag/Cu_2O (-1.0 V_{RHE})	9.0(3)	2.840(5)	0.0142(9)	1.1(2)	2.623(5)	0.003(3)	2.1(2)	0.07
5-Ag/Cu_2O (-1.0 V_{RHE})	8.5(6)	2.787(7)	0.019(2)	0.6(2)	2.596(8)	0.000(4)	0.8(4)	0.23

Thus, we observe the partial miscibility of Cu and Ag under CO_2RR conditions by using *operando* Ag K-edge XAS, which was not provided in comparable studies so far.

We furthermore followed the reduction of the Cu_2O species and the CO or CO-like intermediates chemisorbed on Cu and Ag at different potentials and during CO_2RR via *operando* SERS. Figure 5.17 presents potential-dependent SERS spectra of the Ag NP-decorated and pure Cu_2O NCs acquired at open circuit potential (ocp) and between -0.4 and -1.1 V_{RHE} from 150-700 cm^{-1} and 1850-2350 cm^{-1} (see also Figure A5.7).

In the as-prepared state, the characteristic peaks of Cu_2O are observed at 415 cm^{-1}, 527 cm^{-1}, and 624 cm^{-1}.[32, 209-211] The Cu_2O peaks vanished for all samples after applying a reductive potential of -0.4 V_{RHE}, which indicates a prompt reduction of the surface Cu_2O species independently from the Ag loading. The latter is in agreement with the quasi-*in situ* XPS analysis.

At more negative potentials, the *operando* SERS data of the Ag NP-decorated Cu_2O NCs exhibit significant differences compared to the bare Cu_2O NCs during CO_2RR: (1) At higher Raman shifts, a broad band of the C-O vibrations appeared at 2088 cm^{-1} for Cu_2O NCs during CO_2RR, while for the Ag/Cu_2O a shoulder at 2031 cm^{-1} is more pronounced. This might be assigned to the multisite binding mechanism on the AgCu surface, where each binding

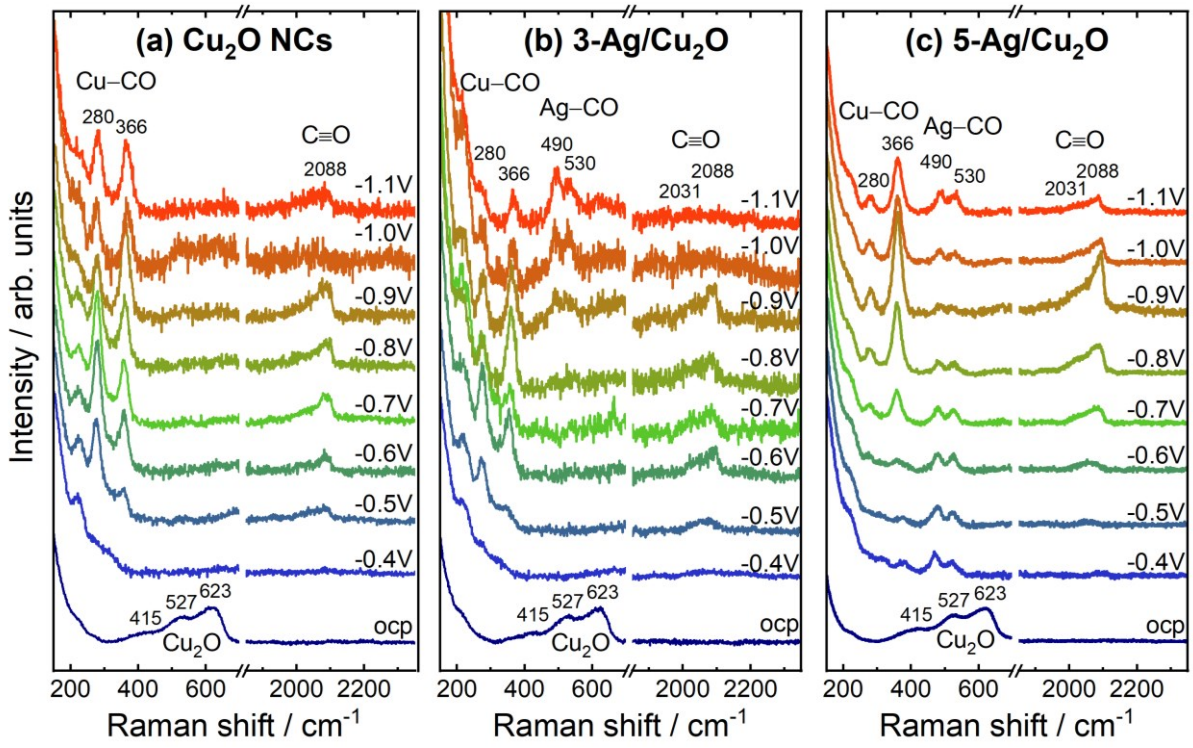

Figure 5.17 *Operando* surface-enhanced Raman spectra of (a) Cu_2O NCs, (b) 3-Ag/Cu_2O, and (c) 5-Ag/Cu_2O at open circuit potential (ocp) and under different applied potentials in CO_2-saturated 0.1 M $KHCO_3$. All potentials are given with reference to RHE.

configuration has a different electron back-donating ability.[212] (2) For the Ag NP-decorated Cu_2O NC samples, two additional peaks at 490 cm^{-1} and 530 cm^{-1} appeared, which might be assigned to Ag-CO vibrations.[116, 213] (3) Two peaks evolve differently at 280 cm^{-1} and 366 cm^{-1}, caused by the Cu-CO frustrated rotation and stretching vibration, respectively.[32, 213] Thus, we can track the CO adsorbed on Cu and Ag separately by using *operando* SERS and identified significant differences in the CO adsorption characteristics on Cu in the presence of dispersed Ag atoms during CO_2RR as, interestingly, the peak intensity ratio of the two Cu-CO Raman peaks shifts toward the Cu-CO stretching vibration with decreasing electrode potential. A similar trend can also be seen with increasing Ag content at -1.0 V_{RHE}. These drastic changes might originate from the way that CO predominantly binds to Cu. While on pure Cu_2O NCs the CO binding configuration is similarly prone to Cu-CO rotation and stretching, the presence of Ag sites gives rise to a CO binding configuration that facilitates the Cu-CO stretching with thus stronger lateral confinement. We anticipate that the latter plays a critical catalytic role in enhancing the C-C coupling of neighboring CO adsorbates and thus increases the C_{2+} liquid product formation.

From the *ex situ* and *operando* studies performed under CO_2RR we gained a detailed insight into the structural evolution of the Ag NP-decorated Cu_2O NC catalysts. In their as-prepared state, the Cu_2O NCs, as well as the Ag NP-decorated samples, mainly consist of Cu_2O, with some contribution from CuO. During CO_2RR, Cu_2O partially reduces to metallic Cu, while the contribution of CuO vanishes. In fact, the *operando* XANES data evidenced the incomplete reduction of Cu_2O in all samples after five hours of CO_2RR (up to 30 % of Cu_2O remained in the 3-Ag/Cu_2O sample). However, we did not find a correlation between the content of Cu_2O (in the bulk, XAS data) and the increased selectivity for C_{2+} liquid products, which might be due to the complete reduction (XPS, SERS) of the surface Cu_2O species to metallic Cu during CO_2RR.

Since the fraction of Ag in the near-surface is low (< 11 at%), intermixing is plausible, although a precise determination of the Ag:Cu ratio in the Ag_xCu_{1-x} regions is not possible. Therefore, our system consists of three classes of potentially active sites during CO_2RR: Ag/AgCu/Cu.

To further understand how the structural/chemical rearrangements influence the reaction mechanism, it is useful to correlate such changes with the formation and stability of different intermediates during CO_2RR. The production of CO increased at lower overpotentials with increasing Ag content in the samples.[40, 214] It has been suggested that *CO, which is a key intermediate for the C-C coupling mechanism,[40, 214] might couple with $*CH_x$[215] to form the

*CH_2CHO intermediate, which plays a central role in the formation of C_{2+} liquid products.[26, 111] The *CH_2CHO intermediate can be hydrogenated to *CH_3CHO and form acetaldehyde (5.1) or be further hydrogenated to yield ethanol (5.2).

$$*CH_2CHO + H^+ + e^- \rightarrow *CH_3CHO \rightarrow CH_3CHO \quad (5.1)$$

$$*CH_3CHO + 2H^+ + 2e^- \rightarrow C_2H_5OH \quad (5.2)$$

If *CH_3CHO couples with another *CO, propionaldehyde (5.3) and 1-propanol (5.4) can be formed.

$$*CH_3CHO + CO + 2H^+ + 2e^- + H_2O \rightarrow *CH_3CH_2CHO + H_2O \rightarrow CH_3CH_2CHO \quad (5.3)$$

$$*CH_3CH_2CHO + 2H^+ + 2e^- \rightarrow 1\text{-}C_3H_7OH \quad (5.4)$$

On Cu surfaces, acetaldehyde and propionaldehyde are usually hydrogenated to ethanol and 1-propanol and are only detected with FE ~1 %, as seen for the Cu_2O NCs. Therefore, we can relate the enhancement of the two aldehyde selectivities to the dispersion of the Ag atoms/small clusters on the Cu surface during CO_2RR, which induces locally strained Cu sites with expanded Cu-Ag interatomic distances compared to Cu-Cu interatomic distances and, most importantly, differences in the predominant CO binding motifs. DFT calculations of our previous study showed that an expanded Cu lattice increases the binding energies for the intermediates of CO_2RR (*e.g.*, *CO on Cu).[202] Additionally, Ag incorporation in Cu weakens the binding energies of the reduced aldehyde intermediates and inhibits their further reduction to ethanol and 1-propanol, as demonstrated in a recent DFT study.[216] However, the structural analysis of the catalysts showed that the surface partially consists of Cu/Ag areas, which also leads to the formation of ethanol and 1-propanol at the Cu sites since they are expected to have higher binding energies for the oxygenated intermediates as compared to the Ag-Cu mixed regions. Therefore, having Ag/AgCu/Cu interfaces as active surface sites appear to enhance the yield of C_{2+} liquid products.

5.4 Conclusion

In summary, Ag NP-decorated Cu_2O nanocubes displayed enhanced selectivity toward C_{2+} liquid products, while the production of formate and hydrogen was suppressed. By means of *ex situ,* quasi-*in situ*, and *operando* spectroscopy studies under CO_2RR conditions, we could gain insight into the structural and chemical transformations of these catalysts that were shown to influence the selectivity trends. In particular, we found the redispersion of the Ag NPs on Cu and a certain Cu-Ag miscibility, leading to expanded Cu-Ag distances compared to metallic

Cu-Cu distances. Such structural rearrangements were found to result in an enhanced formation of alcohols and aldehydes.

By comparing the selectivity of pure Cu_2O and Ag NP-decorated Cu_2O NCs we concluded that even though Cu_2O species were partially preserved under reaction conditions, they are not the sole species responsible for the enhancement in the C_{2+} liquid products, which is favored when large Ag/Cu interfaces are formed. Importantly, we correlate the enhancement to variations in the predominant CO adsorption motif on Cu in the presence of dispersed Ag atoms.

Our work contributes to the fundamental understanding of the CO_2RR by highlighting the intricate interplay of different parameters affecting the selectivity. These include the content of residual Cu_2O species, the presence of a secondary metal near Cu where efficient CO spillover can take place, and the alloying of Cu with another metal that is able to locally increase the interatomic distance, leading to a change in the binding energies of adsorbates and intermediates, thus favoring the formation of C_{2+} liquid products."[158]

6. Time-Resolved *Operando* Raman Spectroscopy Uncovers the Crucial Role of Oxides and Hydroxides for the Enhanced Ethanol Selectivity in Pulsed CO_2 Electroreduction

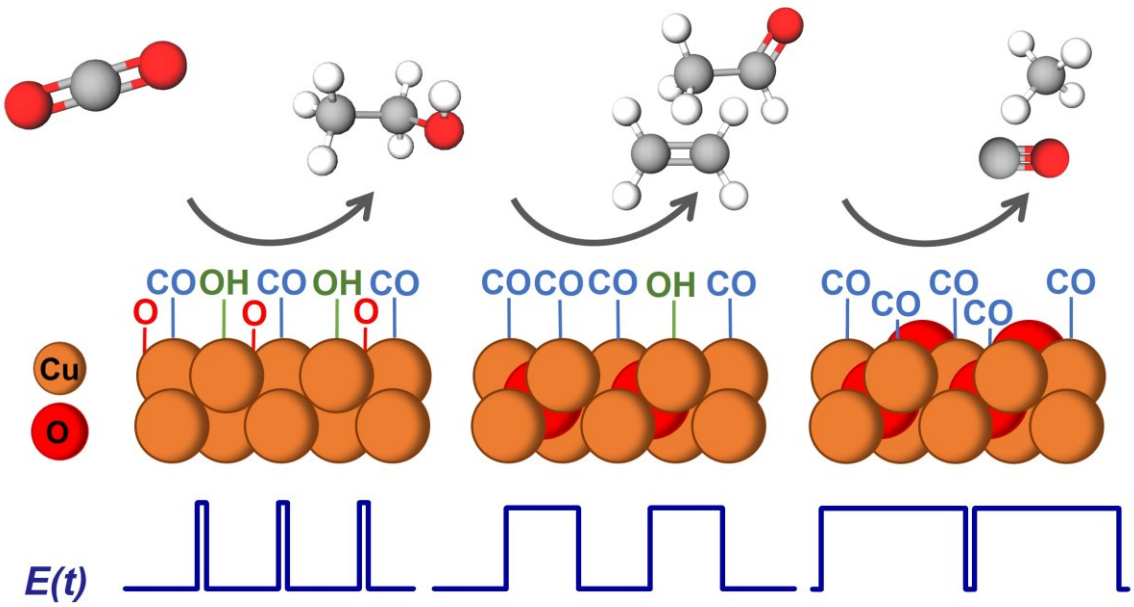

This chapter presents my manuscript draft, ”Time-Resolved *Operando* Raman Spectroscopy Uncovers the Crucial Role of Oxides and Hydroxides for the Enhanced Ethanol Selectivity in Pulsed CO_2 Electroreduction”, which is in preparation for publication. I have planned and analyzed all *operando* SERS experiments presented in this chapter, conducted a part of the pulsed CO_2RR selectivity measurements, and wrote the draft under the supervision of Dr. A. Bergmann and Prof. Dr. B. Roldán Cuenya. I have designed the *operando* SERS flow cell setup in collaboration with Dr. M. Lopez Luna and P. Bischoff. I have prepared the Cu_2O NC samples with an additional contribution from Dr. H. S. Jeon. C. Rettenmaier performed a part of the electrocatalytic CO_2RR selectivity measurements. All co-workers are affiliated with the Fritz Haber Institute of the Max Planck Society.

Pulsed CO_2 electroreduction (CO_2RR) has recently emerged as a facile way to *in situ* tune the product selectivities, in particular toward ethanol, without re-designing the catalytic system. However, in-depth mechanistic understanding requires comprehensive *operando* time-resolved studies to identify the dynamics of the electrocatalytic interface. Here, sub-second time-resolved *operando* Raman spectroscopy was implemented to track the adsorbates and the catalyst state of pre-reduced Cu_2O nanocubes (~30 nm) during pulsed CO_2RR. By screening a variety of product-steering pulse length conditions, the critical role of the oxidative formation of Cu-O_{ad} or $CuO_x/(OH)_y$ species, as well as an optimal OH_{ad} versus CO_{ad} surface coverage during CO_2RR was identified to boost the ethanol selectivity. Notably, a higher CO and/or lower OH coverage following the formation of bulk-like Cu_2O induces a significant increase in the C_1 selectivity. These findings pave the road toward improved catalyst design and for non-conventional dynamic CO_2RR reaction conditions.

6.1 Introduction

Within the scope of reducing global CO_2 emissions to limit climate change, carbon net-zero technologies have gained enormous interest.[1] One promising technology is the CO_2RR, which closes the carbon cycle by using renewable energies to transform CO_2 back into useful chemicals and fuels.[8] Among the metals studied, only copper electrodes have the unique ability to produce the desired energy-dense alcohols and hydrocarbons such as ethanol and ethylene in significant amounts.[14] However, for further commercialization in high-current electrolyzers, Cu-based catalysts still suffer from a broad selectivity distribution, low activity, and low stability during long-term operation.

Several strategies have been evolved to address these issues and to increase the product distribution toward C_{2+} products, which include tuning the catalyst structure and composition,[113, 115, 158, 191, 217] and modifying the electrolyte.[49, 196, 197] Additionally, the oxidation state of Cu plays a major role - particularly oxidized Cu species and oxide-derived Cu materials showed a major improvement in the selectivity and stability of the catalysts.[78, 90, 95, 179, 199, 218] Thus, a simple way to regenerate the desired oxidation state of Cu *in situ* is pulsed potential CO_2RR, where an electrocatalytic potential alternates with an oxidizing potential.[20] Hereby, the key pulse parameters are the applied cathodic and anodic potential, the pulse shape as well as the pulse length.[20]

By varying only the cathodic and anodic pulse length, while keeping the other pulse parameters constant, the catalytic properties of Cu electrodes could be enhanced.[20, 97, 120] In this way, the amount, as well as the type of Cu oxides (Cu^+, Cu^{2+}) on the catalyst surface, was controlled,[21,

[22] and distorted non-crystalline Cu(I)/Cu(II) species were formed at short anodic pulses (below 2 s) as evidenced by *operando* X-ray absorption spectroscopy (XAS) and diffraction (XRD). The latter species were attributed to enhance the ethanol formation.[97] The dynamic alternation of the potential impacts also the restructuring (faceting and defects) and the roughening of the catalyst at longer anodic pulse lengths (above 1 s), which were observed to enhance the selectivity of methane or ethylene.[34, 97, 126] However, the induced dynamics on the surface coverage of hydrogen (H_{ad}), hydroxide (OH_{ad}), and carbon monoxide (CO_{ad}) are crucial to fully understand the underlying principle of selectivity changes via pulsed CO_2RR. Several studies suggested that the application of the anodic pulse leads to higher OH coverage, while H_{ad} is removed due to the positive polarization of the electrodes.[96, 120, 127-129, 135] The resulting higher OH coverage was proposed to stabilize also the active CO_{atop} compared to the inactive CO_{bridge} species,[46, 131, 219] which then enhances the ethanol selectivity. While the CO binding configuration was previously tracked with *operando* surface-enhanced infrared absorption spectroscopy (SEIRAS),[131, 219] there is no experimental evidence of the postulated changes in the OH and CO coverage. Thus, other time-resolved *operando* methods are needed to gain a better mechanistic comprehension of pulsed CO_2RR. Here, *operando* surface-enhanced Raman spectroscopy (SERS) was applied, which is an ideal method to simultaneously track the changes in the surface oxidation state of Cu and the changes in the OH_{ad} and CO_{ad} surface adsorbates as well as their surface coverage. Another advantage of SERS is the high signal intensities due to the surface enhancement effect of nanostructured Cu, which enable sub-second time resolution.[88, 147]

This study presents the impact of the applied pulse lengths during pulsed CO_2RR of the cathodic pulse t_c and of the anodic pulse t_a by the use of *operando* SERS. Therefore, square-wave potential pulses were applied with the electrocatalytic cathodic potential E_c at -1.0 V and the oxidizing anodic potential E_a at +0.6 V versus the reversible hydrogen electrode (RHE, for all shown potentials in this study). Pre-reduced Cu_2O nanocubes (NCs) with ~30 nm in size served as a catalyst, which have been previously studied during pulsed CO_2RR with bulk-sensitive *operando* methods (XAS and XRD).[97] This catalyst was demonstrated to be an ethylene-selective catalyst for static CO_2RR at -1.0 V, while the selectivity could be tuned toward ethanol with selected pulse lengths.[34, 97, 158] Here, the changes in the type and coverage of the surface adsorbates coupled with the surface composition of the electrode were correlated with the obtained selectivity trends in dependence on the applied pulse lengths to gain novel mechanistic insights in a sub-second time-resolved way.

6.2 Experimental Details

6.2.1 Catalyst Preparation

Cu_2O NCs were synthesized by a ligand-free method, as described in a previous study.[158] The reagents were purchased from Sigma Aldrich in ACS grade and used without further purification.

5 mL of a $CuCl_2$ * 2 H_2O solution (0.1 M) and 15 mL of a NaOH solution (0.2 M) were added to 200 mL of ultrapure water (> 18 MΩ cm) at room temperature, and the solution was stirred for 5 min. Then, 10 mL of an L-ascorbic acid solution (0.1 M) were added to the mixture, and the solution was further stirred for 1 h. The solution was centrifuged and washed three times, twice with an ethanol-water mixture (1:1) and once with pure ethanol. The product was dried in vacuum overnight, and the obtained powder was stored in the glove box.

To prepare the electrodes, 1 mg of the catalyst powder was dispersed in 0.5 mL of pure ethanol and ultrasonicated for 15 min to reach a concentration of Cu_2O of 2 mg mL^{-1}. For the *operando* Raman measurements, 31 µL of the dispersion were drop-casted on one side of a polished glassy carbon electrode (8 x 8 mm, Glassy Carbon SIGRADUR®, HTW) and dried at 60 °C for 5 min to obtain a Cu_2O mass-loading of ~100 µg cm^{-2}.

6.2.2 Electrolyte Preparation

0.1 M $KHCO_3$ (Alfa Aesar, 99.7-100.5 %) was purified with a cation-exchange resin (Chelex 100 Resin, Bio-Rad) and saturated with CO_2 (99.995 %) for at least 15 min.

6.2.3 *Operando* Surface-Enhanced Raman Spectroscopy

Operando SERS was performed with a Raman spectrometer (Renishaw, InVia Reflex) coupled with an optical microscope (Leica Microsystems, DM2500M) together with a motorized stage for sample tracking (Renishaw, MS300 encoded stage). Calibration of the system was carried out by using a Si(100) wafer (520.5 cm^{-1}). A near-infrared laser (Renishaw, RL785, λ = 785 nm, P_{max} = 500 mW, grating 1200 lines mm^{-1} and 1800 lines mm^{-1}), as well as a HeNe laser (Renishaw, RL633, λ = 633 nm, P_{max} = 17 mW, grating 1800 lines mm^{-1}), were used as excitation sources. The backscattered light was Rayleigh-filtered and directed to a CCD detector (Renishaw, Centrus). For the *operando* measurements, the excitation source was focused on the surface of the sample, and Raman scattering signals were collected with a water immersion objective (Leica microsystems, 63x, numerical aperture of 0.9). The objective was protected from the electrolyte by a Teflon (FEP) film (Goodfellow, film thickness of 0.0125 mm), which was wrapped around the objective.

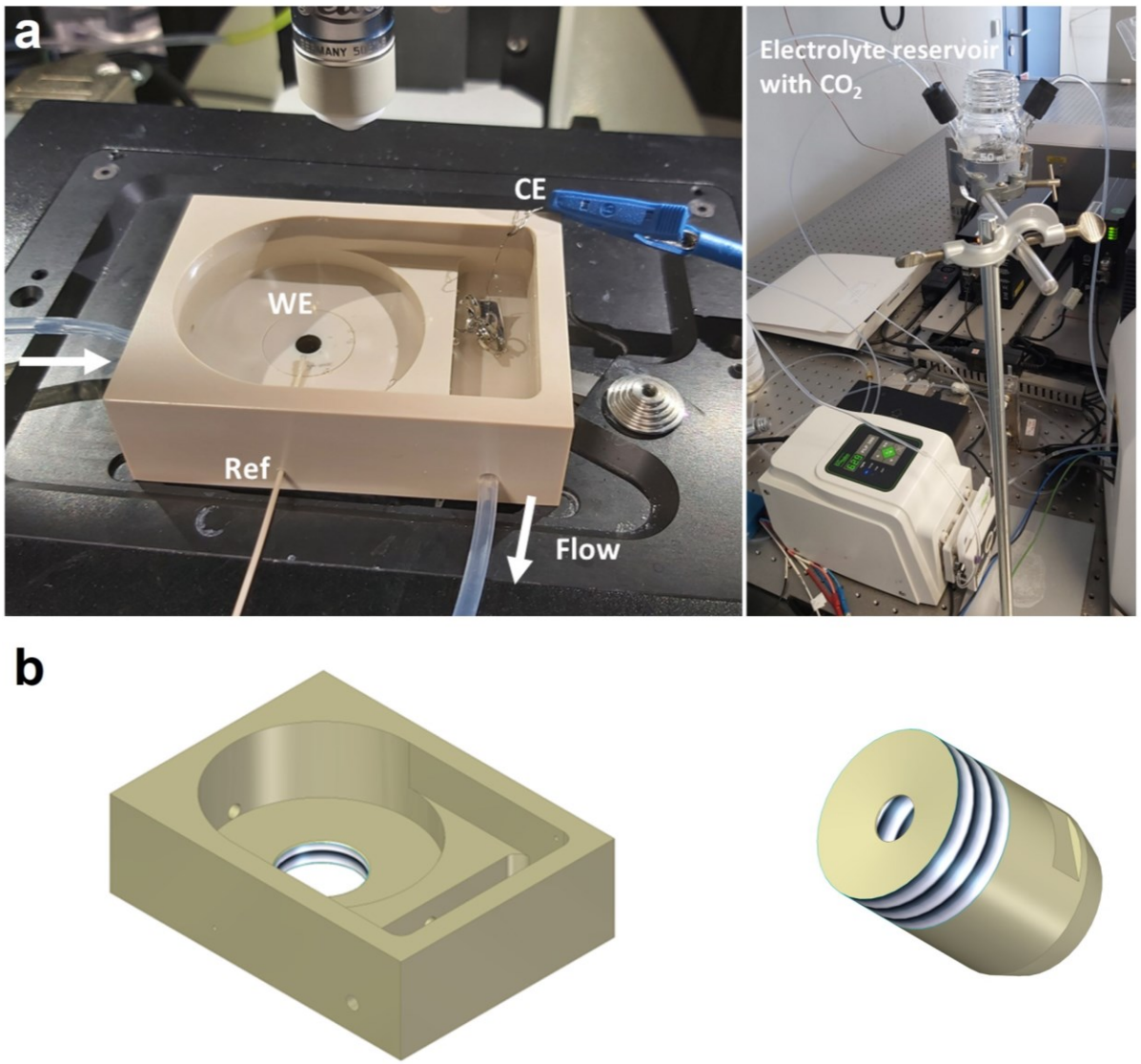

Figure 6.1 Pictures of the home-built spectro-electrochemical *operando* Raman flow cell setup (a) and schemes of the cell body ((b), left) and sample holder ((b), bottom right) drawn by P. Bischoff (FHI).

The electrochemical measurements were conducted in a home-built spectro-electrochemical flow cell made of PEEK and controlled by a Biologic SP240 potentiostat (Figure 6.1). The cell was equipped with a leak-free Ag/AgCl reference electrode (LF-1-63, 1 mm OD, Innovative Instruments, Inc.) positioned close to the sample and a Pt counter electrode in the outlet of the flow. The working electrode with the catalyst drop-casted on glassy carbon was mounted from the bottom of the cell, and the area of the exposed catalyst was 0.25 mm^2. The electrolyte (0.1 M $KHCO_3$) was CO_2-saturated in its reservoir (V = 50 mL) outside of the Raman system and, from there, pumped through the cell with a peristaltic pump (PLP 380, Behr Labor-Technik).

The collection time of each spectrum depends on the applied electrochemical protocol. For the pulsed CO_2RR experiments at the cathodic potential E_c = -1.0 V and the anodic potential E_a = +0.6 V, acquisition times between 0.1 and 0.8 s were used depending on the cathodic and anodic

Table 6.1 Temporal resolution of the spectra for different pulse lengths in the region of 55-1272 cm^{-1} at E_c = -1.0 V and E_a = +0.6 V, including the dead time of the spectrometer (~0.1 s).

t_c [s]	t_a [s]	Time/spectrum [s]
4	0.5	0.2
4	4	0.9
0.5	8	0.2
8	1	0.35
4	2	0.5
1	1	0.3
4	8	0.9
1	32	0.3

pulse lengths t_c and t_a, respectively, to obtain at least three data points per pulse. The exact temporal resolutions for the low Raman shift region are given in Table 6.1. To obtain a high time resolution, usually (if not stated differently), the static Raman mode in the region of 55-1272 cm^{-1} was applied together with the 785 nm laser and the 1200 lines mm^{-1} grating. In the region of 1700-2600 cm^{-1}, the 633 nm laser and the 1800 lines mm^{-1} grating were used. The Raman data were first processed using the Renishaw WiRE 5.2 software to normalize the data and remove cosmic rays. For the normalization, the intensity values were modified to a mean of 0 and a variance of 1. Octave® scripts were written to combine the Raman and the electrochemical data to fit characteristic Raman bands and to average the Raman spectra. Averaged Raman spectra were obtained by averaging the Raman data points collected at the same times after the onset of each pulse cycle.

6.2.4 Selectivity Measurements

The main part of the selectivity measurements was already published in my previous co-authored work[97] except for the new measurements acquired at E_c = -1.0 V, E_a = 0 V and t_c = 4 s, and t_a =1 s. The measurements were carried out in an H-type cell equipped with an anion-exchange membrane (Selemion AMV, AGC) separating the cathodic and the anodic compartments and controlled by an Autolab (Metrohm) potentiostat. A leak-free Ag/AgCl reference electrode (LF-1, Alvatek) served as the reference electrode, a platinum gauze electrode (MaTecK, 3,600 mesh cm^{-2}) as the counter electrode, and Cu_2O NCs deposited on carbon paper as the working electrode. Gas products were detected and quantified every 15 min by online gas chromatography (GC, Agilent 7890B), equipped with a thermal conductivity detector and a flame ionization detector. Liquid products were analyzed after each measurement with a high-performance liquid chromatograph (Shimadzu Prominence), equipped with a NUCLEOGEL SUGAR 810 column and a refractive index detector, and a liquid GC (Shimadzu

2010 plus), equipped with a fused silica capillary column and a flame ionization detector. The Faradaic efficiencies were calculated by taking only the cathodic part into account since there is no catalytic activity during the anodic pulse. More details about the product determination, the electrochemical procedure, and the selectivity calculations can be found in the previous work.[97]

6.3 Results and Discussion

6.3.1 Time-Dependent Evolution of SERS

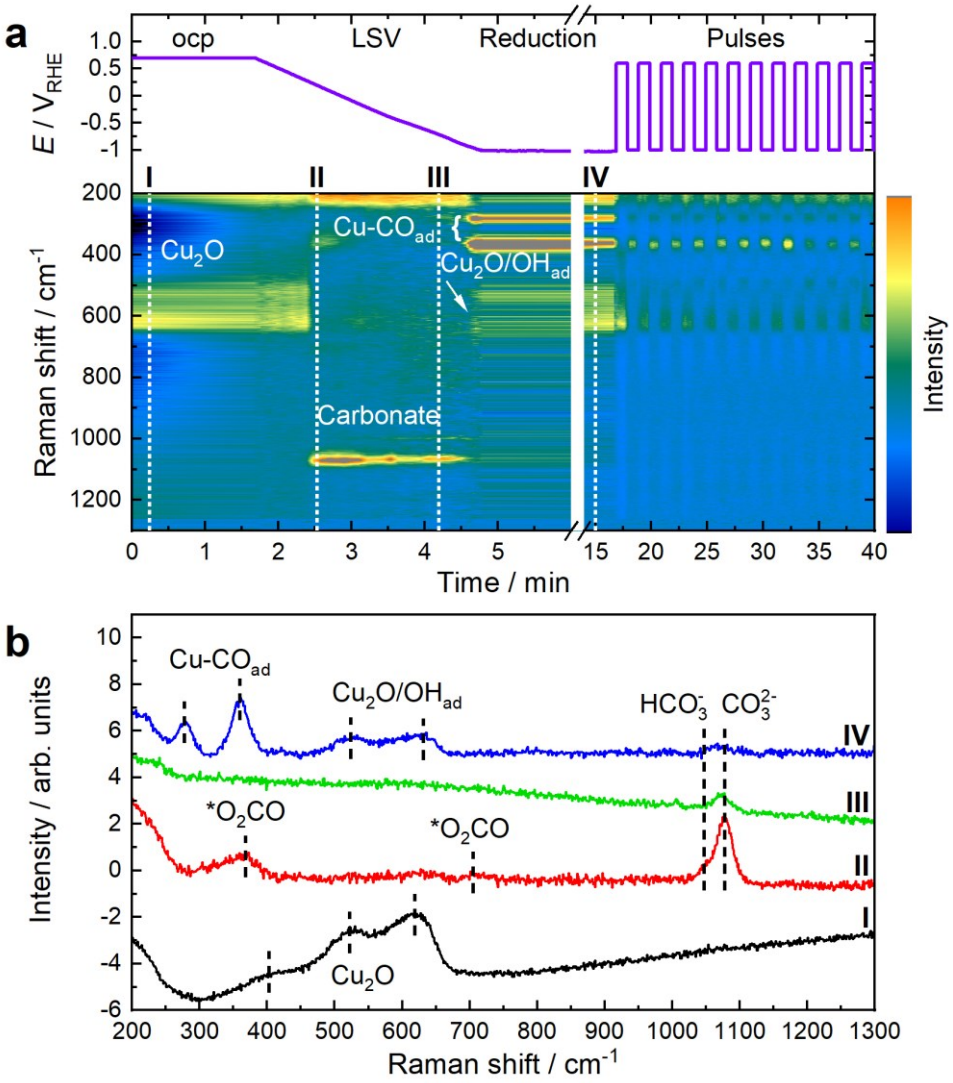

Figure 6.2 Experimental protocol during a representative pulsed experiment. (a) Applied potential over time (top) together with the temporal evolution of the SERS signal intensity of Cu_2O NCs in the range of 200-1300 cm^{-1} with highlighted characteristic bands. (b) Selected normalized SERS spectra from (a) with highlighted Raman shifts, which correspond in (I) to Cu_2O species (402, 526, 620 cm^{-1}); in (II) and (III) to adsorbed bidentate carbonate species (*O_2CO, 360, 705 cm^{-1}), to carbonate (CO_3^{2-}, 1074 cm^{-1}) and to bicarbonate (HCO_3^-, 1050 cm^{-1}); and in (IV) to the Cu-CO rotation (280 cm^{-1}) and Cu-CO stretching bands (360 cm^{-1}) and to Cu_2O and/or OH_{ad} species (530, 630 cm^{-1}).[31, 88, 132, 158]

In the first step, freshly prepared Cu_2O NCs deposited on a glassy carbon electrode were pre-reduced in an electrochemical *operando* Raman flow cell setup (Figure 6.1) in 0.1 M CO_2-saturated potassium bicarbonate ($KHCO_3$) by performing a linear sweep from open circuit potential (ocp) to -1.0 V with 10 mV s^{-1}, where the potential was kept for 15 min. In the second step, pulsed CO_2RR with a selected pulse length and symmetry was applied (Table 6.1). Both steps were followed by *operando* SERS at the same time, and different spectral regions of interest are highlighted in Figure 6.2.

Figure 6.3 a presents the applied potential and the measured current (top) during the symmetric pulses with $t_c = t_a = 4$ s and the corresponding normalized SERS signal intensities over the Raman shift between 250 and 700 cm^{-1} (bottom) as a function of the time. The periodic responses of characteristic SERS bands in this wavenumber region were fitted in Figure 6.3 b (with fit examples in Figure 6.4), which will be focused on over the course of this study.

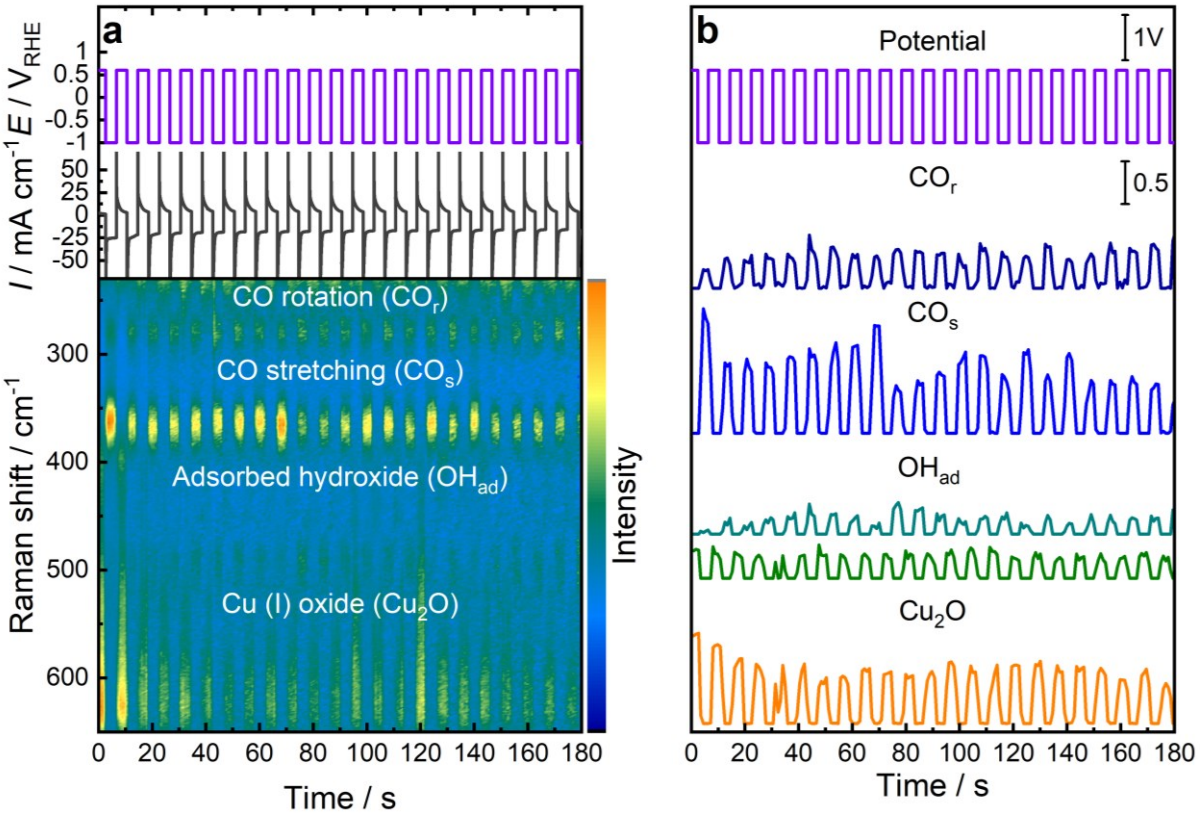

Figure 6.3 Temporal evolution of the SERS signal intensity during pulses with E_c = -1.0 V, E_a = +0.6 V, and $t_c = t_a = 4$ s. (a) Applied potential and current density over time (top) and corresponding temporal evolution of SERS signal intensity with marked Raman bands (bottom). (b) Applied potential over time and intensities of fits in arb. units of selected characteristic Raman bands, namely the Cu-CO rotation (CO_r, 280 cm^{-1}, dark blue), Cu-CO stretching (CO_s, 360 cm^{-1}, light blue), Cu-OH_{ad} (OH_{ad}, 495 cm^{-1} at -1.0 V in turquoise and 450 cm^{-1} at +0.6 V in green) and the copper(I) oxide (Cu_2O, sum of 530 and 620 cm^{-1} divided by two, orange) bands.

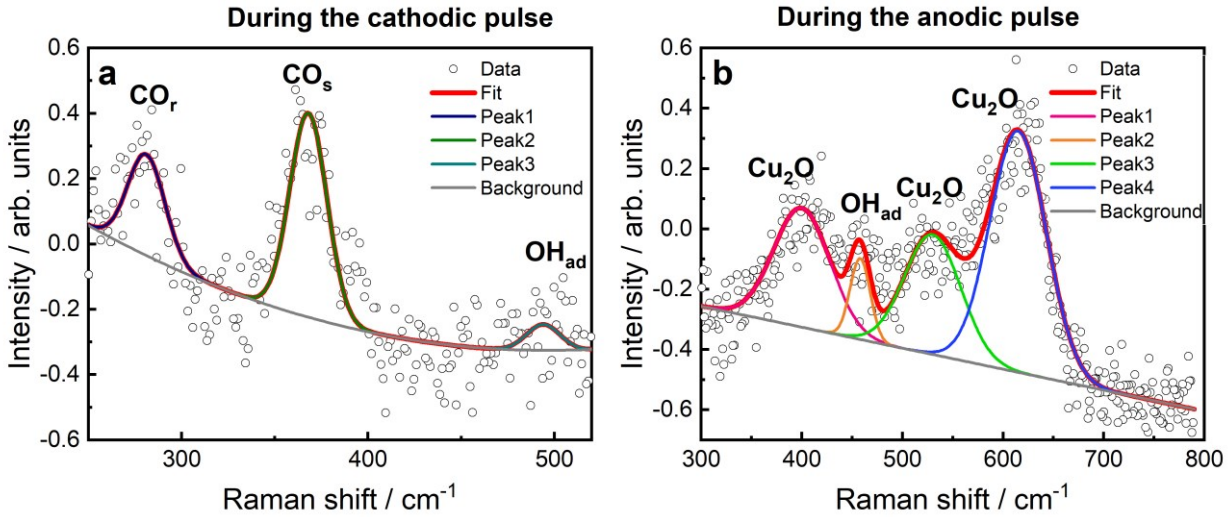

Figure 6.4 Exemplary fits of characteristic peaks of the normalized SERS spectra during the cathodic and anodic pulse of pulsed CO_2RR at $t_c = t_a = 4$ s with $E_c = -1.0$ V and $E_a = +0.6$ V.

In particular, the selected characteristic bands are here:

(I) the CO_{ad} vibrations on Cu, namely the Cu-CO rotation (CO_r) and stretching (CO_s) vibrations at 280 and 360 cm^{-1}, which are essential for the determination of the CO surface coverage (CO_{cov}) obtained by their intensity ratio (CO_s/CO_r),[88] and which appeared during each cathodic pulse as CO_2RR intermediates due to the reduction of CO_2 and disappeared again during each anodic pulse;[88, 132, 158]

(II) the OH_{ad} vibration on Cu at 495 cm^{-1}, which appeared during each cathodic pulse and redshifted to 450 cm^{-1} during each anodic pulse due to the adsorption of OH;[31, 132, 210]

(III) the bands related to Cu_2O on the surface at 410 cm^{-1} (multiphonon process), 530 cm^{-1} (Raman-allowed F_{2g} mode), and 620 cm^{-1} (IR-allowed F_{1u} mode), which appeared during each anodic pulse due to the oxidation of Cu and disappeared again during each cathodic pulse due to the reduction of Cu.[31, 132, 158, 211] One cannot completely exclude the additional presence of CuO or $Cu(OH)_2$ as a minor component due to similar band positions.[209]

While the assignment of CO_{ad} and Cu_2O is straightforward, the assignment of OH_{ad} is still under debate, and some groups also assigned the band at 495 cm^{-1} to Cu-C and Cu-O species.[31, 220] However, experiments with D_2O showed a shift of the band position, which supports the assignment of chemisorbed OH_{ad} on Cu.[210]

Additionally, a weak carbonate band at 1070 cm^{-1} was observed in some of the SERS spectra during the first 20 s, as shown in Figure 6.5.[31, 32, 88]

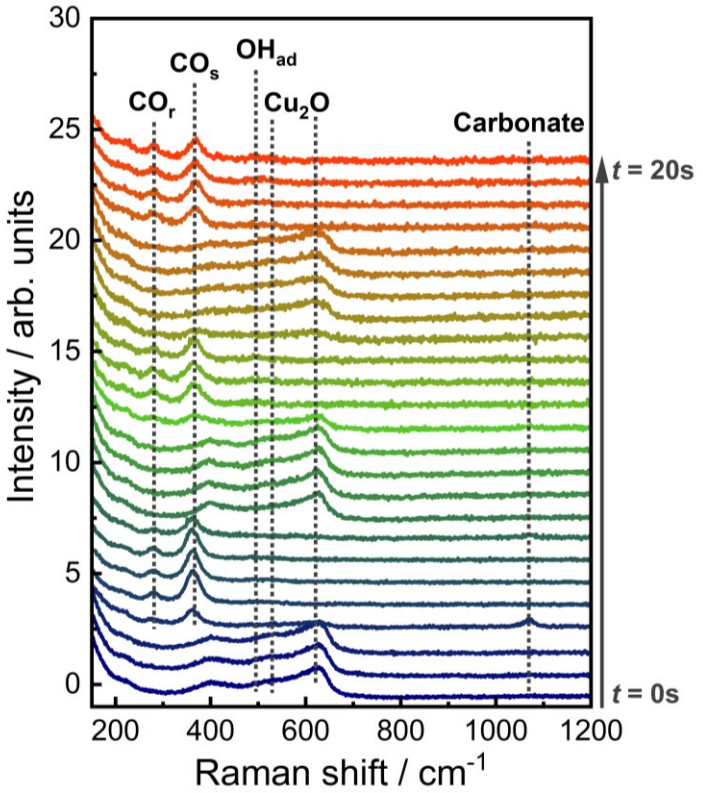

Figure 6.5 Normalized SERS spectra during the first 20 s of pulsed CO_2RR at t_c = t_a = 4 s with E_c = -1.0 V and E_a = +0.6 V. Characteristic bands are highlighted.

6.3.2 Pulse Length-Dependent Evolution of SERS

In order to follow the impact of the applied cathodic and anodic pulse duration on the catalyst and adsorbates, the normalized *operando* SERS spectra of selected pulse conditions were averaged, and the characteristic bands were fitted over one pulse sequence, as shown in Figure 6.6. The emphasis is placed on three pulse regimes that are typical for the highest ethanol (EtOH regime, Figure 6.6 a,d), ethylene/acetaldehyde ($C_2H_4O_x$ regime, Figure 6.6 b,e), and C_1 product (C_1 regime, Figure 6.6 c,f) selectivity. The EtOH regime is characterized by short anodic pulses (t_a = 0.5 s), the $C_2H_4O_x$ regime by intermediate anodic pulses (t_a = 4 s), and in both cases, the cathodic pulses have an intermediate length of 4 s. In contrast, long anodic pulses (t_a = 8 s) combined with short cathodic pulses (t_c = 0.5 s) represent the C_1 regime.[97] Thereby, the intensity of the CO_s compared to the CO_r band decreased with shorter t_a and is the smallest in the EtOH regime. The OH_{ad} band is more intense during shorter t_a (0.5 s, 4 s) in the EtOH/$C_2H_4O_x$ regime, while no OH_{ad} bands, but stronger Cu oxide bands during long t_a (8 s) and subsequent short t_c (0.5 s) could be detected in the C_1 regime. These observations are underlined by additional SERS data at different pulse lengths (Figure A6.1-A6.2). Similarly, the Cu_2O band intensity increased with the duration of the anodic pulse being comparably weak at t_a = 0.5 s in the EtOH regime. Interestingly, there might also be some contribution of Cu-O_{ad} as visible in the EtOH

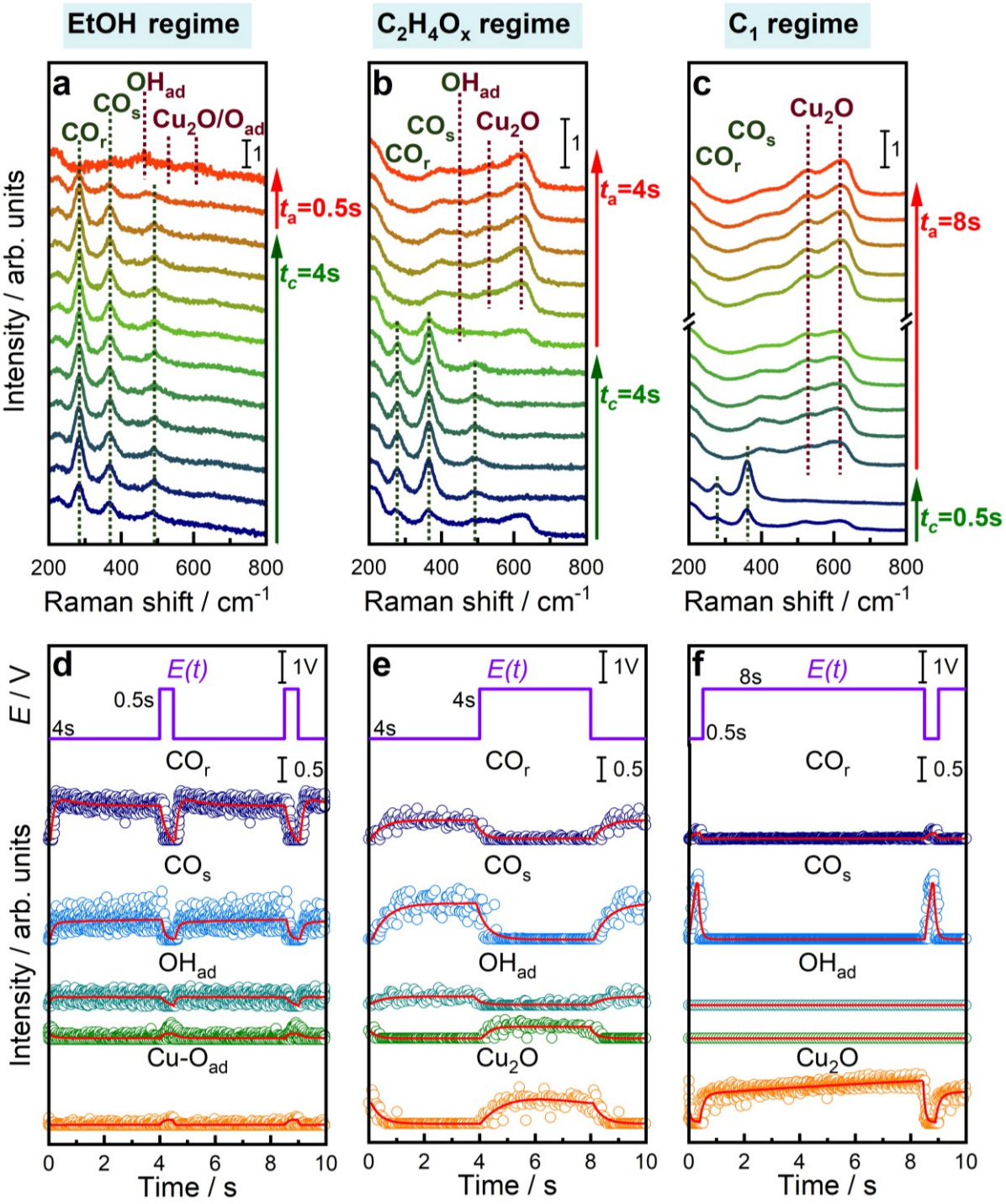

Figure 6.6 Pulse length-dependent evolution of SERS spectra and characteristic bands during pulsed potential CO_2RR measurements at E_c = -1.0 V and E_a = +0.6 V. (a-c) Normalized SERS spectra from bottom to top (as indicated with arrows) with highlighted characteristic SERS bands and (d-f) intensities of fits of characteristic SERS bands averaged over one pulse sequence at selected pulse lengths. All averaged SERS spectra of (c) are shown in Figure A6.4. The data points in (d-f) represent the intensity fits of CO_r (280 cm^{-1}, dark blue), CO_s (360 cm^{-1}, light blue), OH_{ad} (495 cm^{-1} at -1.0 V in turquoise and 450 cm^{-1} at +0.6 V in green), Cu_2O (sum of 530 and 620 cm^{-1} divided by two, orange) and Cu-O_{ad} (610 cm^{-1}, orange) bands. The red lines denote the exponential fits and serve as guides for the eyes.

regime, which was even more pronounced at t_a/t_c = 2 s/4 s and 1 s/1 s in the region of 606-626 cm^{-1} (Figure A6.1).[221] Under these conditions, also intense OH_{ad} bands were detected, as well as additional bands at 370-380 cm^{-1} and 520-540 cm^{-1}, which can be attributed to $CuO_x/(OH)_y$ species.[31, 222] Moreover, the carbonate band at 1070 cm^{-1} was predominantly observed at the onset of both the anodic and cathodic pulses, possibly linked to dynamic alterations of the electrical double layer. However, due to the low intensities of this band under these conditions, it is challenging to thoroughly analyze its characteristics further (Figure A6.1-A6.3).

The exponential fits of the Raman band intensities can provide additional insights into the average surface coverage of the characteristic species and their corresponding adsorption/desorption and oxidation/reduction kinetics. (Figure 6.6 d-f, Figure A6.5, Table 6.2, Table A6.1-A6.2). In particular, the kinetics of the ad- and desorption of CO on Cu altered with the applied pulse lengths (Table A6.1). For example, in the EtOH regime, the CO_s band intensity increased twice as fast during the cathodic pulse as it decreased during the anodic pulse. Additionally, the CO_s/CO_r band intensity ratio, which reflects the CO_{cov}, gradually and persistently escalated throughout the cathodic pulse (Figure A6.6). These findings suggest a change in the CO binding configuration during the cathodic pulse, which is expected to have implications for the catalytic function.

The differences in the CO binding configuration in terms of CO adsorption sites can be further evaluated by the analysis of the C-O stretching vibration at higher wavenumbers (1900-2150 cm^{-1}, Figure 6.7). Therefore, the SERS spectra needed to be deconvoluted (Figure A6.7)

Table 6.2 Averaged SERS band intensity values and standard derivation (arb. units) of the characteristic SERS bands over a cathodic or/and anodic pulse extracted from Figure 6.6 d-f and Figure A6.5.

t_c [s]	t_a [s]	CO_r (t_c)	CO_s (t_c)	OH_{ad} (t_c)	OH_{ad} (t_a)	Cu-O_{ad} (t_a)	Cu_2O (t_a)
4	**0.5**	0.76(9)	0.4(1)	0.20(8)	0.24(1)	0.20(5)	0
4	**4**	0.39(8)	0.7(2)	0.18(7)	0.25(7)	0	0.5(1)
0.5	**8**	0.15(5)	1.1(2)	0	0	0	0.8(1)
8	**1**	1.1(4)	0.6(4)	0.2(1)	0.3(1)	0	0.1(1)
4	**2**	0.5(1)	0.5(2)	0.4(1)	0.22(8)	0.4(1)	0
1	**1**	0.5(2)	0.4(1)	0.6(3)	0.4(2)	0.10(1)	0
4	**8**	0.22(6)	1.3(2)	0.0020(1)	0	0	0.8(1)
1	**32**	0.33(1)	1.08(6)	0	0	0	0.6(2)

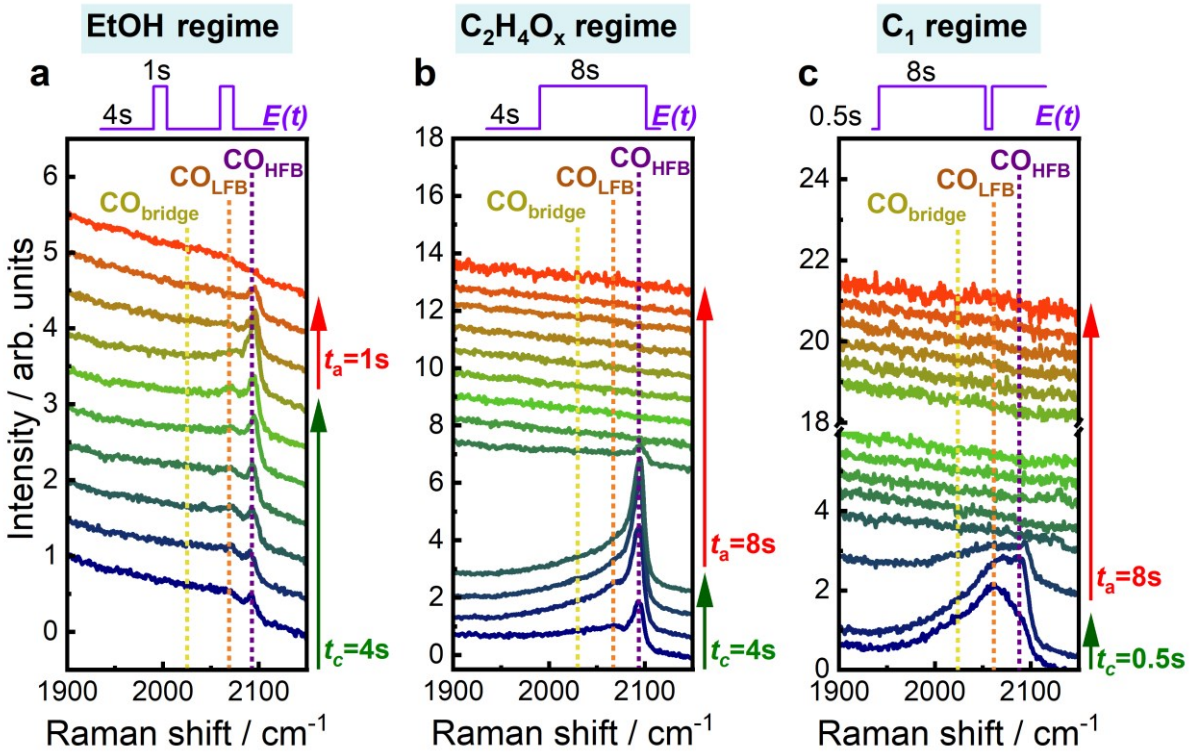

Figure 6.7 Normalized SERS spectra of the C-O vibration region from 1900-2150 cm^{-1} of pulsed potential CO_2RR measurements with varied pulse length during E_c = -1.0 V and E_a = +0.6 V averaged over one pulse sequence from bottom to top (as indicated with arrows). The pulse lengths are in (a) t_c = 4 s, t_a = 1 s (ethanol regime), (b) t_c = 4 s, t_a = 8 s (ethylene/acetaldehyde regime), and (c) t_c = 0.5 s, t_a = 8 s (C_1 regime). The different C-O configurations are highlighted. Spectra were collected with an acquisition time of 0.25 spectra/s.

by fitting the contribution of the bridge CO (CO_{bridge} at 2030 cm^{-1}) and two atop CO (CO_{atop}) bands, namely the low-frequency band linear CO (CO_{LFB} at 2065 cm^{-1}) and high-frequency band linear CO (CO_{HFB} at 2095 cm^{-1}), as described in the literature.[30, 219] The corresponding intensity evolutions of these different contributions averaged over one pulse sequence are displayed in Figure A6.8. The contribution of CO_{atop} sites, usually related to C-C coupling,[30] was indeed higher in the EtOH and $C_2H_4O_x$ regime (Figure A6.9). Instead, the contribution of CO_{bridge} sites, usually considered inactive for C-C coupling,[30, 131, 219] increased in the C_1 regime (Figure A6.8, A6.9). Nevertheless, it is crucial to note that the uncertainties in these averaged contributions are considerably high (Figure A6.8-A6.9) owing to the constantly evolving surface reactions that lead to the dynamic nature of the C-O stretching vibrations at high Raman shifts.[30, 132]

For the OH_{ad} species, in turn, it is not easy to extract the ad- and desorption behavior since the bands additionally shifted upon the potential switch (Figure 6.6 a,b). The shift of the bands probably resulted from the Stark effect, with a Stark tuning rate of ~28 cm^{-1}/V, rather than from

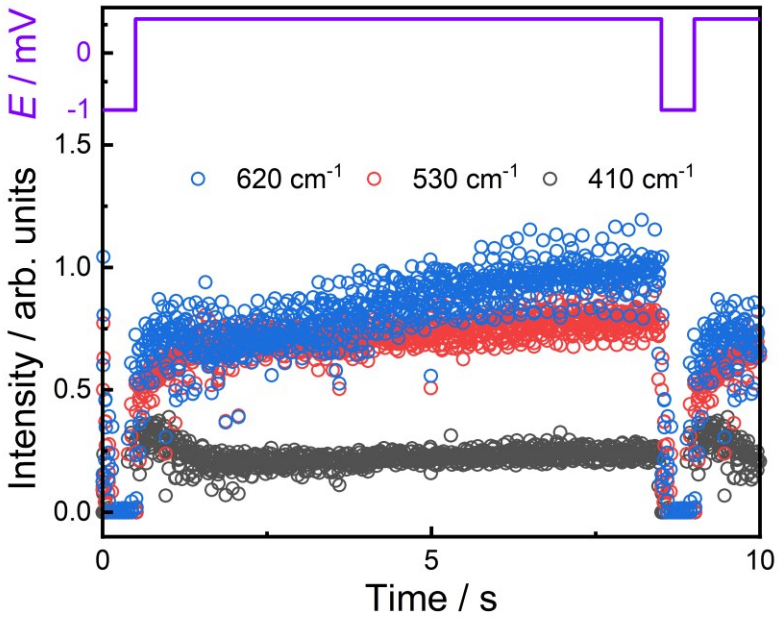

Figure 6.8 Applied potential and intensities of fits of Cu_2O bands at 410, 530, and 620 cm^{-1} during pulsed potential CO_2RR at E_c = -1.0 V and E_a = +0.6 V at t_c = 0.5 s and t_a = 8 s (C_1 regime) averaged over one pulse sequence.

a change in the bonding configuration of OH_{ad}, as also discussed in the literature.[210]

The adsorption of oxygen on Cu and the oxidation to Cu_2O over the anodic pulse was, under all applied pulse conditions, slower than the corresponding desorption/reduction upon the application of the cathodic pulse (Table A6.2). In the C_1 regime, the amount of surface Cu_2O continuously increased the fastest, which indicates a continuous growth of the oxide layer over the course of the anodic pulse. Moreover, the spectroscopic weights of the three deconvoluted Cu_2O bands changed at different applied pulse lengths (Table A6.3). The contribution of the band at 410 cm^{-1} increased at longer cathodic pulses, which may have been influenced by the higher amount of OH_{ad}.[210] On the other hand, the intensity ratio of the 530 and 620 cm^{-1} bands increased at shorter cathodic pulses. If one follows the time-dependent evolution of these bands in the C_1 regime (Figure 6.8), the contribution of the band at 410 cm^{-1} was the highest in the first second, while the intensity ratio of the 530 and 620 cm^{-1} bands decreased during the course of oxidation. These changes might represent the formation/crystallization of the Cu_2O layer, with a minor contribution of other Cu phases (*e.g.*, Cu(II) compounds such as $CuO/Cu(OH)_2$) in the initial phase of the electrochemical oxidation. However, they cannot be directly correlated to a specific cationic Cu (surface) species with SERS.[32, 209]

6.3.3 Correlations of Selectivity, Structure, and Kinetics

Figure 6.9 shows the correlations between the change in the SERS band intensities (Table 6.2) and in the Faradaic efficiencies (ΔFEs) during pulsed CO_2RR in comparison to static CO_2RR

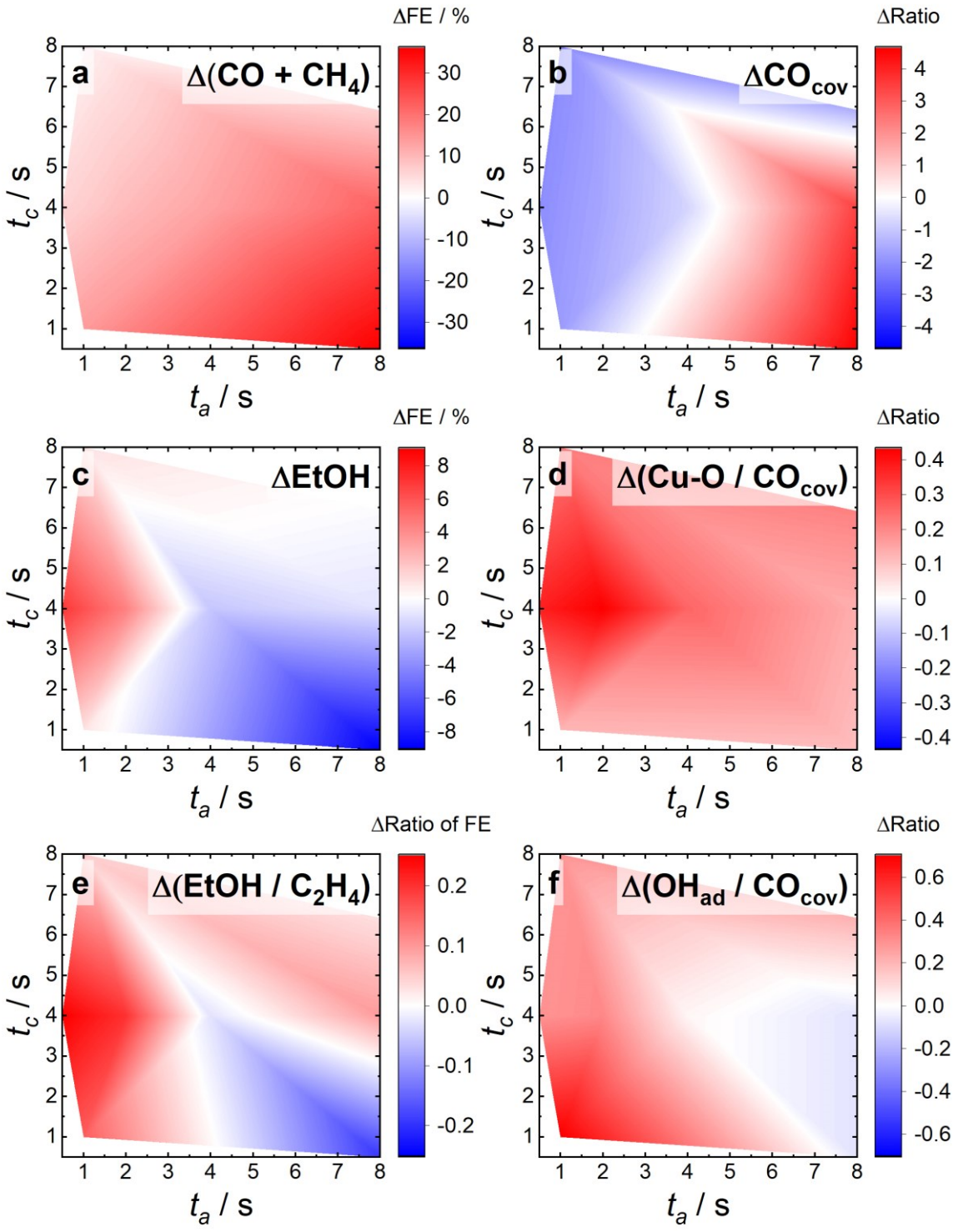

Figure 6.9 Correlations between selectivity distributions[97] and adsorbates/oxide species during pulsed CO_2RR with E_c = -1.0 V, E_a = +0.6 V with respect to the anodic and cathodic pulse lengths subtracted by the corresponding values under static CO_2RR conditions at -1.0 V (indicated with Δ). Changes of (a) sum of Δ Faradaic efficiencies (ΔFEs) of the main C_1 products (CO and CH_4), (b) SERS intensity distribution of ΔCO coverage on Cu (CO_{cov}, determined by the ratio of the SERS intensity of CO_s/CO_r)[88], (c) ΔFEs of ethanol (EtOH), (d) SERS intensity distribution of the Δ ratio of Cu oxide (includes Cu-O_{ad} and Cu_2O) and the CO_{cov}, (e) ratio FEs of EtOH and ethylene (C_2H_4) and (f) SERS intensity distribution of the ratio of OH_{ad} and the CO_{cov}.

conditions at -1.0 V obtained from a variety of anodic and cathodic pulse lengths.[97] Figure 6.9 b depicts the changes in the CO_{cov} during the cathodic part of pulsed CO_2RR, which could be determined by the ratio of the CO_s and CO_r band intensities.[88] The CO_{cov} has been shown to be important for the C-C coupling step, and a higher CO_{cov} could be linked to the increase of C_{2+} products.[88] Under pulsed CO_2RR, the determined CO_{cov} is almost unchanged in the $C_2H_4O_x$ regime but decreased in the EtOH regime and increased in the C_1 regime compared to static CO_2RR conditions (Figure 6.9 a,b). Thus, the CO_{cov} seems to be not the only crucial parameter for the outcoming product selectivities. Furthermore, the kinetics of the ad/-desorption of CO might also be significant for the observed product formation (Table A6.1) due to the introduced dynamics in the system by pulsing the potentials. In the EtOH regime, CO_r and CO_s vibrations adsorbed faster than they desorbed; thus, CO was rapidly available to form EtOH at these pulse lengths (Figure 6.10). Thereby, the kinetics of the ad- and desorption of CO_s versus CO_r, which directly impact the surface CO coverage (Figure A6.10), indicate faster kinetics of CO_s compared to CO_r. This means that the rapidly available CO_{ad} stems first mainly from CO_s which

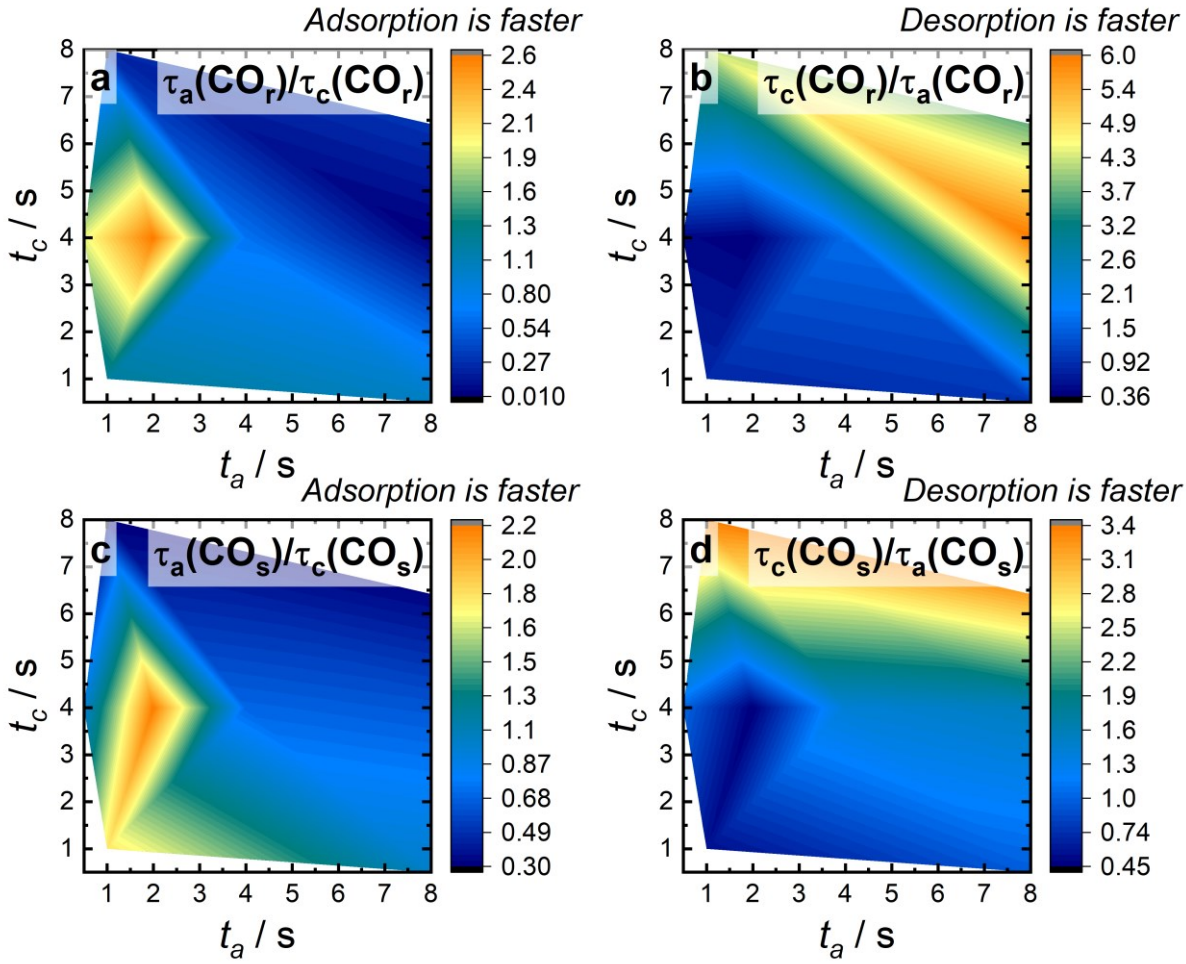

Figure 6.10 Ratios of time constants τ during ad- and desorption of CO_r (a-b) and CO_s (c-d) in dependence of the pulse lengths of pulsed potential CO_2RR measurements with E_c = -1.0 V, E_a = +0.6 V.

has been related to the C-C coupling CO_{atop} in the literature.[88]

In my previous co-authored study, the selectivity trends observed under pulsed conditions were associated with Cu oxide species detected via *operando* XAS and XRD. These species were deemed to play a crucial catalytic role.[97] Therefore, Figure 6.9 c,d displays the changes in the EtOH selectivity as well as the ratio between the Cu-O_{ad}/Cu_2O species during the anodic pulse and the CO_{cov} during the cathodic pulse. Here, an increase in Cu oxygen-related species compared to CO_{cov} could be observed in the EtOH regime, while this ratio decreased in the C_1 regime. Also, kinetically Cu-O_{ad} adsorbed quicker in the EtOH regime compared to the surface Cu_2O in the C_1 regime, which is crucial for the rapid availability of oxygen species to form EtOH (Figure 6.11).

To further investigate the role of OH_{ad}, which was only speculative in previous studies so far, the change in the ratio between the average OH_{ad} and the CO_{cov} during the cathodic pulse was

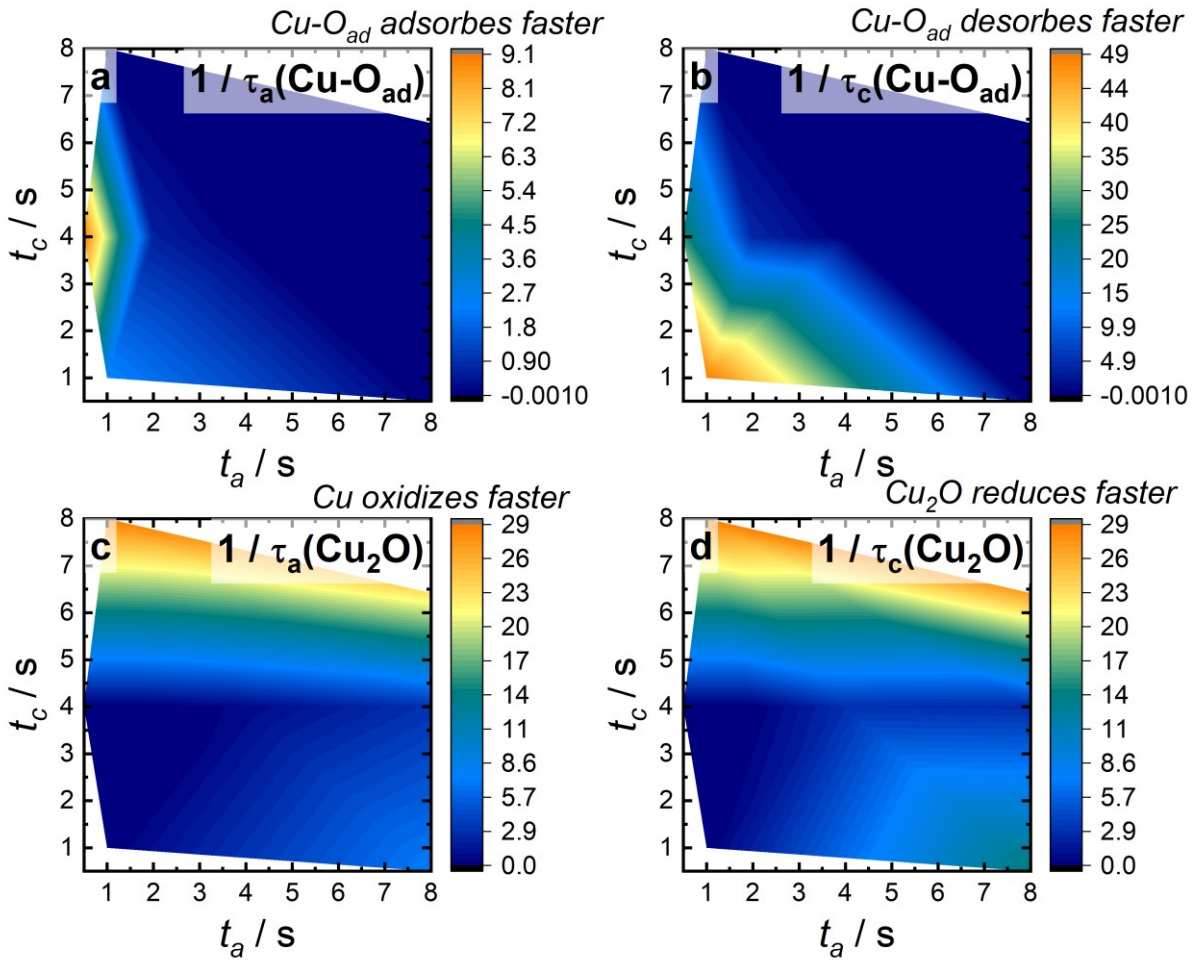

Figure 6.11 Ratios of time constants τ during the adsorption of Cu-O_{ad} (a) and the oxidation of Cu to Cu_2O (c) at the anodic pulse and during the desorption of Cu-O_{ad} (b) and the reduction of Cu_2O to Cu (d) at the cathodic pulse in dependence of the pulse lengths of pulsed potential CO_2RR measurements with E_c = -1.0 V, E_a = +0.6 V.

calculated (Figure 6.9 e,f). Here, three major regions with respect to static CO_2RR conditions could be identified: (i) intermediate OH_{ad} to CO_{cov} ratio characterized by the highest EtOH to C_2H_4 ratio; (ii) low OH_{ad} to CO_{cov} ratio characterized by the lowest EtOH to C_2H_4 ratio; and (iii) highest OH_{ad} to CO_{cov} ratio characterized by a slightly increased EtOH versus C_2H_4 ratio. These findings show a crucial role of OH_{ad} and Cu-O_{ad}/Cu_2O for the formation of EtOH, while fast kinetics of the adsorbates/redox state of CO_{ad}/Cu-O_{ad}/Cu_2O are favorable for the formation of certain products at these induced dynamic reaction conditions.

To generalize this study and defocus from the applied pulse lengths, the Cu-O_{ad}/Cu_2O and OH_{ad} parameters were now directly correlated with the ΔFEs of selected products such as CO, C_2H_4, acetaldehyde, and EtOH (Figure 6.12), as well as the remaining products (Figure 6.13). This analysis shows that the FE of C_2H_4 was lower, irrespective of the surface adsorbate composition, while the selectivity toward CO, acetaldehyde, and EtOH was (mostly) increased. More specifically, high ratios of the Cu-O_{ad}/Cu_2O versus CO_{cov} ratio can be linked to higher EtOH selectivity, while low ratios led instead to a pronounced decrease of the EtOH and all C_{2+} product selectivities. In contrast, in the latter case, CO and other C_1 product selectivities increased. This confirms the importance of oxygen for the formation of EtOH in accordance with the literature.[90, 95, 97, 191, 192, 218]

The link between the product selectivities and the ratio of OH_{ad} versus CO_{ad} is more complex, and several different regions can be identified, as already indicated in Figure 6.9 e,f. The maximal increase in the ΔFE of EtOH, together with other minor alcohols, under pulsed CO_2RR

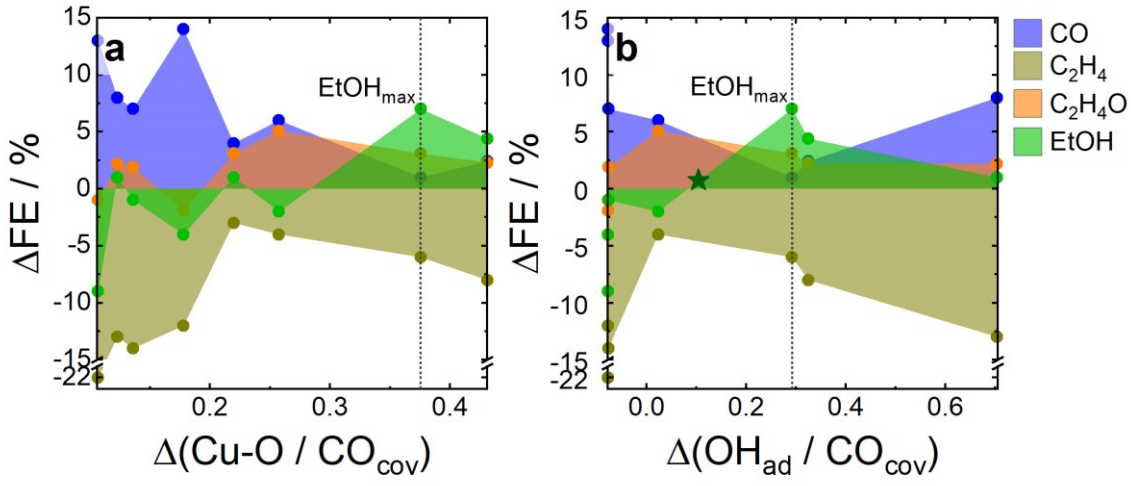

Figure 6.12 Correlations between the selectivity change ΔFE of selected products (CO, ethylene, acetaldehyde, and ethanol) and (a) the Δ(Cu-O_{ad}/Cu_2O versus CO_{cov}) or (b) the Δ(OH_{ad} versus CO_{cov}) in arb. units under pulsed CO_2RR conditions subtracted by the corresponding values under static CO_2RR conditions at -1.0 V. The green star represents the change of ethanol selectivity during pulsed CO_2RR up to non-oxidizing potentials at E_a = 0 V.

is found at an intermediate ratio of OH_{ad}/CO_{ad} (0.3) (Figure 6.12 b, 6.13 b,d), while the ΔFEs of CO, ethylene, and acetaldehyde decreased. At lower OH_{ad}/CO_{cov} ratios, these latter products increased again at the expense of EtOH, while at the lowest ratio (-0.4), the C_1 products, such as CO and CH_4, increased to their maximum at the expense of the C_{2+} products. Similar, higher ratios OH_{ad}/CO_{cov} (> 0.3) are correlated to a lower FE of EtOH and ethylene and an increase of CO and less protonated H_2 and COO^-. However, at these high ratios, the selectivities of EtOH and acetaldehyde were still enhanced compared to static CO_2RR conditions. To verify the dependence of the EtOH selectivity on the OH_{ad} concentration further, pulsed CO_2RR up to non-oxidizing E_a = 0 V at t_c/t_a = 4 s/1 s was also measured (Figure A6.11, Table A6.4). The slight enhancement of EtOH compared to the static conditions goes along with a slight enhancement in OH_{ad} versus CO_{cov}, as also indicated in Figure 6.12 b (green star) and supports the beneficial effect of OH_{ad} for the EtOH production.

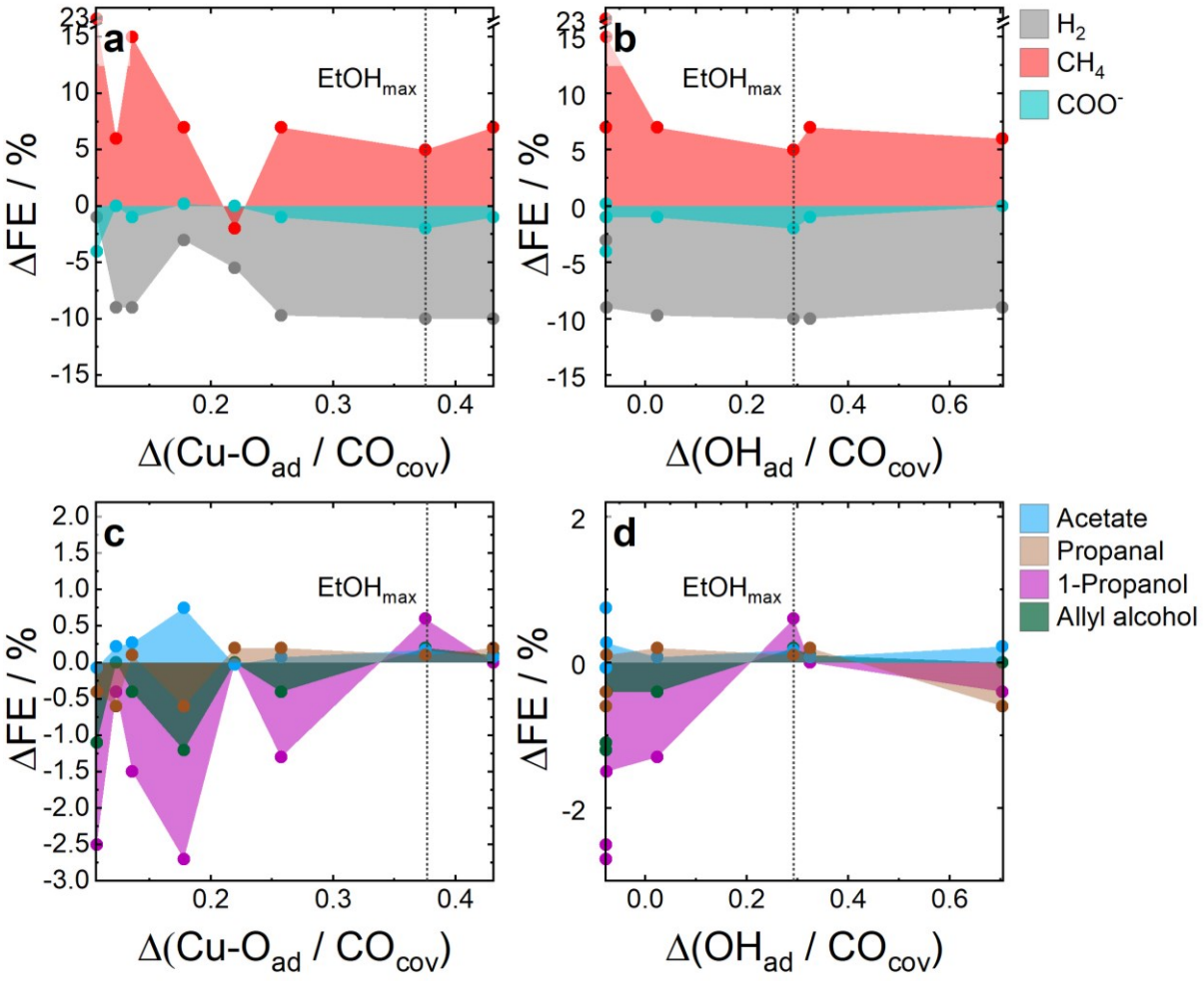

Figure 6.13 Correlations between the selectivity change ΔFE of selected C_1 (top) and minor products (bottom) and (a,c) the Δ(Cu-O_{ad}/Cu_2O versus CO_{cov}) or (b,d) Δ(OH_{ad} versus CO_{cov}) in arb. units under pulsed CO_2RR conditions subtracted by the corresponding values under static CO_2RR conditions at -1.0 V.

From these insights, Figure 6.14 suggest the mechanism for pulsed CO_2RR, where the periodic switching of the applied potential can change the oxidation state of Cu and modify the interfacial adsorbate coverage of OH and CO with distinct kinetic behavior. Cu oxide-related species only formed during the anodic pulse and rapidly reduced again once the cathodic pulse was applied. At short anodic pulse lengths (t_a < 2 s), Cu-O_{ad} vibrations and/or $CuO_x/(OH)_y$ species were detected, which also correlate well with the observation of Cu(II) at short anodic

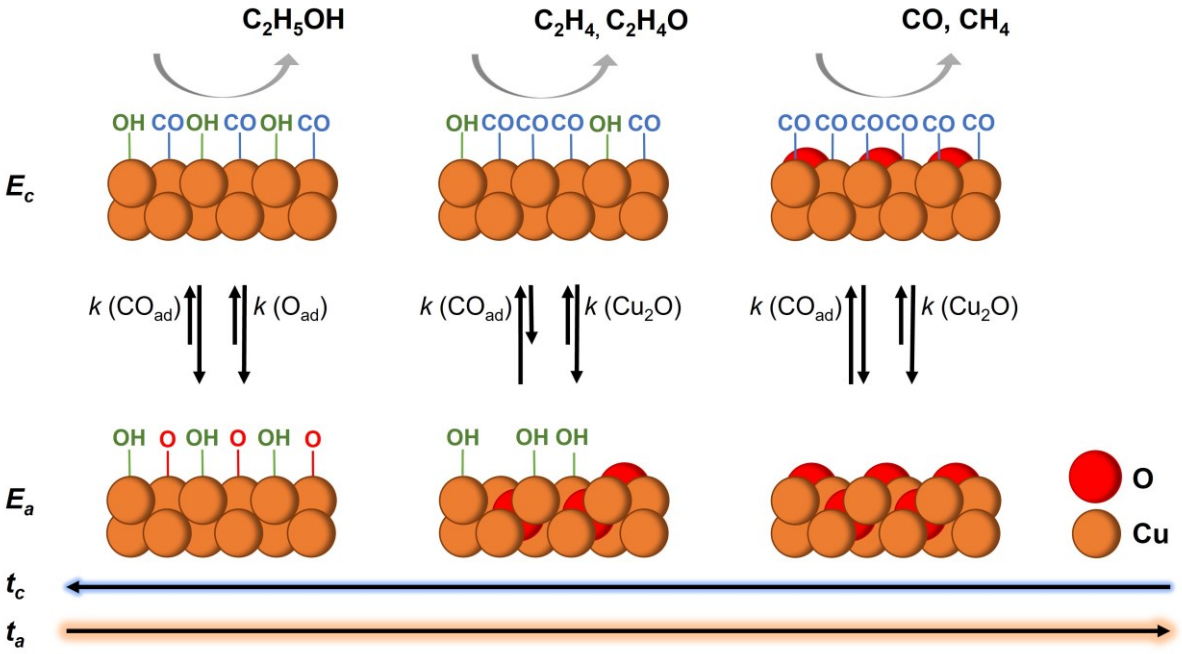

Figure 6.14 Depiction of observed processes during pulsed CO_2RR with E_c = -1.0 V, E_a = +0.6 V of pre-reduced Cu_2O NCs in dependence of the anodic and cathodic pulse length. CO_{ad}, OH_{ad}, and O_{ad} coverage are highlighted, and the oxidation state of Cu is indicated, which both contribute to different product selectivities during the cathodic pulse. The rate constant *k* of the CO ad- and desorption, as well as the Cu reduction and oxidation, are schematically specified by the lengths of the arrows to each other, where a longer arrow is correlated to a faster process.

pulses from *operando* XAS.[97] These $CuO_x/(OH)_y$ species might be essential for the enhanced EtOH selectivities and are directly oxidized from Cu(0) to Cu(II) during the anodic pulse as no characteristic Cu_2O bands could be detected. Additionally, in this region, the ratio of Cu-O_{ad} versus CO_{cov} was the highest. Instead, at longer anodic pulse lengths (t_a > 2 s), typical Cu_2O surface species appeared, where the thickness of the Cu_2O layer grew over the duration of the anodic pulse. Large amounts of bulk-like Cu_2O, which were still present at the beginning of the cathodic pulse, led then to an enhancement in the methane selectivity, as also seen in a previous study.[34] There, the ratio of Cu_2O versus CO_{cov} was the lowest.

Most importantly, the Cu redox transitions, the OH surface coverage, and the local pH seems

to be intertwined. In general, the concentration of OH^- close to and adsorbed on the catalyst surface is expected to increase during pulsed CO_2RR at -1.0 V. Thereby, OH^- species are produced by the reduction of H_2O during the cathodic pulse but are kept close to the catalyst surface due to the positive polarization of the Cu electrode during the anodic pulse. This leads to an effective increase in the local pH during pulsed CO_2RR compared to static CO_2RR. The limited time at short t_a values prevents the formation of an ordered Cu_2O phase and favors the formation of the detected Cu-O_{ad} and/or $CuO_x/(OH)_y$ species. At longer oxidizing pulses, the low OH coverage values likely result from OH_{ad}/OH^- consumption for the formation to Cu_2O (2 Cu + 2 OH^- → 2 Cu-OH → Cu_2O + H_2O),[34, 129] leading to a decrease in the local pH during CO_2RR, which is known to favor methane and CO production.[34] However, higher coverages of OH_{ad} start to block CO_{ad} sites, which leads to an increase in C_1 products and HER.[223] The highest CO_{cov} was reached at long anodic and short cathodic pulse lengths, where no OH_{ad} was detectable, as explained above. Usually, high CO_{cov} are attributed to the increase in C_{2+} products.[88, 158] Nevertheless, the enhanced methane selectivities at these conditions might be, besides the remaining Cu_2O species, also related to the high roughness and/or Cu dissolution of the Cu NCs due to the long duration of the anodic pulse. If the roughness becomes very high, sub-nanometer Cu clusters might form that were observed to be selective for methane formation.[224, 225] Cu-dissolution could also lead to an increased population of low-coordinated sites, which are selective for hydrogen.[60]

Thus, the CO and OH coverage have to be balanced during pulsed CO_2RR to facilitate C-C coupling as well as the protonation of the *CH_xCO intermediates and hamper the O removal, *e.g.*, by a sufficient OH coverage of the adjacent adsorption sites. In addition, the fast kinetics of *CO → CO_{ad} in the EtOH regime might be crucial for the C-C coupling and further protonation. A higher CO_{cov} coupled with a lower OH coverage, similar to the conditions under static CO_2RR, favors the enhancement of deprotonated C_{2+} products such as ethylene and acetaldehyde.

6.4 Conclusion

In conclusion, this study revealed the link between the changes in the adsorbate structure and composition and the catalytic function of an oxide-derived Cu nanocatalyst during pulsed CO_2RR by utilizing time-resolved *operando* SERS. By the implementation of sub-second time resolution, the development of characteristic adsorbates such as OH_{ad} and CO_{ad} could be tracked during each individual pulse. In this way, the observed ethanol enhancement could be attributed to an optimal OH and CO surface coverage, which was found to be crucial for efficient C-C coupling toward alcohols. Furthermore, these OH species had a significantly lower

concentration during stationary CO_2RR and were not present on Cu_2O-derived working catalysts. Thus, only the intermittent formation of an OH/O-covered Cu surface triggers the continuous regeneration of the OH/CO-covered Cu catalyst. Furthermore, the preferable CO ad-/desorption kinetics were found to contribute to higher C_{2+} yields. This is in line with the formation of $Cu\text{-}O_{ad}/CuO_x/(OH)_y$, where the introduced oxygen species is crucial for ethanol enhancement. On the contrary, at longer anodic pulse lengths, OH_{ad} was found to be converted into bulk-like Cu_2O species, which also led to the decrease of the near-surface pH and the formation of unfavorable C_1 products, such as methane and CO, as well as tremendously different reduction mechanisms, not being able to stabilize the OH species. All in all, this study underlines the urgency of time-resolved surface-sensitive techniques such as *operando* SERS to understand the reaction mechanism of pulsed CO_2RR in order to favor the desired product selectivities as well as the necessity to explore experimental methodologies to tackle the interfacial electrolyte composition and pH values.

7. Time-Resolved *Operando* Insights into Cu-Zn Nanocubes during the Pulsed CO_2 Electro-reduction toward Ethanol

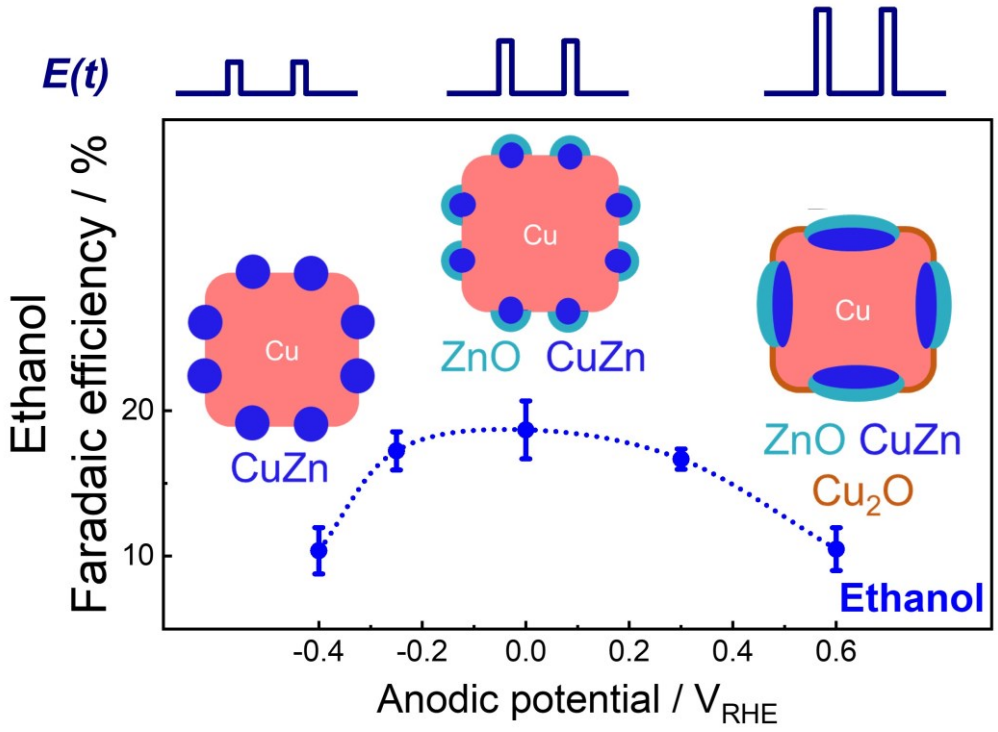

This chapter presents my manuscript draft titled "Time-Resolved *Operando* Insights into Cu-Zn Nanocubes during the Pulsed CO_2 Electroreduction toward Ethanol", which is currently in preparation for publication. I was responsible for planning and interpreting all measurements outlined in this chapter and wrote the draft under the supervision of Dr. A. Bergmann and Prof. Dr. B. Roldán Cuenya. I prepared the samples and conducted and analyzed all electrocatalytic measurements, as well as the *operando* XAS, XRD, and SERS experiments. The machine learning analysis of the XAS data was carried out by M. Rüscher and Dr. J. Timoshenko. Dr. A. Bergmann conducted the XRD Rietveld analysis. Dr. H. S. Jeon, W. Frandsen, and Dr. S. Kühl performed the SEM/STEM measurements, while C. Rettenmaier conducted and analyzed the XPS measurements. Dr. U. Hejral, Dr. E. M. Davis, and F. T. Haase supported the HE-XRD measurements, and D. Kordus the synthesis. All co-workers are affiliated with the Fritz Haber Institute.

Pulsed electrochemical CO_2 reduction (CO_2RR) has emerged as a facile way to alter the product selectivities toward desired multicarbon products, but so far, it has been applied mainly over monometallic Cu-based electrodes, which suffer from stability issues. Here, ZnO-decorated Cu_2O nanocubes were prepared, and different anodic potential values were applied during pulsed CO_2RR to uncover the effect of the redox transitions of both metals on the catalytic function and dynamic catalyst structure and composition. An increase in the ethanol selectivity was observed once pulsed into the oxidation regime of zinc, while parasitic hydrogen evolution drastically increased once pulsed into the oxidation regime of Cu. To understand these changes, time-resolved *operando* XAS, XRD, and SERS were employed. In this way, the dynamically induced interplay between the Zn oxide, CuZn alloy, and metallic Zn formation, the evolution of Cu crystallites, and the adsorption behavior of *CO and $*OH^-$ could be followed. This study highlights the relevance of zinc oxide and an increased OH coverage for the enhancement of the catalyst selectivity toward ethanol.

7.1 Introduction

The CO_2RR provides an attractive way to mitigate the energy crisis by closing the carbon cycle and storing renewable energy in valuable multicarbon fuels and chemicals.[8, 226] Especially, the selective generation of liquid fuels such as ethanol is highly desirable for economical usage due to their high energy densities and ease of storage.[189] Among the metals, Cu is the only catalyst that can yield significant amounts of high-value hydrocarbons and oxygenates such as CH_4, C_2H_4, and C_2H_5OH.[14] However, the Cu-catalyzed CO_2RR suffers from low selectivity toward liquid products and poor long-term stability.[16, 72] The incorporation of a CO-producing second metal (*e.g.*, Ag, Au, and Zn) has been shown to be a promising strategy for the enhancement of liquid products either due to a CO spillover from the second metal to the Cu sites or due to the change in the electronic properties.[116, 158, 215, 227, 228]

Especially Cu-Zn is an appealing system since it consists of low-cost and earth-abundant metals. Nevertheless, the reported CO_2RR selectivities for Cu-Zn systems are often contradictory, and the reaction pathways are disputed. For example, a phase-separated Cu-Zn catalyst with 50 wt% of Zn exhibited a Faradic efficiency of up to 94 % for CO.[229] Moreover, the selectivity of CuZn nanoparticles (NPs) changed from methane on Cu-ZnO NPs to CO on a CuZn alloy.[68, 114] The product selectivity of Cu-ZnO nanocrystals can be switched from methane to ethanol by changing the degree of surface alloying together with the concentration of metallic Zn.[118] Additionally, Cu-rich CuZn alloys were found to increase the C_{2+} product selectivity, while Zn-rich alloy phases increased the formation of CO and H_2.[115] Thus, the

structural, morphological, and chemical arrangement of Cu-Zn is crucial for the observed product selectivities. So far, it has been mainly altered by different synthesis routes, where the synthesized material experiences further *in situ* transformations when exposed to static CO_2RR conditions forming the working catalyst.

An elegant way to modify the Cu-Zn arrangement in a controlled manner *in situ* is by applying pulsed electrolysis, where the electrode potential alternates periodically between a cathodic E_c and an anodic potential E_a.[20] Thereby, the working catalyst can be regenerated or reactivated, resulting in stabilization or even improvement of the catalytic function. So far, studies of pulsed CO_2RR mainly focused on the usage of bare Cu catalysts and revealed an enhancement toward C_{2+} products as well as a suppression of the hydrogen evolution reaction (HER).[34, 120, 126, 135] These trends were mainly attributed to the oxidation of Cu,[96, 97] irreversible morphological changes,[34, 96, 97] an increase in the pH,[34, 135] and the adsorption of OH^- species.[129] However, the Cu catalysts suffered from instability due to the dissolution of Cu and deactivation of active sites during pulsed CO_2RR, which are likely induced by the continuous oxidation-reduction cycles.[97, 230] By the addition of a second metal, the first pulsed potential studies on a Cu-Ag catalyst indicated improvements in selectivity and stability with symmetric pulse lengths of 5 s.[105] However, bimetallic catalysts for pulsed CO_2RR are not well explored and characterized yet, and there is a need for time-resolved *operando* characterization to understand and follow the dynamically induced changes in the system and reaction mechanism.

Here, ZnO-decorated Cu_2O nanocubes (NCs) serve as a model system for bimetallic catalysts for the pulsed CO_2RR. Different anodic potentials E_a were tested, while the cathodic CO_2RR potential E_c (-1.0 V versus RHE), as well as the anodic time t_a (1 s) and the cathodic time t_c (4 s), were fixed following previous findings on optimized conditions for ethanol formation.[97] By employing time-resolved *operando* X-ray absorption spectroscopy (XAS), high energy X-ray diffraction (HE-XRD), and surface-enhanced Raman spectroscopy (SERS), the evolution of the structure, chemical state, composition, and adsorbates of the Cu-Zn catalyst could be followed under pulsed CO_2RR conditions. In this way, the structure of the catalyst and its adsorbates could be dynamically altered to tune the selectivity toward the desired C_2 liquid product, ethanol.

7.2 Experimental Details

7.2.1 Synthesis of Cu-Zn Catalyst

ZnO-Cu_2O NCs were prepared by a wet-chemical ligand-free approach as described in my previous co-authored study.[115] 5 mL of an aqueous $CuSO_4$ solution (0.1 M) were mixed with

457.5 mL of ultrapure water (> 18 MΩ cm) at room temperature followed by the addition of 17.5 mL of a NaOH solution (1.0 M) under stirring. After 5 s, 20 mL of an L-ascorbic acid solution (0.25 M) were added to the reaction solution and further stirred for 12.5 min. In the meantime, a mixture of 5 mL of L-ascorbic acid (0.25 M) and 2.5 mL of $ZnCl_2$ solution (0.1 M) was prepared. This mixture was added to the reaction solution and stirred for one more minute. The reaction solution was centrifuged and washed three times, twice with an ethanol-water mixture (1:1) and once with pure ethanol. The final product was dried overnight in vacuum. The working electrodes were prepared by mixing 2.5 mg of the catalyst powder with 800 µL of pure ethanol and 16 µL of a Nafion solution (Sigma-Aldrich, ~5 wt% in a mixture of alcohols and water). Then, the mixture was ultrasonicated for at least 30 min, and 41 µL of the catalyst dispersion were slowly drop-casted on each side of a 0.5 x 3 cm carbon paper sheet (Alfa Aesar, Toray Carbon Paper, TGP-H-60) to reach a Cu loading of 70 µg cm^{-2} and dried in an oven at 60 °C. Cu_2O NCs, which served as a reference catalyst, were prepared in the same way without adding the mixture of L-ascorbic acid and $ZnCl_2$.

7.2.2 Electrochemical Characterization

The electrochemical CO_2RR experiments were conducted with a Biologic SP-300 potentiostat in a gas-tight H-type cell, in which the cathodic and anodic compartments were separated by an anion exchange membrane (Selemion AMV, AGC Inc.). Platinum gauze (MaTecK, 3600 mesh cm^{-2}) served as the counter electrode, and a leak-free Ag/AgCl electrode (LF-2, Innovative Instruments, Inc.) as the reference electrode. The electrolyte, 0.1 M $KHCO_3$ solution (Sigma-Aldrich, 99.7 %), was previously purified by a cation-exchange resin (Chelex 100 Resin, Bio-Rad) and saturated with CO_2 (99.995 %) for at least 15 min.

Under constant flow of CO_2 (20 mL/min), the catalyst was reduced for 1 h at -1.0 V (pre-reduction). All potentials are referenced to the reversible hydrogen electrode (RHE) and corrected for the iR drop after the measurement by performing potentiostatic electrochemical impedance spectroscopy (PEIS) directly before and directly after the CO_2RR measurement. After pre-reduction of the catalyst, a potential pulse protocol was performed for 1 h with a fixed cathodic potential E_c = -1.0 V, different anodic potentials E_a and a cathodic pulse length t_c = 4 s and an anodic pulse length t_a = 1 s if not noted differently.

Gas products were measured every 15 min and quantified by online gas chromatography (GC, Agilent 7890B) equipped with a thermal conductivity detector (TCD) and a flame ionization detector (FID). Liquid products were analyzed after each measurement with high-performance liquid chromatography (HPLC, Shimadzu Prominence) equipped with a NUCLEOGEL SUGAR 810 column and a refractive index detector (RID) and with a liquid GC (L-GC,

Shimadzu 2010 plus) equipped with a fused silica capillary column and an FID detector. Each presented data point corresponds to an average of at least three different measurements collected with an identical freshly prepared sample under the same experimental conditions, and the error bars represent the standard deviation. The Faradaic efficiencies were calculated as explained in Section 3.1.3.

7.2.3 *Ex Situ* Characterization

The morphology and elemental distribution of the samples before and after static and pulsed CO_2RR were investigated by scanning electron microscopy (SEM, Apreo SEM, Thermo Fisher Scientific), scanning transmission electron microscopy (STEM, FEI Talos F200X microscope, Thermo Fisher Scientific), and energy dispersive spectroscopy (EDX, SuperX 4 SDD EDX detector) maps. The STEM was equipped with an XFEG field emission gun (200 kV) and with brightfield (BF), darkfield (DF), and high-angle annular darkfield (HAADF) detectors. Samples for SEM were measured directly on the carbon paper in the as-prepared state and after different CO_2RR conditions. Samples for STEM were prepared by coating a nickel grid (400 mesh with lacey carbon film, PLANO GmbH) with the catalyst dispersed in EtOH:H_2O (1:1) before and after different CO_2RR conditions.

The bulk composition and amount of Cu and Zn in the as-prepared samples and the concentrations of Cu and Zn after static and pulsed reaction in the electrolyte were determined by inductively coupled plasma-mass spectrometry (ICP-MS, iCAP RQ, Thermo Fisher Scientific). The as-prepared samples were digested in concentrated HNO_3 and heated using microwave irradiation at 180 °C for 20 min, with a ramping step of 10 min (Multiwave GO, Anton Paar). The samples were then diluted with ultrapure water (> 18 MΩ cm) to reach the appropriate concentrations.

The surface composition of the catalysts before and after static and pulsed CO_2RR was determined by quasi-*in situ* X-ray photoelectron spectroscopy (XPS) without exposing the samples to air. Therefore, a custom-made electrochemical cell was directly attached to an ultra-high vacuum system equipped with a hemispherical electron analyzer (Phoibos 100, SPECS GmbH, E_{pass} = 15 eV) and an X-ray source (XR 50, SPECS GmbH) with an aluminum anode (1486.6 keV, 300 W). All spectra were aligned to the Cu $2p_{3/2}$ peak (E_{bin} = 932.7 eV). The Cu, Cu_2O, and CuO amounts were estimated from the integrated areas of a linear combination fit of the Cu LMM Auger profiles with the corresponding reference spectra. These reference spectra were obtained from an *in situ* annealed and sputtered Cu foil (metallic reference) and a plasma oxidized CuO sample, and the reference spectrum of Cu_2O was used from the literature.[169] The Cu to Zn ratio was obtained from the Zn $2p_{3/2}$ to Cu $2p_{3/2}$ regions and calculated

considering the relative sensitivity factors (RSF) of the metals. For the electrochemical measurements, a Metrohm Autolab potentiostat (PGSTAT 302 N) was used. For the determination of the oxidation state at the cathodic and anodic pulse, the potential was stopped at the respective potential as described in previous studies.[96, 97]

7.2.4 *Operando* Characterization

XAS measurements were conducted at three synchrotron beamlines: the ROCK beamline of SOLEIL synchrotron (QXAFS (Quick X-ray absorption fine structure) measurements of the catalyst during the cyclic voltammetry scans), the SAMBA beamline of SOLEIL synchrotron (steady-state measurements of time-averaged *operando* XAS data under pulsed CO_2RR), and the SuperXAS - X10DA beamline at the Paul Scherrer Institute's SLS synchrotron facility (*operando* QXAFS measurements under pulsed CO_2RR).

A channel cut Si(111) monochromator was used for energy selection in the QXAFS measurements at the ROCK and SuperXAS beamlines, with a monochromator oscillation frequency of 2 Hz at ROCK and 1 Hz at SuperXAS. At the SAMBA beamline, a Si(220) double crystal monochromator was used. To ensure approximately 10 % absorption of the X-rays, the intensity of the X-rays before the sample was measured using an ionization chamber filled with pure N_2 (ROCK, SuperXAS) or an N_2 and He mixture (SAMBA). Additionally, the XAS measurements were performed in fluorescence mode with a PIPS detector (ROCK, SuperXAS) or a 35-channel Ge detector (SAMBA).

The XAS measurements were conducted at the Cu K-edge (8979 eV) and the Zn K-edge (9659 eV). A home-built single-compartment cell was used for *operando* XAS measurements, with sample dispersions spray-coated on a gas diffusion electrode (Sigracet 29 BC, SGL Carbon) with an area of 1 cm^2. The sample loading was optimized to approximately 1 mg_{Sample} cm^{-2} to achieve a sufficient signal-to-noise ratio at the Cu K-edge and the Zn K-edge while avoiding self-absorption effects.

To align and calibrate XAS spectra, a Cu foil spectrum collected in transmission mode was used as a reference. In the case of SuperXAS measurements, a Cu foil spectrum was collected at the start of each QXAFS scan before the cell was moved into the X-ray beam. The data calibration at ROCK was performed by adjusting the energies of monochromator glitches, while beamline-specific software was used to calibrate QXAFS data at ROCK and SuperXAS. Further data processing, including data reduction, spectra normalization, averaging, and linear combination analysis of the XANES spectra, was carried out using a set of home-built Wolfram Mathematica scripts. The EXAFS data were obtained from averaged XAS spectra using the Athena software, and analysis of the Zn K-edge EXAFS data was performed using a machine

learning-based approach.

Operando time-resolved HE-XRD experiments were performed at ID31 of the European Synchrotron Radiation Facility (ESRF, Grenoble). The X-ray energy was set to 68 keV (λ = 0.18233 Å). A Dectris Pilatus X CdTe 2 M placed at a working distance of 1.387 m calibrated using a CeO_2 standard was used to record the diffraction pattern. The acquisition time of the individual detector images was set to 10 s under stationary conditions and to 0.127 s for the time-resolved pulse experiments. Primary data treatment (calibration, masking, detector image integration) was conducted using the software package pyFAI.[231]

A homemade electrochemical cell based on a three-electrode configuration and continuous flow of electrolyte using a leak-free miniature Ag/AgCl reference electrode (3.4 M KCl, eDAQ ET072) and a platinum counter-electrode. The electrode potentials were controlled using a Biologic SP-300 potentiostat. The catalyst was deposited on HOPG with a loading of 0.1 $mg_{Cu}\,cm^{-2}$. The incident X-ray angle was tuned between 0° and 1° to ensure an optimal Cu_2O to graphite Bragg peak ratio, and to ensure a sufficiently small spread of the X-rays on the sample, thus avoiding parasitic peak broadening.

The data analysis of the diffraction patterns after integration of the detector images was conducted using a set of GNU Octave scripts to perform background pattern subtraction, peak fitting using Lorentz profiles, and averaging of the XRD data collected under pulsed CO_2RR. Rietveld refinement was used to analyze the XRD pattern using the software package TOPAS (Bruker-AXS) in combination with the package Powder3D parametric.[232] Here, variations in the zero error and the structural parameters of the Cu and Cu_2O phases were considered (scale factor, lattice parameter, Gaussian size-induced and Lorentzian-type microstrain-induced peak broadening).

Furthermore, the analysis of single Bragg peaks such as Cu(311), Cu(111), Cu_2O(111), and Cu_2O(200) was also performed. The structural coherence length (size) of the crystalline domains was determined from the integral breadth of the Bragg peaks by use of the Scherrer equation (Equation 3.24) with a shape factor of 0.89. The lattice strain was calculated from the lattice spacing $d = \lambda/(2\sin\Theta)$ with the strain = $(d - d_0)/d_0$, where d_0 denotes the lattice spacing determined from the Bragg peak position at the end of the cathodic pulse.

Operando SERS was performed with a Raman spectrometer (Renishaw, InVia Reflex) together with an optical microscope (Leica Microsystems, DM2500M) and a motorized stage for tracking the sample (Renishaw, MS300 encoded stage). Calibration of the system was performed prior to each measurement using a Si(100) wafer (520.5 cm^{-1}). A near-infrared laser (Renishaw, RL785, λ = 785 nm, P_{max} = 500 mW) was used as an excitation source. *Operando*

Raman was collected with a water immersion objective (Leica microsystems, 63x, numerical aperture of 0.9), which was covered by a Teflon film (DuPont, film thickness of 0.013 mm) to protect it from the electrolyte. The electrochemical measurements were conducted in a custom-made spectro-electrochemical cell made of PTFE and controlled by a Biologic SP-240 potentiostat. The working electrode consists of the catalyst drop-casted onto a glassy carbon piece. The cell was further equipped with a leak-free Ag/AgCl reference electrode and a Pt counter electrode. A CO_2-saturated 0.1 M $KHCO_3$ solution was used as the electrolyte. The collection of each spectrum was performed with 0.25 s (for 4 s/1 s pulses) and 1 s (for 10 s/10 s pulses) of exposure time. The Raman data were first processed using the Renishaw WiRE 5.2 software to normalize the spectra and remove the cosmic rays. Then, GNU Octave scripts were used to perform to correlate the electrochemical and Raman data, to fit the peaks using Gaussian profiles, and to average the SERS data.

7.3 Results and Discussion

7.3.1 Microscopy Characterization

Bimetallic shape and size-selected Cu_2O NCs with around 20 nm edge length covered with a 2 nm layer of ZnO deposited preferentially at the NC corners were prepared via a wet-chemical approach (Table 7.1, Figure 7.1 a,e,i). STEM-EDX, as well as ICP-MS analysis, revealed a Cu:Zn composition of 94:6 at% in the as-prepared state (Table 7.2 and Table A7.1). In the first step, the ZnO/Cu_2O NCs were pre-reduced for 1 h under static CO_2RR conditions (in CO_2-saturated 0.1 M $KHCO_3$ at -1.0 V). The structure of the pre-reduced Cu-Zn catalyst changed irreversibly, as shown by *ex situ* SEM and TEM-EDX images (Figure 7.1 b,f,j). In fact, the NCs increased by about 4 nm in size (Table 7.1) and formed a porous structure, while Zn interacted with the Cu surface, mixing with Cu and forming some Zn/CuZn islands and particles. In the second step, a freshly prepared pre-reduced Cu-Zn sample was used for each cyclic voltamme-

Table 7.1 Edge lengths and corresponding size distribution of Cu-Zn obtained from the analysis of STEM images in the as-prepared state, after 1 h of static CO_2RR, and after different pulse protocols with fixed E_c = -1.0 V, t_c = 4 s and t_a = 1 s.

Sample	Edge length / Particle diameter of Cu [nm]	Length of Zn [nm]
As-prepared	20.0 ± 3.3	2.0 ± 0.5 (Edges)
Static at -1.0 V	24.3 ± 4.0	4.0 ± 0.6 (Particles)
Pulsed with E_a = 0 V	23.8 ± 4.6	5.3 ± 1.0 (Particles)
Pulsed with E_a = 0.6 V	27.8 ± 5.1	21.4 ± 7.8 (Islands)

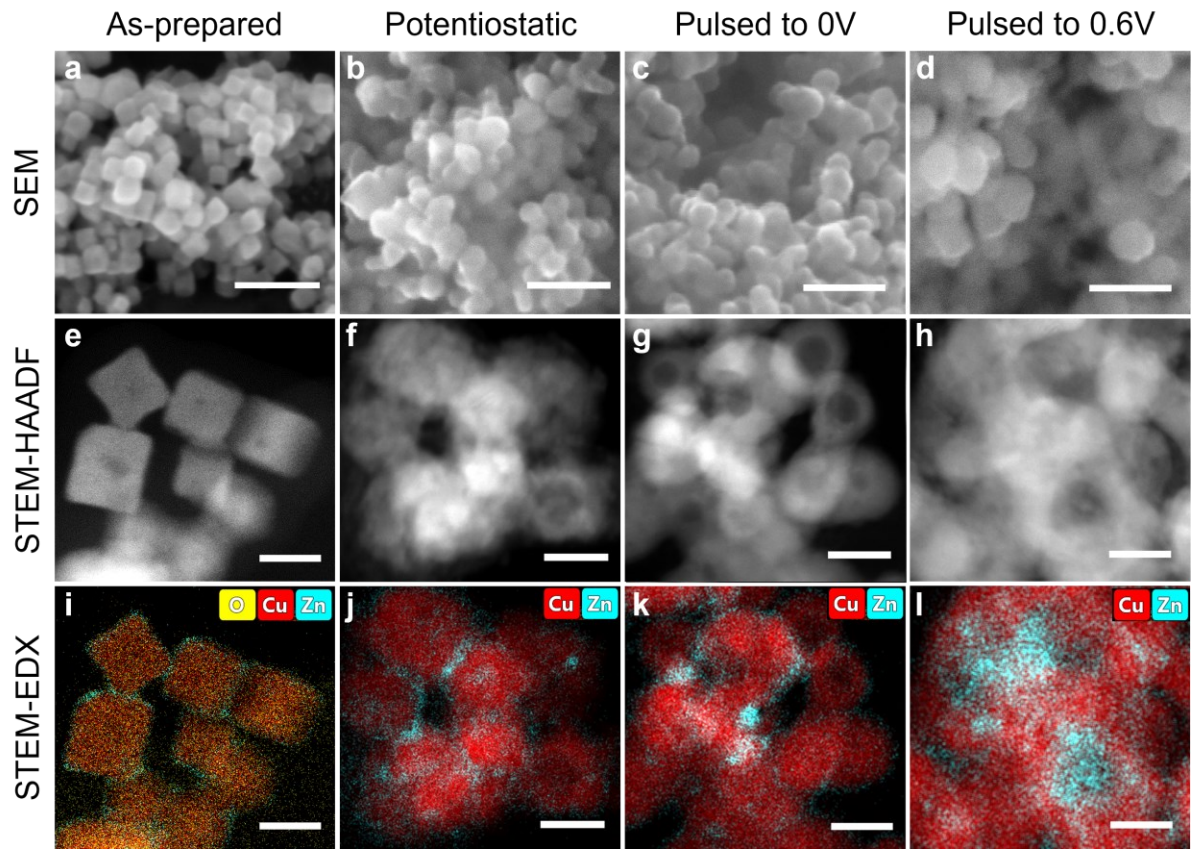

Figure 7.1 Microscopy characterization of the Cu-Zn catalyst after different reaction conditions. (a-d) SEM, (e-h) STEM-HAADF, and (i-l) STEM-EDX images of the Cu-Zn catalyst. (a,e,i) show the as-prepared state, (b,f,j) after 1 h of potentiostatic CO_2RR, (c,g,k) after 1 h of pulsed CO_2RR with E_a = 0 V and (d,h,l) after 1 h of pulsed CO_2RR with E_a = 0.6 V (fixed E_c = -1.0 V, t_c = 4 s and t_a = 1 s). The given scale bars of the SEM images correspond to 100 nm and of the STEM images to 20 nm.

try (CV) and pulsed CO_2RR measurement (microscopy characterization after pulsed CO_2RR is shown in Figure 7.1 c-d,g-h,k-l). Note that the amount of oxygen after the reaction cannot be quantified by *ex situ* TEM-EDX maps due to the reoxidation of the catalyst in air (Figure A7.1). A more detailed characterization of the *ex situ* SEM and TEM images with additional SEM and

Table 7.2 Elemental quantification of Cu and Zn extracted from the STEM-EDX images of Figure 7.1 of Cu-Zn in the as-prepared state, after 1 h of static CO_2RR and after different pulse protocols with fixed E_c = -1.0 V, t_c = 4 s and t_a = 1 s.

Sample	Cu [%]	Zn [%]
As-prepared	93.6(8)	6.4(8)
Static at -1.0 V	95.8(6)	4.2(6)
Pulsed with E_a = 0 V	97.1(4)	3.0(4)
Pulsed with E_a = 0.6 V	96.1(5)	3.9(5)

TEM images of the Cu-Zn catalyst and TEM images of the bare Cu_2O NCs as a reference can be found in Appendix A7 (Figure A7.2-A7.4, Table A7.2-A7.3).

7.3.2 Characterization of As-Prepared and Pre-Reduced Catalyst

The Cu-Zn catalyst was characterized by using *operando* and quasi-*in situ* methods in the as-prepared state or at open circuit potential (ocp) and in the pre-reduced state (1 h under CO_2RR conditions at -1.0 V), as shown in Figure 7.2. The position of the absorption edge in the Cu K-edge XANES spectrum (Figure 7.2 a) of the sample under ocp compared to the reference spectra indicates that the sample is mainly in the Cu(I) oxidation state. After 1 h of static CO_2RR, the spectrum of the pre-reduced catalyst resembles that of the metallic Cu foil reference. Nevertheless, linear combination analysis (LCA) revealed that a significant fraction of Cu(I) of 12 % was preserved under static CO_2RR conditions (Figure 7.3 a,c, Figure A7.5 a,b) in line with previous studies on Cu_2O NCs.[97, 158] On the other hand, the Zn K-edge XANES spectrum (Figure 7.2 b) at ocp resembles the ZnO reference, while the spectrum of the pre-reduced catalyst resembles rather the one of the metallic Zn or that of the CuZn brass alloy foil. In principle, Zn K-edge XANES data can also be qualitatively analyzed by LCA (Figure 7.3 b,d,

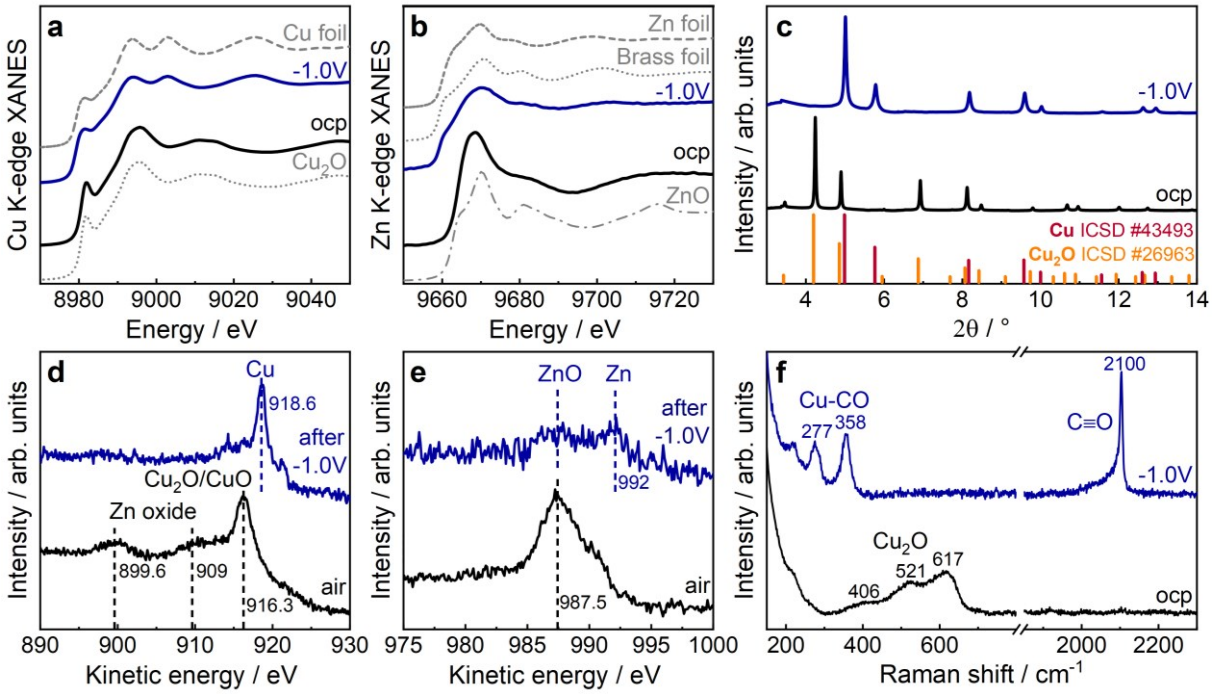

Figure 7.2 Characterization of the Cu-Zn catalyst at ocp/in air and after around 1 h of static CO_2RR at -1.0 V. (a,b) *Operando* XANES of Cu K-edge with corresponding reference spectra of Cu_2O and Cu foil and Zn K-edge with corresponding reference spectra of ZnO, metallic Zn foil and $Cu_{70}Zn_{30}$ brass alloy foil, respectively. (c) *Operando* HE-XRD with reference positions of Cu_2O and Cu. (d,e) Quasi-*in situ* XAES spectra of Cu and Zn LMM, respectively. (f) *Operando* SERS with peak assignments.

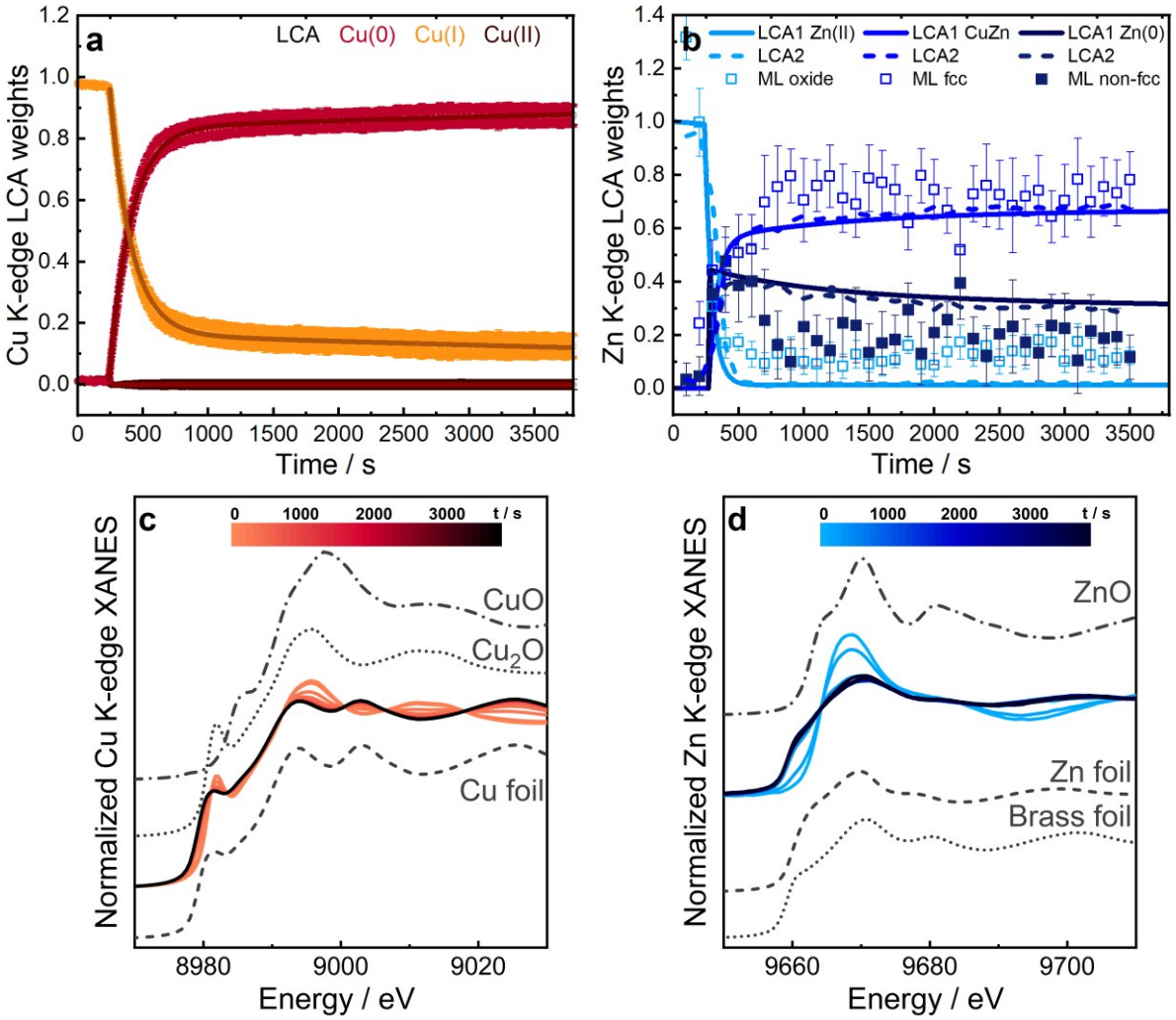

Figure 7.3 Evolution of XAS data of the Cu-Zn catalyst of Cu and Zn K-edge during the initial static CO_2RR for 1 h at -1.0 V. (a) Concentration of Cu(0), Cu(I) and Cu(II) species obtained by LCA of Cu K-edge and (b) averaged concentration of Zn(0), Zn(II) and CuZn species obtained by LCA (LCA1 with standard references and LCA2 with oxide reference from as-prepared state spectra) and concentrations of oxide, fcc-like and non-fcc-like phases obtained from ML-EXAFS analysis of Zn K-edge. (c) and (d) show the averaged and normalized XANES spectra (100 spectra are averaged) of the Cu and Zn K-edge, respectively, with the corresponding references for both edges.

Figure A7.5 c,d). However, since the actual alloy structures and compositions of Zn species in the catalyst can differ significantly from those of standard reference materials, the LCA can suffer from systematic errors, as discussed in more detail in Appendix Note 1. Therefore for the quantification of different Zn species concentrations, one relies on the analysis of EXAFS spectra and on a supervised machine learning (ML) approach that was developed in my recent co-authored study.[115] The ML-based approach allows us to extract partial radial distribution functions (RDFs) for Zn species with the crystallographically non-equivalent environment (Figure A7.6).[115] By integrating the latter, the relative concentrations of different species can

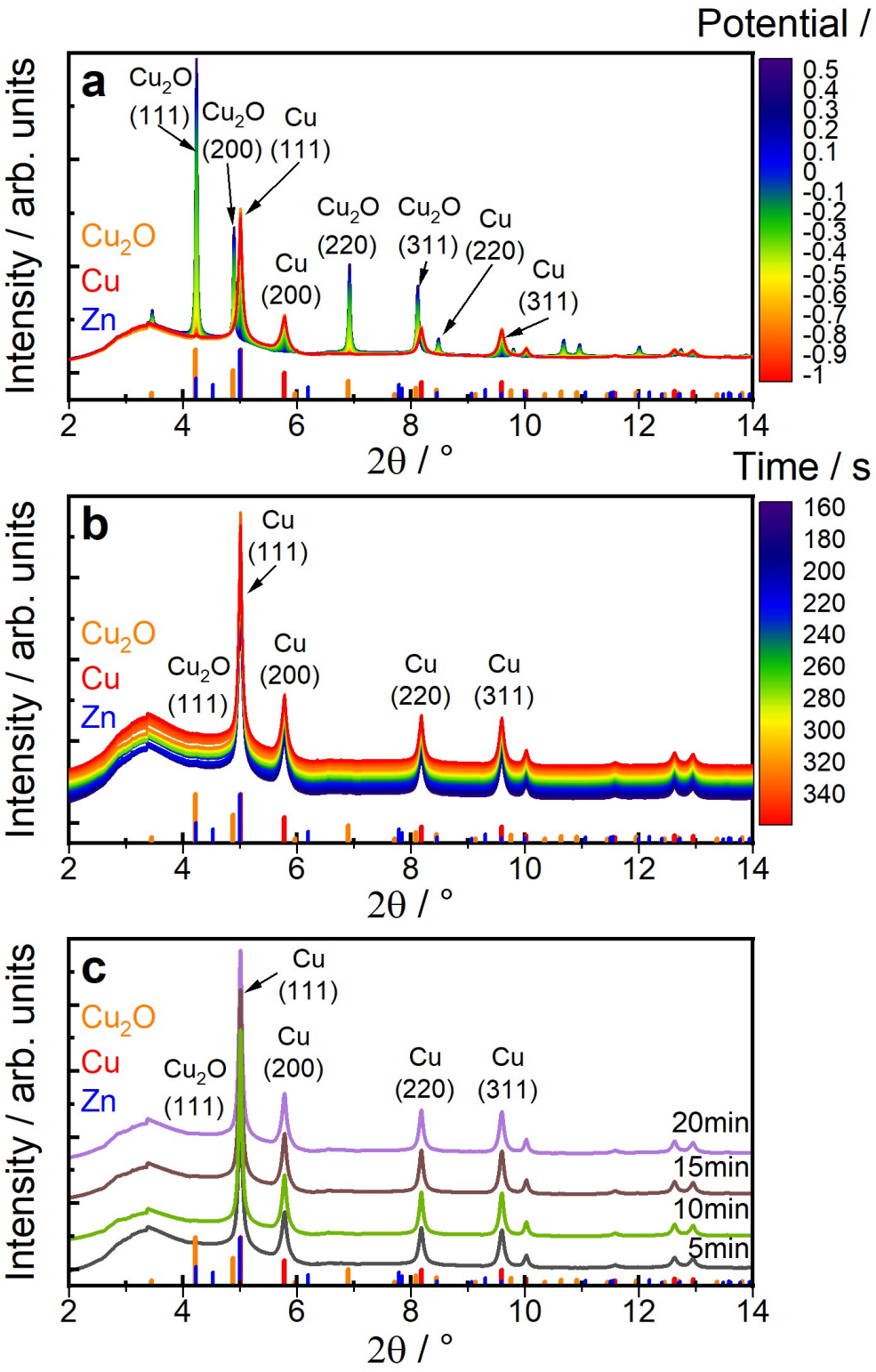

Figure 7.4 HE-XRD pattern of the Cu-Zn catalyst during static CO_2RR conditions with reference peaks of Cu_2O, Cu, and Zn. (a) Averaged XRD patterns during LSV scan from ocp to -1.0 V with a scan rate of 10 mV s^{-1}. (b) Averaged XRD patterns during the first five minutes at -1.0 V with an offset of the diffractograms for better visibility of changes. (c) XRD pattern at 5, 10, 15, and 20 minutes at -1.0 V (with a time resolution of 5 s/diffractogram). The XRD patterns correspond to the average of 5 XRD patterns, acquired with 0.2 s/diffractogram, that can be translated into a time resolution of 1 s/diffractogram shown here.

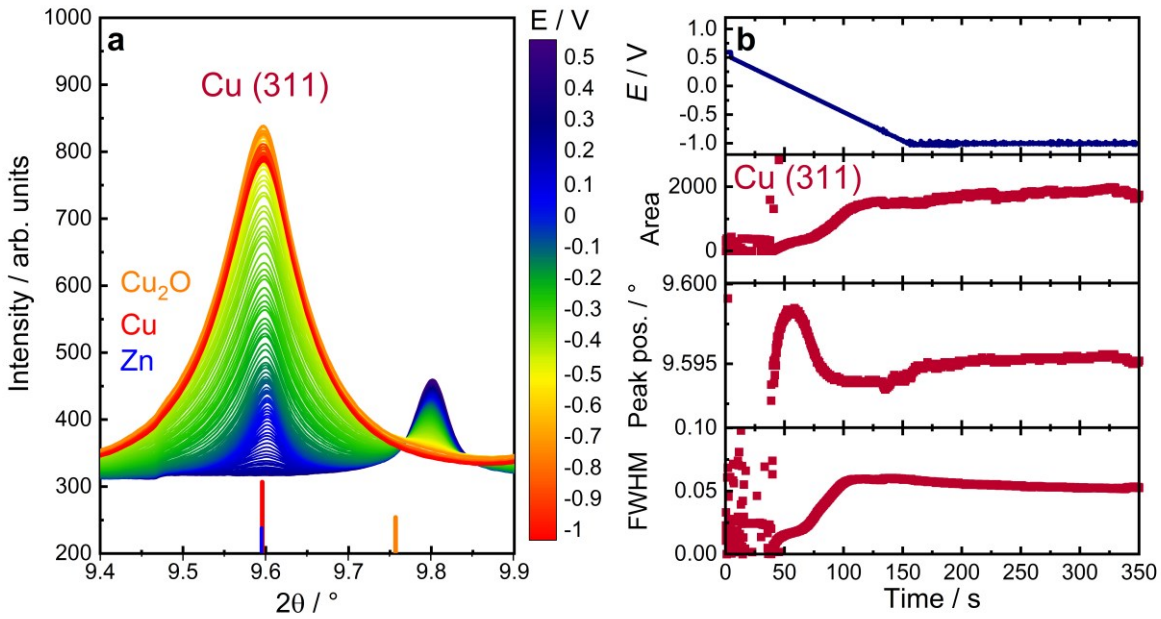

Figure 7.5 Extract of HE-XRD pattern of Cu(311) and corresponding fits of the Cu-Zn catalyst during LSV and static CO_2RR conditions. (a) Extract of averaged XRD patterns during the LSV scan from ocp to -1.0 V with a scan rate of 10 mV s^{-1}. (b) Area (second row), peak position (third row), and FWHM (fourth row) extracted from fits of Cu(311) with respect to the applied potential (top). The XRD patterns correspond to the average of 5 XRD patterns, acquired with 0.2 s/diffractogram, that can be translated into a time resolution of 1 s/diffractogram shown here.

be calculated. As demonstrated in Appendix Note 1 and Figure A7.7, the ML-EXAFS-based approach provided more accurate values of the concentrations of oxidized, metallic alloyed, and metallic segregated Zn species. In particular, after 1 h of static CO_2RR, the contribution of an oxide-like Zn(II) species was ca. 12 %, while the majority of Zn species (78 %) formed an fcc-like Cu-rich CuZn alloy. The remaining 10 % of Zn formed non-fcc metallic species (metallic Zn or Zn-rich CuZn alloys).

HE-XRD patterns (Figure 7.2 c) exhibit characteristic Cu_2O peaks at ocp, while these peaks almost disappeared starting from -0.2 to -1.0 V during the initial linear sweep voltammogram (LSV) and the subsequent static CO_2RR (Figure 7.4). At the same time, peaks corresponding to metallic Cu appeared. No characteristic Zn or CuZn-related peaks could be detected, which indicates the amorphous character of Zn and/or the small crystallite sizes of the alloy. The temporal evolution of the crystal structure during the pre-reduction was analyzed by fitting the characteristic peaks of $Cu_2O(111)$, $Cu_2O(200)$, Cu(111) (Figure A7.8-A7.9), and Cu(311) (Figure 7.5). This analysis confirms the almost complete reduction of the crystalline (bulk-like) Cu_2O phase after t = 150 s (Figure A7.8) and the evolution of a metallic Cu phase (Figure 7.5). It should be highlighted here that the apparent disagreement between the reduction of Cu_2O to

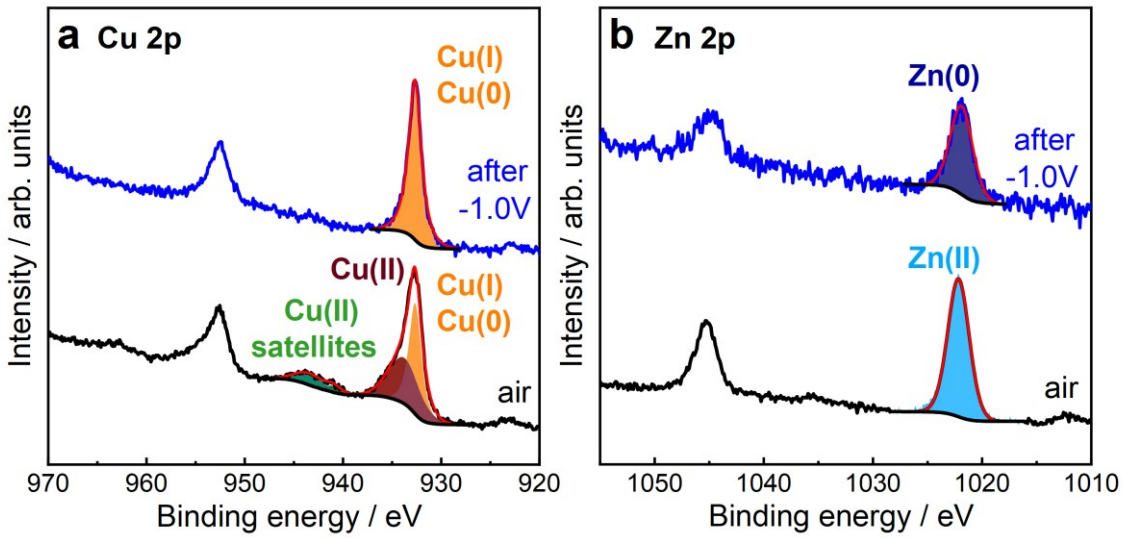

Figure 7.6 Quasi-*in situ* core level regions of the Cu-Zn catalyst in the as-prepared state (corresponds to the state in air) and after 1 h of static CO_2RR at -1.0 V (without air exposure). (a) Cu 2p region and (b) Zn 2p region with corresponding fits (red line). The Cu 2p core level region of the as-prepared sample shows the presence of Cu(0)/Cu(I) and a shake-up satellite corresponding to Cu(II).

Cu from XAS and XRD (where the latter shows a nearly complete reduction after a few minutes, while the former shows the presence of oxides even after 1 h of CO_2RR) is attributed to the different sensitivities of these methods. In particular, XRD tracks well-ordered crystalline regions of the sample, while XAS is sensitive to both ordered and disordered structures. The slower reduction observed by XAS is thus a consequence of the disordered structure of the remaining oxide species.

While XAS and XRD are both bulk-sensitive techniques, the more surface-sensitive Cu LMM spectrum in the as-prepared state (Figure 7.2 d) shows a mix of Cu(I) and Cu(II) species, which overlap with the Zn(II) Auger peaks. After 1 h at -1.0 V, the Cu surface oxide was fully reduced to metallic Cu. The Zn LMM spectra (Figure 7.2 e) present only the contribution of Zn(II) in the as-prepared state, while Zn(II) partially reduced after static CO_2RR to metallic Zn on the surface. One can also extract the Cu:Zn surface composition ratio from the Cu and Zn 2p core level regions (Figure 7.6), which gives a lower Cu:Zn ratio of 85:15 at% since ZnO was partially covering the Cu_2O NCs. After static CO_2RR, the amount of Cu on the surface increased mainly due to the mixing of Cu with Zn species on the catalyst surface (Table A7.4) since the amount of Zn found in the electrolyte after the reaction corresponds to only 1 % of the total amount of Zn that is present in the catalyst (ICP-MS measurements in Table 7.3).

Table 7.3 Cu and Zn mass and composition of Cu-Zn catalyst in the electrolyte by ICP-MS measurements after 1 h of different reaction conditions.

Sample	m_{Cu} [µg]	Cu [at%]	m_{Zn} [µg]	Zn [at%]
Static at -1.0 V	0.62(8)	0.44(5)	0.13(2)	1.4(3)
Pulsed to -0.4 V	0.355(2)	0.253(2)	0.51(1)	5.5(5)
Pulsed to -0.25 V	0.683(3)	0.488(3)	1.044(1)	1.044(1)
Pulsed to 0 V	0.3158(9)	0.2256(7)	0.994(6)	10.75(7)
Pulsed to 0.3 V	0.997(4)	0.712(3)	2.239(5)	24.20(5)
Pulsed to 0.6 V	1.457(1)	1.0407(9)	1.914(6)	20.70(6)

Moreover, the surface-sensitive SERS spectra of the Cu-Zn catalyst (Figure 7.2 f, 7.7) confirm the oxidized state of Cu at ocp with the characteristic Cu_2O peaks at 406, 521, 617 cm^{-1},[32] while no ZnO related bands at 430 and 560 cm^{-1} could be observed, probably due to the overlap with the Cu_2O peaks.[228] During CO_2RR, no Cu or Zn-related oxide peaks could be detected, which indicates the complete reduction of the metals on the surface. Additionally, SERS gives information about the adsorbate structure, namely the Cu-CO vibrations at 280 cm^{-1} (rotation) and 360 cm^{-1} (stretching)[32, 213] as well as the C-O vibrations at ~2100 cm^{-1}.[30] However, XPS indicates some remaining Zn(II) species. Overall, the pre-reduced Cu-Zn sample consists of metallic Cu and CuZn/Zn/Zn(II) islands and particles on the surface with some small contribution of Cu(I) in the bulk. This pre-reduced structure was used in the following as the starting point for the dynamic pulsed CO_2RR measurements.

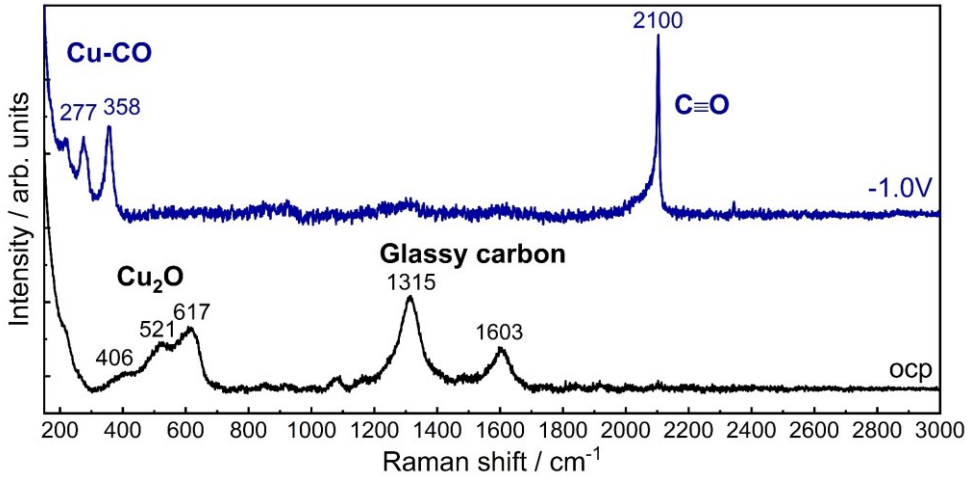

Figure 7.7 *Operando* SERS spectra of the Cu-Zn catalyst at ocp and during static CO_2RR. The peaks at 1005 and 1072 cm^{-1} can be assigned to the vibrations of HCO_3^- and CO_3^{2-} in aqueous solution, respectively, and the peaks at 1313 and 1600 cm^{-1} correspond to the glassy carbon support.[207, 233] No peaks were detected in the C-H vibration region from 2700 to 3000 cm^{-1}.

7.3.3 Selectivity during Static and Pulsed CO_2RR

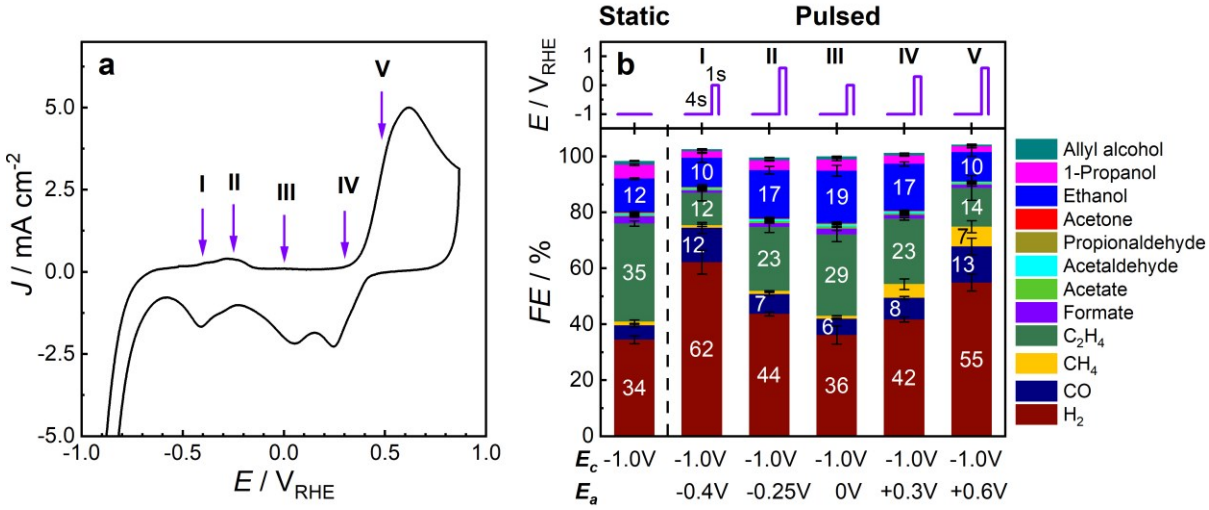

Figure 7.8 Choice of anodic potentials by cyclic voltammogram and selectivities of pulsed CO_2RR. (a) CV of Cu-Zn (50 mV s^{-1}) after 1 h of reduction at -1.0 V in CO_2-saturated 0.1 M $KHCO_3$ with marked regions. (b) Pulse profile of one pulse sequence (top) and Faradaic efficiencies (bottom) of Cu-Zn under potentiostatic conditions (-1.0 V) and under pulsed electrolysis conditions with a fixed E_c value at -1.0 V and different E_a values with t_c = 4 s and t_a = 1 s during 1 h of reaction.

To establish the relevant anodic potential values for optimal pulsed CO_2RR conditions, Figure 7.8 a presents the CV of the pre-reduced Cu-Zn catalyst in 0.1 M $KHCO_3$ electrolyte. In the CV, two distinct peaks at -0.25 and 0.6 V appeared, corresponding to the oxidation of Zn and Cu species, respectively.

To investigate the role of the Cu and Zn oxidation state on the catalyst functionality during the pulsed CO_2RR experiments, the values of the upper ("anodic") potential were selected below, on, and in between these peaks as indicated in Figure 7.8 a with arrows. Note that the term "anodic potential" means here a more positive potential value than the cathodic potential and

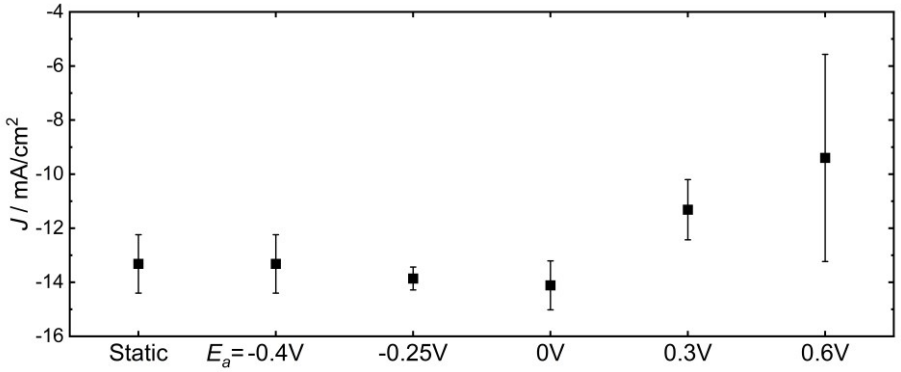

Figure 7.9 Averaged current densities J of the Cu-Zn catalyst under potentiostatic conditions (-1.0 V) and under pulsed electrolysis conditions with a fixed E_c value at -1.0 V and different E_a values and t_c = 4 s and t_a = 1 s during 1 h of the reaction.

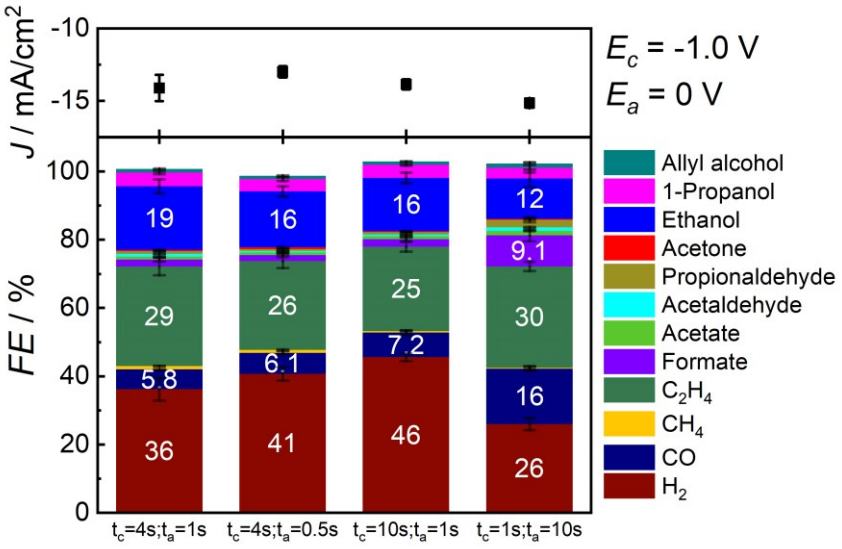

Figure 7.10 Averaged current densities (top) and Faradaic efficiencies (bottom) of the Cu-Zn catalyst under pulsed electrolysis conditions with a fixed cathodic potential E_c and anodic potential E_a values at -1.0 V and 0 V, respectively, and varied cathodic and anodic time lengths t_c and t_a during 1 h of reaction.

does not have to be a positive potential value. The cathodic potential in all cases was fixed at E_c = -1.0 V. Figure 7.8 b presents the averaged Faradaic efficiencies (FEs) during static CO_2RR at -1.0 V for 1 h as well as under pulsed CO_2RR for 1 h with a cathodic potential E_c = -1.0 V and a different anodic potential E_a from -0.4 V to 0.6 V. The corresponding averaged current densities can be found in Figure 7.9, and a current profile during pulsed CO_2RR with E_a = 0 V in Figure A7.10. The duration of the cathodic and anodic pulses was chosen based on my previous co-authored work of pulsed CO_2RR with bare Cu_2O NCs[97] and on the selectivity test measurements of the Cu-Zn catalyst that were performed with different pulse durations at E_c = -1.0 V and E_a = 0 V (Figure 7.10). This gives evidence that the combination of 1 s anodic with 4 s of cathodic pulse duration is the most promising for achieving high selectivities for multicarbon products.

The selectivities under static CO_2RR conditions (Figure 7.8 b) were similar to those for the bare Cu_2O NCs (Figure 7.11) with FE_{EtOH} = 12 %, but there is an increase of the FEs of the HER and CO, while the ethylene production decreases. Thus, we cannot observe a strong beneficial CO spillover effect from the Zn to the Cu sites under static CO_2RR. However, it is possible to tune the C_{2+} selectivity values by pulsing the potential to different E_a values, as seen in the E_a-dependent FE_{EtOH}. The best FE for ethanol production (FE_{EtOH} = 19 %) and C_{2+} products (FE_{C2+} = 56 %) is obtained at E_a = 0 V during 1 h of pulsed CO_2RR. There, the time-dependent evolution of the gaseous products (Figure 7.12) indicates an activation time of the system for the C_{2+} product formation of ~30 min after pulsed CO_2RR was started. Interestingly, the HER production increased significantly at lower and higher E_a values, making hydrogen the main

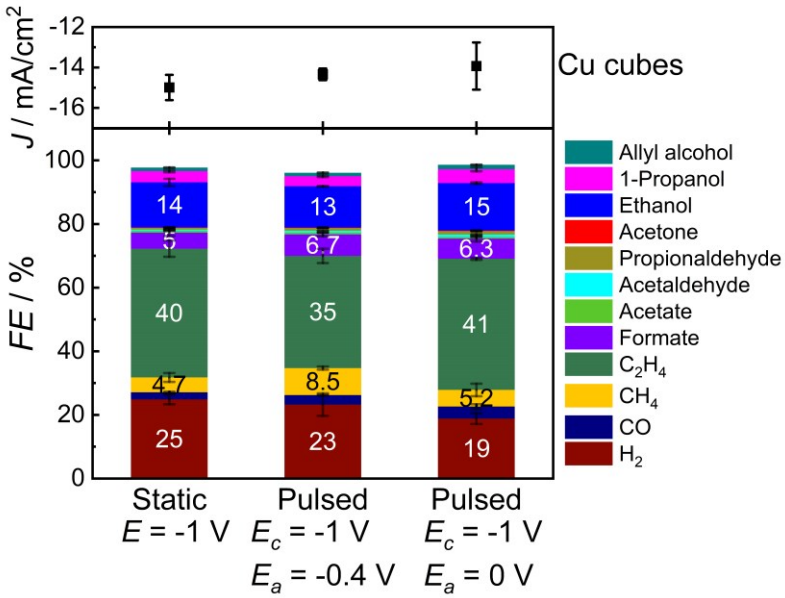

Figure 7.11 Averaged current densities (top) and Faradaic efficiencies (bottom) of Cu cubes as reference catalyst under static CO_2RR at -1.0 V and under pulsed electrolysis conditions with E_c = -1.0 V, E_a = 0 V, t_c = 4 s and t_a = 1 s during 1 h of reaction.

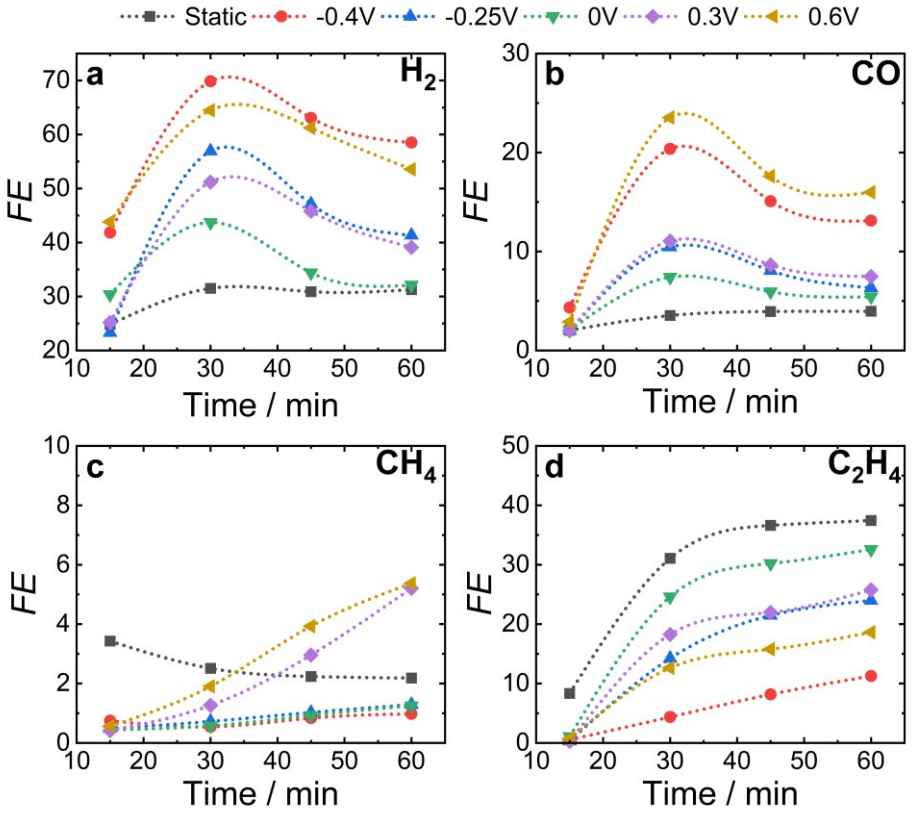

Figure 7.12 Evolution of the selectivities of the gaseous products during pulsed CO_2RR with E_c = -1.0 V, E_a = 0 V, t_c = 4 s, and t_a = 1 s for 1 h of the pre-reduced Cu-Zn catalyst. (a) shows the Faradaic efficiency of hydrogen, (b) carbon monoxide, (c) methane, and (d) ethylene.

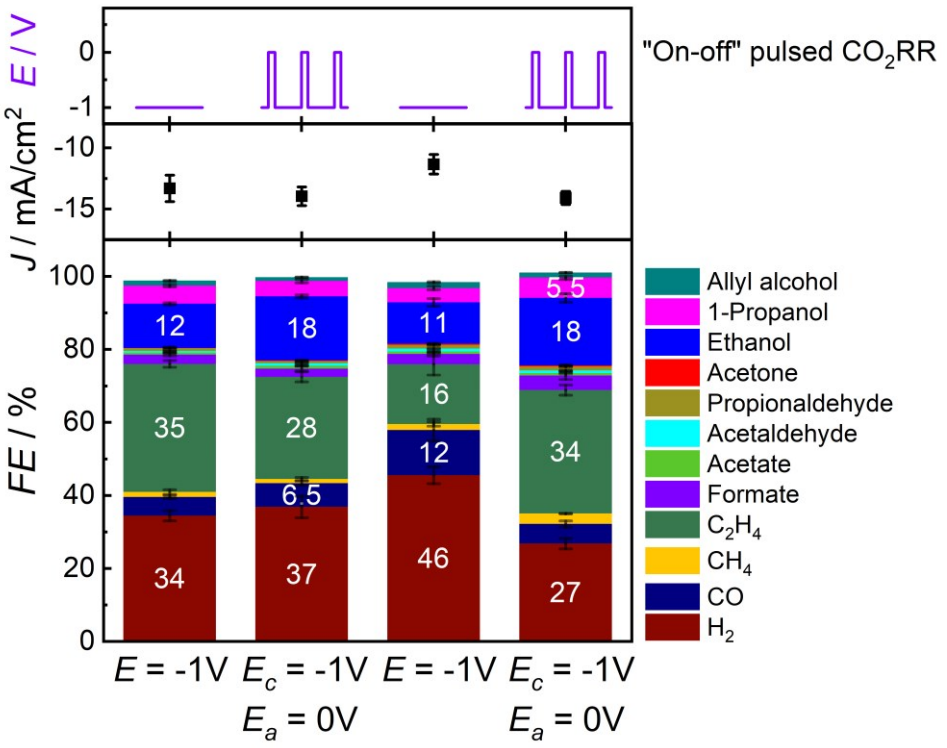

Figure 7.13 Schematic potential sequences (top), averaged current densities (middle), and Faradaic efficiencies (bottom) of the Cu-Zn catalyst under sequentially changing static CO_2RR at -1.0 V for 1 h each time and pulsed CO_2RR with E_c = -1.0 V, E_a = 0 V, t_c = 4 s and t_a = 1 s for 2 h each time.

product at E_a = -0.4 V and 0.6 V. This is in contrast to the behavior of bare Cu cubes, which showed a significant increase in the ethanol selectivity at E_a = 0.6 V.[97] Thus, the Cu-Zn catalyst can boost the ethanol selectivity at lower E_a values (optimal E_a = 0 V) compared to the bare Cu_2O NCs (optimal E_a = 0.6 V)[97], which has the advantage of a lower Cu dissolution (as shown by ICP-MS in Table 7.3) and Cu rearrangement (as shown by STEM in Figure 7.1 k) and leads to a stable current density and catalytic performance.

To distinguish if the changes in the catalyst selectivity are mainly attributed to dynamic transformations in the catalyst structure and composition during pulsed CO_2RR or if they originate from concomitant irreversible changes in the catalyst structure and morphology, static conditions at -1.0 V were applied for another hour, and then set under pulsed conditions for 2 h at E_a = 0 V again. The reaction time was set to 2 h of pulsed CO_2RR to ensure a stabilized selectivity evolution due to the activation time of the catalyst. Figure 7.13 shows that the FEs of HER and CO increased noticeably under reapplied potentiostatic conditions in comparison to those for the catalyst before the pulses. At the same time, the ethylene production under reapplied static CO_2RR was cut by half with respect to the FE of the fresh catalyst. Changes in the FEs were paralleled by a decrease in current density. The FEs of the liquid products remained stable in comparison to the first static CO_2RR measurement. Thus, the suppressed C_2

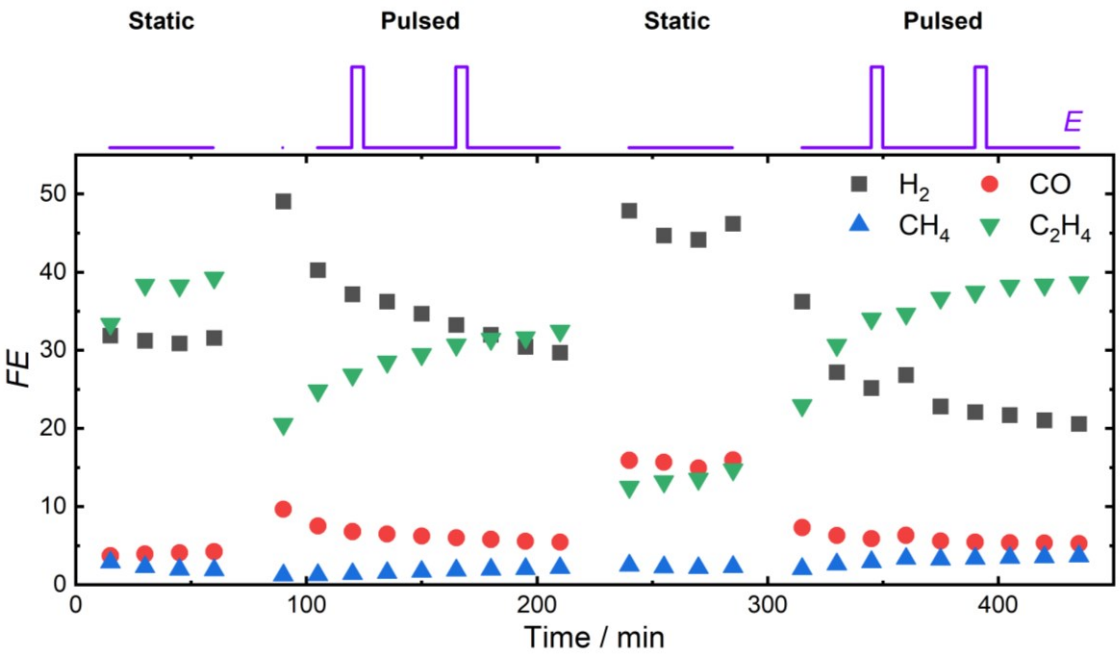

Figure 7.14 Evolution of the selectivities of the gaseous products during static CO_2RR for 1 h and pulsed CO_2RR with E_c = -1.0 V, E_a = 0 V, t_c = 4 s, and t_a = 1 s for 2 h of the Cu-Zn catalyst. The gaseous products here are hydrogen, carbon monoxide, methane, and ethylene. Potential pulses are only shown schematically.

product formation was induced by irreversible changes associated with the pulse treatment, which can be attributed, in part, to the changes in the Cu/Zn interface arrangement since there were no major structural changes visible in the *ex situ* TEM-EDX image in Figure 7.1 k and Figure A7.3 g. Nevertheless, when performing pulsed CO_2RR for the second time, the HER and CO production was suppressed again, while the ethylene production and current density value were restored. In fact, they even improved compared to the values observed during the first pulse sequence. Also, here the FEs of the liquid products remained stable in comparison to the first pulsed CO_2RR measurements and are significantly higher than under static CO_2RR. Interestingly, the time-dependent evolution of the gaseous products (Figure 7.14) indicates again an activation time for the C_{2+} product formation of ~30 min after each (re-)started pulsed CO_2RR experiment. Thus, the increase of the C_{2+} product formation, the suppression of the HER and CO selectivity, and the increase in current density under pulsed CO_2RR for the Cu-Zn catalyst in the regime investigated stemmed mostly from the dynamic and reversible changes induced by the pulsed reaction conditions.

In order to reveal the role of Zn for the selectivity improvements during pulsed CO_2RR, Figure 7.11 presents the selectivities of bare pre-reduced Cu_2O NCs under pulsed CO_2RR at E_a = 0 V, which are similar to the selectivity during static conditions of Cu_2O NCs. Furthermore, the

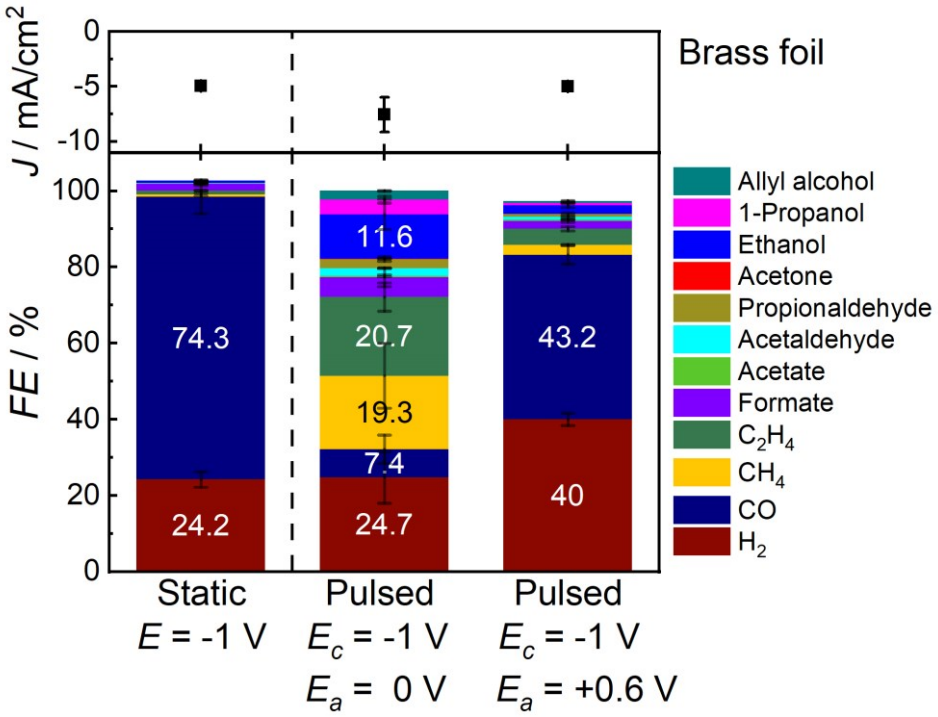

Figure 7.15 Averaged current densities (top) and Faradaic efficiencies (bottom) of a CuZn bulk brass foil as reference catalyst under static CO_2RR at -1.0 V and under pulsed CO_2RR with E_c = -1.0 V and E_a = 0 V or 0.6 V, and t_c = 4 s and t_a = 1 s during 1 h of reaction.

selectivities of a commercial brass foil (Figure 7.15) qualitatively resemble the behavior of the Cu-Zn catalyst during pulsed CO_2RR conditions, where the selectivity toward C_{2+} products improved at E_a = 0 V and diminished at E_a = 0.6 V. Thus, the Zn and Cu interplay, as well as their redox transitions, play a key role in the selectivity changes during pulsed CO_2RR of the Cu-Zn catalyst and demand *operando* methods for their further investigation and understanding.

7.3.4 Structural Evolution during Cyclic Voltammetry

To reveal the evolution of the structure, composition, redox state, and adsorbate structure of the pre-reduced Cu-Zn catalyst, time-resolved *operando* methods (with a time resolution of 100-1000 ms per spectrum or image) were employed during a CV scan starting from -1.0 V up to 0.7/0.9 V (Figure 7.16) and back to -1.0 V (Figure 7.17). Changes in the catalyst structure were evidenced by the corresponding spectra and diffractograms of XAS, XRD, and SERS. In particular, the white line of the Zn K-edge XANES spectra (Figure 7.16 a) significantly increased starting from at E > -0.4 V, while the white line of the Cu K-edge XANES spectra (Figure 7.16 b) only slightly increased at E > 0.4 V during the anodic scan attributed to the partial oxidation of Zn and Cu. This is in line with the subtracted XRD pattern (subtracted with the XRD pattern during static CO_2RR at -1.0 V), which shows the formation of the $Cu_2O(111)$

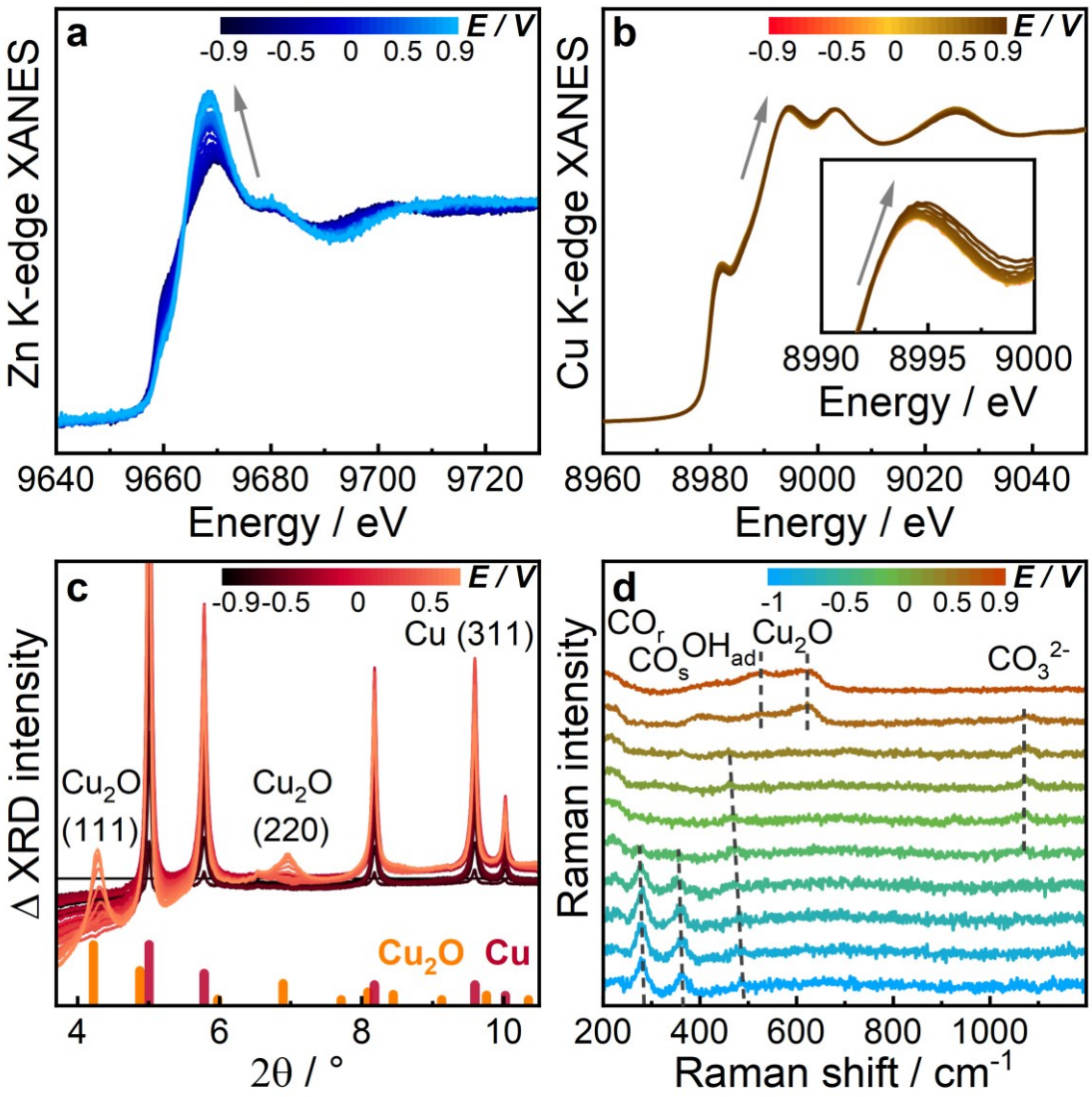

Figure 7.16 Structural changes during a cyclic voltammogram by *operando* measurements. (a,b) Normalized averaged XANES data of Zn and Cu K-edge, respectively, during the anodic scan from -0.9 to 0.9 V of the CV. (c) Averaged Δ HE-XRD patterns (subtracted with the XRD pattern during static CO_2RR at -1.0 V before CV) during the anodic scan from -0.9 to 0.7 V. (d) Averaged SERS spectra during the anodic scan from -1.0 to 0.9 V. The Cu-Zn sample was pre-reduced for 1 h at -1.0 V under CO_2RR conditions before the CV.

peak only starting from $E > 0.4$ V, while the peaks related to metallic Cu, such as Cu(311), even increased in intensity until E ~0.4 V before they started to decrease. SERS spectra show the characteristic Cu-CO rotation (CO_r) and stretching (CO_s) vibrations (~280 and 360 cm^{-1})[32, 213] and OH_{ad} vibrations (450-490 cm^{-1})[31, 210, 234] on Cu, which redshifted at higher potential due to the Stark effect (which depends on the electric field),[31, 88] until they disappeared at -0.4 V. Then, a band corresponding to carbonate formed at 1080 cm^{-1} until 0.6 V, followed by the formation of Cu(I) and Cu(II) oxides from 0.6 V to 0.9 V. To further correlate this data, the characteristic parameters need to be analyzed and compared with each other.

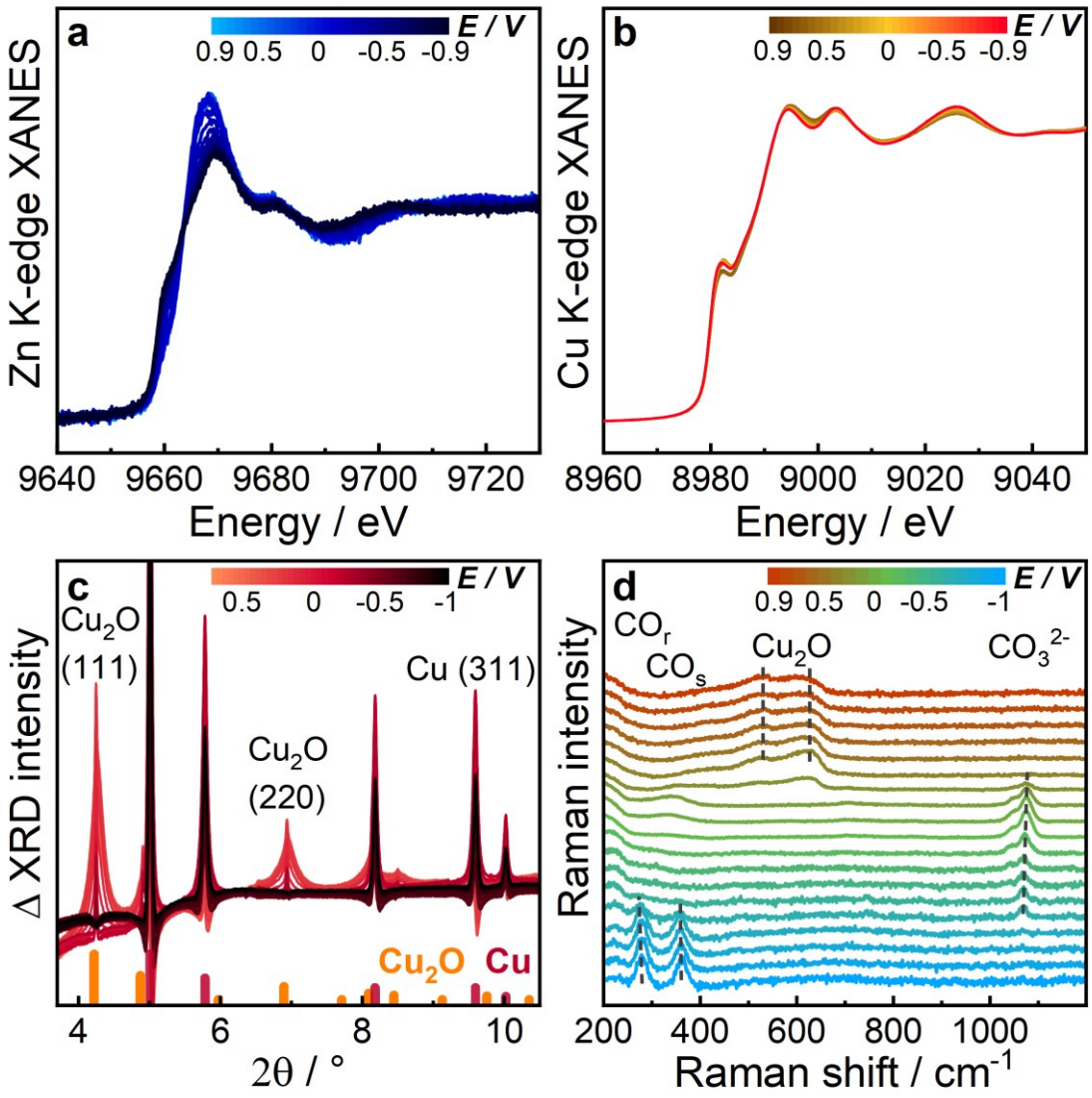

Figure 7.17 Averaged spectra and diffractograms during the cathodic scan of a CV voltammogram. (a,b) XANES spectra of Zn K-edge and Cu K-edge, respectively, from 0.9 to -0.9 V. (c) HE-XRD patterns from -0.7 to -1.0 V. (d) SERS data from 0.9 to -1.0 V.

Figure 7.18 displays selected characteristic parameters, namely the variations of the concentrations of the different Zn and Cu species from LCA-XANES of the Zn and Cu K-edge (with Cu(0) in Figure A7.11), the evolution of the weight fraction of crystalline Cu_2O and the size of the crystalline Cu and Cu_2O domains (L) from the Rietveld analysis (Fits of Cu(311) in Figure 7.19 and Rietveld parameters in Figure A7.12), as well as the variations of the characteristic Raman bands of surface Cu_2O and $Cu(OH)_2$ species and of the Cu-CO stretching and carbonate bands extracted from the peak intensities of the SERS spectra. The different potential regions are described in the following.

-1.0 to -0.4 V: This is the CO_2RR region, where the bulk composition consists of CuZn, Zn(0), Cu(0), and Cu(I) species (LCA-XANES). Additionally, SERS indicates a metallic surface (no

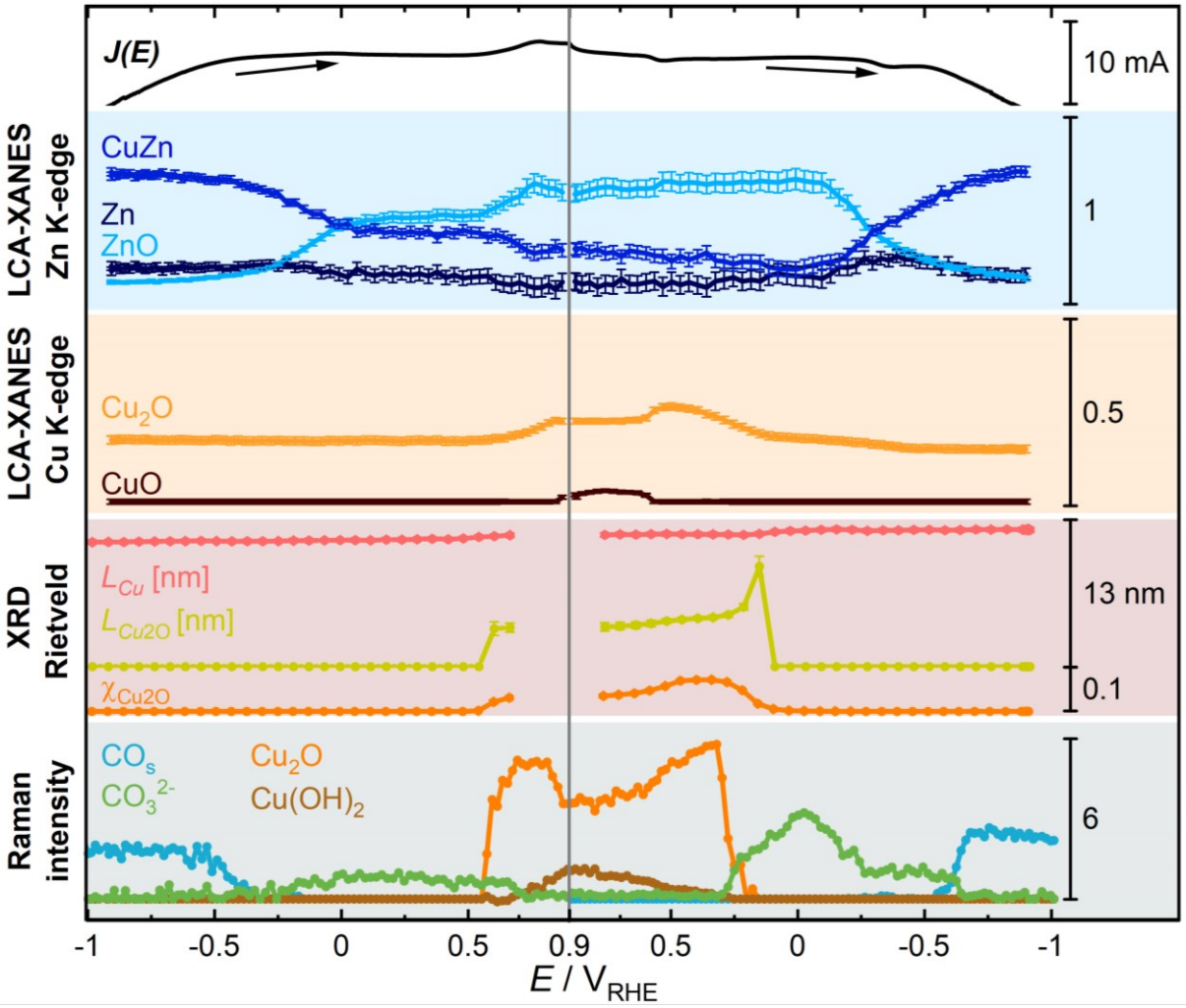

Figure 7.18 Changes of the oxidation state and adsorbates during a CV extracted from *operando* XAS, HE-XRD, and SERS measurements. Potential-dependencies of the concentrations of CuZn, Zn, ZnO (Zn K-edge), Cu_2O, and CuO (Cu K-edge) from the LCA-XANES analysis of Zn K-edge and Cu K-edge XANES spectra (top), potential-dependencies of the weight of crystallite Cu_2O and crystalline sizes of Cu/Cu_2O obtained by Rietveld analysis of the HE-XRD patterns, and potential-dependencies of adsorbates as CO_s and CO_3^{2-} and Cu_2O and $Cu(OH)_2$ species obtained by fitting the normalized intensities (arb. units.) of the bands from the SERS spectra.

oxide bands could be detected). The crystallite size of the Cu domains is around 11 nm (XRD), and CO is adsorbed on Cu (SERS), which correlates with the product formation. At -0.5 V, CO starts to desorb from the surface.

-0.4 to 0 V: At -0.3 V, CO is completely desorbed from Cu, followed by the formation of a carbonate band on/close to Cu (SERS). At -0.25 V, which corresponds to region II in Figure 7.8 a, CuZn is partially oxidized to Zn(II), while the fraction of Cu(0) is unchanged (LCA-XANES). Note that the concentration of Zn(0) remains relatively stable over the whole CV, and the changes appear mainly between the concentrations of the CuZn alloy and Zn(II) species. Moreover, the size of the metallic Cu crystallites and the area of the Cu(311) peak (XRD,

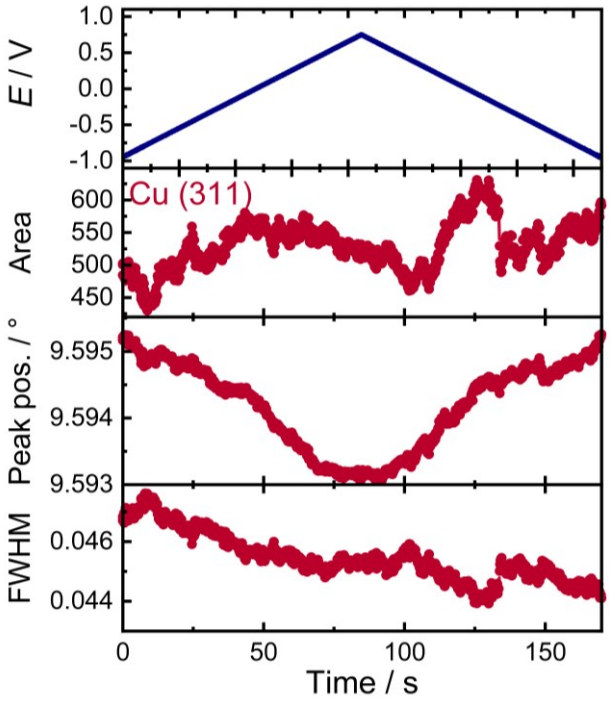

Figure 7.19 Fits of HE-XRD patterns of Cu(311) of the Cu-Zn catalyst during CV from -1.0 V → 0.7 V → -1.0 V. Area (second column), peak position (third column) and FWHM (fourth column) extracted from fits of Cu(311) in respect to the applied potential (top).

Figure 7.19) slightly increases around 0 V (corresponding to region III in Figure 7.8 a), together with an increase of the carbonate band (SERS).

0 to 0.9 V: At 0.6 V (corresponding to region V in Figure 7.8 a), surface Cu_2O starts to form (SERS), and crystalline Cu_2O evolves (XRD), with a crystallite size of 4 nm. At the same potential, another oxidation step of CuZn to Zn(II) appears (Zn LCA-XANES), while bulk Cu(I) forms at 0.7 V (Cu LCA-XANES). The late oxidation of Zn in the second step could stem from the high stability of the CuZn alloy. Moreover, surface $Cu(OH)_2$ evolves at 0.7 V (SERS), while bulk Cu(II) species start to form at 0.9 V. Please note that for XRD, the potential was already reversed at 0.7 V, while for XAS and SERS it was reversed at 0.9 V.

0.9 to -1.0 V: The cathodic scan of the CV shows an almost reversible transformation of the main structural characteristics as well as the adsorption behavior. However, the potentials of the transformations in the cathodic scan are shifted to lower potentials compared to the anodic scan so that Cu(II) is first reduced to Cu(I) at 0.5 V and then reduced to Cu(0) at 0.4/0.3 V (LCA-XANES, XRD, and SERS). The concentration of Zn(II) slightly increases further until -0.2 V and then decreases due to the reduction of Zn(II) to CuZn and Zn(0) (Zn LCA-XANES). The reduction of Zn happens in only one step in contrast to its oxidation with two steps. At 0 V, the carbonate feature appears much more intense again (SERS). The CO_2RR starts again at -0.6 V with the adsorption of CO on Cu. In the final state, the concentration of

Zn(II) adds up 5 % more to the total concentration of Zn species than in the initial state (Zn LCA-XANES), and the crystalline size of metallic Cu increased to 12 nm compared to the initial size of 11 nm (XRD).

7.3.5 Structural Evolution during Pulsed CO_2RR

To follow the periodic and reversible changes in the catalyst and adsorbate structure during pulsed CO_2RR, time-resolved *operando* XAS, XRD, and SERS data were collected. The XAS (Figure 7.20, Figure A7.13), XRD (Figure 7.21, Figure A7.14), and SERS (Figure 7.22, Figure A7.15) data clearly show the evolution of the catalyst structure, chemical state, and adsorbates behavior during individual potential pulses. Here, for better visibility, the results obtained under pulsed CO_2RR with t_c = 4 s, t_a = 1 s, are compared with those collected under pulsed CO_2RR with $t_c = t_a$ = 10 s. Additionally, the focus lies here on the application of E_a values equal to 0 V (ethanol regime) and 0.6 V (C_1 regime), which show different selectivity trends and correspond to different redox transitions of Zn and Cu, as described earlier (Figure 7.8 b).

The following pages present the figures of time-resolved *operando* XAS (Figure 7.20), XRD (Figure 7.21), and SERS (Figure 7.22) data with $t_c = t_a$ = 10 s for both E_a values. The temporal evolution of this data highlights the periodic response of the structure, composition, and adsorbates of the Cu-Zn catalyst under pulsed CO_2RR conditions.

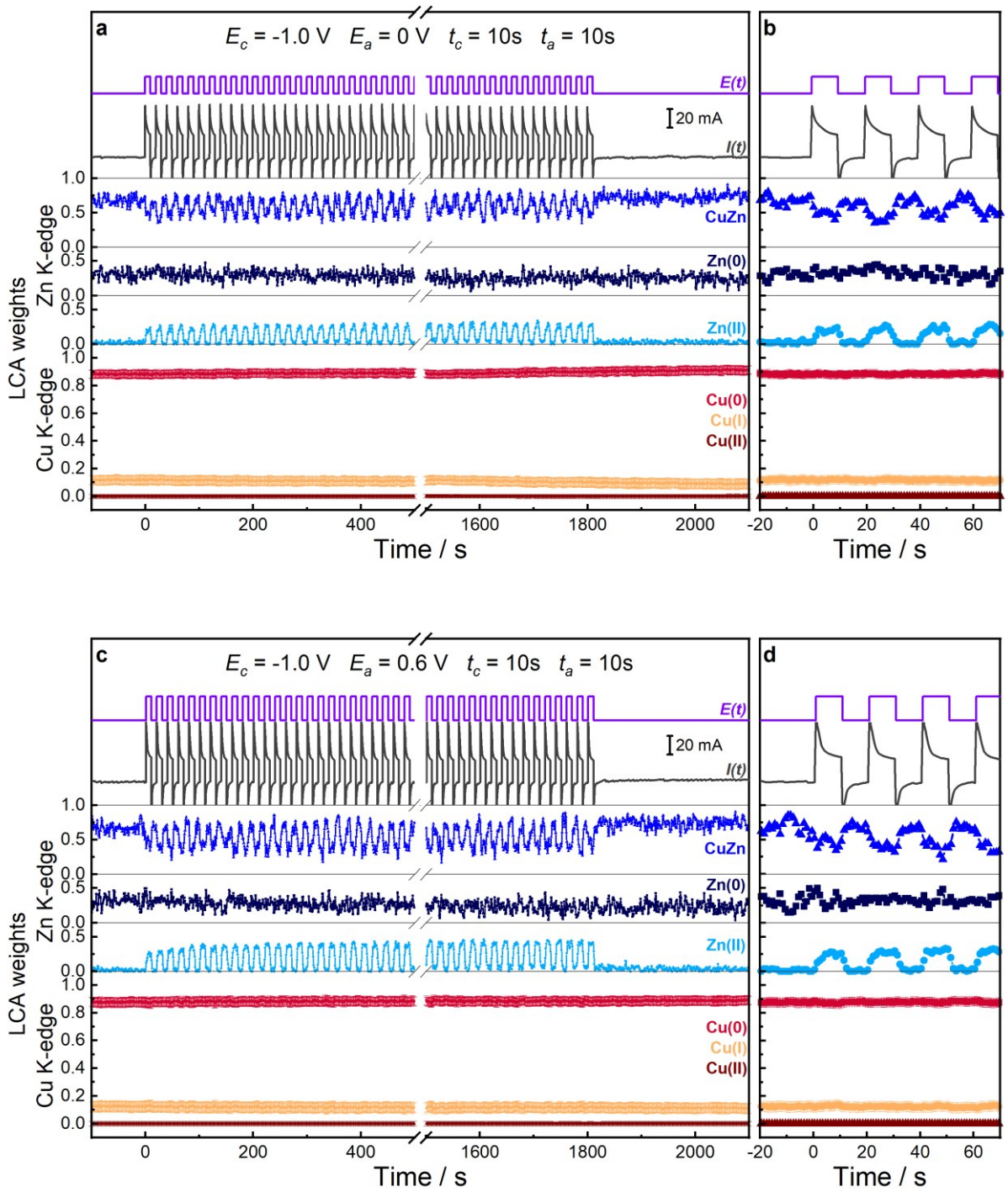

Figure 7.20 LCA-XANES analysis results of Zn and Cu K-edge of pre-reduced Cu-Zn catalyst during pulsed CO_2RR with $t_c = t_a = 10$ s. E_c is constant at -1.0 V, while $E_a = 0$ V in (a,b) and 0.6 V in (c,d). (b,d) show an extract of the full-time pulsed CO_2RR for better visibility.

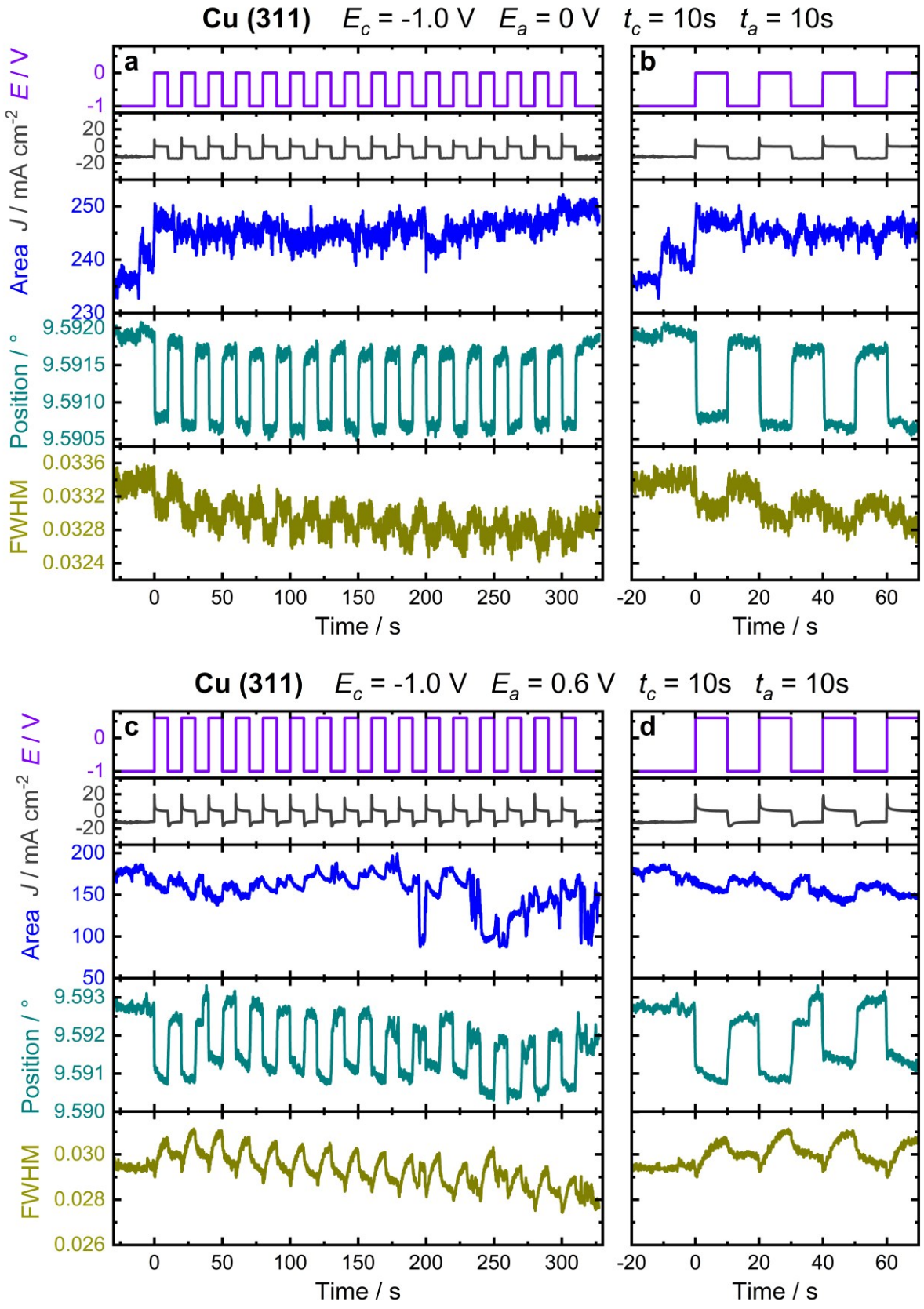

Figure 7.21 Temporal evolution of the area, peak position, and FWHM extracted from the fits of Cu(311) of HE-XRD patterns with respect to the applied potential and current density (top) during pulsed CO_2RR with $t_c = t_a = 10$ s. E_c is constant at -1.0 V, while $E_a = 0$ V in (a,b) and 0.6 V in (c,d). (b,d) show an extract of the full-time pulsed CO_2RR for better visibility.

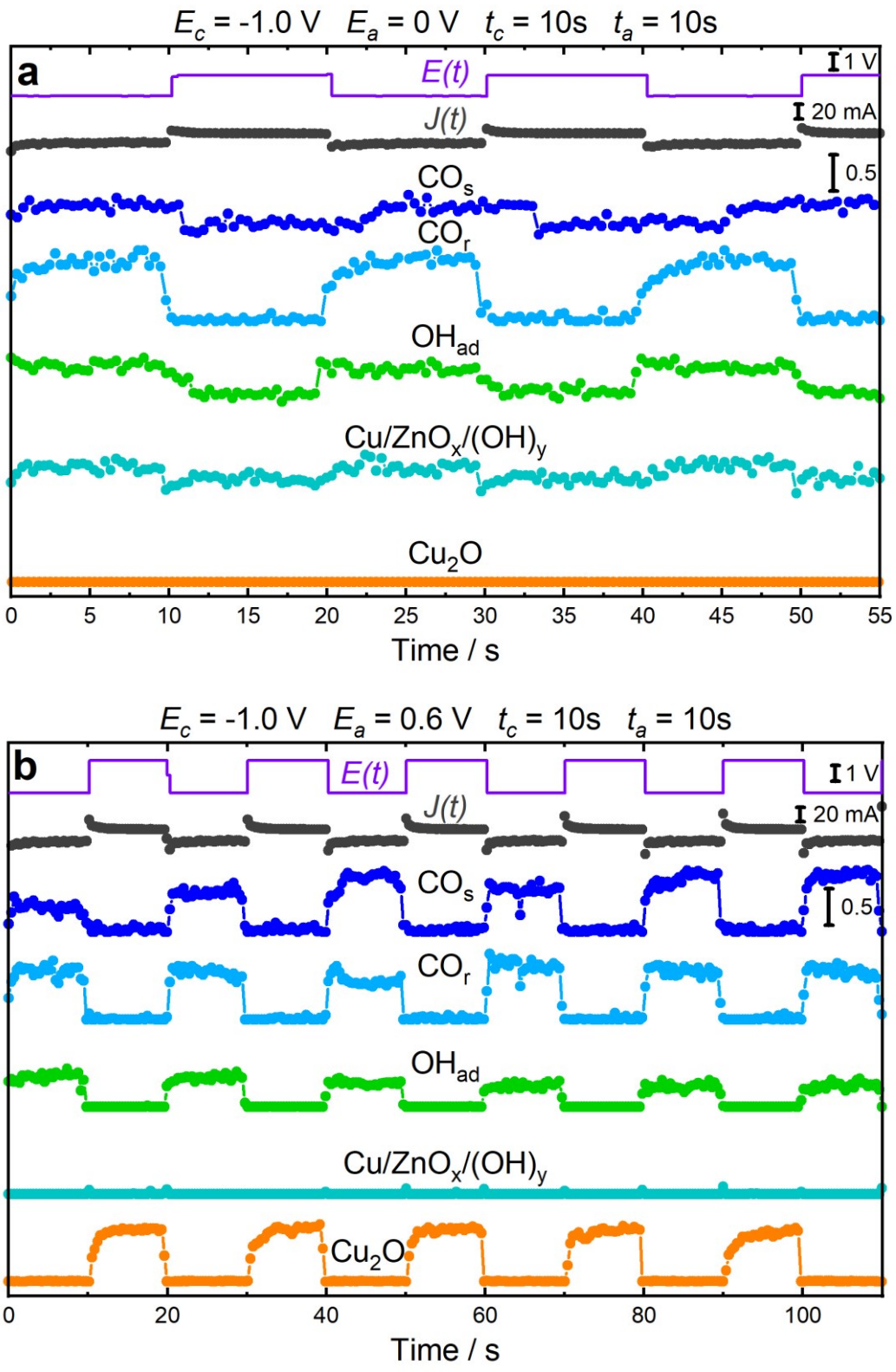

Figure 7.22 Temporal evolution of the chemical state and adsorbate coverage as Cu-CO stretching (CO_s, 360 cm^{-1}) and rotation (CO_r, 280 cm^{-1}) vibrations, OH_{ad} vibration on Cu (490 cm^{-1}), Cu/ZnO_x/$(OH)_y$ species (370 cm^{-1}) and Cu_2O species (405, 530, 610 cm^{-1}) obtained by fitting the intensities of the bands from the SERS spectra in respect to the applied potential and current density (top) during pulsed CO_2RR with $t_c = t_a$ = 10 s. E_c is constant at -1.0 V, while E_a = 0 V in (a,b) and 0.6 V in (c,d). (b,d) show an extract of the full-time pulsed CO_2RR for better visibility.

Figure 7.23 represents the results of the quantitative analysis of the spectra, which are averaged over the same time moments after the onset of each potential pulse under pulsed CO_2RR with $t_c = t_a = 10$ s. The results of the LCA-XANES analysis of the Cu K-edge and of the ML-based analysis of the Zn K-edge EXAFS data are shown in Figure 7.23 a and 7.24 (complementary LCA-XANES analysis of Zn K-edge shown in Figure A7.17). The ML-EXAFS approach revealed distinct transformations of the Zn species during pulsed CO_2RR when going up to different E_a values (with corresponding RDF functions and absolute weights in Figure 7.24) together with an analogous decrease of the fcc CuZn alloy phase contribution, while the non-fcc Zn-rich phase is almost not contributing during the anodic pulse. Once the cathodic pulse was applied in the first case ($E_a = 0$ V), the contribution of oxidized Zn species decreased down to 10 %, while the contribution of the Zn-rich phase increased in the first second by 10 % and

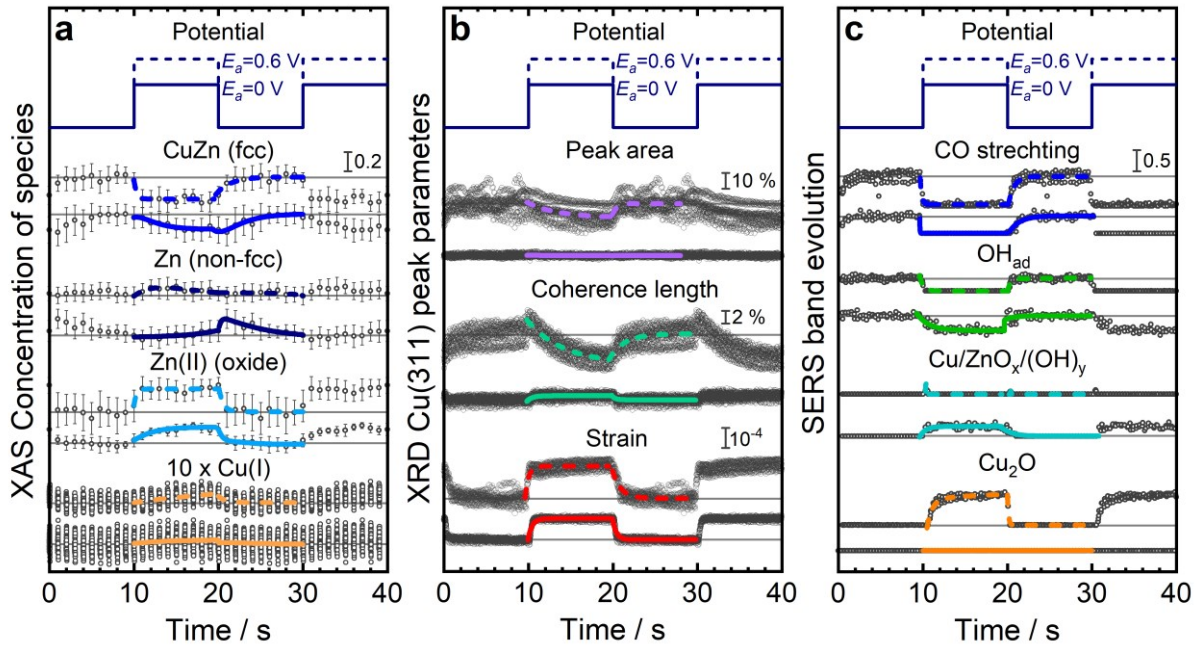

Figure 7.23 Averaged changes in the structure and adsorbates during a pulse sequence with E_c = -1.0 V and E_a = 0 V (bottom) or E_a = 0.6 V (top) for $t_c = t_a = 10$ s by *operando* measurements. (a) ML-EXAFS analysis results for the Zn K-edge show the concentrations of different Zn species, and LCA-XANES analysis results for Cu K-edge show variations in Cu(I) concentration. The concentration profile of Cu(I) is multiplied by 10 for better visibility. (b) HE-XRD Cu(311) Bragg peak parameters such as the relative changes in the Bragg peak area, the Cu coherence length, and the lattice strain. (c) Raman band evolution of adsorbed CO (stretching band at 360 cm^{-1}), OH_{ad} (adsorbed on Cu at 490 cm^{-1}), $Cu/ZnO_x/(OH)_y$ species (370 cm^{-1}), and Cu_2O species (average of 530 and 620 cm^{-1}) obtained by fitting the intensities of the bands from the SERS spectra. The colored lines are exponential fits, and the solid lines represent the anodic pulse to 0 V, and the dashed lines the anodic pulse to 0.6 V. The solid grey lines indicate the respective values for each parameter at the end of the cathodic pulse.

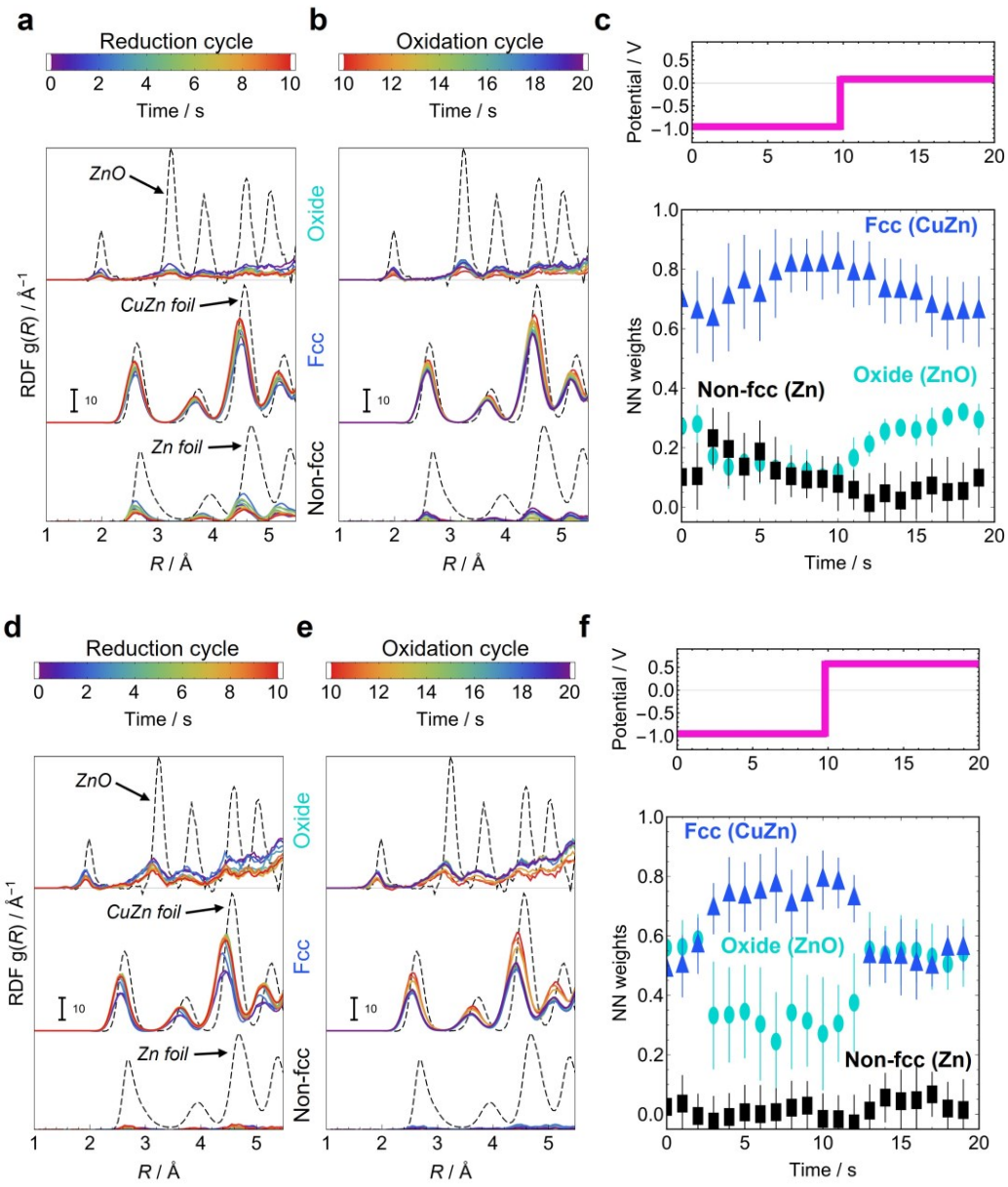

Figure 7.24 Averaged time-dependent evolution of the radial distribution functions *g(R)* and the concentrations obtained by the NN-EXAFS analysis from *operando* Zn K-edge EXAFS data during pulsed CO_2RR with $t_c = t_a = 10$ s. The partial RDFs correspond to an oxide phase, an fcc-type phase, and a non-fcc-type phase. (a,b) RDFs during the reduction and oxidation cycle, respectively, and (c) NN weights at E_c = -1.0 V and E_a = 0 V. (d,e) RDFs during the reduction and oxidation cycle, respectively, and (f) NN weights at E_c = -1.0 V and E_a = 0.6 V. For clarity the RDFs are shifted vertically.

then decreased again in favor of the CuZn alloy phase. In contrast, in the other case (E_a = 0.6 V), during the cathodic pulse, mainly the Zn oxide contribution decreased down to 30 % in favor of the CuZn alloy phase, while the Zn-rich phase was not involved here. Intriguingly, the changes of the LCA analysis of the Cu K-edge (Figure 7.23 a, Figure A7.17 a,c) in the chemical state of Cu to Cu(I) in the Cu-Zn catalyst are small, with ~1 % even during pulsed CO_2RR at 0.6 V. This corresponds to about one-third of the fraction of Cu(I) that was formed reversibly

and periodically for bare Cu_2O NCs at the similar conditions.[97] The lower Cu(I) concentration might result from the concurrent oxidation of CuZn to Zn(II) in the Cu-Zn catalyst, which was also observed in my recent co-authored work.[115] During the cathodic pulse, the Cu-related oxide species reduced again into metallic species.

Moreover, the main fraction of Zn oxide at E_a = 0 V and E_a = 0.6 V formed within the first five and two seconds, respectively, during the anodic pulse, while the reduction of Zn(II) occurred at a similar time scale. Thus, the oxidation of Zn(II)/CuZn and the reduction of CuZn/Zn(II) show a relative symmetric redox behavior. This is in contrast to the kinetics of the Cu(0) oxidation and Cu(I) reduction at E_a = 0.6 V in LCA-XANES, where the oxidation process is significantly slower than the reduction. In particular, for the Cu-Zn catalyst, the characteristic time constant of the Cu(I) reduction is around 0.5 s, which is in agreement with the observations for bare Cu_2O NCs.[97] For the characteristic time constant of the Cu(0) oxidation, only its lower limit could be estimated due to the small amounts of oxide formed within 10 s of the anodic pulse, which is around 10 s. Again, this value is in good agreement with the observations for bare Cu_2O NCs.[97] The asymmetry between the oxidation and reduction times can also be seen in the XRD and SERS data at E_a = 0.6 V. The peak area of the metallic Cu(311) Bragg peak decreased slowly during the anodic pulse and increased back fast with around 1 s during the cathodic pulse (Figure 7.23 b), while the XRD pattern also shows the evolution of the Cu_2O(111) peak at 4.2° during the anodic pulse (Figure 7.25 b). This also corresponds to the slow increase during the anodic pulse of the SERS peaks corresponding to surface Cu_2O (Figure 7.23 c), which was immediately removed again after 0.2 s of the cathodic pulse. As expected, during the pulses at E_a = 0 V (which is below the oxidation potential of Cu), no Cu(I) species formed, as indicated by the XAS, XRD, or SERS data.

Additionally, the Cu lattice strain, as probed by XRD (Figure 7.23 b), increased rapidly upon the anodic pulse and shrank rapidly back upon the cathodic pulse. The degree of this lattice expansion increased with a higher E_a value. This process is most likely linked to the charging of Cu and is independent of Cu oxidation.[97] Moreover, the coherence length of Cu increased slightly upon the anodic pulse at E_a = 0 V, which could reflect the oxidation of Zn from the CuZn alloy and the rearrangement of the Cu phase. At E_a = 0.6 V, the coherence length increased in the first second of the anodic pulse before it decreased due to the oxidation to Cu_2O. Upon the cathodic pulse, this process was reversed.

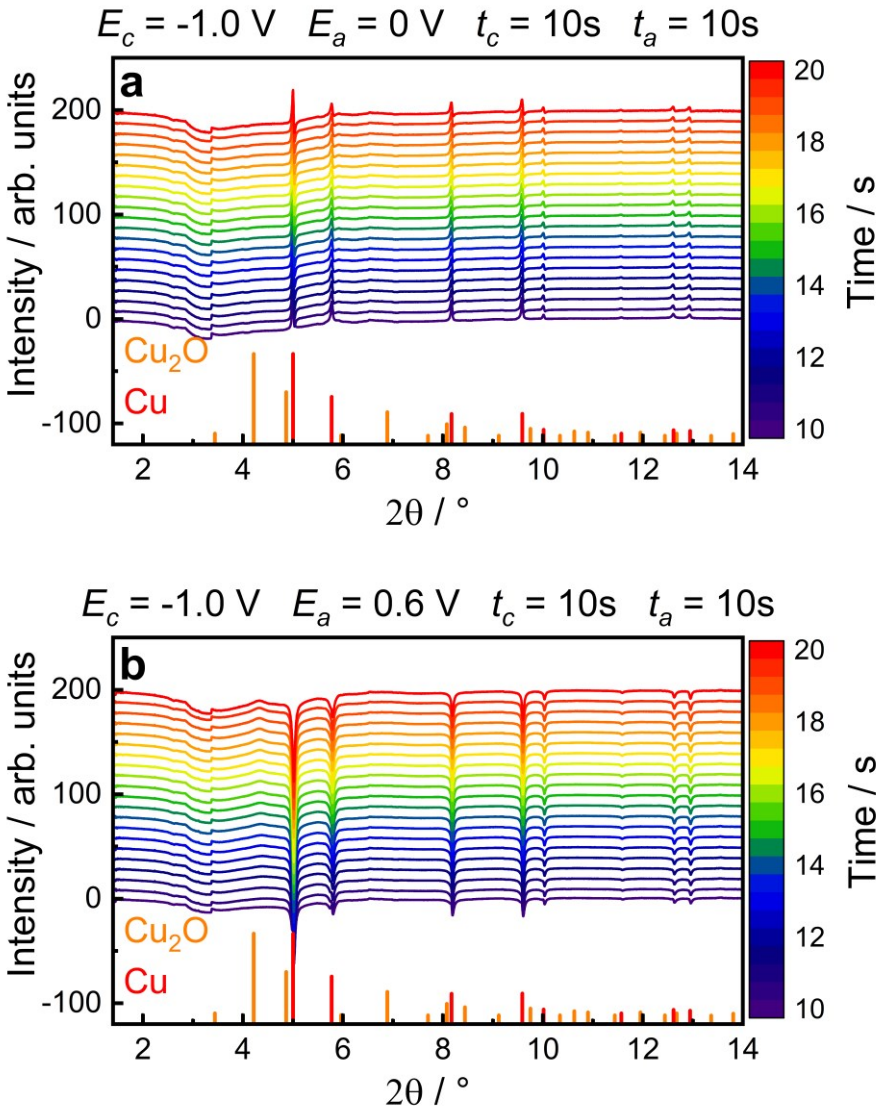

Figure 7.25 Evolution of the differential HE-XRD patterns of the pre-reduced Cu-Zn catalyst during the anodic pulse with t_c = t_a = 10 s and E_a = 0 V (a) and 0.6 V (b). The averaged diffraction patterns during the anodic pulse (t = 10-20 s) are subtracted from the averaged time-dependent diffraction pattern collected under pulsed CO_2RR conditions.

Catalytically, the evolution of the adsorbate structure during pulsed CO_2RR is of the highest importance for selective product formation and can be followed by SERS (Figure 7.23 c, 7.26, Figure A7.20-A7.21). In particular, the CO stretching band at 360 cm^{-1}, which was related in a previous study to the formation of C_{2+} products,[88] evolved upon the cathodic pulse (product formation) and was completely removed during the anodic pulse (no product formation). Additional information regarding the adsorbed CO could be obtained from the peaks corresponding to the C-O vibrations (Figure A7.21). Here, the contribution of low-frequency CO at 2060 cm^{-1} increased in intensity compared to the high-frequency CO band at 2090 cm^{-1} at E_a = 0 V (compared to E_a = 0.6 V), which was related to C-C coupling and C_{2+} product

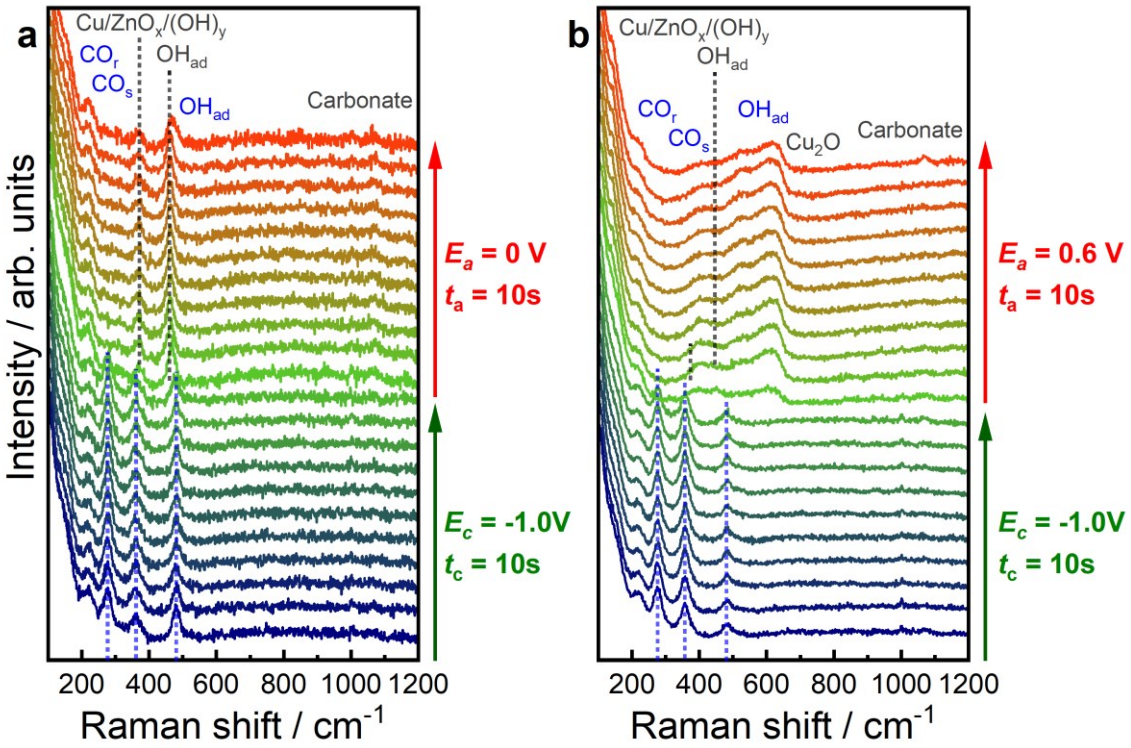

Figure 7.26 Evolution of the averaged SERS spectra of the pre-reduced Cu-Zn catalyst from 150-1200 cm^{-1} during one pulse sequence with $t_c = t_a = 10$ s with $E_a = 0$ V (a) and 0.6 V (b). Characteristic bands are marked.

formation in a previous study.[30] Besides, as discussed in Chapter 6, the adsorption of hydroxides on Cu or Zn sites might be key for the enhancement toward ethanol at $E_a = 0$ V.[47] The intensity of the hydroxide band at 490 cm^{-1}, related to OH_{ad} on Cu, increased rapidly during the cathodic pulse at both E_a values investigated and decreased upon the anodic pulse. However, this band redshifted in position due to the Stark shift upon the anodic pulse (Figure 7.26) and decreased during Cu oxidation at $E_a = 0.6$ V. This indicates that the contribution of adsorbed OH might be larger at $E_a = 0$ V, which can be attributed to the competition between OH adsorption and Cu oxide formation at $E_a = 0.6$ V. Interestingly, a band appeared at 370 cm^{-1}, which is mainly visible during the anodic pulses at $E_a = 0$ V and is not pronounced when pulsing up to $E_a = 0.6$ V. This band can be ascribed to the formation of Cu/$ZnO_x(OH)_y$ based on the literature, which might also be favorable for the ethanol production.[31, 222, 235]

The corresponding analysis for $t_c = 4$ s and $t_a = 1$ s (Figure 7.27) shows qualitatively similar changes to those observed under $t_c = t_a = 10$ s pulses. Due to the short anodic time, smaller fractions of oxides were formed, as indicated by XAS analysis (Figure A7.16, A7.18). The surface sensitive quasi-*in situ* LMMs also confirm the metallic state of Cu at the catalyst surface, as well as show the partial oxidation of Zn during pulsed CO_2RR at $E_a = 0$ V (Figure 7.28). Interestingly, the Cu:Zn ratio on the surface significantly increased after the application

of the cathodic pulse, which might be related to Cu surface segregation simultaneously with CuZn alloy formation (Figure 7.29). During the anodic pulse, the Cu:Zn ratio decreased again due to the formation of ZnO, which segregates to the surface. The increase in the Cu:Zn ratio might also be related to the dissolution of the unstable Zn(II) species. In fact, ICP-MS measurements of the electrolyte indicate an increasing dissolution of Zn with higher E_a values (Table 7.3). However, at E_a = 0 V, the loss of Zn was only 10 %, and thus surface segregation is likely to be the main reason for the detected change in surface composition.

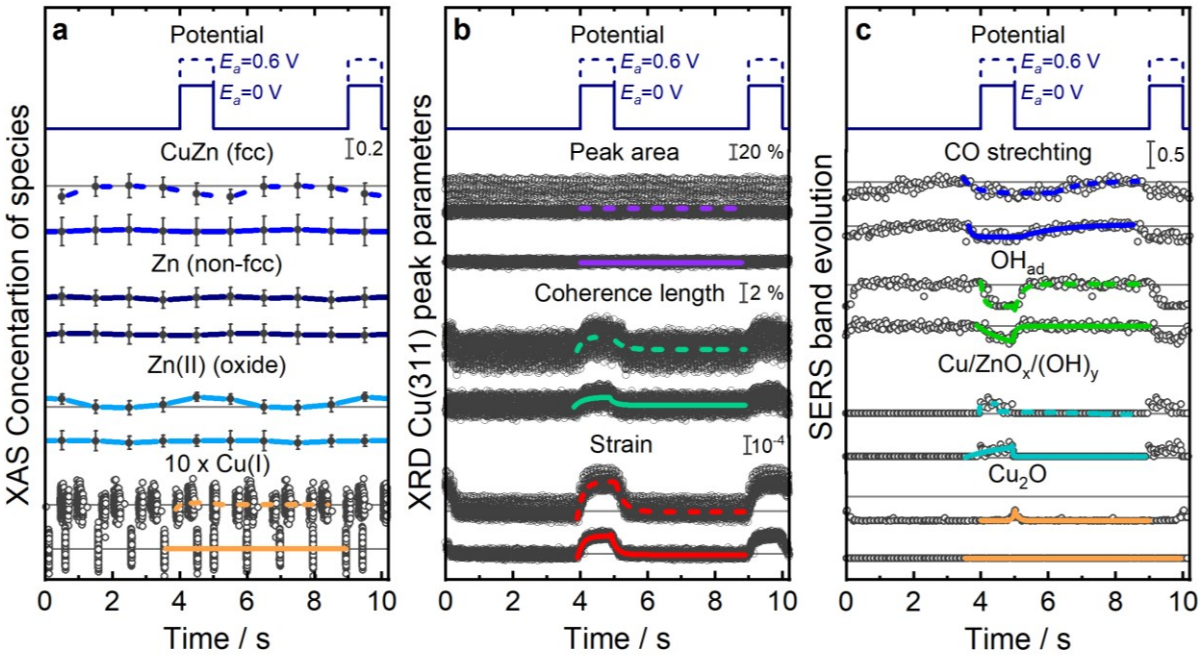

Figure 7.27 Averaged changes in the structure and adsorbates during a pulse sequence with E_c = -1.0 V and E_a = 0 V (bottom) or E_a = 0.6 V (top) for t_c = 4 s and t_a = 1 s by *operando* measurements. (a) ML-EXAFS analysis results for the Zn K-edge show the concentrations of different Zn species, and LCA-XANES analysis results for Cu K-edge show variations in Cu(I) concentration. The concentration profile of Cu(I) is multiplied by 10 for better visibility. (b) HE-XRD Cu(311) Bragg peak parameters such as the relative changes in the Bragg peak area, the Cu coherence length, and the lattice strain. (c) Raman band evolution of adsorbed CO (stretching band at 360 cm^{-1}), OH_{ad} (adsorbed on Cu at 490 cm^{-1}), $Cu/ZnO_x/(OH)_y$ species (370 cm^{-1}), and Cu_2O species (average of 530 and 620 cm^{-1}) obtained by fitting the intensities of the bands from the SERS spectra. The colored lines are exponential fits, and the solid lines represent the anodic pulse to 0 V, and the dashed lines the anodic pulse to 0.6 V. The solid grey lines indicate the respective values for each parameter at the end of the cathodic pulse.

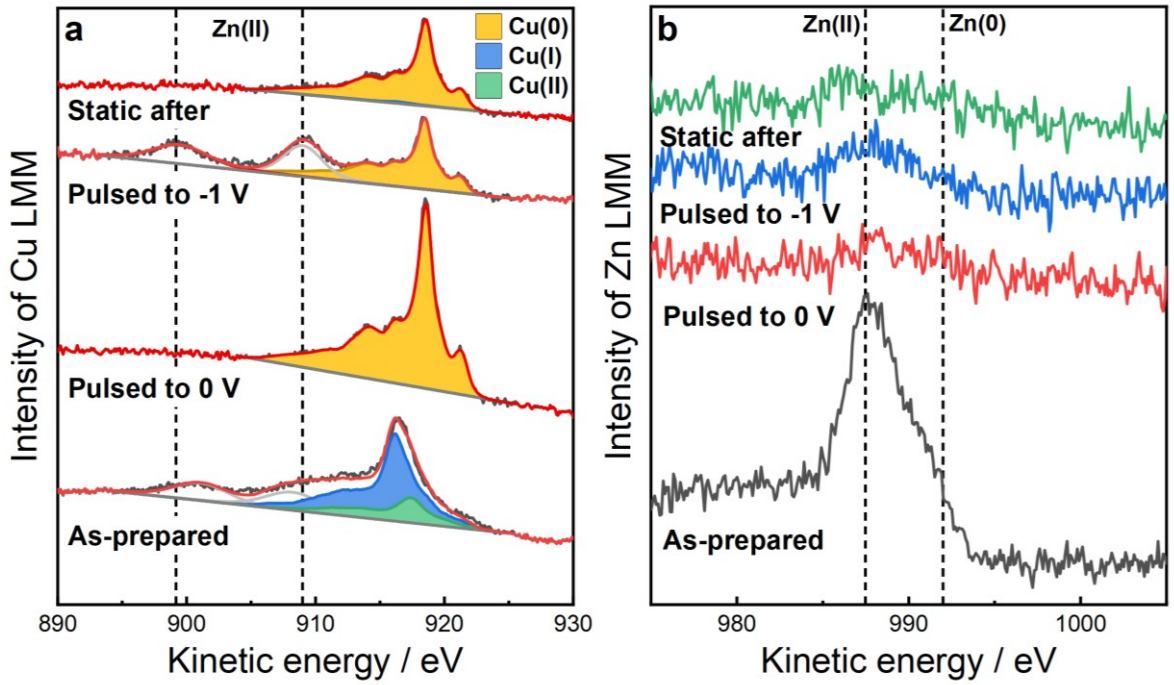

Figure 7.28 Quasi-*in situ* Cu LMM (a) and Zn LMM (b) Auger spectra of the Cu-Zn catalyst during different conditions. Spectra for samples are compared where the pulse sequence (t_c = 4 s and t_a = 1 s, E_a = 0 V) was interrupted at the cathodic or anodic pulse. Zn(II) peaks in Cu LMM correspond to the ^{1}P and ^{3}P final state of Zn LMM.

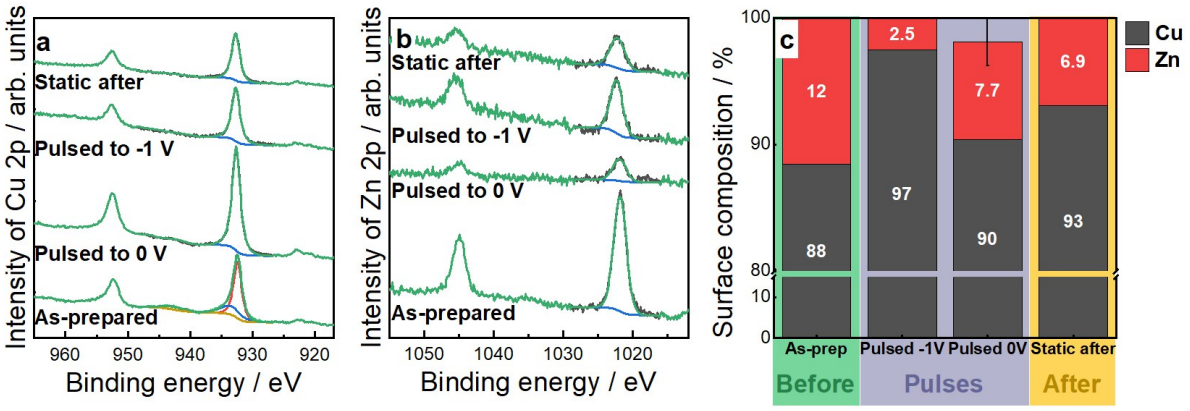

Figure 7.29 Quasi-*in situ* Cu 2p (a) and Zn 2p (b) core level regions of the Cu-Zn catalyst as well as the surface composition during different conditions (c). Spectra for samples are compared where the pulse sequence (t_c = 4 s and t_a = 1 s, E_a = 0 V) was interrupted at the cathodic or anodic pulse.

7.3.6 Correlation of Structure and Selectivity

For the pulsed CO_2RR with t_c = 4 s and t_a = 1 s, the structural and chemical changes within each individual pulse are small and are also hard to detect, in particular by XAS, due to the limited time resolution of the measurements. Therefore, additional "slow" (standard temporal resolution) XAS spectra were analyzed with an acquisition time of 10 min/spectrum. Figure 7.30 presents (a) the weights of the different Zn species as extracted by the ML-EXAFS approach during the cathodic and anodic pulse from "slow" XAS data (with corresponding XAS data and RDFs in Figure A7.22-A7.23); (b) the averaged coherence length at each end of an anodic pulse (Figure A7.24); and (c) the ratios of the adsorbed OH species (OH^-_{ad} on Cu at 490 cm^{-1}) and the CO coverage (CO_{cov}; calculated by the ratio of the intensities of the CO_s and CO_r band)[88] during the cathodic pulse as well as the ratio of the $Cu/ZnO_x(OH)_y$ (at 370 cm^{-1}) during the anodic pulse and the CO_{cov} during the cathodic pulse (Figure A7.25).

The ultimate goal of this study was to correlate the structural *operando* data with the catalytic selectivity at different E_a values during pulsed CO_2RR of the Cu-Zn sample. Based on the XAS, XRD, and SERS results, as well as on the selectivity data (Figure 7.8 b), three regions of pulse parameter space could be determined with different catalyst surface and adsorbate structures, as shown in Figure 7.30 d. At lower anodic pulse potentials (E_a < -0.25 V), the HER and CO production increased significantly. This is the region where the concentration of Zn oxide is the lowest, and the ratio of Zn-rich and Cu-rich CuZn alloy phases is relatively high (Figure 7.30 a). Only minor changes in the Cu lattice were observed in this regime, as evidenced by the XRD data (Figure 7.30 b, Figure A7.24). These insights indicate that the catalyst structure under these conditions resembles the structure under static conditions, where the C_{2+} selectivity was still much higher (Figure 7.8 b). A similar decrease in the C_{2+} products at E_a = -0.4 V has been measured for the bare Cu_2O NCs (Figure 7.11).[129] Thus, the decrease in C_{2+} products under pulsed CO_2RR at lower E_a values is not only related to the catalyst structure and composition but also to the change in the adsorbate type and coverage. Indeed, SERS data suggest a decrease of OH^-_{ad} and $Cu/ZnO_x(OH)_y$ species, which are beneficial for the formation of oxygenated products. These low "anodic" pulses might not remove the CO and H species far enough from the catalyst surface and might then be directly released during the cathodic pulse. Further studies need to be performed to confirm the reaction mechanism at low E_a.

Similarly, at high anodic pulse potentials (E_a > 0.3 V), the HER and CO production also increased significantly. However, here ML-EXAFS analysis of the Zn K-edge shows that the fraction of Zn oxide increased (Figure 7.30 a) in combination with the evolution of a small fraction of Cu_2O (LCA-XANES analysis of Cu K-edge). This is in line with a decrease in the

coherence length as well as of the Bragg peak area over the course of the anodic pulse, which indicates the start of Cu oxidation (Figure 7.30 b, Figure A7.24). The increased amount of Zn oxide at high E_a values might lead to the (irreversible) segregation of Zn species (ZnO or Zn), as observed in EDX-STEM (Figure 7.1 l), which results in the higher HER and CO formation stemming from the Zn-rich domains.[236] The enhanced CH_4 formation at these conditions was also observed with the bare Cu_2O NCs and can be assigned to irreversible morphological changes of Cu.[97]

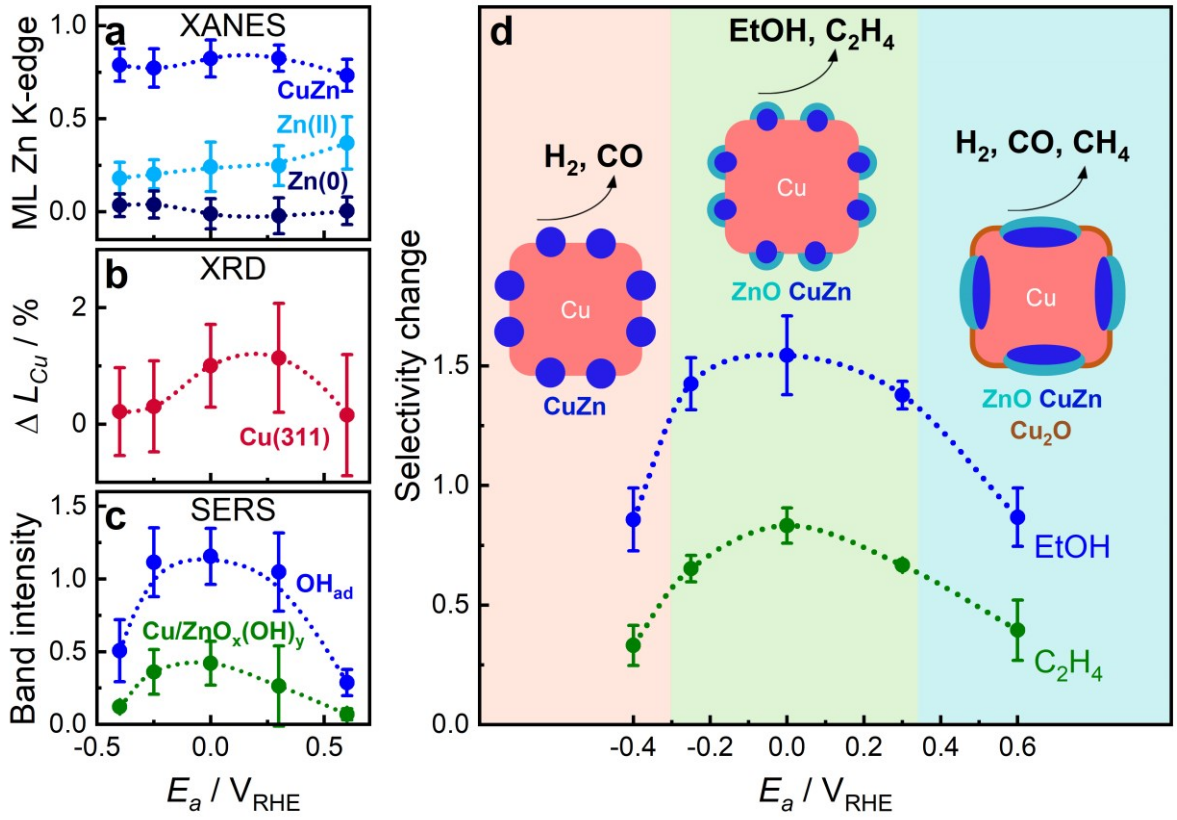

Figure 7.30 Effect of the anodic potential E_a on the structure, adsorbates, and catalytic performance. (a) Machine-learning (ML) analysis results of the averaged concentrations of Zn(0) (non-fcc-type structure), CuZn (fcc-type structure), ZnO species (oxide-type structure) from the Zn K-edge during the cathodic and anodic pulse with t_c = 4 s and t_a = 1 s in dependence of the E_a value. (b) Change of the coherence length of the Cu(311) Bragg peak at the end of each anodic pulse with t_c = 4 s and t_a = 1 s. (c) Blue dots show the averaged ratio of the intensities of the OH^-_{ad} band (~490 cm^{-1}) and the CO_{cov} (ratio of the intensities of CO_s at 360 cm^{-1} and CO_r at 280 cm^{-1}) during the cathodic pulse (each cathodic pulse is averaged), and the green dots show the evolution of the averaged intensities of $Cu/ZnO_x/(OH)_y$ during each anodic pulse with $t_c = t_a$ = 10 s. (d) Scheme of the proposed electrode structure, composition, and reaction products extracted from the analysis of XANES, HE-XRD, and SERS measurements during pulsed CO_2RR and change of Faradaic efficiencies of ethanol and ethylene during pulsed CO_2RR compared to static CO_2RR conditions.

In contrast, an intermediate anodic pulse potential (E_a = 0 V) resulted in the highest selectivity for ethanol and ethylene formation. In this case, there is an optimal adjustment of the composition of ZnO and the CuZn alloy in combination with metallic Cu (Figure 7.30 a). The formation of Zn oxide species during pulsed CO_2RR, as observed from XAS, seems to be essential for the ethanol formation as it was also observed for bare Cu_2O NCs, where disordered Cu oxide was formed during pulsed CO_2RR.[96, 97] Additionally, the increase in the coherence length of crystalline Cu (Figure 7.30 b) due to the dealloying of CuZn and a rearrangement of the Cu phase might be crucial for the enhancement in these C_{2+} products. Moreover, the ratio of OH_{ad} versus CO_{cov} in SERS correlates directly with the observed ethanol selectivity at different E_a values (Figure 7.30 c, Figure A7.25), as also observed for pulsed CO_2RR of bare Cu_2O NCs in Chapter 6. Thus, this study highlights the importance of OH_{ad} and CO_{ad} sites, since OH_{ad} might then directly couple with C-C adsorbates to form ethanol while blocking the H_{ad} sites at the same time.[46, 129, 223] Furthermore, the $Cu/ZnO_x(OH)_y$ band appeared during the anodic pulse mainly between E_a = -0.25 V to 0 V, which seems to be also linked with the enhancement of the OH_{ad} during the cathodic pulse to enhance the C_{2+} products at these potentials.[31, 222]

7.4 Conclusion

This study combines for the first time (sub)-second time-resolved *operando* XAS, HE-XRD, and SERS to uncover the complex interplay of Cu-ZnO nanocatalysts under potentiodynamic CO_2RR reaction conditions. In this way, the compositional changes, such as Zn oxide and CuZn alloy formation, as well as Cu crystallite size and strain evolution, could be linked to changes in the adsorbate structure, such as CO_{ad} and OH^-_{ad} evolution to understand the selectivity behavior. The transformation of a low amount of zinc oxide into a CuZn alloy resulted in the formation of important $Cu/ZnO_x(OH)_y$ species. In this way, the OH coverage in the CO_2RR regime could be increased, which enhanced the ethanol selectivity. On the contrary, if Zn was oxidized to a greater extent, Zn and ZnO agglomerations started to form on the Cu surface and blocked the Cu sites, which led to an increase in the selectivities of the parasitic HER and in CO. Thus, this study presents crucial *operando* mechanistic insights on the potential routes to enhance the ethanol formation in CO_2RR. Overall, the application of potential pulses on a Cu-based bimetallic catalyst offers an easy way to alter the catalyst selectivity and stability toward valuable C_{2+} products such as ethanol by tuning the oxidation state of the second metal (Zn).

8. Conclusion and Outlook

The goal of this study was to enhance the understanding of the intricate CO_2RR process, specifically toward the production of valuable C_{2+} products. This was accomplished by designing well-defined cubic-shaped Cu-based nanocatalysts, which could be decorated with a second metal, such as Ag and Zn. The CO_2RR was carried out under both static and pulsed potential conditions, while various experimental techniques, including *in situ* and *operando* characterization methods performed under working conditions, were utilized to correlate the selectivities, the structure and composition of the catalyst, as well as the relevant adsorbates. Ultimately, this research is expected to advance the CO_2RR catalyst design, which supports the development of a net-zero CO_2 cycle for producing chemicals and fuels to aid in preventing the catastrophic consequences of climate change.

The first objective was to gain a better understanding of Cu-based bimetallic catalysts, specifically of the promising Cu-Ag system. To achieve this, well-defined Ag NP-decorated Cu_2O nanocubes were designed, which exhibited improved selectivity toward C_{2+} liquid products such as ethanol and acetaldehyde (Chapter 5). Previous studies on Cu-Ag catalysts have shown vastly different product selectivities, but it has been difficult to understand the underlying reasons since these studies only used *ex situ* characterization methods. Through the investigations of the structural and chemical transformations of the catalyst during CO_2RR, *operando* XAS of the Cu and Ag K-edge revealed that Cu_2O underwent partial reduction under reaction conditions, which led to the redispersion of Ag on the CuO_x NCs and the formation of Ag-Cu alloy sites. This reaction-driven redispersion of Ag was found to be a key factor for the enhanced selectivity of the catalyst toward C_{2+} products. Additionally, *operando* SERS demonstrated that the Ag-Cu sites significantly altered the CO binding to Cu. According to a newer study,[88] the change of the Cu-CO bonding configuration can also be directly correlated to an enhanced CO coverage, which might be crucial for the C-C coupling in the Cu-Ag system as well.

In addition to the important *CO intermediates, as observed in Chapter 5, the important role of hydroxides in the formation of ethanol has been speculated, but there has been no experimental evidence so far.[47] Therefore, the second objective was the investigation of the adsorbate structure and composition of a Cu_2O nanocube-derived catalyst by *operando* SERS (Chapter 6).

Here, CO_2RR was carried out under pulsed potential conditions, where the pulse durations of the anodic and cathodic pulse were varied to tune the product selectivities toward different products, such as ethanol, ethylene/acetaldehyde, or C_1 products. In this way, different catalytic conditions could be easily simulated. To increase the temporal resolution down to the sub-second time regime, an *operando* SERS flow cell was designed, enabling the tracking of characteristic adsorbates such as OH_{ad} and CO_{ad} during each individual pulse. It was found that the formation of bulk-like Cu_2O led to a decrease in the near-surface pH, resulting in a lower OH_{ad} versus CO coverage, which increased the C_1 selectivity. On the other hand, the oxidative formation of Cu-O_{ad} or $CuO_x/(OH)_y$ species, as well as an intermediate OH_{ad} versus CO coverage during CO_2RR, were found to be necessary to enhance the selectivity toward ethanol. Until now, most studies have focused primarily on investigating the pulsed CO_2RR behavior of bare Cu-derived catalysts. Thus, the third objective was to understand Cu-Zn bimetallic catalysts under pulsed potential CO_2RR conditions (Chapter 7). Therefore, well-defined ZnO-covered Cu_2O nanocube-derived catalysts were prepared similarly to the Cu-Ag catalyst (Chapter 5). Here, the pulse durations were fixed, and the selectivities could be tuned by varying the anodic potential to control the redox states of the metals. The combination and correlation of sub-second time-resolved *operando* XAS, HE-XRD, and SERS could decipher the complex interplay between Zn oxide and CuZn alloy formation, Cu crystallite size and strain evolution, and the adsorption behavior of CO_{ad} and OH_{ad} during pulsed CO_2RR conditions. By applying similar pulsed conditions as for the bare Cu catalysts within the oxidation regime of Zn and Cu, excessive oxidation of Zn led to the agglomeration of Zn on the Cu surface, blocking Cu sites, and causing an increase in parasitic HER. However, the ideal conditions for ethanol formation were discovered by pulsing to lower anodic potentials within the Zn oxidation regime alone. This was linked to the conversion of a small proportion of the CuZn alloy into zinc oxide, forming $Cu/ZnO_x(OH)_y$ species and enhancing OH coverage in the CO_2RR regime. Compared to bare Cu catalysts, the Cu-Zn system has the added advantage of increased catalyst stability owing to the milder pulse conditions at lower anodic potentials.

Overall, these studies significantly contribute to our understanding of CO_2RR by uncovering the complex interplay of various factors that impact on the selectivity toward C_{2+} products. For bimetallic catalysts like Cu-Ag (Chapter 5) and Cu-Zn (Chapter 7), the interactions between both metals play a critical role. While Cu-Ag intermixed only at the interface under harsh CO_2RR conditions, Zn readily formed a stable CuZn alloy under reaction conditions. Local alloying of Cu with Ag increased the interatomic distance, altering the binding energies of adsorbates and intermediates, thereby favoring the formation of C_{2+} liquid products (Chapter 5).

Moreover, pulsed CO_2RR conditions significantly tuned the catalyst properties and adsorbate coverages, thereby providing useful insights into crucial features for enhancing the ethanol selectivity and improving catalyst design (Chapter 6 and Chapter 7). One of the key findings of this study is that the formation of oxide and adsorbed hydroxide species plays a vital role in boosting ethanol production. This effect can be induced by either oxidizing Cu or Zn via pulsed potential CO_2RR with distinct pulse durations and potentials. Moreover, the combination of Cu with a second metal such as Zn enhanced the catalytic stability during pulsed CO_2RR. On the other hand, the studies of the Cu-Ag system under static CO_2RR conditions (Chapter 5) highlighted the importance of an increased CO coverage resulting from the Cu-Ag intermixing for boosting the C_{2+} liquid products including ethanol. To comprehend the results obtained in this study, the use of *operando* spectroscopic and diffraction methods, such as *operando* XAS, XRD, and SERS, were essential, especially in a time-resolved manner.

Taking the next step in gaining a more comprehensive understanding of the CO_2RR mechanism, we should combine all *operando* methods simultaneously with rapid product selectivity analysis devices. This approach will be highly advantageous in gaining a deeper understanding of the CO_2RR process, and this study represents a significant step forward in this direction. Additionally, employing these *in situ* and *operando* techniques to explore not only the CO_2RR but also other electrocatalytic reactions in liquid environments can substantially contribute to advancing the field of electrocatalysis, which is crucial for building up a sustainable energy economy.

A5. Appendix to Chapter 5

A5.1 Appendix Figures

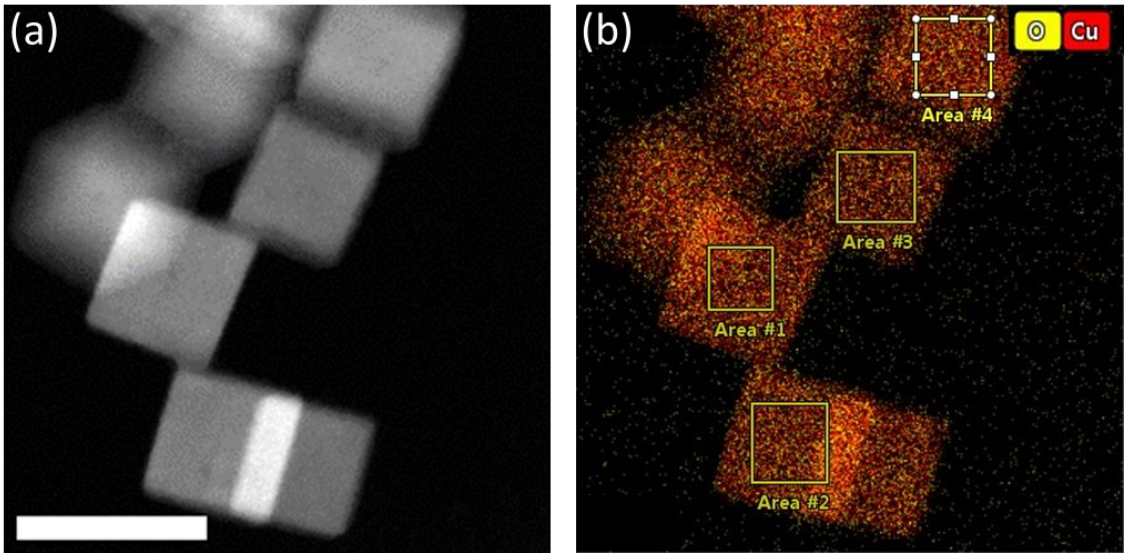

Figure A5.1 STEM-HAADF image (a) with corresponding EDX map (b) of an as-prepared Cu_2O NC sample. The STEM-EDX image shows four selected areas to determine the Cu:O atomic ratio. The scale bar corresponds to 50 nm.

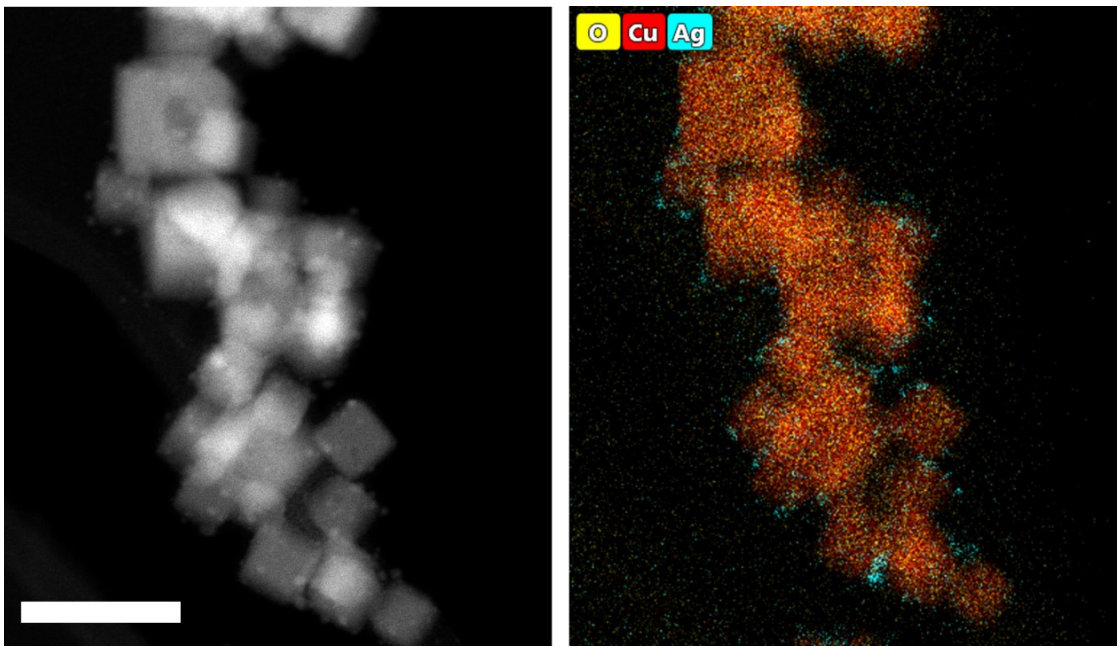

Figure A5.2 STEM-HAADF image (left) with corresponding EDX map (right) of an as-prepared 3-Ag/Cu_2O sample. The scale bar corresponds to 100 nm.

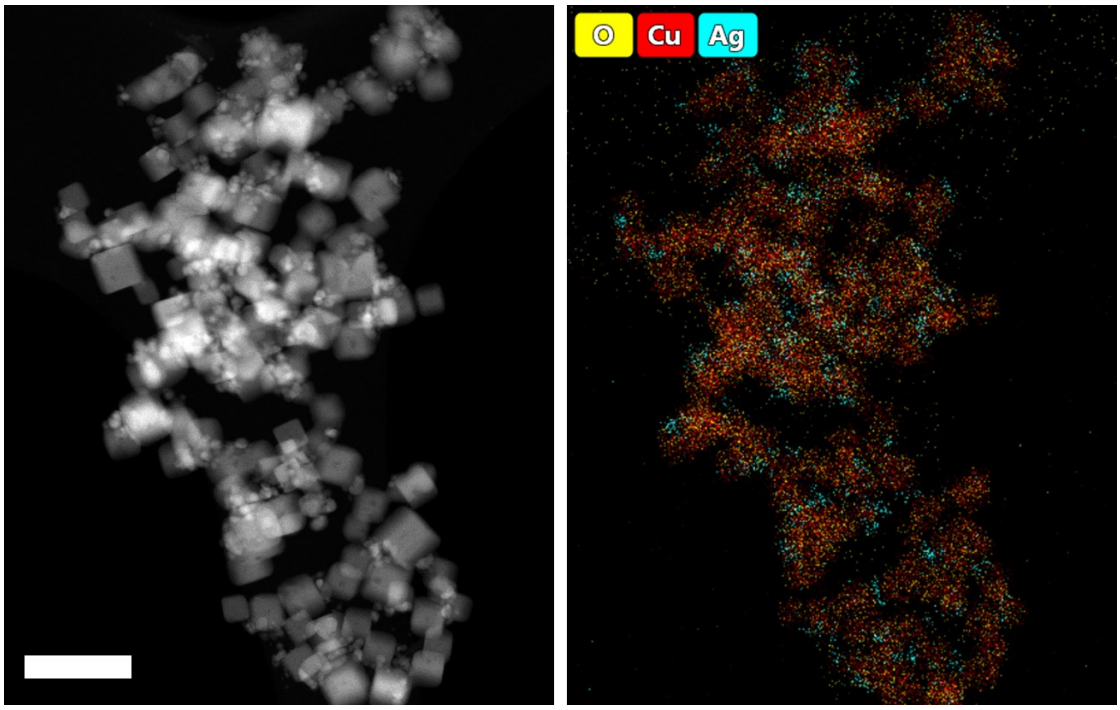

Figure A5.3 STEM-HAADF image (left) with corresponding EDX map (right) of an as-prepared 5-Ag/Cu_2O sample. The scale bar corresponds to 100 nm.

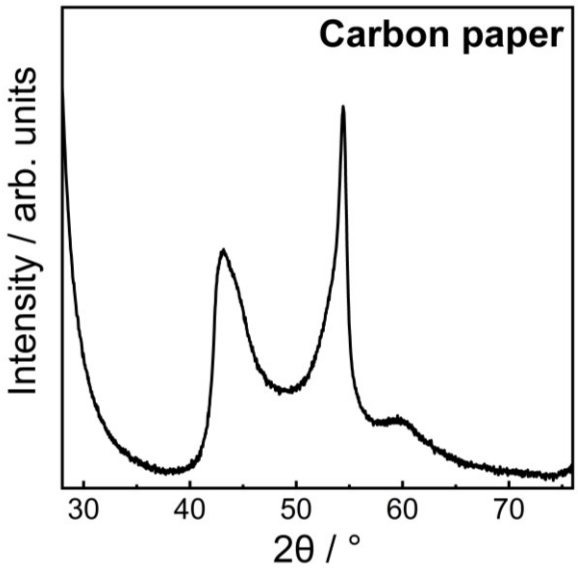

Figure A5.4 *Ex situ* grazing incidence XRD pattern of the carbon paper support.

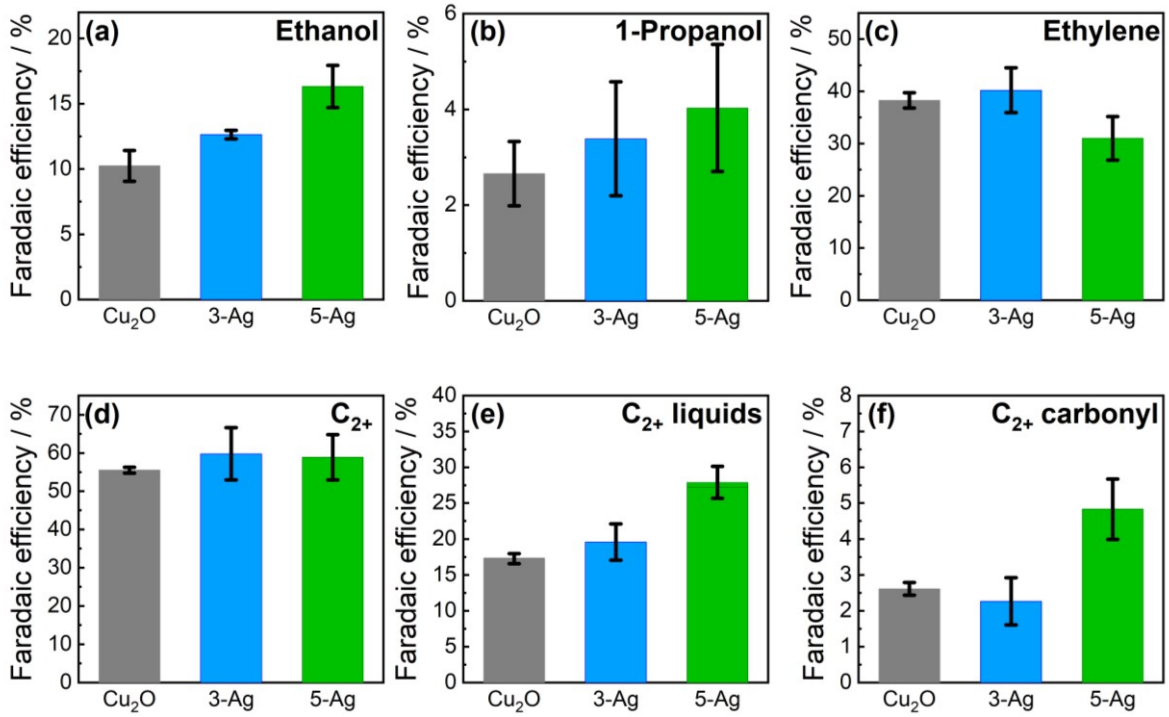

Figure A5.5 Faradaic efficiencies after 2 h electrolysis at -1.0 V_{RHE} of (a) ethanol, (b) 1-propanol, (c) ethylene, (d) C_{2+} products, (e) C_{2+} liquid products and (f) C_{2+} carbonyl products of Cu_2O NCs (gray), 3-Ag/Cu_2O (blue) and 5-Ag/Cu_2O (green) in CO_2-saturated 0.1 M $KHCO_3$.

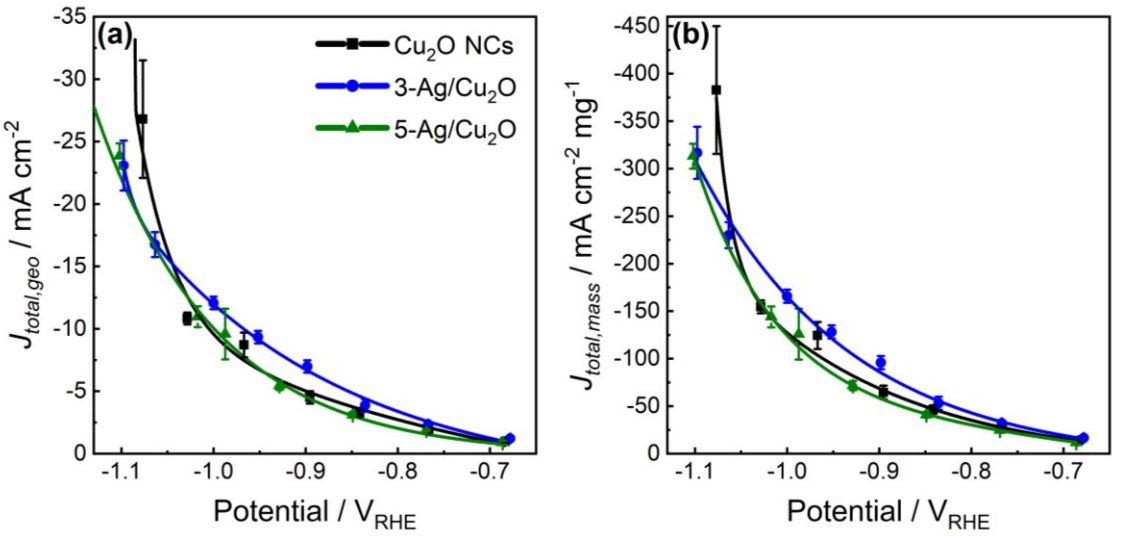

Figure A5.6 (a) Potential-dependent current densities normalized to the geometric area of the electrode ($J_{total,geo}$) and (b) to the deposited mass of Cu and Ag ($J_{total,mass}$) of Cu_2O NCs (black), 3-Ag/Cu_2O (blue) and 5-Ag/Cu_2O (green) in CO_2-saturated 0.1 M $KHCO_3$. The geometric and mass current densities of the samples are similar, suggesting similar total activities. The reported values represent the averaged currents of 2 h of electrolysis. Solid lines are a guide for the eye.

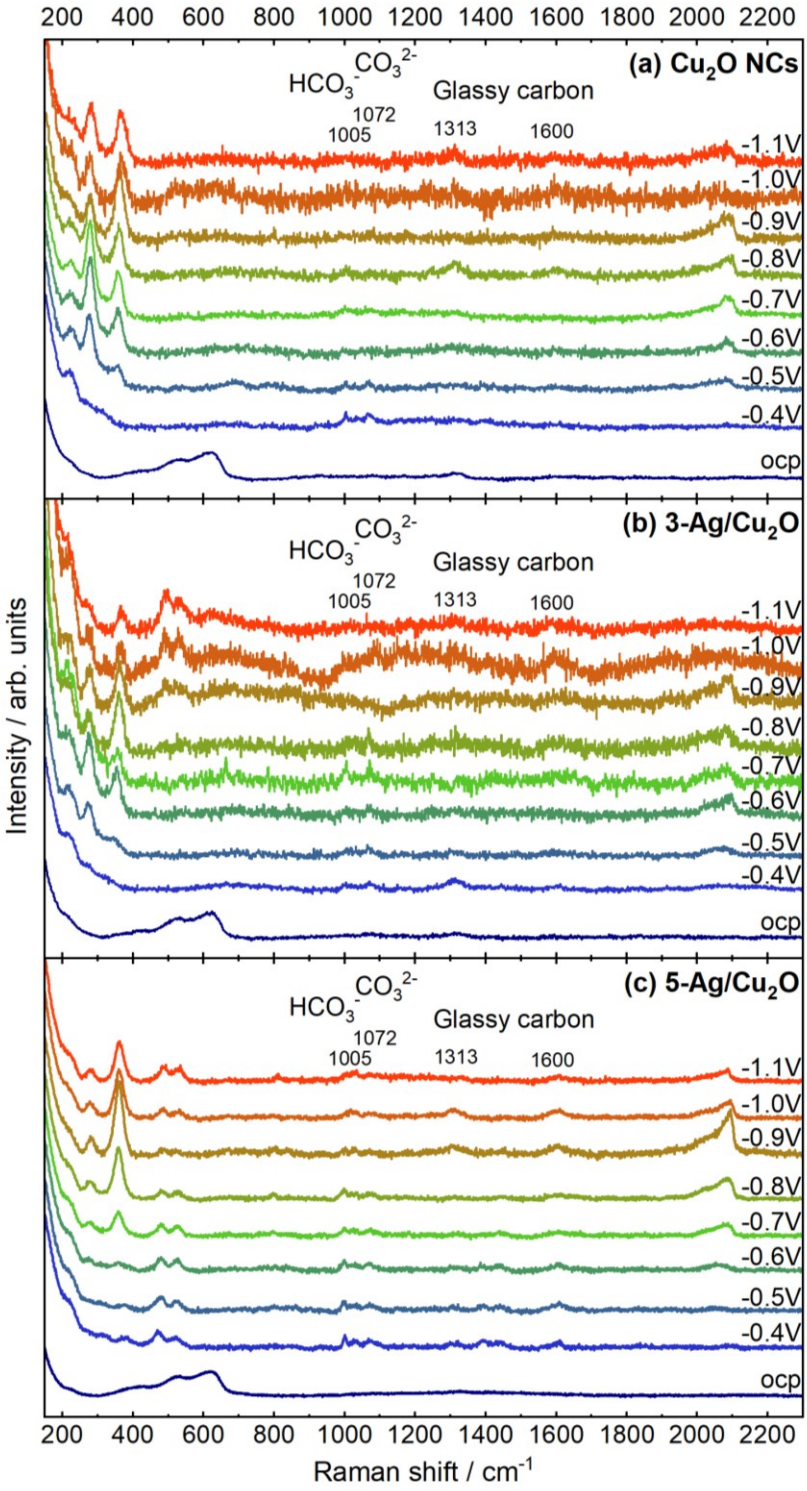

Figure A5.7 *Operando* surface-enhanced Raman spectra of (a) Cu_2O NCs, (b) 3-Ag/Cu_2O and (c) 5-Ag/Cu_2O at open circuit potential (ocp) and different applied potentials in CO_2-saturated 0.1 M $KHCO_3$. The potentials are given with reference to RHE. The characteristic peaks of Cu_2O are observed at 415 cm^{-1} (multiphonon process), at 527 cm^{-1} (Raman active F_{2g} mode), and at 624 cm^{-1} (IR active F_{1u} mode).[32, 209-211] The peaks at 1005 and 1072 cm^{-1} can be assigned to the vibrations of HCO_3^- and CO_3^{2-} in aqueous solution, respectively, and the peaks at 1313 and 1600 cm^{-1} correspond to the glassy carbon support.[207, 233] No peaks were detected from 2300 to 3000 cm^{-1}.

A5.2 Appendix Tables

Table A5.1 Cu:O atomic ratio of as-prepared Cu_2O NCs obtained from the STEM-EDX maps in Figure A5.1.

Area [#]	Cu [at%]	O [at%]
1	67(15)	33(6)
2	65(15)	35(7)
3	65(15)	35(7)
4	67(16)	33(6)

Table A5.2 Lattice parameters extracted from Rietveld refinement of *ex situ* XRD pattern of as-prepared Cu_2O NCs, 3-Ag/Cu_2O, and 5-Ag/Cu_2O samples; and of 5-Ag/Cu_2O deposited on carbon paper after 2 h of CO_2RR at -1.0 V_{RHE}. A comparison to literature values of the lattice parameters of Cu_2O, Cu, and Ag bulk is given below.

Sample	Lattice parameters [Å]		
	Cu_2O	**fcc Cu**	**fcc Ag**
As-prepared			
Cu_2O NC	4.2656(19)	-	-
3-Ag/Cu_2O	4.2674(5)	-	4.094(4)
5-Ag/Cu_2O	4.2641(8)	-	4.092(3)
After CO_2RR			
5-Ag/Cu_2O	4.2653(9)	3.612(2)	4.088(3)
References			
Cu_2O bulk	4.27[237]	-	-
Cu bulk	-	3.597[238]	-
Ag bulk	-	-	4.079[238]

Table A5.3 Capacitance values of the catalysts and references determined by the electrochemical double layer capacitance measurements acquired directly after 2 h of CO_2RR at -1.0 V_{RHE}.

Sample	Capacitance [mF cm^{-2}]
Catalysts	
Cu_2O NCs	0.15(2)
3-Ag/Cu_2O	0.27(2)
5-Ag/Cu_2O	0.40(2)
References	
Cu foil	0.027[239]
Ag foil	0.042[240]
Carbon paper	0.05(1)

Table A5.4 Comparison of Cu(0) and Cu(I) concentrations, as determined by XANES and EXAFS analysis for Cu_2O NCs and Ag-decorated NCs during CO_2RR at -1.0 V_{RHE}. The ratios of the different Cu species could be obtained from the EXAFS analysis since the reduced Cu-Cu coordination number for NCs under reaction conditions is a result of sample-averaging effect, where the measured EXAFS signal is an average of contributions from metallic and oxidized phases. In fact, the deviation of the Cu-Cu coordination number values from the bulk values can be used to independently estimate the concentrations of Cu(0) and Cu(I) species (providing that size effects on the FT-EXAFS spectra are negligible).

Sample	XANES		EXAFS	
	Cu(0) [%]	Cu(I) [%]	Cu(0) [%]	Cu(I) [%]
Cu_2O NCs	86(2)	14(2)	80(12)	20(12)
3-Ag/Cu_2O	77(3)	23(3)	80(5)	20(5)
5-Ag/Cu_2O	82(2)	18(2)	83(5)	17(5)

Table A5.5 Structural parameters (coordination numbers *N*, interatomic distances *R* and disorder factors σ^2) obtained from the fit of experimental Cu K-edge EXAFS data acquired before and during CO_2RR at -1.0 V_{RHE}.

Sample	N_{Cu-Cu}	R_{Cu-Cu} [Å]	σ^2_{Cu-Cu} [Å²]	N_{Cu-O}	R_{Cu-O} [Å]	σ^2_{Cu-O} [Å²]	ΔE_0 [eV]	*R*- factor [%]
Cu foil (Ref)	12	2.527(2)	0.009(3)	0	-	.	2.5(3)	0.24
Cu_2O (Ref)	-	-	-	2	1.850(3)	0.0012(5)	1.4(5)	0.59
Cu_2O NCs (as-prep)	-	-	-	2.4(1)	1.900(6)	0.003(1)	1.5(7)	2.01
3-Ag/Cu_2O (as-prep)	-	-	-	1.8(1)	1.863(3)	0.0009(5)	1.4(4)	0.61
5-Ag/Cu_2O (as-prep)	-	-	-	2.0(1)	1.870(3)	0.0028(5)	0.7(4)	0.52
Cu_2O NCs (-1.0 V_{RHE})	9.4(4)	2.524(3)	0.0082(4)	0.4(3)	1.81(5)	0.01(2)	2.6(5)	0.56
3-Ag/Cu_2O (-1.0 V_{RHE})	7.4(3)	2.558(3)	0.0074(4)	0.3(1)	1.81(3)	0.001(7)	4.4(4)	0.53
5-Ag/Cu_2O (-1.0 V_{RHE})	8.7(3)	2.521(2)	0.0091(3)	0.3(1)	1.93(2)	0.002(7)	2.1(4)	0.36

A6. Appendix to Chapter 6

A6.1 Appendix Figures

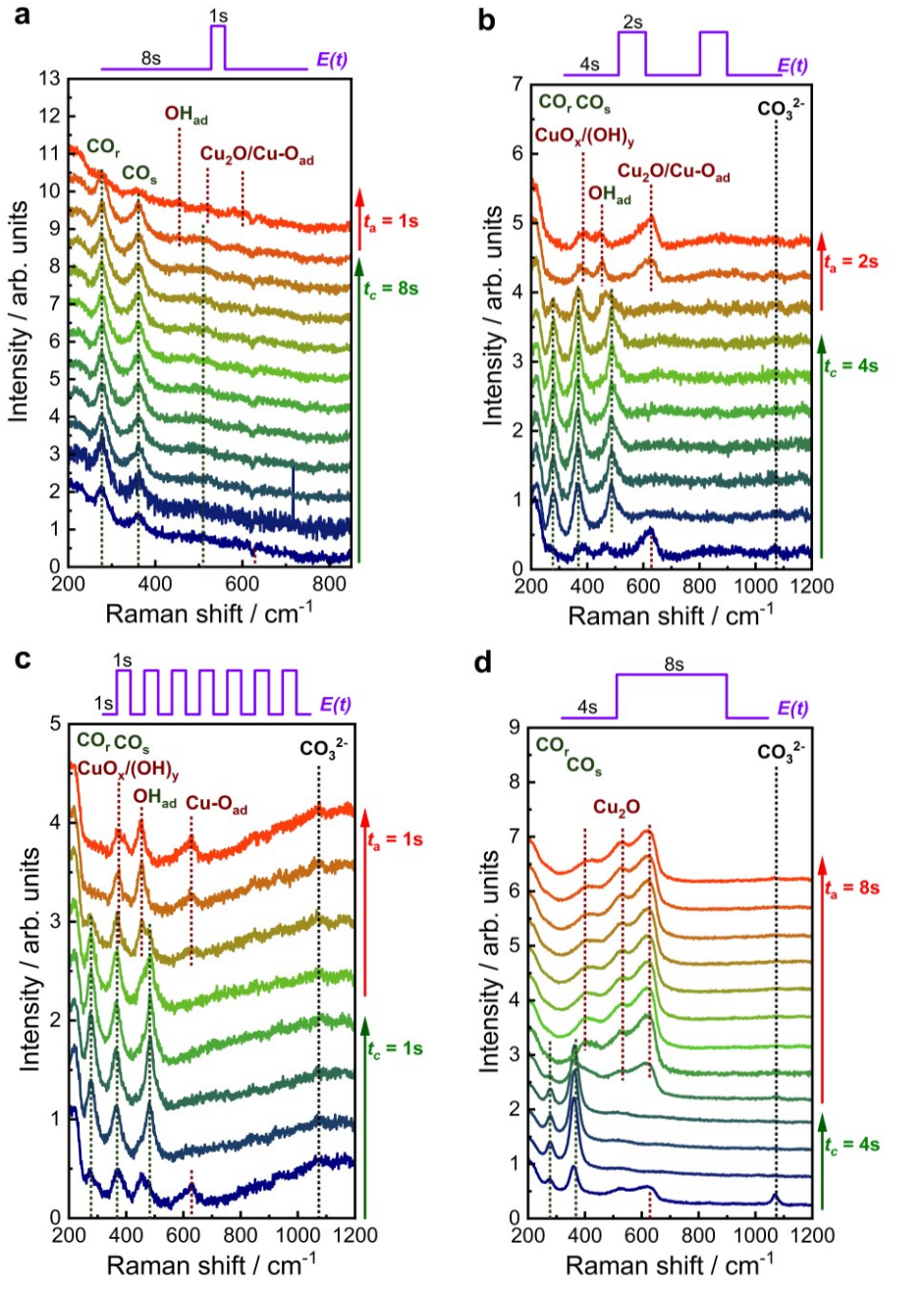

Figure A6.1 Normalized SERS spectra of pulsed potential CO_2RR measurements during E_c = -1.0 V and E_a = +0.6 V from bottom to top (as indicated with arrows) and with the pulse lengths of (a) t_c = 8 s, t_a = 1 s, (b) t_c = 4 s, t_a = 2 s, (c) t_c = t_a = 1 s and (d) t_c = 4 s, t_a = 8 s averaged over one pulse sequence. Characteristic SERS bands are highlighted.

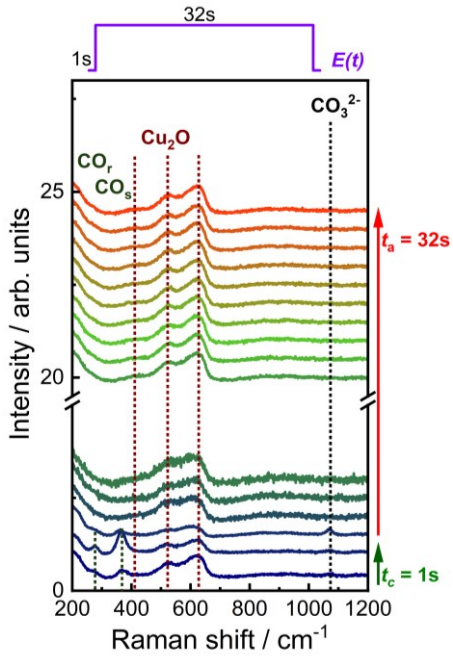

Figure A6.2 Normalized SERS spectra of pulsed potential CO_2RR measurements during E_c = -1.0 V and E_a = +0.6 V from bottom to top (as indicated with arrows) and with the pulse lengths of t_c = 1 s, t_a = 32 s averaged over one pulse sequence. Characteristic SERS bands are highlighted.

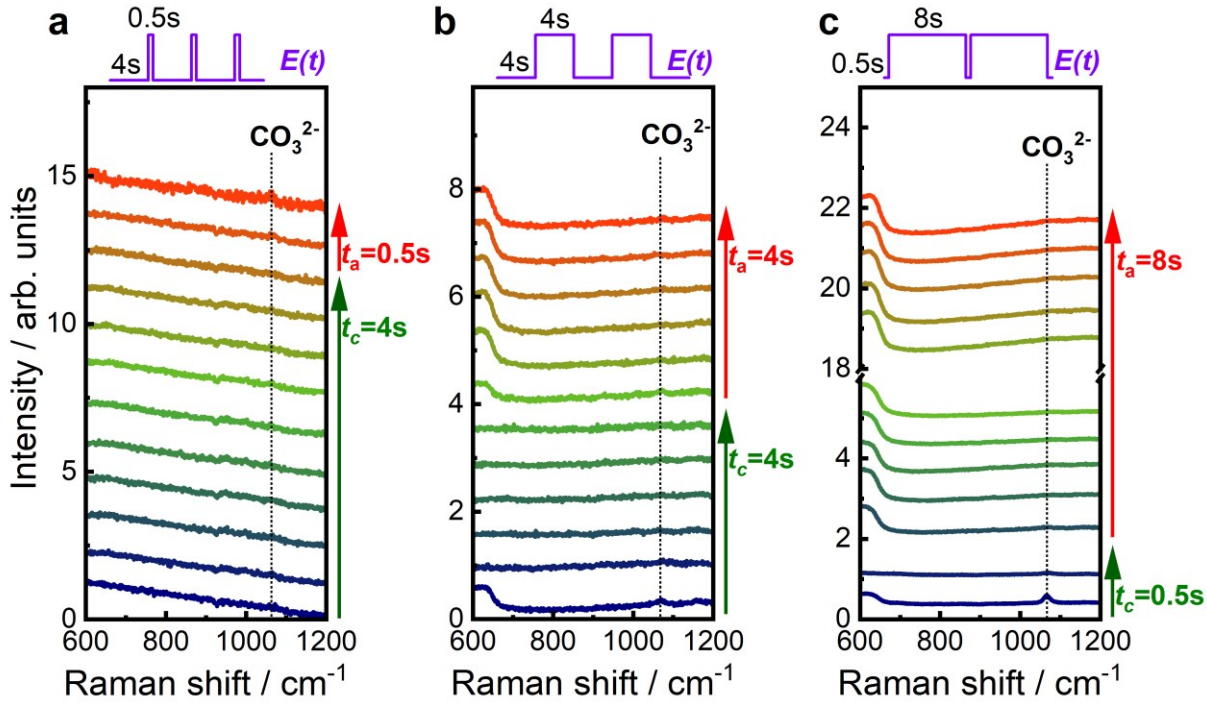

Figure A6.3 Normalized SERS spectra of the carbonate region from 600-1200 cm^{-1} of pulsed potential CO_2RR measurements during E_c = -1.0 V and during E_a = +0.6 V from bottom to top (as indicated with arrows) and with the pulse lengths of (a) t_c = 4 s, t_a = 0.5 s, (b) t_c = t_a = 4 s and (c) t_c = 0.5 s, t_a = 8 s averaged over one pulse sequence. Characteristic SERS bands are highlighted.

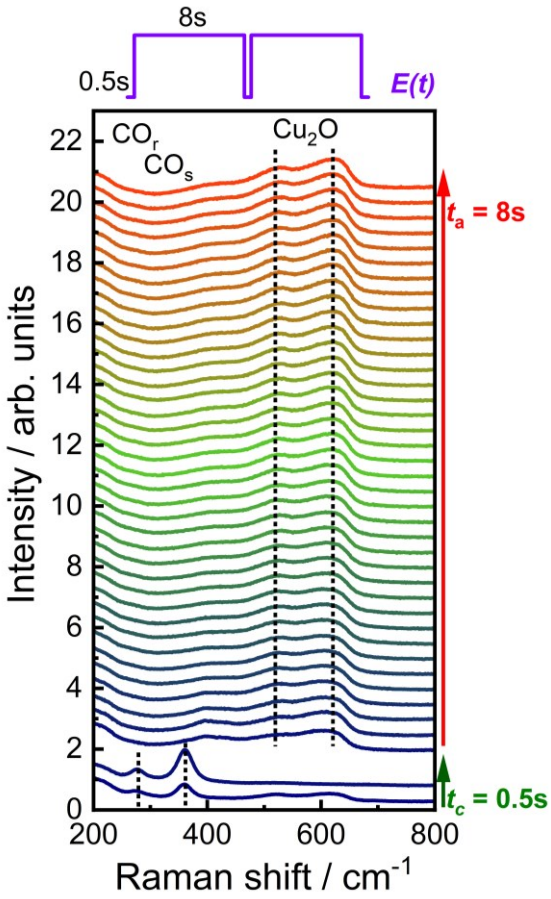

Figure A6.4 Normalized SERS spectra of pulsed potential CO_2RR measurements during E_c = -1.0 V and during E_a = +0.6 V from bottom to top (as indicated with arrows) and with the pulse lengths of t_c = 0.5 s, t_a = 8 s averaged over one pulse sequence. Characteristic SERS bands are highlighted.

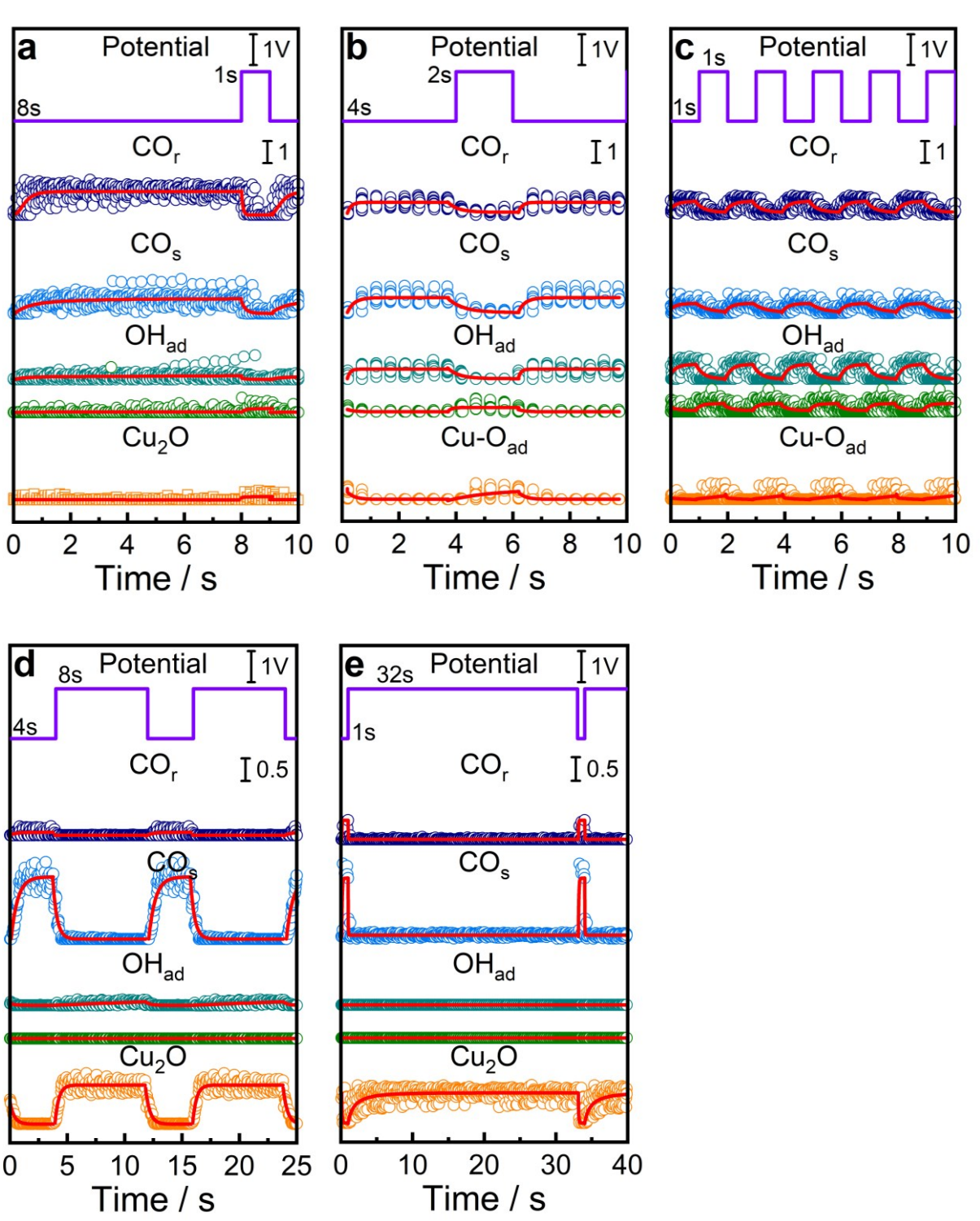

Figure A6.5 Applied potential and intensities of fits of characteristic SERS bands of pulsed potential CO_2RR at E_c = -1.0 V and E_a = +0.6 V with different pulse lengths averaged over one pulse sequence (a-e). The data points are the intensity fits of the Cu-CO rotation (CO_r at 280 cm^{-1}, dark blue), the Cu-CO stretching (CO_s at 360 cm^{-1}, light blue), Cu-OH_{ad} (OH_{ad} at 495 cm^{-1} at -1.0 V in turquoise and 450 cm^{-1} at +0.6 V in green), Cu_2O (sum of 530 and 620 cm^{-1} divided by two, orange) and Cu-O_{ad} (610 cm^{-1}, orange) bands. The red lines represent the exponential fit and are guides for the eyes.

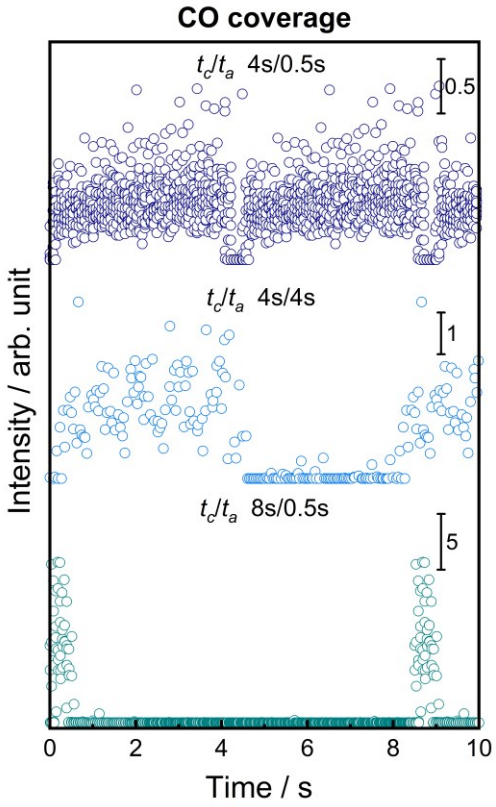

Figure A6.6 CO coverage of selected pulse lengths over one averaged pulse sequence of pulsed potential CO_2RR measurements with E_c = -1.0 V, E_a = +0.6 V. The CO coverage was determined by the ratio of the intensity of CO_s and CO_r.[88]

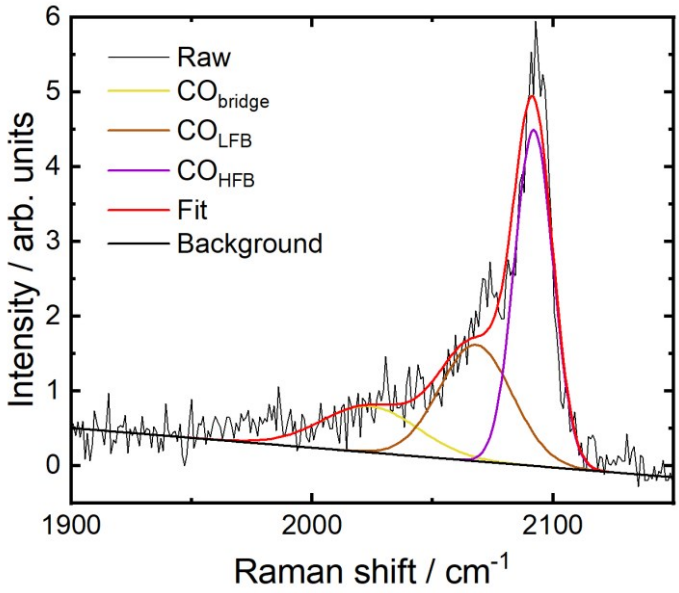

Figure A6.7 Exemplary fits of C-O vibration region of the normalized SERS spectra with the contribution of bridge CO (CO_{bridge} at 2030 cm^{-1}), low-frequency band linear CO (CO_{LFB} at 2065 cm^{-1}), and high-frequency band linear CO (CO_{HFB} at 2095 cm^{-1}) during pulsed CO_2RR with the cathodic pulse at t_c = 4 s, t_a = 8 s with E_c = -1.0 V and E_a = +0.6 V.

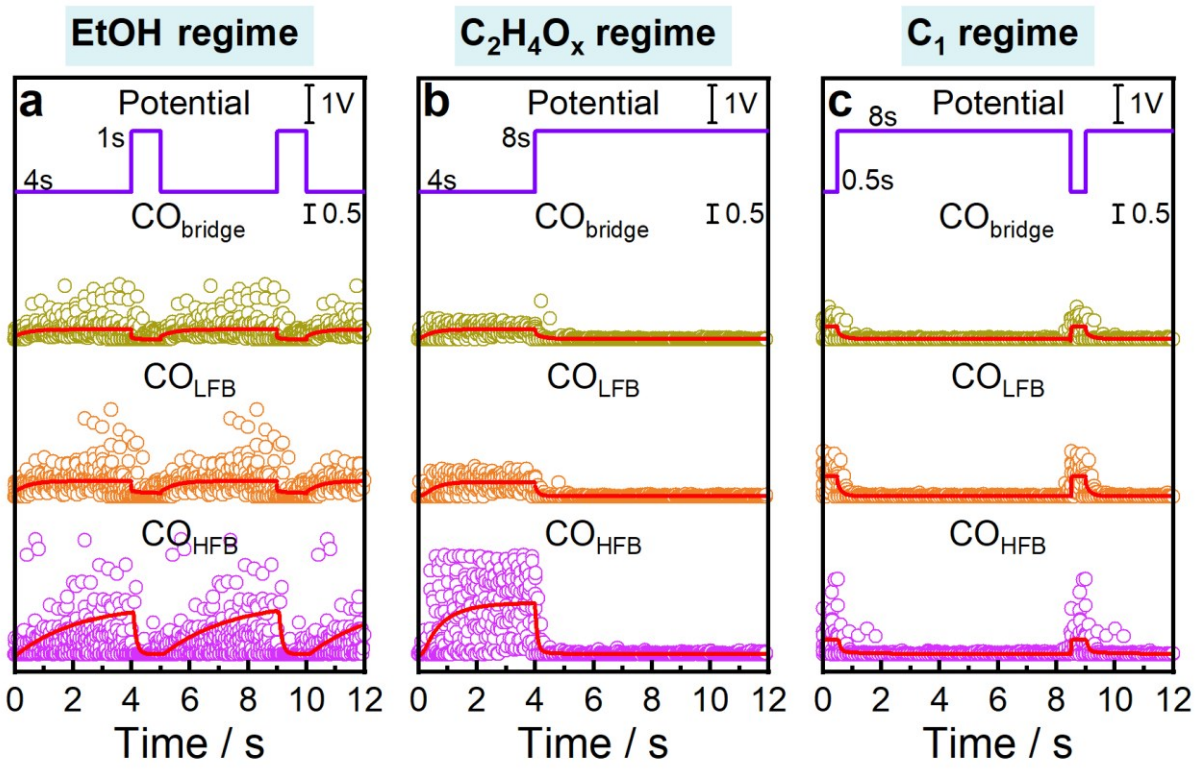

Figure A6.8 Applied potential and averaged intensities of the C-O vibration fits as shown in Figure A6.7 during pulsed potential CO_2RR measurements over one pulse sequence with varied pulse length and E_c = -1.0 V, E_a = +0.6 V. The pulse lengths are in (a) t_c = 4 s, t_a = 1 s (ethanol regime), (b) t_c = t_a = 4 s (ethylene/acetaldehyde regime), and (c) t_c = 0.5 s, t_a = 8 s (C_1 regime). The red lines represent the exponential fits and are guides for the eyes.

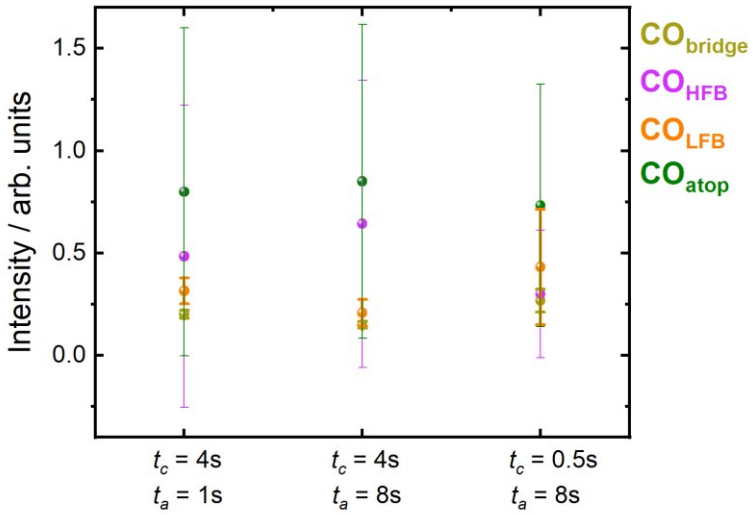

Figure A6.9 Evolution of the contribution of different CO configurations at selected pulse lengths as determined from Figure A6.8. CO_{atop} corresponds to the sum of CO_{HFB} and CO_{LFB}. The data points represent the normalized average contribution over the cathodic pulse together with the standard derivation.

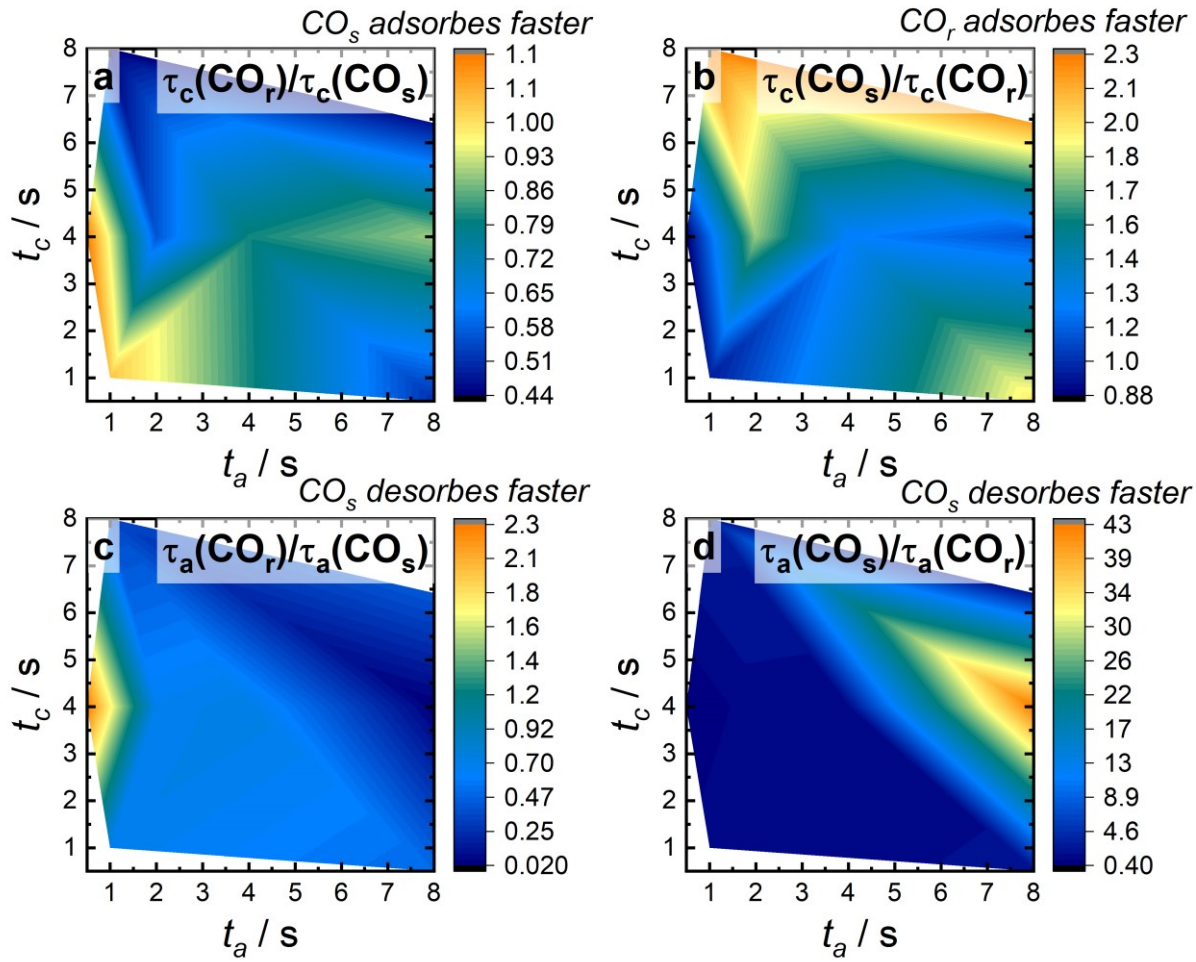

Figure A6.10 Ratio of time constants τ during the adsorption of (a) CO_r versus CO_s and of (b) CO_s versus CO_r during the cathodic pulse, as well as the ratio during desorption of (c) CO_r versus CO_s and of (d) CO_s versus CO_r during the anodic pulse in dependence of the pulse lengths of pulsed potential CO_2RR measurements with E_c = -1.0 V, E_a = +0.6 V.

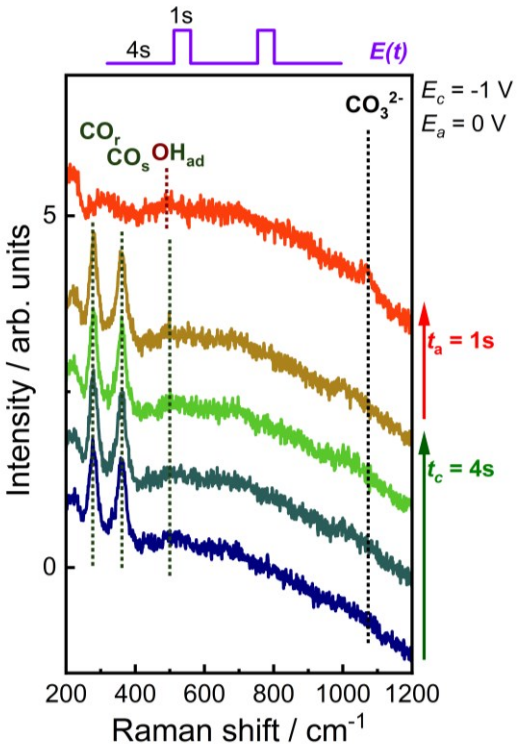

Figure A6.11 Normalized SERS spectra of pulsed potential CO_2RR measurements during E_c = -1.0 V and E_a = 0.0 V with the pulse lengths of t_c = 4 s, t_a = 1 s from bottom to top (as indicated with arrows) averaged over one pulse sequence. Characteristic SERS bands are highlighted.

A6.2 Appendix Tables

Table A6.1 Time constants τ of evolution and disappearance of the CO_r and CO_s bands in arb. units during the cathodic and during the anodic pulse, respectively, extracted from the exponential decay fits in Figure 6.6 d-f and Figure A6.5. R^2 values indicate the goodness of the exponential fits.

t_c [s]	t_a [s]	CO_r (t_c)	R^2	CO_r (t_a)	R^2	CO_s (t_c)	R^2	CO_s (t_a)	R^2
4	**0.5**	0.12	0.55	0.24	0.71	0.11	0.20	0.10	0.48
4	**4**	0.44	0.54	0.27	0.75	0.54	0.61	0.38	0.70
0.5	**8**	0.043	0.50	0.04	0.29	0.08	0.75	0.08	0.76
8	**1**	0.20	0.29	0.05	0.22	0.45	0.20	0.13	0.20
4	**2**	0.13	0.47	0.35	0.69	0.24	0.58	0.53	0.77
1	**1**	0.23	0.26	0.28	0.29	0.23	0.28	0.41	0.34
4	**8**	0.51	0.20	0.01	0.77	0.57	0.84	0.36	0.90
1	**32**	0.03	0.25	0.02	0.77	0.06	0.20	0.02	0.52

Table A6.2 Time constants τ of disappearance and evolution of Cu-O_{ad} and Cu_2O bands in arb. units during the cathodic and during the anodic pulse, respectively, extracted from the exponential decay fits in Figure 6.6 d-f and Figure A6.5. R^2 values indicate the goodness of the exponential fits.

t_c [s]	t_a [s]	Cu-O_{ad} (t_c)	R^2	Cu-O_{ad} (t_a)	R^2	Cu_2O (t_c)	R^2	Cu_2O (t_a)	R^2
4	**0.5**	0.04	0.20	0.11	0.20				
4	**4**					0.35	0.71	1.60	0.58
0.5	**8**					0.07	0.74	0.14	0.70
8	**1**					0.04	0.20	0.04	0.20
4	**2**	0.25	0.69	1.57	0.39				
1	**1**	0.02	0.67	0.41	0.20				
4	**8**					0.38	0.90	0.33	0.69
1	**32**					0.05	0.25	0.28	0.39

Table A6.3 Averaged SERS band intensity values and standard derivation (in arb. units) of Cu_2O bands at 410, 530 and 620 cm^{-1} over an averaged anodic pulse and their ratios to each other.

t_c [s]	t_a [s]	*I* 410	*I* 530	*I* 620	Ratio 410/all	Ratio 530/all	Ratio 620/all	Ratio 410/ (530+620)
4	**4**	0.17(9)	0.33(7)	0.7(1)	0.15	0.28	0.57	0.17
4	**8**	0.28(7)	0.67(9)	0.9(2)	0.15	0.36	0.49	0.18
0.5	**8**	0.22(7)	0.8(1)	0.9(3)	0.12	0.41	0.47	0.14
1	**32**	0.10(4)	0.5(1)	0.8(1)	0.07	0.39	0.54	0.08

Table A6.4 Change of Faradaic efficiencies (ΔFE) under pulsed conditions (-1.0 V/0 V and 4 s/1 s) subtracted by static CO_2RR conditions at -1.0 V.

Product	ΔFE [%]
H_2	-6.0(5)
CO	1.5(3)
CH_4	0.5(2)
C_2H_4	0.761(6)
$HCOO^-$	1.3(2)
CH_3COO^-	0.018(6)
Acetaldehyde	0.31(7)
Propionaldehyde	0.55(4)
Acetone	0.03(8)
EtOH	0.76(1)
1-PrOH	0.8(1)
Allyl alcohol	0.29(4)

A7. Appendix to Chapter 7

A7.1 Appendix Notes

Appendix Note 1 Validation of the machine learning approach.

To extract the weights of Cu and Zn species, conventional linear combination analysis (LCA) for the Cu K-edge was used, while for the Zn K-edge, the LCA fitting faced some limitations. First of all, as demonstrated in my previous co-authored study,[115] the Cu-Zn samples contain a Zn-oxide phase with a much higher degree of disorder and thus vary in structure from the wurtzite-type ZnO that was used as a reference. Further, alloy formation under reaction conditions can lead to a heterogenous mix of different Cu-Zn alloy structures (Cu-rich versus Zn-rich structures), while for our reference sample, the common $Cu_{70}Zn_{30}$ brass foil was used. To overcome these limitations, a machine learning (ML) approach was developed, which is described in more detail in the previous study.[115] The ML approach is based on the extraction of radial distribution functions of neighboring atoms from EXAFS data. In particular, a neural network (NN) is trained by using large sets of theoretically relevant structure models (oxide, fcc, and non-fcc phases) obtained from molecular dynamics (MD) and Monte Carlo (MC) simulations using empirical force field models. After validation of the NN with known structures (Zn, CuZn, and ZnO), the NN was applied to the EXAFS data of the *operando* measurements to extract the partial RDFs. The weight of different phases was obtained by integrating specific peaks of the partial RDFs divided by the true number of neighbors for the corresponding phase (oxide, fcc, or non-fcc). Compared to the LCA fitting, the NN-EXAFS analysis showed that a much higher contribution of an oxide phase remained in the sample even at -1.0 V. To verify those results, a conventional FEFFIT was applied to the data after 1 h of reduction, and a coordination number of 0.37 ± 0.26 was received (Figure A7.7). This equals an oxide contribution of around 9 ± 6 %, which is in agreement with the results from the ML approach (ca. 12 %). Additionally, the LCA analysis (LCA2) was performed by using the spectrum collected under ocp as a reference instead of the wurtzite-type ZnO, which also resulted in higher amounts of this initial oxide structure (ca. 6 %) after 1 hour of reduction (Figure 7.3). The trained NN could not be applied to the Zn K-edge XANES data set used for the cyclic voltammogram measurements in this study in Section 7.3.4 due to a glitch in the

EXAFS spectra at 9878 eV (k-value: 7.5) of the QXAFS data collected at the ROCK beamline of the SOLEIL synchrotron. However, when performing the LCA fit on the QXAFS data from the initial reduction prior to the CV scan, the results for the weights of the species (Zn foil, CuZn foil, and wurtzite-tye ZnO) are much closer to those of the NN-EXAFS analysis performed for the data collected at the SuperXAS-X10DA beamline. Moreover, as already observed before, the general redox behavior of our sample remained the same and followed the same trends. Therefore, for the CV data set, only the conventional LCA was used for both edges (Cu and Zn K-edge) to follow the changes of species during the CV scans.

A7.2 Appendix Figures

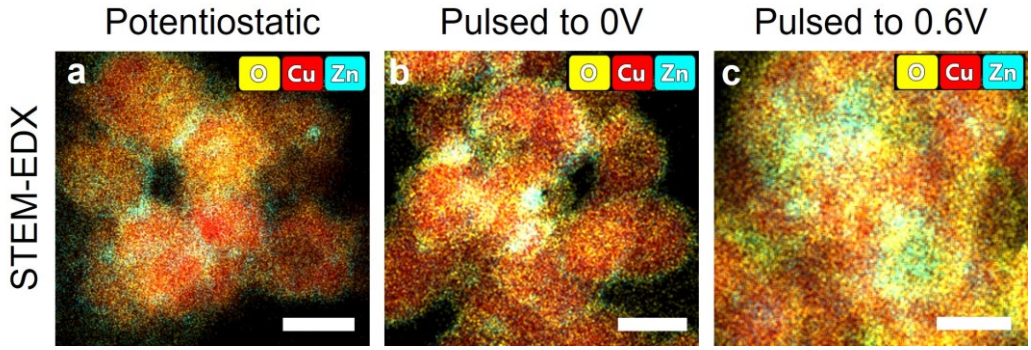

Figure A7.1 STEM-EDX images of the Cu-Zn catalyst after different conditions with oxygen signal. (a) shows the catalyst after 1 h of potentiostatic CO_2RR, (b) after 1 h of pulsed CO_2RR with E_a = 0 V and (c) after 1 h of pulsed CO_2RR with E_a = 0.6 V, while E_c = -1.0 V, t_c = 4 s and t_a = 1 s were fixed. The given scale bars correspond to 20 nm.

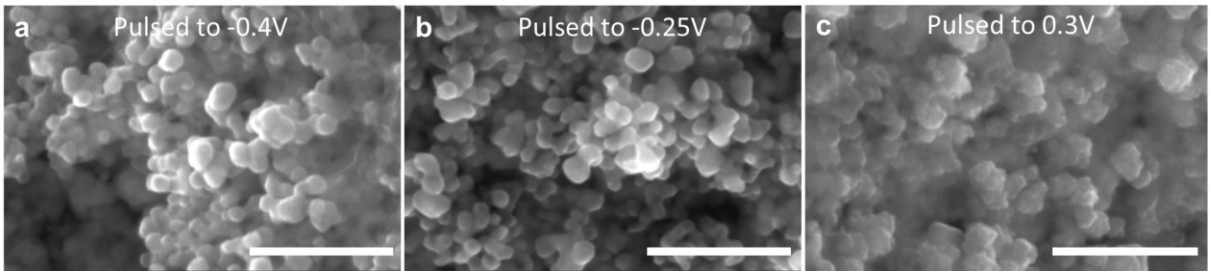

Figure A7.2 SEM images of Cu-Zn after different pulse protocols on carbon paper. E_c = -1.0 V with t_c = 4 s and t_a = 1 s were fixed during pulsed CO_2RR for 1 h, while the anodic potential was varied in (a) to E_a = -0.4 V, in (b) to E_a = -0.25 V and in (c) to E_a = 0.3 V. The scale bar corresponds to 300 nm.

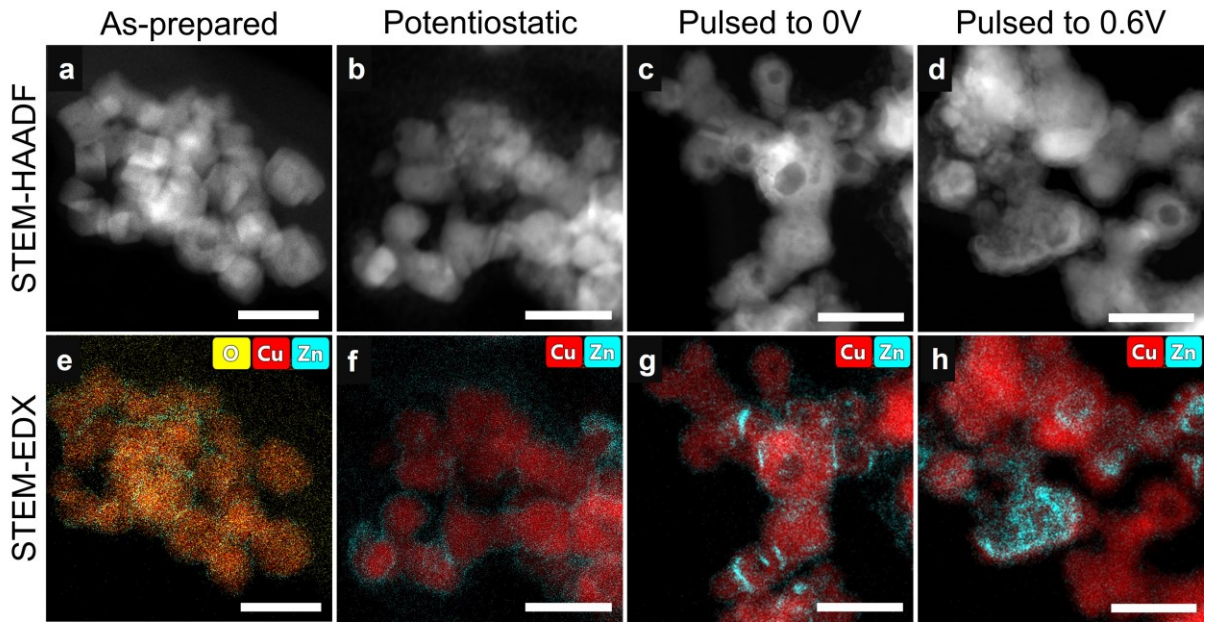

Figure A7.3 Additional STEM-HAADF and STEM-EDX images of the Cu-Zn catalyst after different conditions in the upper and lower panel, respectively. (a,e) show the as-prepared state, (b,f) after 1 h of potentiostatic CO_2RR, (c,g) after 1 h of pulsed CO_2RR with E_a = 0 V, and (d,h) after 1 h of pulsed CO_2RR with E_a = 0.6 V (fixed E_c = -1.0 V, t_c = 4 s and t_a = 1 s). The given scale bars correspond to 50 nm.

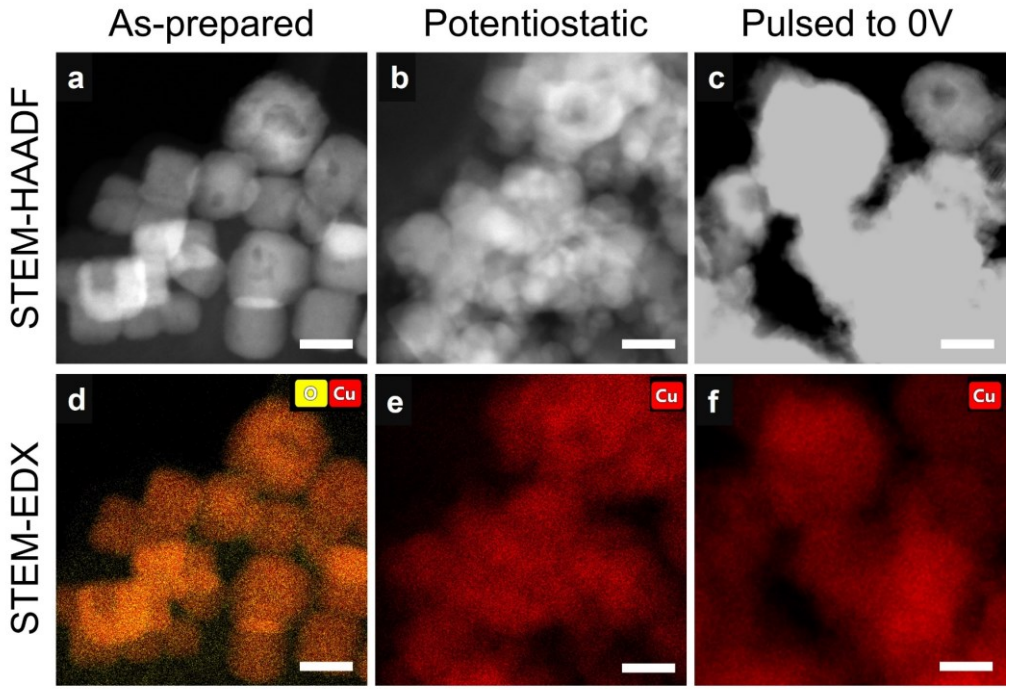

Figure A7.4 STEM-HAADF and STEM-EDX images of the bare Cu_2O cubes after different conditions in the upper and lower panel, respectively. (a,d) show the as-prepared state, (b,e) after 1 h of potentiostatic CO_2RR and (c,f) after 1 h of pulsed CO_2RR with E_a = 0 V (fixed E_c = -1.0 V, t_c = 4 s and t_a = 1 s). The given scale bars correspond to 20 nm.

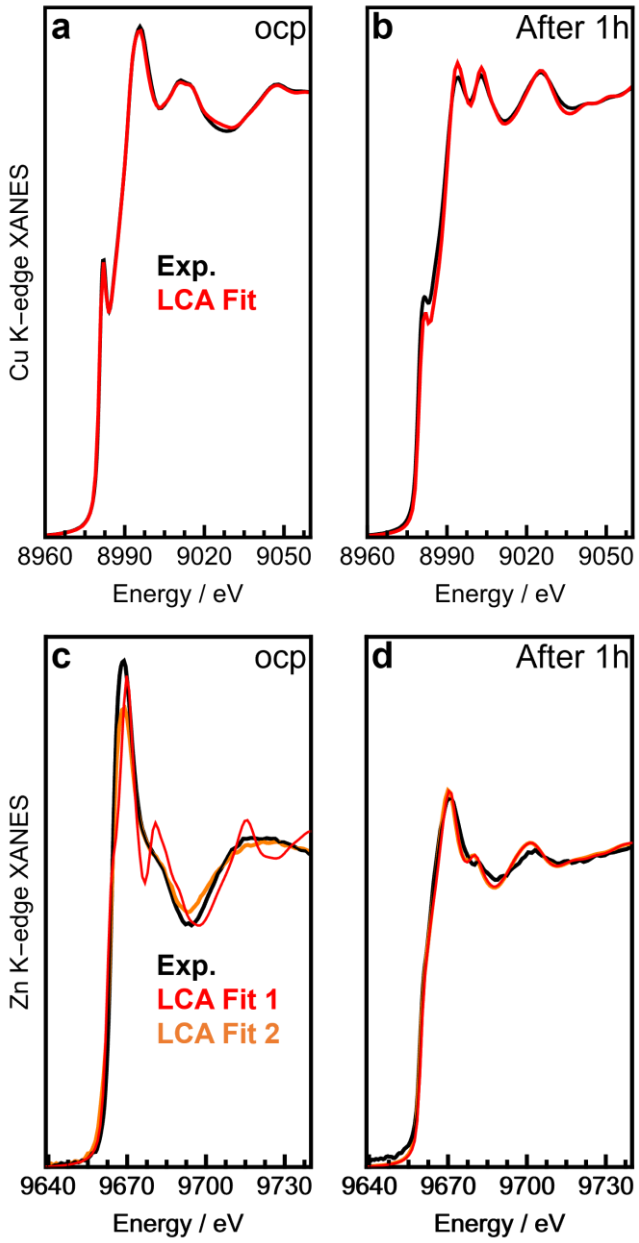

Figure A7.5 Exemplary LCA fits of the experimental XANES spectra. (a) and (b) Cu K-edge under ocp and after 1 h of initial static CO_2RR at -1.0 V, respectively. (c) and (d) Zn K-edge under ocp and after 1 h of initial static CO_2RR at -1.0 V fitted with LCA1 (with standard references) and LCA2 (oxide reference equals as-prepared state spectra), respectively.

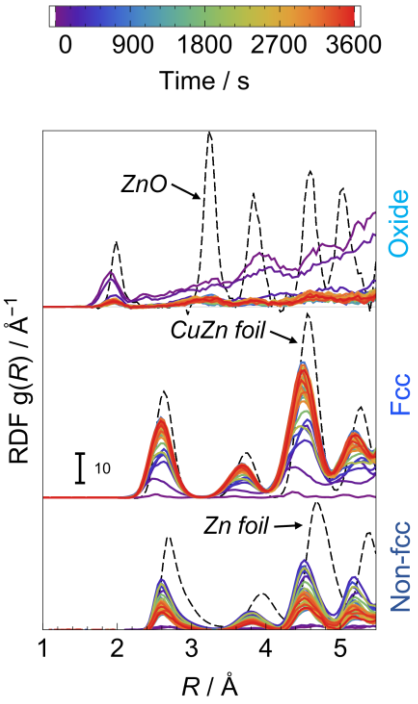

Figure A7.6 Time-dependent evolution of the radial distribution functions *g(R)* (RDFs) obtained by the NN-EXAFS analysis from *operando* Zn K-edge EXAFS data during initial static CO_2RR for 1 h at -1.0 V. The partial RDFs correspond to an oxide phase, a metallic phase with fcc-type structure and a metallic phase with non-fcc type structure. For clarity the RDFs are shifted vertically.

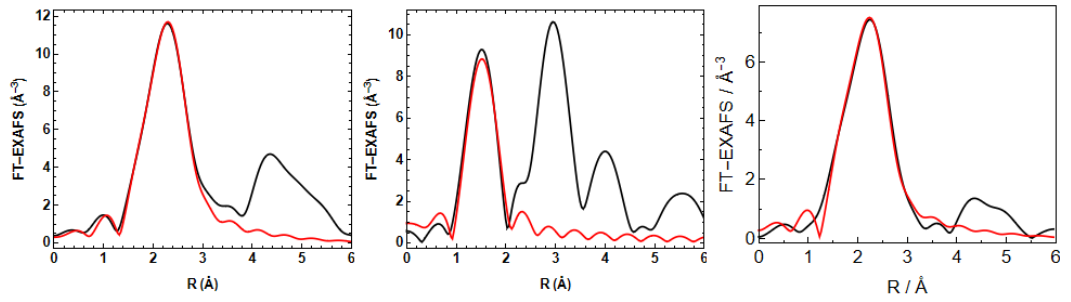

CuZn foil		
R-factor	0.000189	
Variable	Value	Uncertainty
e1	2.5773	0.355723
delr1	0.060969	0.002895
sigma1	0.014392	0.000613
s1	1.24733	0.063791
{R:, 2.61717}		

ZnO		
R-factor	0.016682	
Variable	Value	Uncertainty
e1	1.99864	0.747265
delr1	-0.007439	0.011008
sigma1	0.	0.002244
s1	0.777011	0.080887
{R:, 1.96636}		

after 1h / 500 spec ave		
R-factor	0.005101	
Variable	Value	Uncertainty
e1	0.73604	0.676938
delr1	0.02642	0.006839
delr2	0.020039	0.025982
sigma1	0.014259	0.000889
sigma2	$2.\times10^{-6}$	0.014064
n1	7.79367	0.550164
n2	0.374612	0.261978
{R_{CuZn}:, 2.58262, R_{ZnO}:, 1.99384}		

Figure A7.7 NN-EXAFS analysis results were verified by applying a conventional FEFFIT to the data after 1 h of at -1.0 V, where a coordination number of 0.37 ± 0.26 for the oxide species (equals a fraction of 9 ± 6 %) was obtained in agreement with the results from the ML approach.

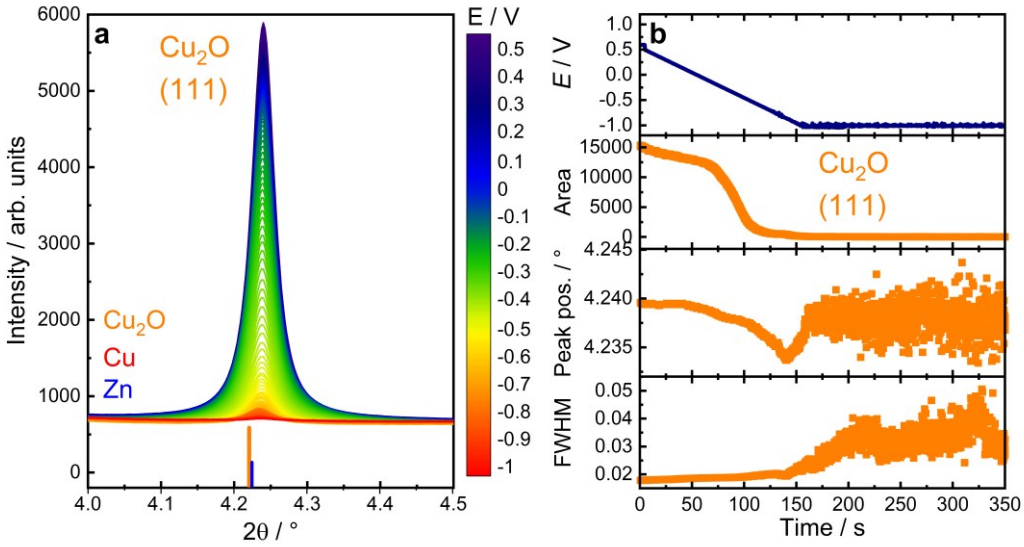

Figure A7.8 Extract of HE-XRD patterns of $Cu_2O(111)$ and corresponding fits of Cu-Zn catalyst during LSV and static CO_2RR conditions. (a) Extract of averaged XRD pattern during the LSV scan from ocp to -1.0 V with a scan rate of 10 mV s^{-1}. (b) Area (second row), peak position (third row), and FWHM (fourth row) extracted from fits of $Cu_2O(111)$ with respect to the applied potential (top). The XRD patterns correspond to the average of 5 XRD patterns, acquired with 0.2 s/diffractogram, that can be translated into a time resolution of 1 s/diffractogram shown here.

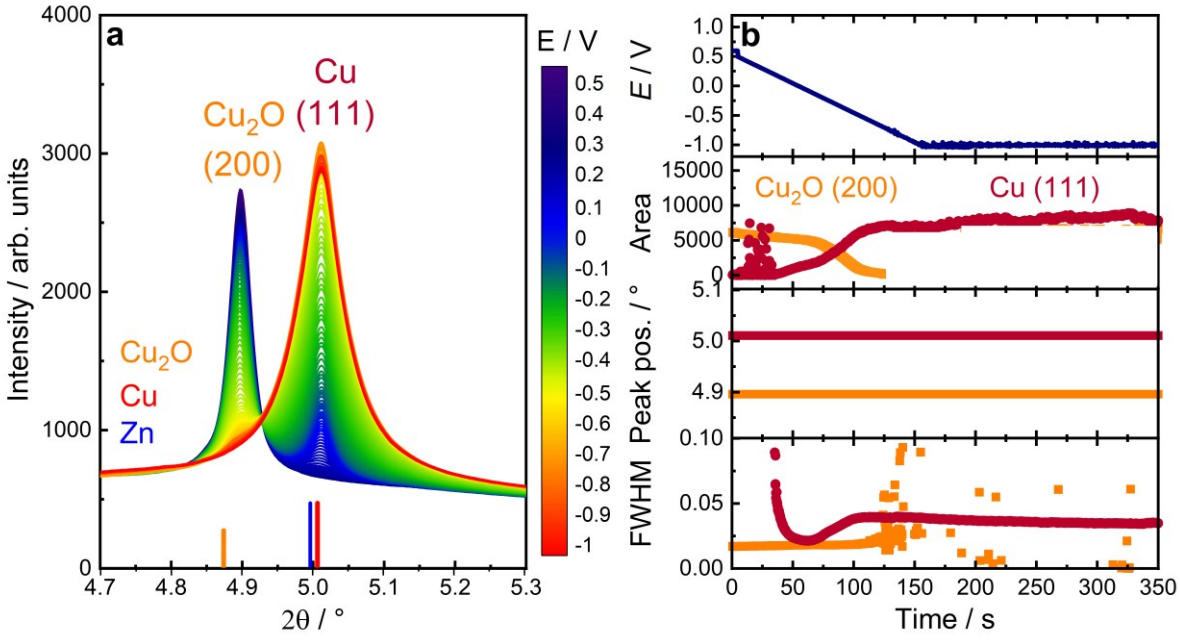

Figure A7.9 Extract of HE-XRD pattern of $Cu_2O(200)$ and Cu(111) and corresponding fits of Cu-Zn catalyst during LSV and static CO_2RR conditions. (a) Extract of averaged XRD pattern during the LSV scan from ocp to -1.0 V with a scan rate of 10 mV/s. (b) Area (second row), peak position (third row), and FWHM (fourth row) extracted from fits of $Cu_2O(200)$ and Cu(111) with respect to the applied potential (top). The XRD patterns correspond to the average of 5 XRD patterns, acquired with 0.2 s/diffractogram, that can be translated into a time resolution of 1 s/diffractogram shown here.

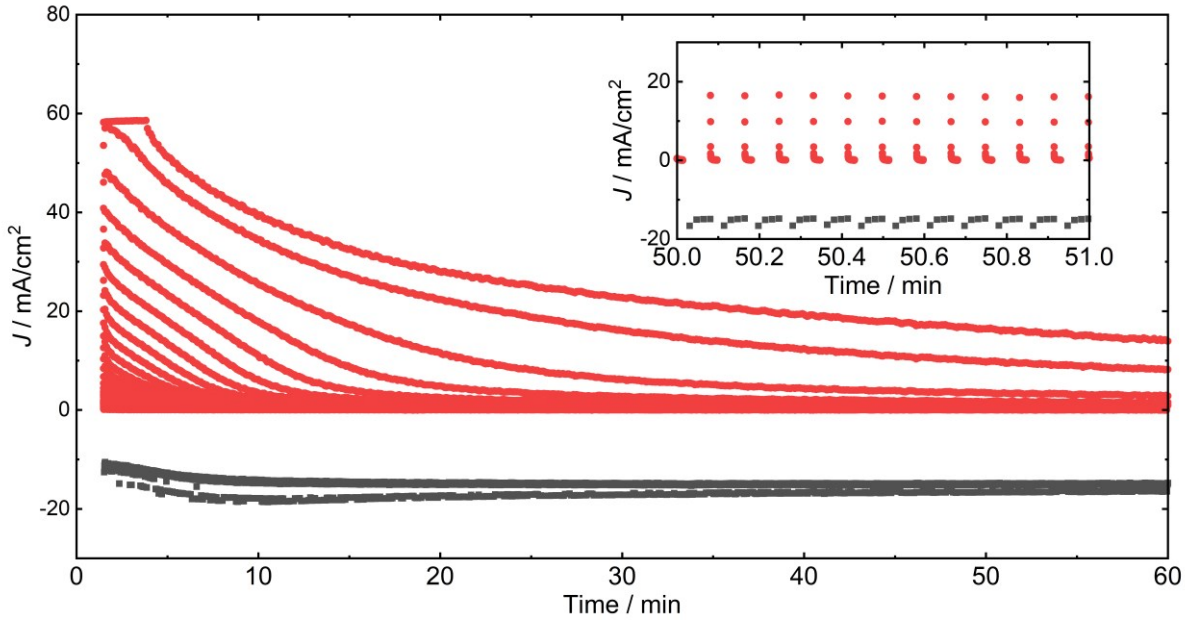

Figure A7.10 Temporal evolution of the current density *J* of the Cu-Zn catalyst under pulsed electrolysis with E_c = -1.0 V, E_a = 0 V, and t_c = 4 s, and t_a = 1 s during 1 h of reaction.

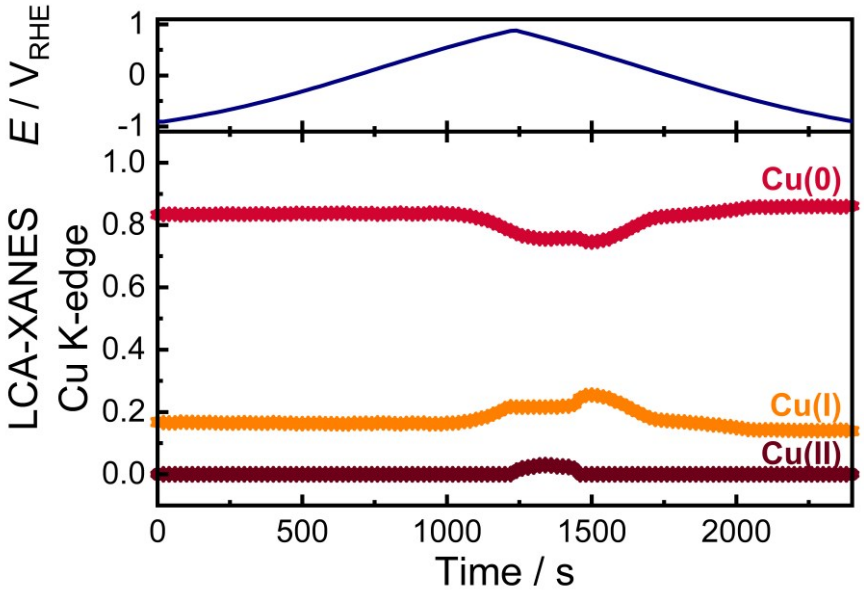

Figure A7.11 LCA-XANES analysis results of Cu K-edge of pre-reduced Cu-Zn catalyst during a CV scan from -0.9 V → 0.9 V → -0.9 V with corresponding applied potential.

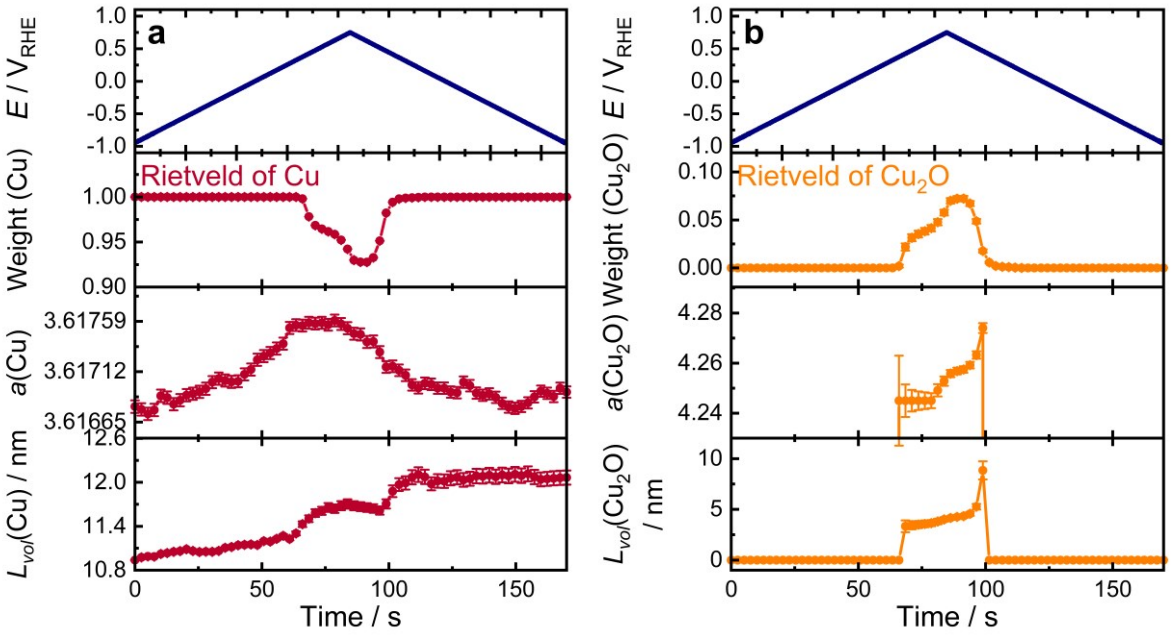

Figure A7.12 Rietveld analysis of HE-XRD pattern of Cu and Cu_2O of the Cu-Zn catalyst during a CV from -1.0 V → 0.7 V → -1.0 V. Weight (second column), lattice parameter *a* (third column) and coherence length L_{vol} (fourth column) in respect to the applied potential (top) of Cu (a) and Cu_2O (b).

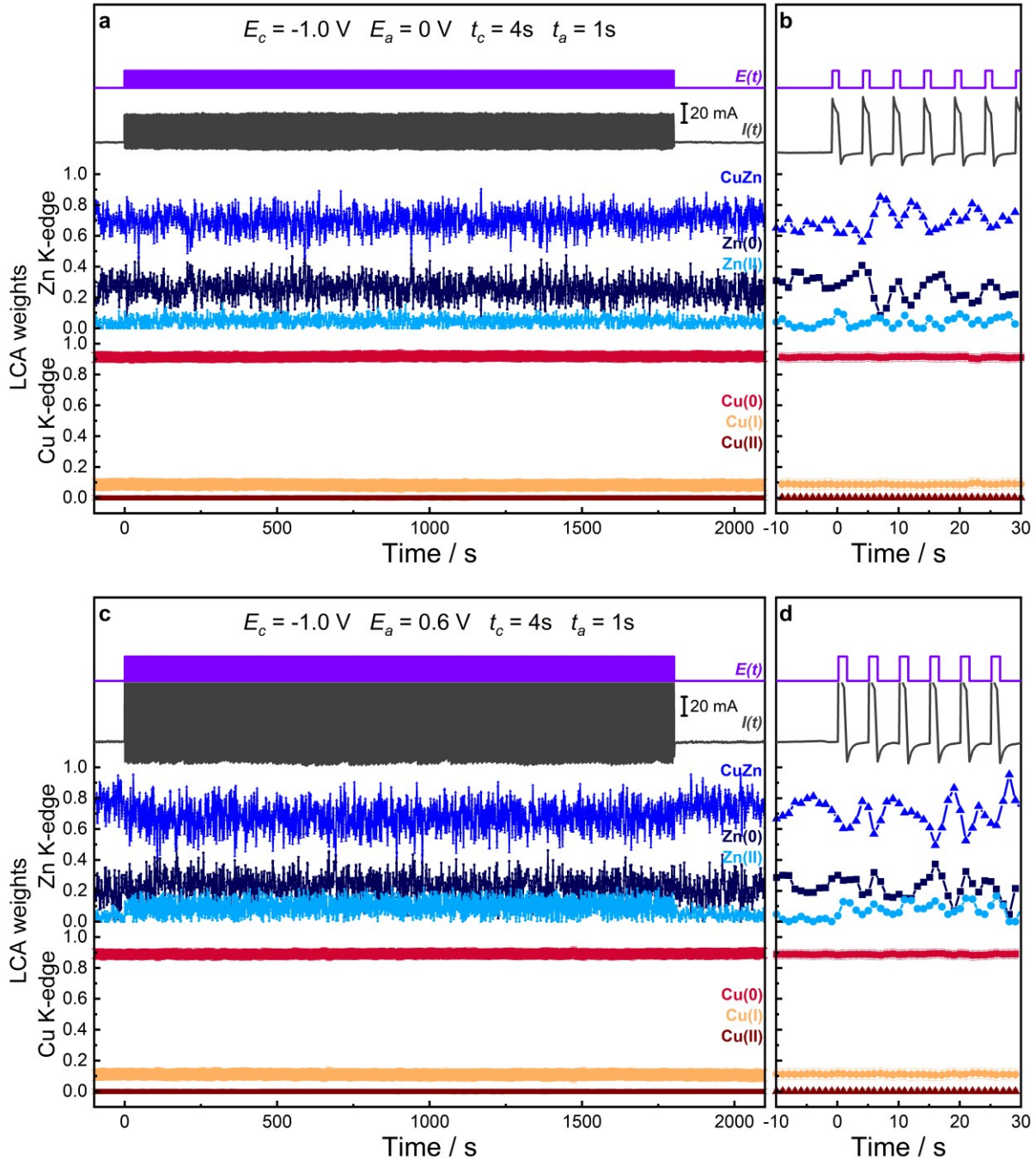

Figure A7.13 LCA-XANES analysis results of Zn and Cu K-edge of pre-reduced Cu-Zn catalyst during pulsed CO_2RR with t_c = 4 s and t_a = 1 s. E_c is constant at -1.0 V, while E_a = 0 V in (a,b) and 0.6 V in (c,d). (b,d) show an extract of the full-time pulsed CO_2RR for better visibility.

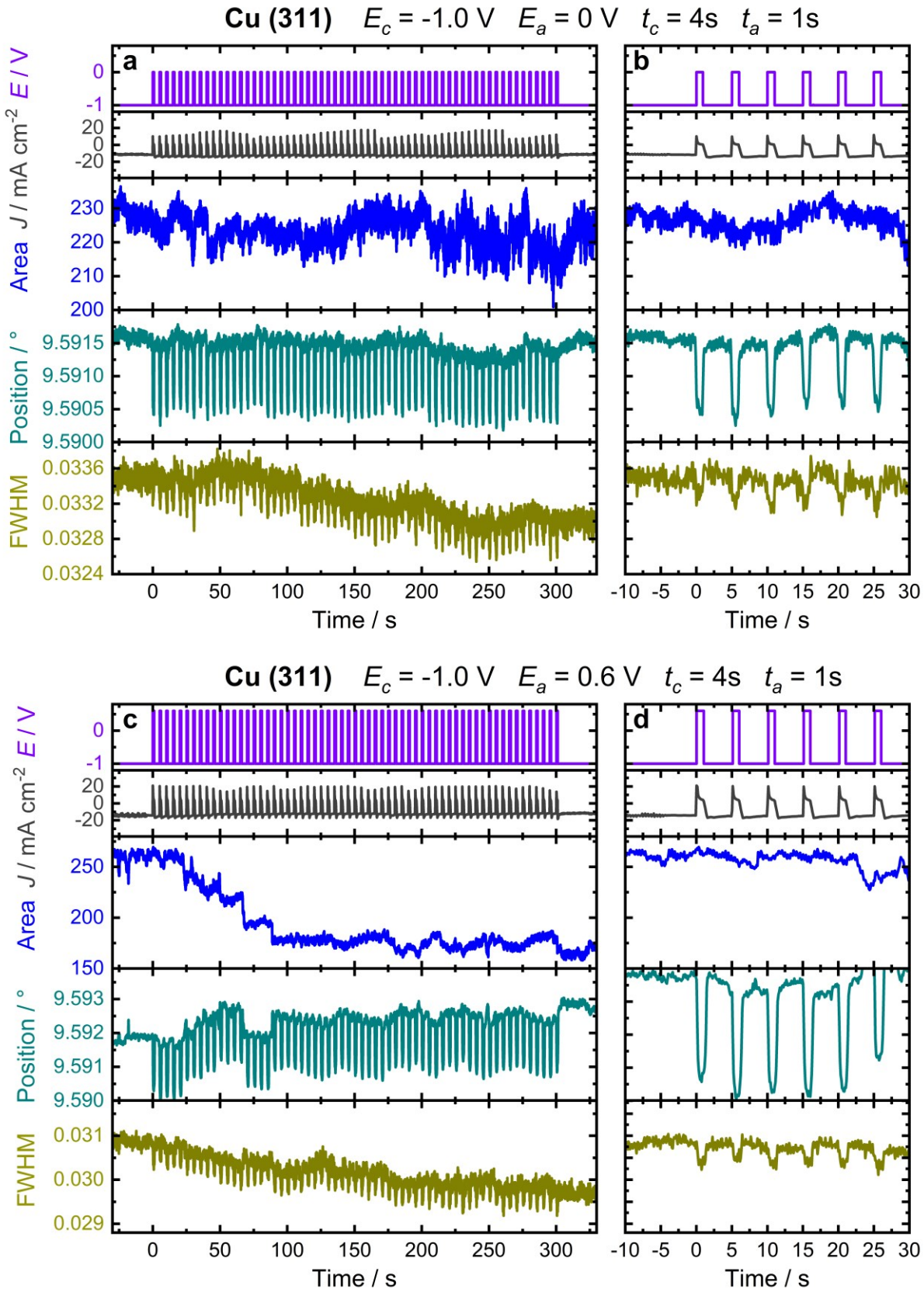

Figure A7.14 Temporal evolution of the area, peak position, and FWHM extracted from the fits of Cu(311) of the HE-XRD patterns with respect to the applied potential and current density (top) during pulsed CO_2RR with t_c = 4 s and t_a = 1 s. E_c is constant at -1.0 V, while E_a = 0 V in (a,b) and 0.6 V in (c,d). (b,d) show an extract of the full-time pulsed CO_2RR for better visibility.

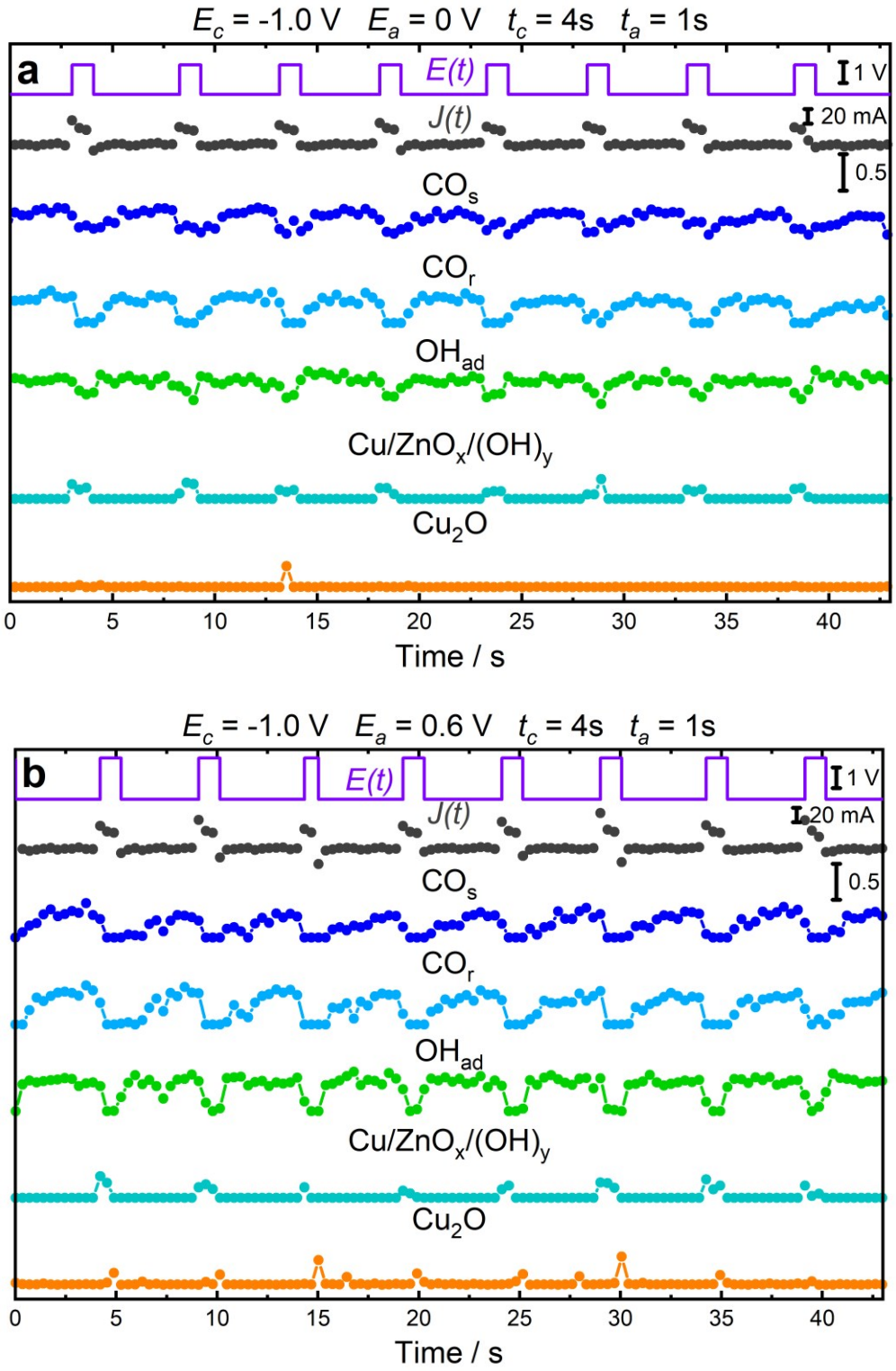

Figure A7.15 Temporal evolution of the chemical state and adsorbate coverage as Cu-CO stretching (CO_s, 360 cm^{-1}) and rotation (CO_r, 280 cm^{-1}) vibrations, OH_{ad} vibration on Cu (490 cm^{-1}), $Cu/ZnO_x/(OH)_y$ species (370 cm^{-1}) and Cu_2O species (405, 530, 610 cm^{-1}) obtained by fitting the intensities of the bands from the SERS spectra in respect to the applied potential and current density (top) during pulsed CO_2RR with t_c = 4 s and t_a = 1 s. E_c is constant at -1.0 V, while E_a = 0 V in (a,b) and 0.6 V in (c,d). (b,d) show an extract of the full-time pulsed CO_2RR for better visibility.

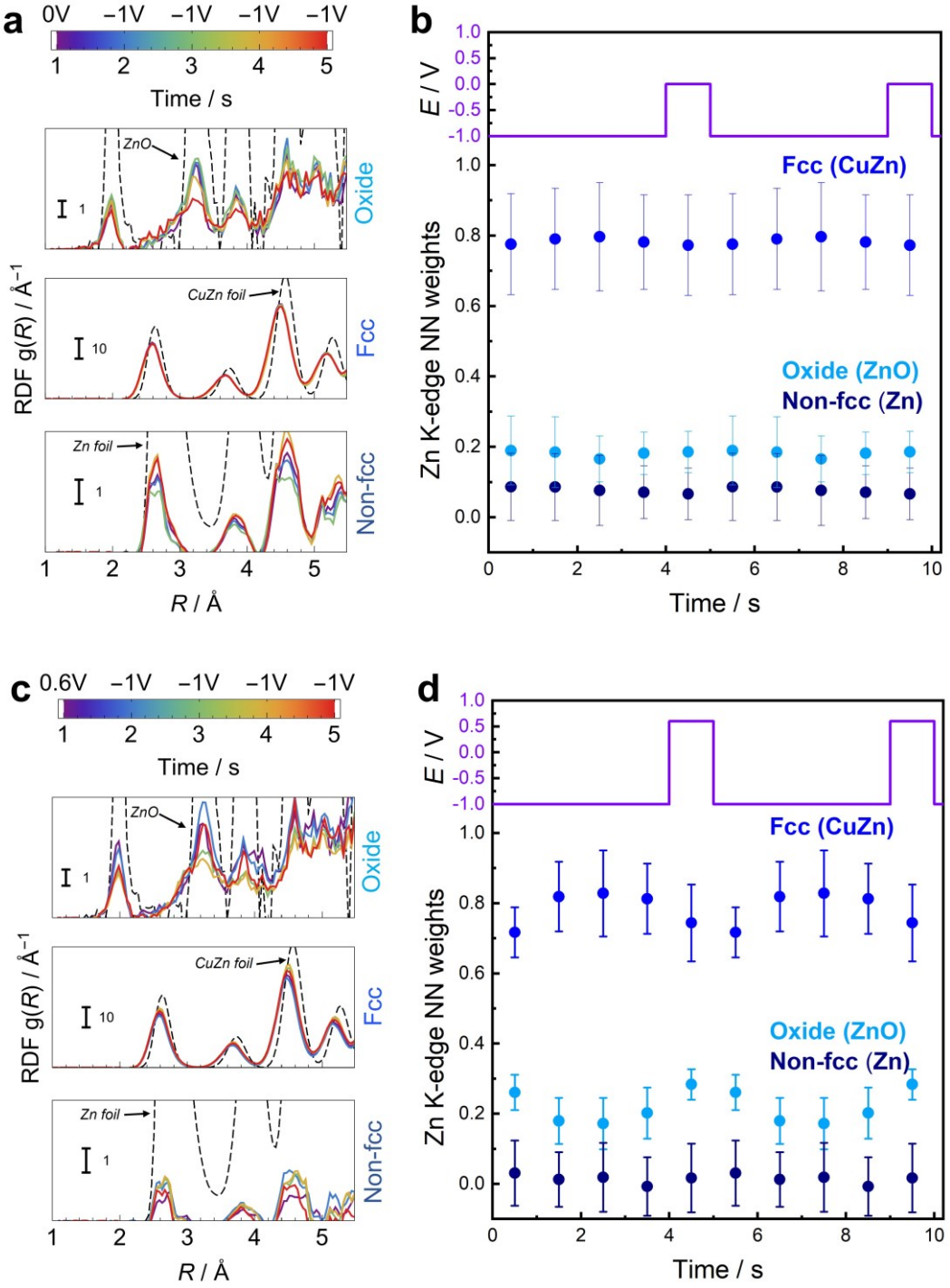

Figure A7.16 Averaged time-dependent evolution of the radial distribution functions *g(R)* (RDFs) and the concentrations obtained by the NN-EXAFS analysis from *operando* Zn K-edge EXAFS data during pulsed CO_2RR with t_c = 4 s and t_a = 1 s. The partial RDFs correspond to an oxide phase, an fcc-type phase, and a non-fcc-type phase. (a) RDFs during the reduction and oxidation cycle, and (b) NN weights at E_c = -1.0 V and E_a = 0 V. (c) RDFs during the reduction and oxidation cycle, and (d) NN weights at E_c = -1.0 V and E_a = 0.6 V. For clarity the RDFs are shifted vertically.

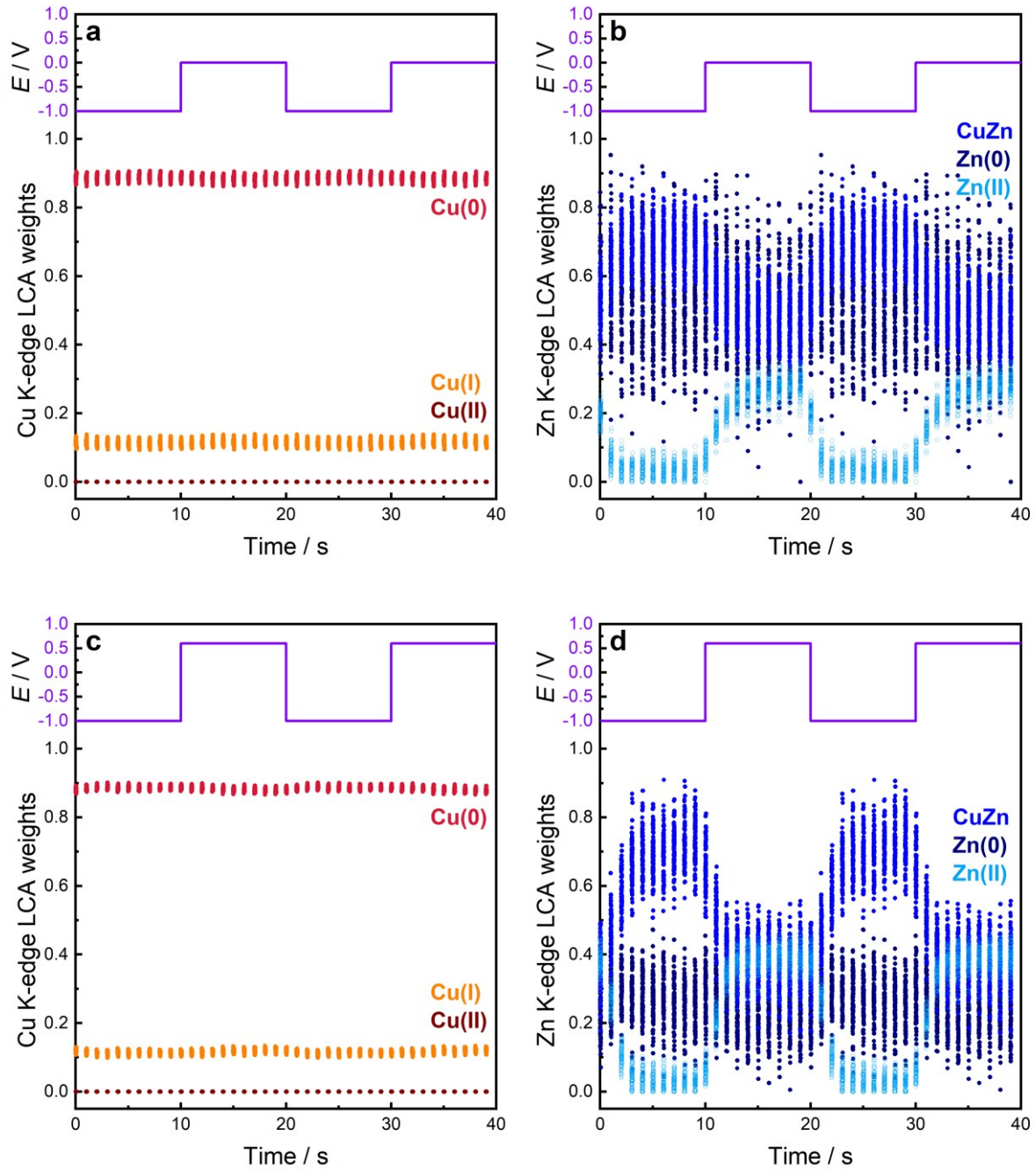

Figure A7.17 LCA-XANES analysis results of Cu and Zn, K-edge of pre-reduced Cu-Zn catalyst, averaged over one pulse sequence during pulsed CO_2RR with $t_c = t_a = 10$ s. E_c is constant at -1.0 V, while $E_a = 0$ V in (a,b) and 0.6 V in (c,d).

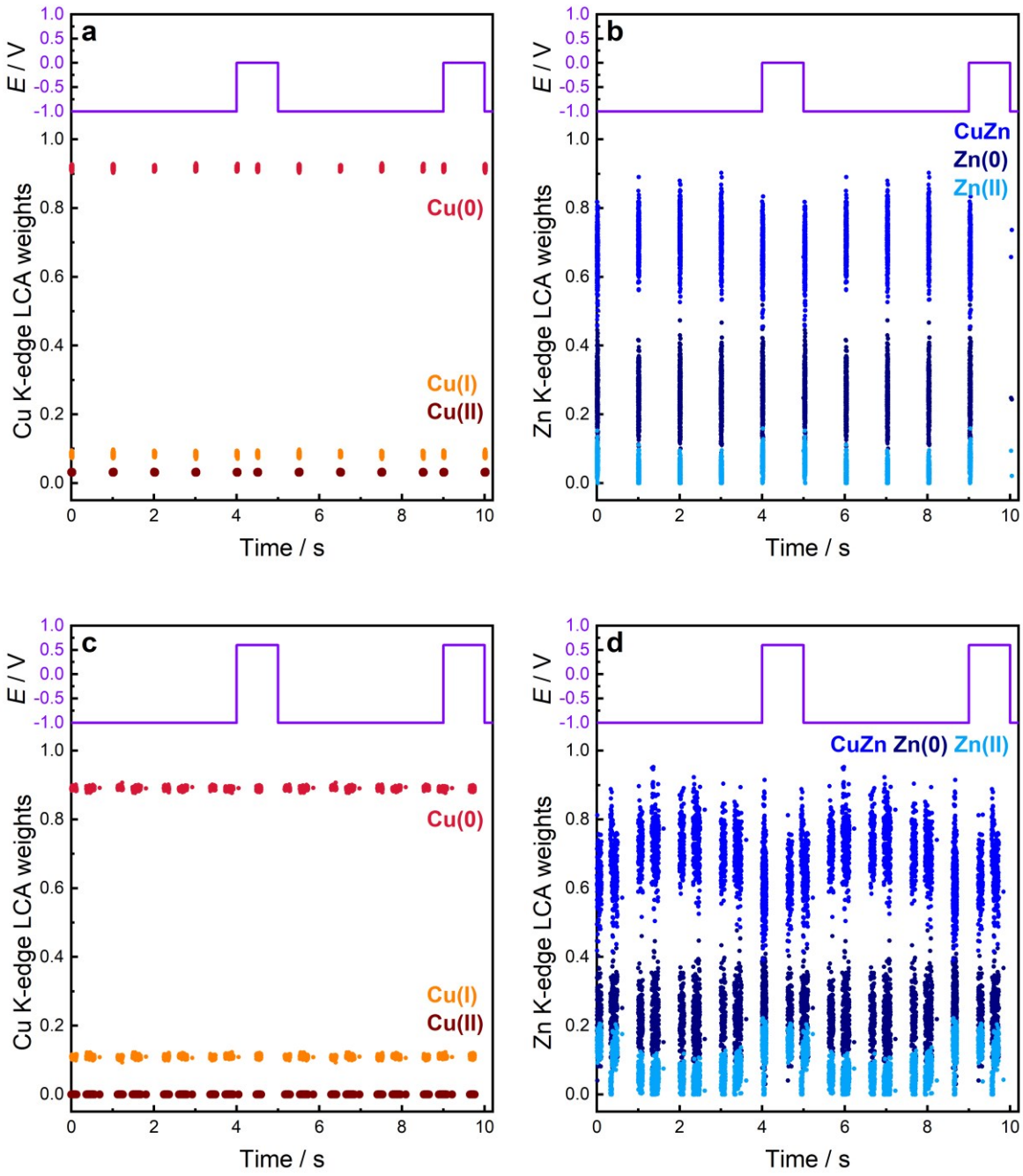

Figure A7.18 LCA-XANES analysis results of Cu and Zn K-edge of pre-reduced Cu-Zn catalyst averaged over one pulse sequence during pulsed CO_2RR with t_c = 4 s and t_a = 1 s. E_c is constant at -1.0 V, while E_a = 0 V in (a,b) and 0.6 V in (c,d).

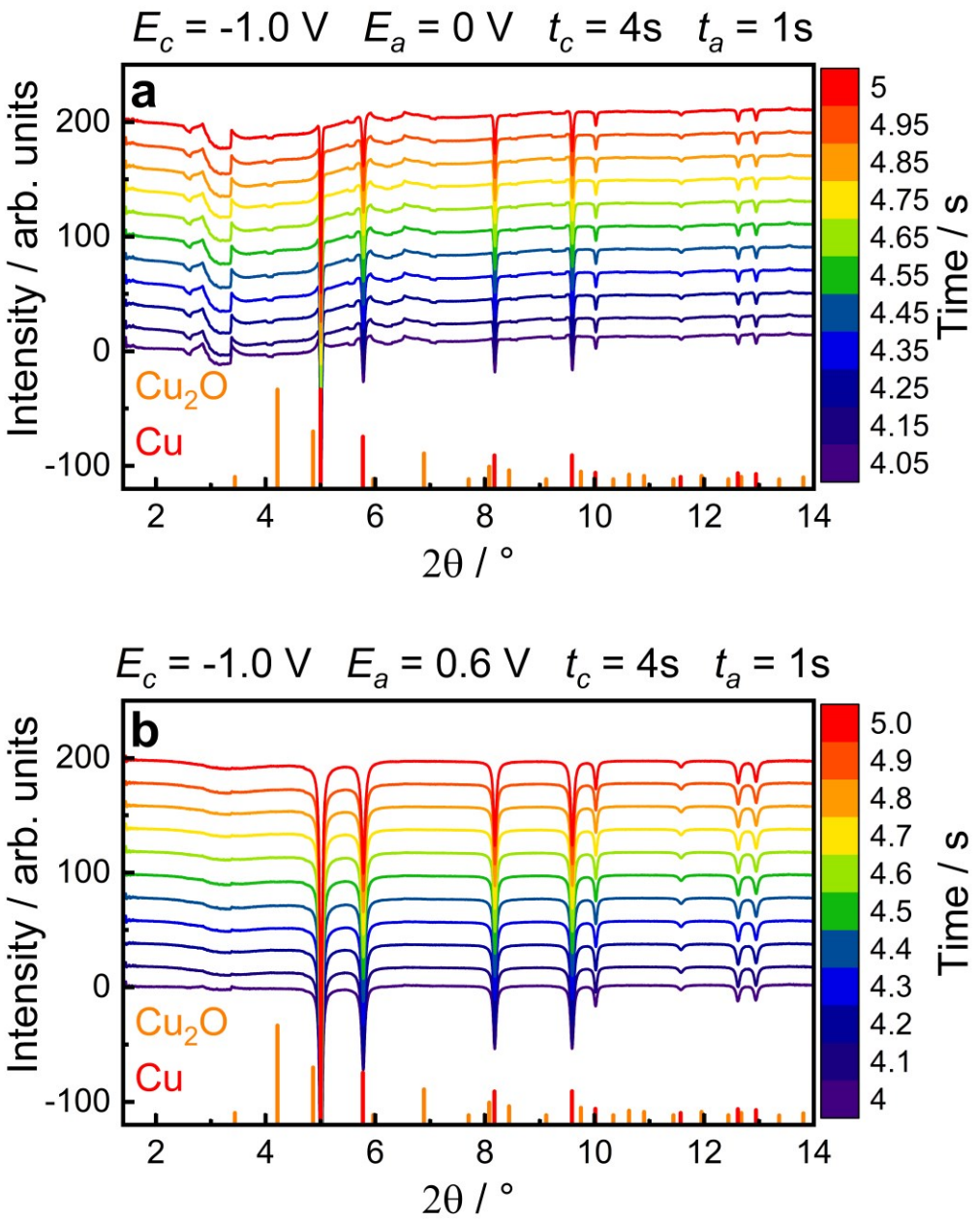

Figure A7.19 Evolution of the differential HE-XRD patterns of the pre-reduced Cu-Zn catalyst during the anodic pulse with t_c = 4 s and t_a = 1 s at E_a = 0 V (a) and 0.6 V (b). The averaged diffraction patterns during the anodic pulse (t = 10 -20 s) are subtracted from the averaged time-dependent diffraction pattern collected under pulsed CO_2RR conditions.

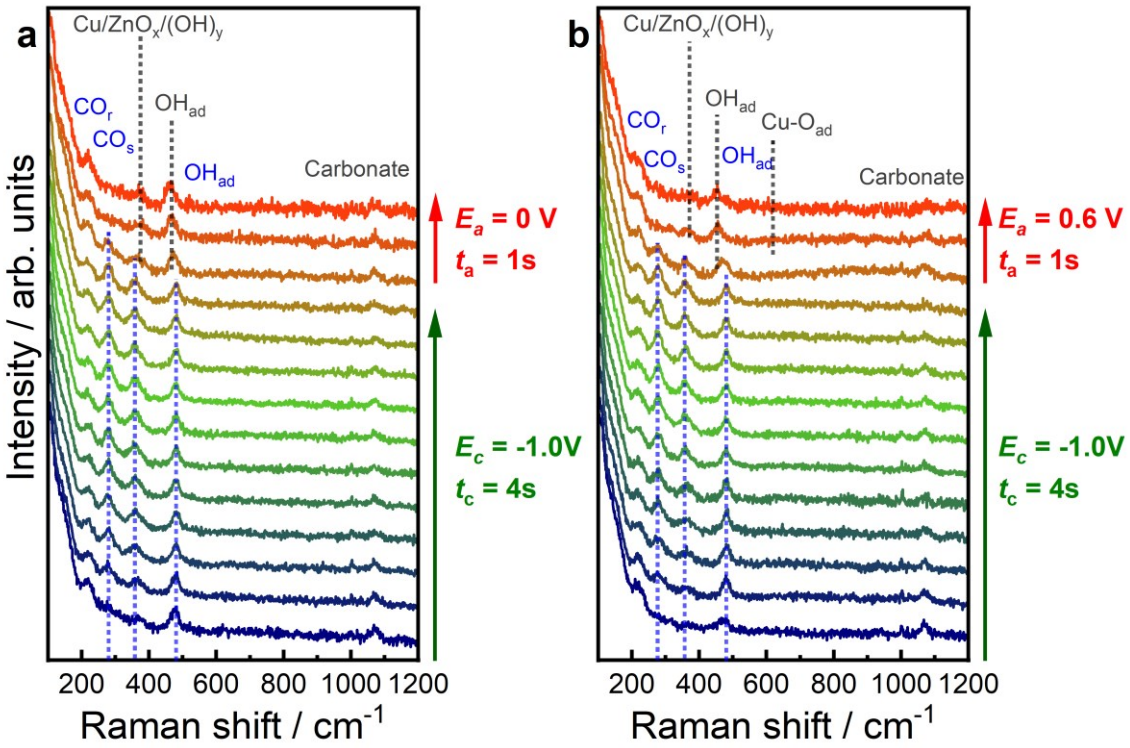

Figure A7.20 Evolution of the averaged SERS spectra of the pre-reduced Cu-Zn catalyst from 150-1200 cm^{-1} during one pulse sequence with t_c = 4 s and t_a = 1 s at E_a = 0 V (a) and 0.6 V (b). Characteristic bands are marked.

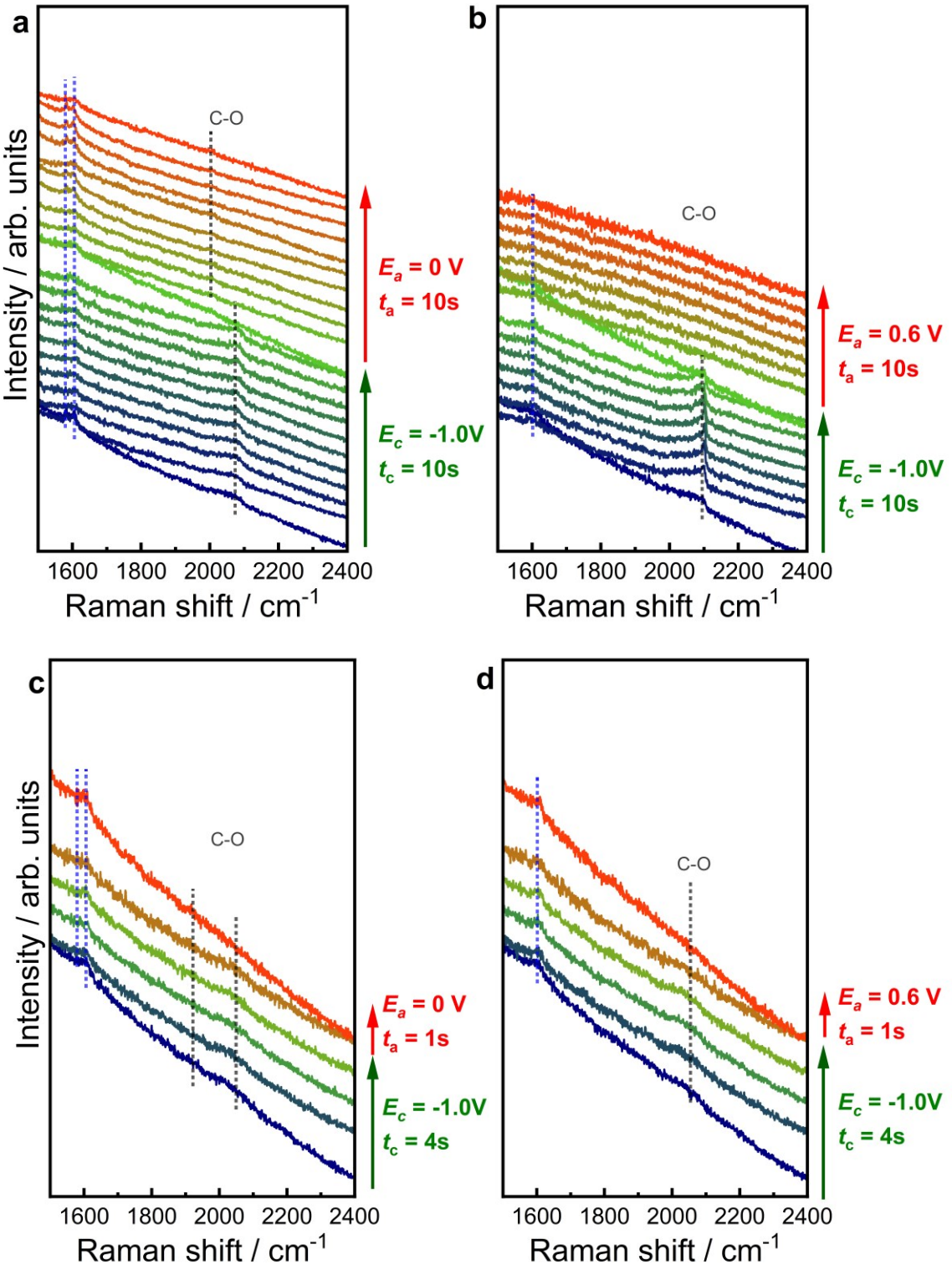

Figure A7.21 Evolution of the averaged SERS spectra of the pre-reduced Cu-Zn catalyst from 1500-2400 cm^{-1} during one pulse sequence with $t_c = t_a = 10$ s (a,b) and $t_c = 4$ s and $t_a = 1$ s (c,d) at $E_a = 0$ V and 0.6 V. Characteristic bands are marked.

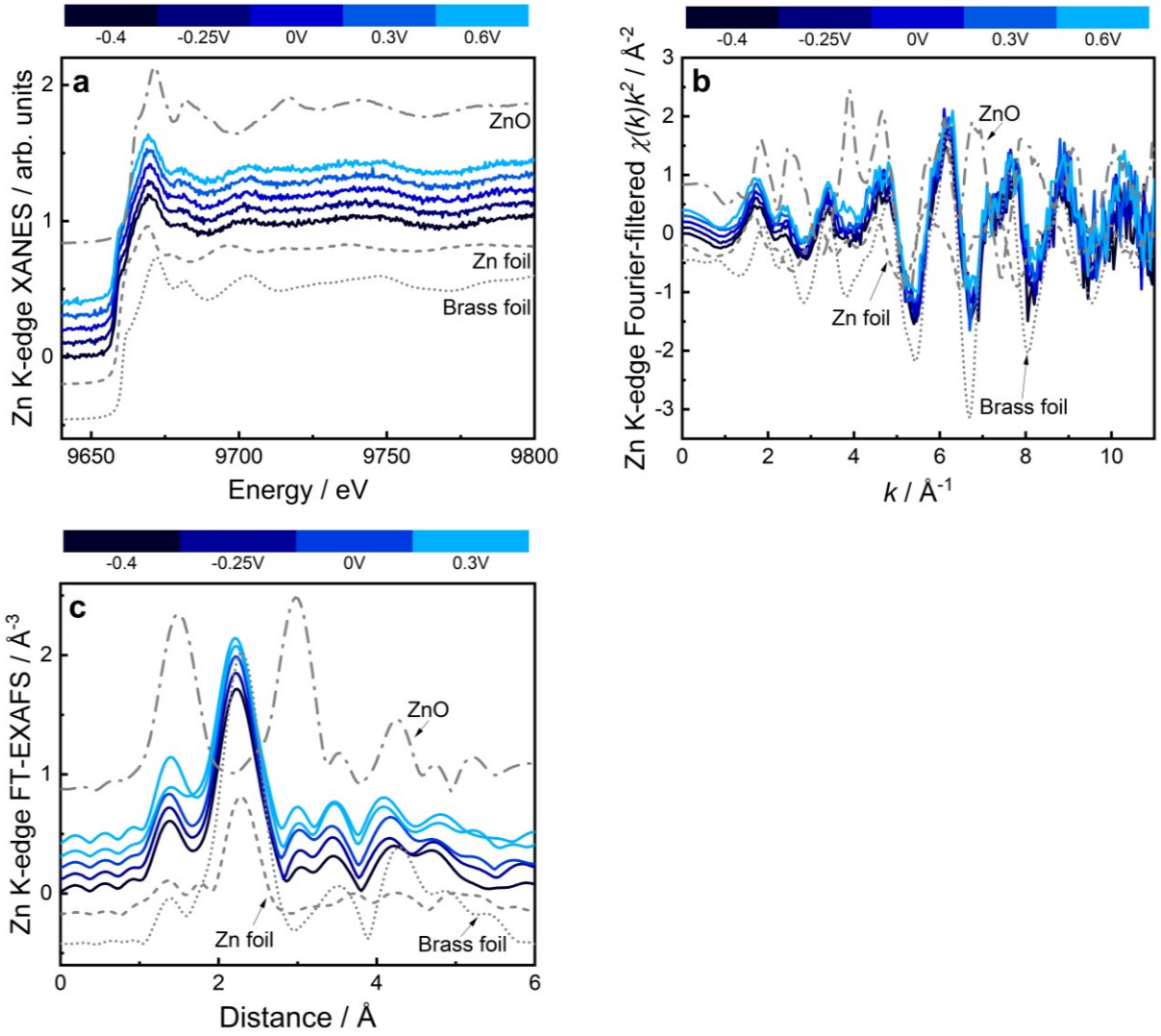

Figure A7.22 "Slow" (standard temporal resolution) *operando* Zn K-edge XANES (a), k-space (b), and EXAFS (c) data during pulsed CO_2RR with t_c = 4 s and t_a = 1 s at different E_a values, while E_c = -1.0 V. All data is shown with an offset in the y-axis.

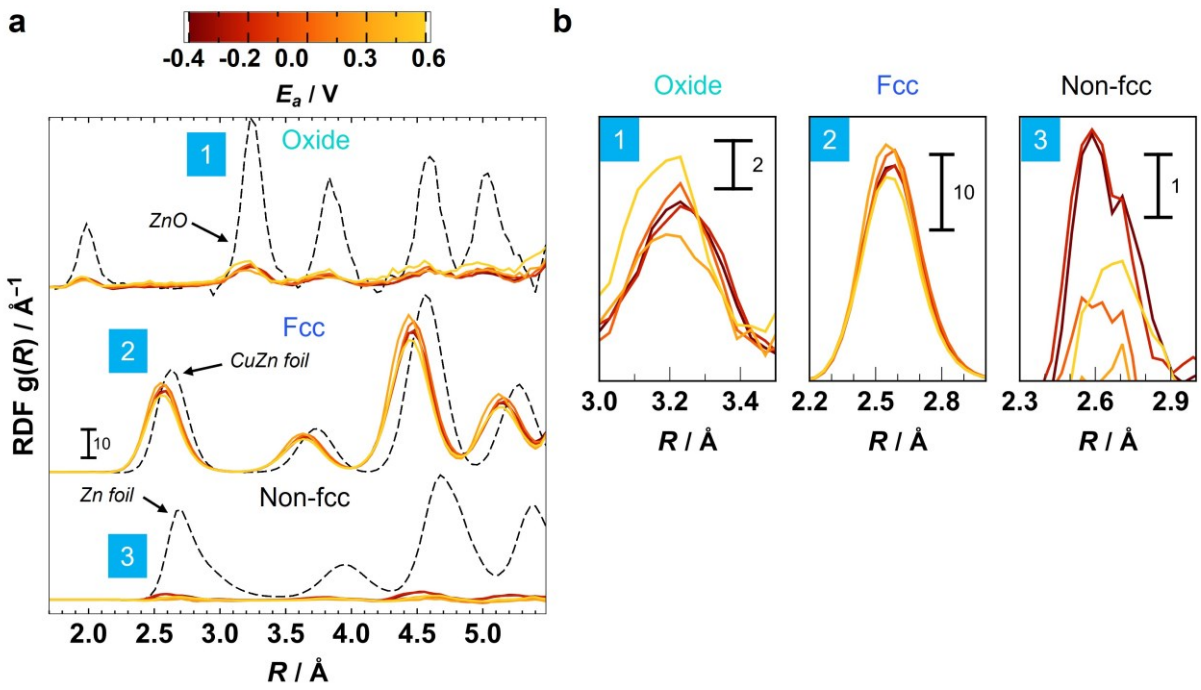

Figure A7.23 RDFs obtained by the NN-EXAFS analysis from *operando* Zn K-edge EXAFS data during pulsed CO_2RR with t_c = 4 s and t_a = 1 s at different E_a values, while E_c = -1.0 V. The partial RDFs correspond to an oxide phase, an fcc-type phase, and a non-fcc-type phase. (a) RDFs are shifted vertically for clarity. (b) shows excerpts of enlarged RDFs.

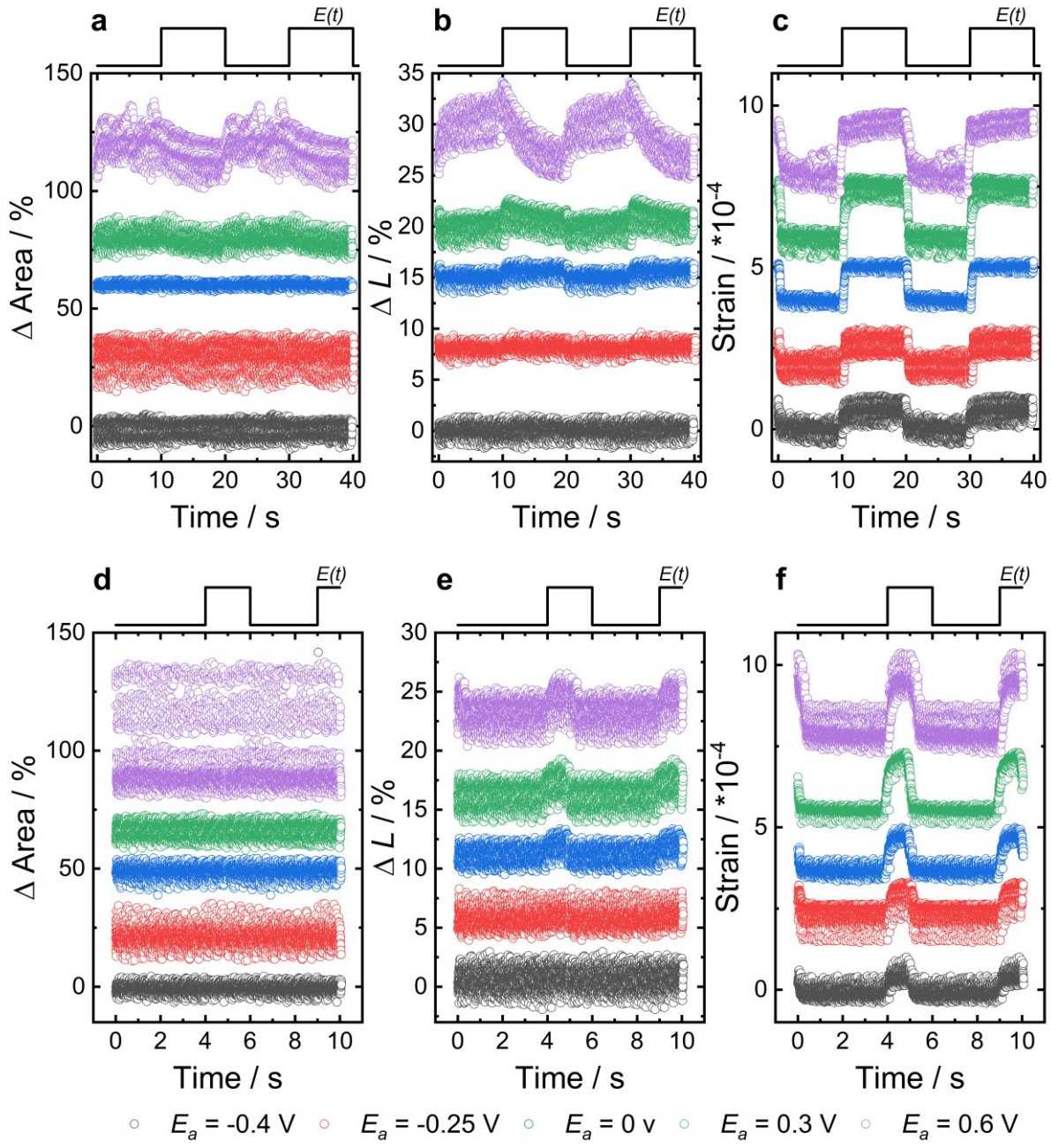

Figure A7.24 Averaged changes of the Cu(311) Bragg peak parameters during a pulse sequence with E_c = -1.0 V and E_a = -0.4 V (black), -0.25 V (red), 0 V (blue), 0.3 V (green) and 0.6 V (purple) for different time lengths by *operando* HE-XRD. (a) Relative changes in the Bragg peak area, (b) the Cu coherence length, and (c) the lattice strain for $t_c = t_a$ = 10 s. (d) Relative changes in the Bragg peak area, (e) the Cu coherence length, and (f) the lattice strain for t_c = 4 s and t_a = 1 s.

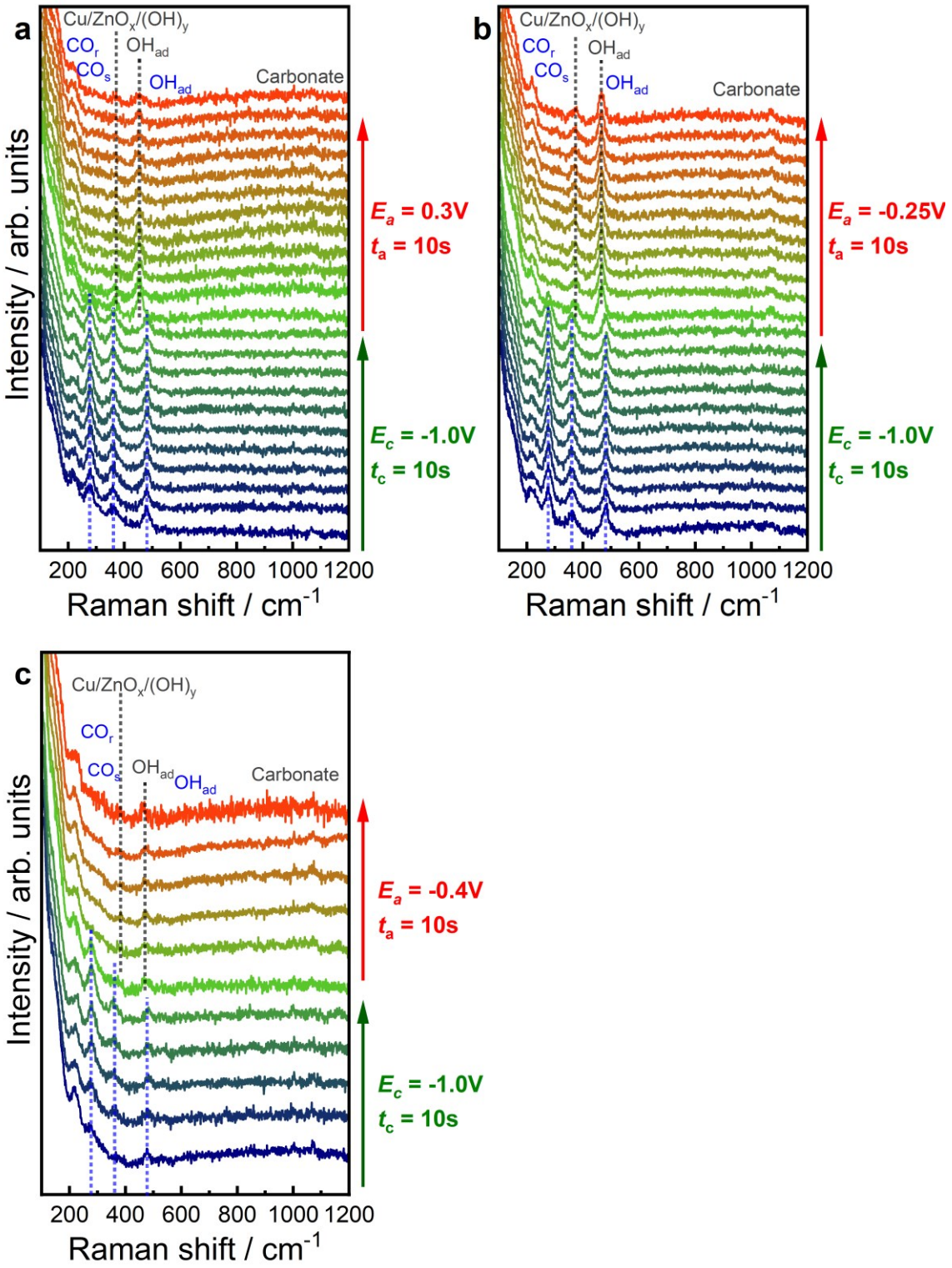

Figure A7.25 Evolution of the averaged SERS spectra of the pre-reduced Cu-Zn catalyst from 150-1200 cm^{-1} during one pulse sequence with t_c = t_a = 10 s at E_a = 0.3 V (a), -0.25 V (b) and -0.4 V (c). Characteristic bands are marked.

A7.3 Appendix Tables

Table A7.1 Cu and Zn composition of as-prepared Zn/Cu_2O NCs (powder) obtained by ICP-MS.

Sample	Cu [at%]	Zn [at%]
As-prepared	93.5(7)	6.5(7)

Table A7.2 Edge lengths and corresponding size distribution of Cu-Zn obtained from the analysis of SEM images in the as-prepared state, after 1h of static CO_2RR and after different pulse protocols (with fixed E_c = -1.0 V, t_c = 4 s and t_a = 1 s).

Sample	Edge length [nm]
As-prepared	23.3 ± 4.4
Static at -1.0 V	26.1 ± 6.5
Pulsed with E_a = -0.4 V	27.1 ± 5.4
Pulsed with E_a = -0.25 V	26.7 ± 5.8
Pulsed with E_a = 0 V	27.2 ± 6.4
Pulsed with E_a = 0.3 V	32.7 ± 7.7
Pulsed with E_a = 0.6 V	34.5 ± 6.0

Table A7.3 Edge lengths and corresponding size distribution of the bare Cu_2O cubes obtained from the analysis of STEM images in the as-prepared state, after 1h of static CO_2RR and after 1 h of pulsed CO_2RR with E_a = 0 V (E_c = -1.0 V, t_c = 4 s and t_a = 1 s).

Sample	Edge length of Cu [nm]
As-prepared	24.3 ± 4.1
Static at -1.0 V	27.4 ± 6.0
Pulsed with E_a = 0 V	34.7 ± 6.1

Table A7.4 Composition of Cu and Zn in the as-prepared state and after 1 h of static CO_2RR of the Cu-Zn catalyst obtained by the comparison of the 2p quasi-*in situ* XPS spectra (Figure 7.6).

Sample	Cu 2p [at%]	Zn 2p [at%]
As-prepared	85	15
Static after -1.0 V	90	10

Bibliography

1. Wang, F.; Harindintwali, J. D.; Yuan, Z.; Wang, M.; Wang, F.; Li, S.; Yin, Z.; Huang, L.; Fu, Y.; Li, L.; Chang, S. X.; Zhang, L.; Rinklebe, J.; Yuan, Z.; Zhu, Q.; Xiang, L.; Tsang, D. C. W.; Xu, L.; Jiang, X.; Liu, J.; Wei, N.; Kästner, M.; Zou, Y.; Ok, Y. S.; Shen, J.; Peng, D.; Zhang, W.; Barceló, D.; Zhou, Y.; Bai, Z.; Li, B.; Zhang, B.; Wei, K.; Cao, H.; Tan, Z.; Zhao, L.-b.; He, X.; Zheng, J.; Bolan, N.; Liu, X.; Huang, C.; Dietmann, S.; Luo, M.; Sun, N.; Gong, J.; Gong, Y.; Brahushi, F.; Zhang, T.; Xiao, C.; Li, X.; Chen, W.; Jiao, N.; Lehmann, J.; Zhu, Y.-G.; Jin, H.; Schäffer, A.; Tiedje, J. M.; Chen, J. M.; Technologies and perspectives for achieving carbon neutrality, *Innov. J.* **2021**, *2* (4), 100180-100202.

2. United Nations Framework Convention on Climate Change (UNFCCC), *Paris Agreement* **2015**, https://unfccc.int/process-and-meetings/the-paris-agreement.

3. Liu, Z.; Deng, Z.; Davis, S.; Ciais, P.; Monitoring global carbon emissions in 2022, *Nat. Rev. Earth Environ.* **2023**, *4*, 205-206.

4. Liu, Z.; Deng, Z.; Davis, S. J.; Giron, C.; Ciais, P.; Monitoring global carbon emissions in 2021, *Nat. Rev. Earth Environ.* **2022**, *3*, 217-219.

5. Intergovernmental Panel on Climate Change (IPCC), *AR6 Synthesis Report: Climate Change* **2023**, https://www.ipcc.ch/report/ar6/syr/.

6. Tian, Y.; Zeng, G.; Rutt, A.; Shi, T.; Kim, H.; Wang, J.; Koettgen, J.; Sun, Y.; Ouyang, B.; Chen, T.; Lun, Z.; Rong, Z.; Persson, K.; Ceder, G.; Promises and Challenges of Next-Generation "Beyond Li-ion" Batteries for Electric Vehicles and Grid Decarbonization, *Chem. Rev.* **2021**, *121* (3), 1623-1669.

7. Van der Spek, M.; Banet, C.; Bauer, C.; Gabrielli, P.; Goldthorpe, W.; Mazzotti, M.; Munkejord, S. T.; Røkke, N. A.; Shah, N.; Sunny, N.; Sutter, D.; Trusler, J. M.; Gazzani, M.; Perspective on the hydrogen economy as a pathway to reach net-zero CO2 emissions in Europe, *Energy Environ. Sci.* **2022**, *15* (3), 1034-1077.

8. Nitopi, S.; Bertheussen, E.; Scott, S. B.; Liu, X. Y.; Engstfeld, A. K.; Horch, S.; Seger, B.; Stephens, I. E. L.; Chan, K.; Hahn, C.; Norskov, J. K.; Jaramillo, T. F.; Chorkendorff, I.; Progress and Perspectives of Electrochemical CO2 Reduction on Copper in Aqueous Electrolyte, *Chem. Rev.* **2019**, *119* (12), 7610-7672.

9. Global CCS Institute, *Global Status of CCS* **2022**, https://status22.globalccsinstitute.com/.

10. Li, W.; Wang, H.; Jiang, X.; Zhu, J.; Liu, Z.; Guo, X.; Song, C.; A short review of recent advances in CO2 hydrogenation to hydrocarbons over heterogeneous catalysts, *RSC Adv.* **2018**, *8* (14), 7651-7669.

11. Hori, Y.; Kikuchi, K.; Murata, A.; Suzuki, S.; Production of Methane and Ethylene in Electrochemical Reduction of Carbon-Dioxide at Copper Electrode in Aqueous Hydrogencarbonate Solution, *Chem. Lett.* **1986**, *15* (6), 897-898.

12. Arán-Ais, R. M.; Gao, D.; Roldan Cuenya, B.; Structure- and Electrolyte-Sensitivity in CO2 Electroreduction, *Acc. Chem. Res.* **2018**, *51* (11), 2906-2917.

13. Tan, X.; Yu, C.; Ren, Y.; Cui, S.; Li, W.; Qiu, J.; Recent advances in innovative strategies for the CO2 electroreduction reaction, *Energy Environ. Sci.* **2021**, *14* (2), 765-780.

14. Hori, Y.; *Electrochemical CO2 Reduction on Metal Electrodes*, Springer New York **2008**, 89-189.

15. Bagger, A.; Ju, W.; Varela, A. S.; Strasser, P.; Rossmeisl, J.; Electrochemical CO2 Reduction: A Classification Problem, *ChemPhysChem* **2017**, *18* (22), 3266-3273.

16. Kuhl, K. P.; Cave, E. R.; Abram, D. N.; Jaramillo, T. F.; New insights into the electrochemical reduction of carbon dioxide on metallic copper surfaces, *Energy Environ. Sci.* **2012**, *5* (5), 7050-7059.

17. Greenblatt, J. B.; Miller, D. J.; Ager, J. W.; Houle, F. A.; Sharp, I. D.; The Technical and Energetic Challenges of Separating (Photo)Electrochemical Carbon Dioxide Reduction Products, *Joule* **2018**, *2* (3), 381-420.

18. Zaza, L.; Rossi, K.; Buonsanti, R.; Well-Defined Copper-Based Nanocatalysts for Selective Electrochemical Reduction of CO2 to C2 Products, *ACS Energy Lett.* **2022**, *7* (4), 1284-1291.

19. Gao, D.; Arán-Ais, R. M.; Jeon, H. S.; Roldan Cuenya, B.; Rational catalyst and electrolyte design for CO2 electroreduction towards multicarbon products, *Nat. Catal.* **2019**, *2* (3), 198-210.

20. Casebolt, R.; Levine, K.; Suntivich, J.; Hanrath, T.; Pulse check: Potential opportunities in pulsed electrochemical CO2 reduction, *Joule* **2021**, *5* (8), 1987-2026.

21. Schlögl, R.; Catalysis 4.0, *ChemCatChem* **2017**, *9* (4), 533-541.

22. Song, X.; Xu, L.; Sun, X.; Han, B.; In situ/operando characterization techniques for electrochemical CO2 reduction, *Sci. China Chem.* **2023**, *66* (2), 315-323.

23. Vasileff, A.; Xu, C.; Jiao, Y.; Zheng, Y.; Qiao, S.-Z.; Surface and Interface Engineering in Copper-Based Bimetallic Materials for Selective CO2 Electroreduction, *Chem.* **2018**, *4* (8), 1809-1831.

24. Sun, Z.; Ma, T.; Tao, H.; Fan, Q.; Han, B.; Fundamentals and Challenges of Electrochemical CO2 Reduction Using Two-Dimensional Materials, *Chem* **2017**, *3* (4), 560-587.

25. Pei, Y.; Zhong, H.; Jin, F.; A brief review of electrocatalytic reduction of CO2-Materials, reaction conditions, and devices, *Energy Environ. Sci.* **2021**, *9* (7), 1012-1032.

26. Kortlever, R.; Shen, J.; Schouten, K. J. P.; Calle-Vallejo, F.; Koper, M. T. M.; Catalysts and Reaction Pathways for the Electrochemical Reduction of Carbon Dioxide, *J. Phys. Chem. Lett.* **2015**, *6* (20), 4073-4082.

27. Zhang, G.-R.; Straub, S.-D.; Shen, L.-L.; Hermans, Y.; Schmatz, P.; Reichert, A. M.; Hofmann, J. P.; Katsounaros, I.; Etzold, B. J. M.; Probing CO2 Reduction Pathways for Copper Catalysis Using an Ionic Liquid as a Chemical Trapping Agent, *Angew. Chem. Int. Ed.* **2020**, *59* (41), 18095-18102.

28. Feaster, J. T.; Shi, C.; Cave, E. R.; Hatsukade, T.; Abram, D. N.; Kuhl, K. P.; Hahn, C.; Nørskov, J. K.; Jaramillo, T. F.; Understanding Selectivity for the Electrochemical Reduction of Carbon Dioxide to Formic Acid and Carbon Monoxide on Metal Electrodes, *ACS Catal.* **2017**, *7* (7), 4822-4827.

29. Nie, X.; Esopi, M. R.; Janik, M. J.; Asthagiri, A.; Selectivity of CO2 Reduction on Copper Electrodes: The Role of the Kinetics of Elementary Steps, *Angew. Chem. Int. Ed.* **2013**, *52* (9), 2459-2462.

30. An, H.; Wu, L.; Mandemaker, L. D. B.; Yang, S.; de Ruiter, J.; Wijten, J. H. J.; Janssens, J. C. L.; Hartman, T.; van der Stam, W.; Weckhuysen, B. M.; Sub-Second Time-Resolved Surface-Enhanced Raman Spectroscopy Reveals Dynamic CO Intermediates during Electrochemical CO2 Reduction on Copper, *Angew. Chem. Int. Ed.* **2021**, *60* (30), 16576-16584.

31. Moradzaman, M.; Mul, G.; In Situ Raman Study of Potential-Dependent Surface Adsorbed Carbonate, CO, OH, and C Species on Cu Electrodes During Electrochemical Reduction of CO2, *ChemElectroChem* **2021**, *8* (8), 1478-1485.

32. Jiang, S.; Klingan, K.; Pasquini, C.; Dau, H.; New aspects of operando Raman spectroscopy applied to electrochemical CO2 reduction on Cu foams, *J. Chem. Phys.* **2019**, *150* (4), 041718-041729.

33. Zhu, S.; Li, T.; Cai, W.-B.; Shao, M.; CO2 Electrochemical Reduction As Probed through Infrared Spectroscopy, *ACS Energy Lett.* **2019**, *4* (3), 682-689.

34. Jeon, H. S.; Timoshenko, J.; Rettenmaier, C.; Herzog, A.; Yoon, A.; Chee, S. W.; Oener, S.; Hejral, U.; Haase, F. T.; Roldan Cuenya, B.; Selectivity Control of Cu Nanocrystals in a Gas-Fed Flow Cell through CO2 Pulsed Electroreduction, *J. Am. Chem. Soc.* **2021**, *143* (19), 7578-7587.

35. Liu, X.; Schlexer, P.; Xiao, J.; Ji, Y.; Wang, L.; Sandberg, R. B.; Tang, M.; Brown, K. S.; Peng, H.; Ringe, S.; Hahn, C.; Jaramillo, T. F.; Nørskov, J. K.; Chan, K.; pH effects on the electrochemical reduction of CO(2) towards C2 products on stepped copper, *Nat. Commun.* **2019**, *10* (1), 32-41.

36. Kastlunger, G.; Wang, L.; Govindarajan, N.; Heenen, H. H.; Ringe, S.; Jaramillo, T.; Hahn, C.; Chan, K.; Using pH Dependence to Understand Mechanisms in Electrochemical CO Reduction, *ACS Catal.* **2022**, *12* (8), 4344-4357.

37. Xiao, H.; Cheng, T.; Goddard, W. A., III; Sundararaman, R.; Mechanistic Explanation of the pH Dependence and Onset Potentials for Hydrocarbon Products from Electrochemical Reduction of CO on Cu (111), *J. Am. Chem. Soc.* **2016**, *138* (2), 483-486.

38. Schouten, K. J. P.; Pérez Gallent, E.; Koper, M. T. M.; The influence of pH on the reduction of CO and CO2 to hydrocarbons on copper electrodes, *J. Electroanal. Chem.* **2014**, *716*, 53-57.

39. Schouten, K. J. P.; Kwon, Y.; van der Ham, C. J. M.; Qin, Z.; Koper, M. T. M.; A new mechanism for the selectivity to C1 and C2 species in the electrochemical reduction of carbon dioxide on copper electrodes, *Chem. Sci.* **2011**, *2* (10), 1902-1909.

40. Montoya, J. H.; Shi, C.; Chan, K.; Norskov, J. K.; Theoretical Insights into a CO Dimerization Mechanism in CO2 Electroreduction, *J. Phys. Chem. Lett.* **2015**, *6* (11), 2032-2037.

41. Cheng, T.; Xiao, H.; Goddard, W. A., III; Free-Energy Barriers and Reaction Mechanisms for the Electrochemical Reduction of CO on the Cu(100) Surface, Including Multiple Layers of Explicit Solvent at pH 0, *J. Phys. Chem. Lett.* **2015**, *6* (23), 4767-4773.

42. Hori, Y.; Takahashi, R.; Yoshinami, Y.; Murata, A.; Electrochemical Reduction of CO at a Copper Electrode, *J. Phys. Chem. B* **1997**, *101* (36), 7075-7081.

43. Garza, A. J.; Bell, A. T.; Head-Gordon, M.; Mechanism of CO2 Reduction at Copper Surfaces: Pathways to C2 Products, *ACS Catal.* **2018**, *8* (2), 1490-1499.

44. Bertheussen, E.; Verdaguer-Casadevall, A.; Ravasio, D.; Montoya, J. H.; Trimarco, D. B.; Roy, C.; Meier, S.; Wendland, J.; Nørskov, J. K.; Stephens, I. E. L.; Chorkendorff, I.; Acetaldehyde as an Intermediate in the Electroreduction of Carbon Monoxide to Ethanol on Oxide-Derived Copper, *Angew. Chem. Int. Ed.* **2016**, *55* (4), 1450-1454.

45. Lum, Y.; Cheng, T.; Goddard, W. A., III; Ager, J. W.; Electrochemical CO Reduction Builds Solvent Water into Oxygenate Products, *J. Am. Chem. Soc.* **2018**, *140* (30), 9337-9340.

46. Iijima, G.; Inomata, T.; Yamaguchi, H.; Ito, M.; Masuda, H.; Role of a Hydroxide Layer on Cu Electrodes in Electrochemical CO2 Reduction, *ACS Catal.* **2019**, *9* (7), 6305-6319.

47. Luo, M.; Wang, Z.; Li, Y. C.; Li, J.; Li, F.; Lum, Y.; Nam, D.-H.; Chen, B.; Wicks, J.; Xu, A.; Zhuang, T.; Leow, W. R.; Wang, X.; Dinh, C.-T.; Wang, Y.; Wang, Y.; Sinton, D.; Sargent, E. H.; Hydroxide promotes carbon dioxide electroreduction to ethanol on copper via tuning of adsorbed hydrogen, *Nat. Commun.* **2019**, *10* (1), 5814-5820.

48. Pablo-García, S.; Veenstra, F. L. P.; Ting, L. R. L.; García-Muelas, R.; Dattila, F.; Martín, A. J.; Yeo, B. S.; Pérez-Ramírez, J.; López, N.; Mechanistic routes toward C3 products in copper-catalysed CO2 electroreduction, *Catal. Sci. Technol.* **2022**, *12* (2), 409-417.

49. Singh, M. R.; Kwon, Y.; Lum, Y.; Ager, J. W.; Bell, A. T.; Hydrolysis of Electrolyte Cations Enhances the Electrochemical Reduction of CO2 over Ag and Cu, *J. Am. Chem. Soc.* **2016**, *138* (39), 13006-13012.

50. Zhu, S.; Jiang, B.; Cai, W.-B.; Shao, M.; Direct Observation on Reaction Intermediates and the Role of Bicarbonate Anions in CO2 Electrochemical Reduction Reaction on Cu Surfaces, *J. Am. Chem. Soc.* **2017**, *139* (44), 15664-15667.

51. Varela, A. S.; The importance of pH in controlling the selectivity of the electrochemical CO2 reduction, *Curr. Opin. Green Sustain. Chem.* **2020**, *26*, 100371.

52. Lees, E. W.; Mowbray, B. A. W.; Parlane, F. G. L.; Berlinguette, C. P.; Gas diffusion electrodes and membranes for CO2 reduction electrolysers, *Nat. Rev. Mater.* **2022**, *7* (1), 55-64.

53. Hori, Y.; Takahashi, I.; Koga, O.; Hoshi, N.; Selective Formation of C2 Compounds from Electrochemical Reduction of CO2 at a Series of Copper Single Crystal Electrodes, *J. Phys. Chem. B* **2002**, *106* (1), 15-17.

54. Huang, Y.; Handoko, A. D.; Hirunsit, P.; Yeo, B. S.; Electrochemical Reduction of CO2 Using Copper Single-Crystal Surfaces: Effects of CO* Coverage on the Selective Formation of Ethylene, *ACS Catal.* **2017**, *7* (3), 1749-1756.

55. Scholten, F.; Nguyen, K.-L. C.; Bruce, J. P.; Heyde, M.; Roldan Cuenya, B.; Identifying Structure–Selectivity Correlations in the Electrochemical Reduction of CO2: A Comparison of Well-Ordered Atomically Clean and Chemically Etched Copper Single-Crystal Surfaces, *Angew. Chem. Int. Ed.* **2021**, *60* (35), 19169-19175.

56. Hori, Y.; Takahashi, I.; Koga, O.; Hoshi, N.; Electrochemical reduction of carbon dioxide at various series of copper single crystal electrodes, *J. Mol. Catal. A Chem.* **2003**, *199* (1), 39-47.

57. Hahn, C.; Hatsukade, T.; Kim, Y.-G.; Vailionis, A.; Baricuatro, J. H.; Higgins, D. C.; Nitopi, S. A.; Soriaga, M. P.; Jaramillo, T. F.; Engineering Cu surfaces for the electrocatalytic conversion of CO2: Controlling selectivity toward oxygenates and hydrocarbons, *Proc. Natl. Acad. Sci. U.S.A.* **2017**, *114* (23), 5918-5923.

58. Suen, N.-T.; Kong, Z.-R.; Hsu, C.-S.; Chen, H.-C.; Tung, C.-W.; Lu, Y.-R.; Dong, C.-L.; Shen, C.-C.; Chung, J.-C.; Chen, H. M.; Morphology Manipulation of Copper Nanocrystals and Product Selectivity in the Electrocatalytic Reduction of Carbon Dioxide, *ACS Catal.* **2019**, *9* (6), 5217-5222.

59. Iyengar, P.; Huang, J.; De Gregorio, G. L.; Gadiyar, C.; Buonsanti, R.; Size dependent selectivity of Cu nano-octahedra catalysts for the electrochemical reduction of CO2 to CH4, *ChemComm.* **2019**, *55* (60), 8796-8799.

60. Reske, R.; Mistry, H.; Behafarid, F.; Roldan Cuenya, B.; Strasser, P.; Particle Size Effects in the Catalytic Electroreduction of CO2 on Cu Nanoparticles, *J. Am. Chem. Soc.* **2014**, *136* (19), 6978-6986.

61. Loiudice, A.; Lobaccaro, P.; Kamali, E. A.; Thao, T.; Huang, B. H.; Ager, J. W.; Buonsanti, R.; Tailoring Copper Nanocrystals towards C2 Products in Electrochemical CO2 Reduction, *Angew. Chem. Int. Ed.* **2016**, *55* (19), 5789-5792.

62. Grosse, P.; Gao, D. F.; Scholten, F.; Sinev, I.; Mistry, H.; Roldan Cuenya, B.; Dynamic Changes in the Structure, Chemical State and Catalytic Selectivity of Cu Nanocubes

during CO2 Electroreduction: Size and Support Effects, *Angew. Chem. Int. Ed.* **2018**, *57* (21), 6192-6197.

63. Grosse, P.; Yoon, A.; Rettenmaier, C.; Herzog, A.; Chee, S. W.; Roldan Cuenya, B.; Dynamic transformation of cubic copper catalysts during CO2 electroreduction and its impact on catalytic selectivity, *Nat. Commun.* **2021**, *12* (1), 6736-6746.

64. Stephens, I. E. L.; Bondarenko, A. S.; Grønbjerg, U.; Rossmeisl, J.; Chorkendorff, I.; Understanding the electrocatalysis of oxygen reduction on platinum and its alloys, *Energy Environ. Sci.* **2012**, *5* (5), 6744-6762.

65. Mavrikakis, M.; Hammer, B.; Nørskov, J. K.; Effect of Strain on the Reactivity of Metal Surfaces, *Phys. Rev. Lett.* **1998**, *81* (13), 2819-2822.

66. Lei, Q.; Huang, L.; Yin, J.; Davaasuren, B.; Yuan, Y.; Dong, X.; Wu, Z.-P.; Wang, X.; Yao, K. X.; Lu, X.; Han, Y.; Structural evolution and strain generation of derived-Cu catalysts during CO2 electroreduction, *Nat. Commun.* **2022**, *13* (1), 4857-4868.

67. Deng, X.; Alfonso, D.; Nguyen-Phan, T.-D.; Kauffman, D. R.; Resolving the Size-Dependent Transition between CO2 Reduction Reaction and H2 Evolution Reaction Selectivity in Sub-5 nm Silver Nanoparticle Electrocatalysts, *ACS Catal.* **2022**, *12* (10), 5921-5929.

68. Jeon, H. S.; Sinev, I.; Scholten, F.; Divins, N. J.; Zegkinoglou, I.; Pielsticker, L.; Cuenya, B. R.; Operando Evolution of the Structure and Oxidation State of Size-Controlled Zn Nanoparticles during CO2 Electroreduction, *J. Am. Chem. Soc.* **2018**, *140* (30), 9383-9386.

69. Mistry, H.; Behafarid, F.; Reske, R.; Varela, A. S.; Strasser, P.; Roldan Cuenya, B.; Tuning Catalytic Selectivity at the Mesoscale via Interparticle Interactions, *ACS Catal.* **2016**, *6* (2), 1075-1080.

70. Kim, D.; Kley, C. S.; Li, Y.; Yang, P.; Copper nanoparticle ensembles for selective electroreduction of CO2 to C2-C3 products, *Proc. Natl. Acad. Sci. U.S.A.* **2017**, *114* (40), 10560-10565.

71. Yang, Y.; Louisia, S.; Yu, S.; Jin, J.; Roh, I.; Chen, C.; Fonseca Guzman, M. V.; Feijóo, J.; Chen, P.-C.; Wang, H.; Pollock, C. J.; Huang, X.; Shao, Y.-T.; Wang, C.; Muller, D. A.; Abruña, H. D.; Yang, P.; Operando studies reveal active Cu nanograins for CO2 electroreduction, *Nature* **2023**, *614* (7947), 262-269.

72. Li, C. W.; Kanan, M. W.; CO2 Reduction at Low Overpotential on Cu Electrodes Resulting from the Reduction of Thick Cu2O Films, *J. Am. Chem. Soc.* **2012**, *134* (17), 7231-7234.

73. Li, C. W.; Ciston, J.; Kanan, M. W.; Electroreduction of carbon monoxide to liquid fuel on oxide-derived nanocrystalline copper, *Nature* **2014**, *508* (7497), 504-507.

74. Chen, C. S.; Handoko, A. D.; Wan, J. H.; Ma, L.; Ren, D.; Yeo, B. S.; Stable and selective electrochemical reduction of carbon dioxide to ethylene on copper mesocrystals, *Catal. Sci. Technol.* **2015**, *5* (1), 161-168.

75. Gao, D. F.; Zegkinoglou, I.; Divins, N. J.; Scholten, F.; Sinev, I.; Grosse, P.; Roldan Cuenya, B.; Plasma-Activated Copper Nanocube Catalysts for Efficient Carbon Dioxide Electroreduction to Hydrocarbons and Alcohols, *ACS Nano* **2017**, *11* (5), 4825-4831.

76. Scholten, F.; Sinev, I.; Bernal, M.; Roldan Cuenya, B.; Plasma-Modified Dendritic Cu Catalyst for CO2 Electroreduction, *ACS Catal.* **2019**, *9* (6), 5496-5502.

77. Kas, R.; Kortlever, R.; Milbrat, A.; Koper, M. T. M.; Mul, G.; Baltrusaitis, J.; Electrochemical CO2 reduction on Cu2O-derived copper nanoparticles: controlling the catalytic selectivity of hydrocarbons, *Phys. Chem. Chem. Phys.* **2014**, *16* (24), 12194-12201.

78. Ren, D.; Deng, Y.; Handoko, A. D.; Chen, C. S.; Malkhandi, S.; Yeo, B. S.; Selective Electrochemical Reduction of Carbon Dioxide to Ethylene and Ethanol on Copper(I) Oxide Catalysts, *ACS Catal.* **2015**, *5* (5), 2814-2821.

79. Möller, T.; Scholten, F.; Thanh, T. N.; Sinev, I.; Timoshenko, J.; Wang, X.; Jovanov, Z.; Gliech, M.; Roldan Cuenya, B.; Varela, A. S.; Strasser, P.; Electrocatalytic CO2 Reduction on CuOx Nanocubes: Tracking the Evolution of Chemical State, Geometric Structure, and Catalytic Selectivity using Operando Spectroscopy, *Angew. Chem. Int. Ed.* **2020**, *59* (41), 17974-17983.

80. Wang, L.; Nitopi, S. A.; Bertheussen, E.; Orazov, M.; Morales-Guio, C. G.; Liu, X.; Higgins, D. C.; Chan, K.; Nørskov, J. K.; Hahn, C.; Jaramillo, T. F.; Electrochemical Carbon Monoxide Reduction on Polycrystalline Copper: Effects of Potential, Pressure, and pH on Selectivity toward Multicarbon and Oxygenated Products, *ACS Catal.* **2018**, *8* (8), 7445-7454.

81. Ma, M.; Djanashvili, K.; Smith, W. A.; Controllable Hydrocarbon Formation from the Electrochemical Reduction of CO2 over Cu Nanowire Arrays, *Angew. Chem. Int. Ed.* **2016**, *55* (23), 6680-6684.

82. Rahaman, M.; Dutta, A.; Zanetti, A.; Broekmann, P.; Electrochemical Reduction of CO2 into Multicarbon Alcohols on Activated Cu Mesh Catalysts: An Identical Location (IL) Study, *ACS Catal.* **2017**, *7* (11), 7946-7956.

83. Feng, X.; Jiang, K.; Fan, S.; Kanan, M. W.; A Direct Grain-Boundary-Activity Correlation for CO Electroreduction on Cu Nanoparticles, *ACS Cent. Sci.* **2016**, *2* (3), 169-174.

84. Platzman, I.; Brener, R.; Haick, H.; Tannenbaum, R.; Oxidation of Polycrystalline Copper Thin Films at Ambient Conditions, *J. Phys. Chem. C* **2008**, *112* (4), 1101-1108.

85. Cavalca, F.; Ferragut, R.; Aghion, S.; Eilert, A.; Diaz-Morales, O.; Liu, C.; Koh, A. L.; Hansen, T. W.; Pettersson, L. G. M.; Nilsson, A.; Nature and Distribution of Stable Subsurface Oxygen in Copper Electrodes During Electrochemical CO2 Reduction, *J. Phys. Chem. C* **2017**, *121* (45), 25003-25009.

86. Lee, S. Y.; Jung, H.; Kim, N.-K.; Oh, H.-S.; Min, B. K.; Hwang, Y. J.; Mixed Copper States in Anodized Cu Electrocatalyst for Stable and Selective Ethylene Production from CO2 Reduction, *J. Am. Chem. Soc.* **2018**, *140* (28), 8681-8689.

87. Mandal, L.; Yang, K. R.; Motapothula, M. R.; Ren, D.; Lobaccaro, P.; Patra, A.; Sherburne, M.; Batista, V. S.; Yeo, B. S.; Ager, J. W.; Martin, J.; Venkatesan, T.; Investigating the Role of Copper Oxide in Electrochemical CO2 Reduction in Real Time, *ACS Appl. Mater. Interfaces* **2018**, *10* (10), 8574-8584.

88. Zhan, C.; Dattila, F.; Rettenmaier, C.; Bergmann, A.; Kühl, S.; García-Muelas, R.; López, N.; Roldan Cuenya, B.; Revealing the CO Coverage-Driven C–C Coupling Mechanism for Electrochemical CO2 Reduction on Cu2O Nanocubes via Operando Raman Spectroscopy, *ACS Catal.* **2021**, *11* (13), 7694-7701.

89. Lum, Y.; Ager, J. W.; Stability of Residual Oxides in Oxide-Derived Copper Catalysts for Electrochemical CO2 Reduction Investigated with 18O Labeling, *Angew. Chem. Int. Ed.* **2018**, *57* (2), 551-554.

90. Mistry, H.; Varela, A. S.; Bonifacio, C. S.; Zegkinoglou, I.; Sinev, I.; Choi, Y.-W.; Kisslinger, K.; Stach, E. A.; Yang, J. C.; Strasser, P.; Roldan Cuenya, B.; Highly selective plasma-activated copper catalysts for carbon dioxide reduction to ethylene, *Nat. Commun.* **2016**, *7* (1), 12123-12130.

91. Favaro, M.; Xiao, H.; Cheng, T.; Goddard, W. A.; Yano, J.; Crumlin, E. J.; Subsurface oxide plays a critical role in CO2 activation by Cu(111) surfaces to form chemisorbed CO2, the first step in reduction of CO2, *Proc. Natl. Acad. Sci. U.S.A.* **2017**, *114* (26), 6706-6711.

92. Gao, D.; Sinev, I.; Scholten, F.; Arán-Ais, R. M.; Divins, N. J.; Kvashnina, K.; Timoshenko, J.; Roldan Cuenya, B.; Selective CO2 Electroreduction to Ethylene and Multicarbon Alcohols via Electrolyte-Driven Nanostructuring, *Angew. Chem. Int. Ed.* **2019**, *58* (47), 17047-17053.

93. Yoon, A.; Poon, J.; Grosse, P.; Chee, S. W.; Cuenya, B. R.; Iodide-mediated Cu catalyst restructuring during CO2 electroreduction, *J. Mater. Chem. A* **2022**, *10* (26), 14041-14050.

94. Zhou, Y.; Che, F.; Liu, M.; Zou, C.; Liang, Z.; De Luna, P.; Yuan, H.; Li, J.; Wang, Z.; Xie, H.; Li, H.; Chen, P.; Bladt, E.; Quintero-Bermudez, R.; Sham, T.-K.; Bals, S.; Hofkens, J.; Sinton, D.; Chen, G.; Sargent, E. H.; Dopant-induced electron localization drives CO2 reduction to C2 hydrocarbons, *Nat. Chem.* **2018**, *10* (9), 974-980.

95. Zhou, Y.; Yao, Y.; Zhao, R.; Wang, X.; Fu, Z.; Wang, D.; Wang, H.; Zhao, L.; Ni, W.; Yang, Z.; Yan, Y.-M.; Stabilization of Cu+ via Strong Electronic Interaction for Selective and Stable CO2 Electroreduction, *Angew. Chem. Int. Ed.* **2022**, *61* (31), e202205832.

96. Arán-Ais, R. M.; Scholten, F.; Kunze, S.; Rizo, R.; Roldan Cuenya, B.; The role of in situ generated morphological motifs and Cu(i) species in C2+ product selectivity during CO2 pulsed electroreduction, *Nat. Energy* **2020**, *5* (4), 317-325.

97. Timoshenko, J.; Bergmann, A.; Rettenmaier, C.; Herzog, A.; Arán-Ais, R. M.; Jeon, H. S.; Haase, F. T.; Hejral, U.; Grosse, P.; Kühl, S.; Davis, E. M.; Tian, J.; Magnussen, O.; Roldan Cuenya, B.; Steering the structure and selectivity of CO2 electroreduction catalysts by potential pulses, *Nat. Catal.* **2022**, *5* (4), 259-267.

98. Yoshio, H.; Akira, M.; Shin-ya, I.; Yuzuru, Y.; Osamu, K.; Nickel and Iron Modified Copper Electrode for Electroreduction of CO2 by In-situ Electrodeposition, *Chem. Lett.* **1989**, *18* (9), 1567-1570.

99. Todoroki, N.; Yokota, N.; Nakahata, S.; Nakamura, H.; Wadayama, T.; Electrochemical Reduction of CO2 on Ni- and Pt-Epitaxially Grown Cu(111) Surfaces, *Electrocatalysis* **2016**, *7* (1), 97-103.

100. Luo, W.; Xie, W.; Mutschler, R.; Oveisi, E.; De Gregorio, G. L.; Buonsanti, R.; Züttel, A.; Selective and Stable Electroreduction of CO2 to CO at the Copper/Indium Interface, *ACS Catal.* **2018**, *8* (7), 6571-6581.

101. Li, Q.; Fu, J.; Zhu, W.; Chen, Z.; Shen, B.; Wu, L.; Xi, Z.; Wang, T.; Lu, G.; Zhu, J.-j.; Sun, S.; Tuning Sn-Catalysis for Electrochemical Reduction of CO2 to CO via the Core/Shell Cu/SnO2 Structure, *J. Am. Chem. Soc.* **2017**, *139* (12), 4290-4293.

102. Wang, Y.; Zhou, J.; Lv, W.; Fang, H.; Wang, W.; Electrochemical reduction of CO2 to formate catalyzed by electroplated tin coating on copper foam, *Appl. Surf. Sci.* **2016**, *362*, 394-398.

103. Hoffman, Z. B.; Gray, T. S.; Moraveck, K. B.; Gunnoe, T. B.; Zangari, G.; Electrochemical Reduction of Carbon Dioxide to Syngas and Formate at Dendritic Copper–Indium Electrocatalysts, *ACS Catal.* **2017**, *7* (8), 5381-5390.

104. Clark, E. L.; Hahn, C.; Jaramillo, T. F.; Bell, A. T.; Electrochemical CO2 Reduction over Compressively Strained CuAg Surface Alloys with Enhanced Multi-Carbon Oxygenate Selectivity, *J. Am. Chem. Soc.* **2017**, *139* (44), 15848-15857.

105. Ishimaru, S.; Shiratsuchi, R.; Nogami, G.; Pulsed Electroreduction of CO2 on Cu-Ag Alloy Electrodes, *J. Electrochem. Soc.* **2000**, *147* (5), 1864.

106. Da Silva, A. H. M.; Raaijman, S. J.; Santana, C. S.; Assaf, J. M.; Gomes, J. F.; Koper, M. T. M.; Electrocatalytic CO2 reduction to C2+ products on Cu and CuxZny electrodes: Effects of chemical composition and surface morphology, *J. Electroanal. Chem.* **2021**, *880*, 114750-114756.

107. Ren, D.; Gao, J.; Pan, L.; Wang, Z.; Luo, J.; Zakeeruddin, S. M.; Hagfeldt, A.; Grätzel, M.; Atomic Layer Deposition of ZnO on CuO Enables Selective and Efficient Electroreduction of Carbon Dioxide to Liquid Fuels, *Angew. Chem. Int. Ed.* **2019**, *58* (42), 15036-15040.

108. Kim, D.; Resasco, J.; Yu, Y.; Asiri, A. M.; Yang, P.; Synergistic geometric and electronic effects for electrochemical reduction of carbon dioxide using gold–copper bimetallic nanoparticles, *Nat. Commun.* **2014**, *5* (1), 4948-4955.

109. Choi, J.; Kim, M. J.; Ahn, S. H.; Choi, I.; Jang, J. H.; Ham, Y. S.; Kim, J. J.; Kim, S.-K.; Electrochemical CO2 reduction to CO on dendritic Ag–Cu electrocatalysts prepared by electrodeposition, *Chem. Eng. J.* **2016**, *299*, 37-44.

110. Nørskov, J. K.; Rossmeisl, J.; Logadottir, A.; Lindqvist, L.; Kitchin, J. R.; Bligaard, T.; Jónsson, H.; Origin of the Overpotential for Oxygen Reduction at a Fuel-Cell Cathode, *J. Phys. Chem. B* **2004**, *108* (46), 17886-17892.

111. Clark, E. L.; Bell, A. T.; Direct Observation of the Local Reaction Environment during the Electrochemical Reduction of CO2, *J. Am. Chem. Soc.* **2018**, *140* (22), 7012-7020.

112. Higgins, D.; Landers, A. T.; Ji, Y.; Nitopi, S.; Morales-Guio, C. G.; Wang, L.; Chan, K.; Hahn, C.; Jaramillo, T. F.; Guiding Electrochemical Carbon Dioxide Reduction toward Carbonyls Using Copper Silver Thin Films with Interphase Miscibility, *ACS Energy Lett.* **2018**, *3* (12), 2947-2955.

113. Jeon, H. S.; Timoshenko, J.; Scholten, F.; Sinev, I.; Herzog, A.; Haase, F. T.; Roldan Cuenya, B.; Operando Insight into the Correlation between the Structure and Composition of CuZn Nanoparticles and Their Selectivity for the Electrochemical CO2 Reduction, *J. Am. Chem. Soc.* **2019**, *141* (50), 19879-19887.

114. Timoshenko, J.; Jeon, H. S.; Sinev, I.; Haase, F. T.; Herzog, A.; Roldan Cuenya, B.; Linking the evolution of catalytic properties and structural changes in copper–zinc nanocatalysts using operando EXAFS and neural-networks, *Chem. Sci.* **2020**, *11* (14), 3727-3736.

115. Rüscher, M.; Herzog, A.; Timoshenko, J.; Jeon, H. S.; Frandsen, W.; Kühl, S.; Roldan Cuenya, B.; Tracking heterogeneous structural motifs and the redox behaviour of copper–zinc nanocatalysts for the electrocatalytic CO2 reduction using operando time resolved spectroscopy and machine learning, *Catal. Sci. Technol.* **2022**, *12* (9), 3028-3043.

116. Gao, J.; Zhang, H.; Guo, X.; Luo, J.; Zakeeruddin, S. M.; Ren, D.; Grätzel, M.; Selective C–C Coupling in Carbon Dioxide Electroreduction via Efficient Spillover of Intermediates As Supported by Operando Raman Spectroscopy, *J. Am. Chem. Soc.* **2019**, *141* (47), 18704-18714.

117. Lee, S.; Park, G.; Lee, J.; Importance of Ag-Cu Biphasic Boundaries for Selective Electrochemical Reduction of CO2 to Ethanol, *ACS Catal.* **2017**, *7* (12), 8594-8604.

118. Varandili, S. B.; Stoian, D.; Vavra, J.; Rossi, K.; Pankhurst, J. R.; Guntern, Y. T.; López, N.; Buonsanti, R.; Elucidating the structure-dependent selectivity of CuZn towards methane and ethanol in CO2 electroreduction using tailored Cu/ZnO precatalysts, *Chem. Sci.* **2021**, *12* (43), 14484-14493.

119. Feng, Y.; Li, Z.; Liu, H.; Dong, C.; Wang, J.; Kulinich, S. A.; Du, X.; Laser-Prepared CuZn Alloy Catalyst for Selective Electrochemical Reduction of CO2 to Ethylene, *Langmuir* **2018**, *34* (45), 13544-13549.

120. Kimura, K. W.; Fritz, K. E.; Kim, J.; Suntivich, J.; Abruña, H. D.; Hanrath, T.; Controlled Selectivity of CO2 Reduction on Copper by Pulsing the Electrochemical Potential, *ChemSusChem* **2018**, *11* (11), 1781-1786.

121. Lin, S.-C.; Chang, C.-C.; Chiu, S.-Y.; Pai, H.-T.; Liao, T.-Y.; Hsu, C.-S.; Chiang, W.-H.; Tsai, M.-K.; Chen, H. M.; Operando time-resolved X-ray absorption spectroscopy reveals the chemical nature enabling highly selective CO2 reduction, *Nat. Commun.* **2020**, *11* (1), 3525-3536.

122. Tang, Z.; Nishiwaki, E.; Fritz, K. E.; Hanrath, T.; Suntivich, J.; Cu(I) Reducibility Controls Ethylene vs Ethanol Selectivity on (100)-Textured Copper during Pulsed CO2 Reduction, *ACS Appl. Mater. Interfaces* **2021**, *13* (12), 14050-14055.

123. Beverskog, B.; Puigdomenech, I.; Revised Pourbaix Diagrams for Copper at 25 to 300°C, *J. Am. Chem. Soc.* **1997**, *144* (10), 3476-3483.

124. Beverskog, B.; Puigdomenech, I.; Revised pourbaix diagrams for zinc at 25–300 °C, *Corros. Sci.* **1997**, *39* (1), 107-114.

125. Lee, J.; Tak, Y.; Electrocatalytic activity of Cu electrode in electroreduction of CO2, *Electrochim. Acta* **2001**, *46* (19), 3015-3022.

126. Engelbrecht, A.; Uhlig, C.; Stark, O.; Hämmerle, M.; Schmid, G.; Magori, E.; Wiesner-Fleischer, K.; Fleischer, M.; Moos, R.; On the Electrochemical CO2 Reduction at Copper Sheet Electrodes with Enhanced Long-Term Stability by Pulsed Electrolysis, *J. Electrochem. Soc.* **2018**, *165* (15), J3059-J3068.

127. Shiratsuchi, R.; Nogami, G.; Pulsed Electroreduction of CO 2 on Silver Electrodes, *J. Electrochem. Soc.* **1996**, *143* (2), 582-586.

128. Le Duff, C. S.; Lawrence, M. J.; Rodriguez, P.; Role of the Adsorbed Oxygen Species in the Selective Electrochemical Reduction of CO2 to Alcohols and Carbonyls on Copper Electrodes, *Angew. Chem. Int. Ed.* **2017**, *56* (42), 12919-12924.

129. Kimura, K. W.; Casebolt, R.; Cimada DaSilva, J.; Kauffman, E.; Kim, J.; Dunbar, T. A.; Pollock, C. J.; Suntivich, J.; Hanrath, T.; Selective Electrochemical CO2 Reduction during Pulsed Potential Stems from Dynamic Interface, *ACS Catal.* **2020**, *10* (15), 8632-8639.

130. Dinh, C.-T.; Burdyny, T.; Kibria, M. G.; Seifitokaldani, A.; Gabardo, C. M.; García de Arquer, F. P.; Kiani, A.; Edwards, J. P.; De Luna, P.; Bushuyev, O. S.; Zou, C.; Quintero-Bermudez, R.; Pang, Y.; Sinton, D.; Sargent, E. H.; CO2 electroreduction to ethylene via hydroxide-mediated copper catalysis at an abrupt interface, *Science* **2018**, *360* (6390), 783-787.

131. Chou, T.-C.; Chang, C.-C.; Yu, H.-L.; Yu, W.-Y.; Dong, C.-L.; Velasco-Vélez, J.-J.; Chuang, C.-H.; Chen, L.-C.; Lee, J.-F.; Chen, J.-M.; Wu, H.-L.; Controlling the Oxidation State of the Cu Electrode and Reaction Intermediates for Electrochemical CO2 Reduction to Ethylene, *J. Am. Chem. Soc.* **2020**, *142* (6), 2857-2867.

132. De Ruiter, J.; An, H.; Wu, L.; Gijsberg, Z.; Yang, S.; Hartman, T.; Weckhuysen, B. M.; van der Stam, W.; Probing the Dynamics of Low-Overpotential CO2-to-CO Activation on Copper Electrodes with Time-Resolved Raman Spectroscopy, *J. Am. Chem. Soc.* **2022**, *144* (33), 15047-15058.

133. Shiratsuchi, R.; Aikoh, Y.; Nogami, G.; Pulsed Electroreduction of CO2 on Copper Electrodes, *J. Electrochem. Soc.* **1993**, *140* (12), 3479.

134. Gupta, N.; Gattrell, M.; MacDougall, B.; Calculation for the cathode surface concentrations in the electrochemical reduction of CO2 in KHCO3 solutions, *J. Appl. Electrochem.* **2006**, *36* (2), 161-172.

135. Kim, C.; Weng, L.-C.; Bell, A. T.; Impact of Pulsed Electrochemical Reduction of CO2 on the Formation of C2+ Products over Cu, *ACS Catal.* **2020**, *10* (21), 12403-12413.

136. Bard, A. J. F., L. R.; *Electrochemical methods : fundamentals and applications*, John Wiley & Sons **2001**, Second edition.

137. Brett, C. M. A. B., A. M. O.; *Electrochemistry Pronciples, Methods, and Applications*, Oxford University Press **1993**, First edition.

138. Carl H. Hamann , A. H., Wolf Vielstich; *Electrochemistry*, Wiley-VCH **2007**, Second edition.

139. Oldham, K. B. M., J. C.; Bond, A M.; *Electrochemical Science and Technology*, John Wiley & Sons, Ltd. **2012**, First edition.

140. Swift, M. W.; Swift, J. W.; Qi, Y.; Modeling the electrical double layer at solid-state electrochemical interfaces, *Nat. Comput. Sci* **2021**, *1* (3), 212-220.

141. Morales, D. M.; Risch, M.; Seven steps to reliable cyclic voltammetry measurements for the determination of double layer capacitance, *J. Phys. Energy* **2021**, *3* (3), 034013.

142. Wang, S.; Zhang, J.; Gharbi, O.; Vivier, V.; Gao, M.; Orazem, M. E.; Electrochemical impedance spectroscopy, *Nat. Rev. Methods Primers* **2021**, *1* (1), 41-61.

143. Kirkland, A. I. H., A. J.; *Nanocharacterisation*, The Royal Society of Chemistry **2015**, Second edition.

144. Chorkendorff, I.; Niemantsverdriet, J. W.; *Concepts of modern catalysis and kinetics*, Wiley-VCH **2007**, Second edition.

145. Egerton, R. F.; *Physical Principles of Electron Microscopy: An Introduction to TEM, SEM, and AEM*, Springer International Publishing **2016**, Second edition, 1-26.

146. Chee, S. W.; Lunkenbein, T.; Schlögl, R.; Cuenya, B. R.; In situ and operando electron microscopy in heterogeneous catalysis-insights into multi-scale chemical dynamics, *J. Phys. Condens. Matter.* **2021**, *33* (15).

147. Han, X. X.; Rodriguez, R. S.; Haynes, C. L.; Ozaki, Y.; Zhao, B.; Surface-enhanced Raman spectroscopy, *Nat. Rev. Methods Primers* **2022**, *1* (1), 87-103.

148. Joya, K. S.; Sala, X.; In situ Raman and surface-enhanced Raman spectroscopy on working electrodes: spectroelectrochemical characterization of water oxidation electrocatalysts, *Phys. Chem. Chem. Phys.* **2015**, *17* (33), 21094-21103.

149. Raman, C. V.; Krishnan, K. S.; A New Type of Secondary Radiation, *Nature* **1928**, *121* (3048), 501-502.

150. Smith, E. D., G.; *Modern Raman Spectroscopy - a pratical approach*, John Wiley & Sons Ltd **2019**, Second edition.

151. Ferraro, J. R. N., K.; Brown, C. W.; *Introductory Raman Spectroscopy*, Elsevier **2003** Second edition.

152. Davis, A. R.; Oliver, B. G.; A vibrational-spectroscopic study of the species present in the CO2-H2O system, *J. Solution Chem.* **1972**, *1* (4), 329-339.

153. Fleischmann, M.; Hendra, P. J.; McQuillan, A. J.; Raman spectra of pyridine adsorbed at a silver electrode, *Chem. Phys. Lett.* **1974**, *26* (2), 163-166.

154. Le Ru, E. C.; Blackie, E.; Meyer, M.; Etchegoin, P. G.; Surface Enhanced Raman Scattering Enhancement Factors: A Comprehensive Study, *J. Phys. Chem. C* **2007**, *111* (37), 13794-13803.

155. Moskovits, M.; Suh, J. S.; Surface selection rules for surface-enhanced Raman spectroscopy: calculations and application to the surface-enhanced Raman spectrum of phthalazine on silver, *J. Phys. Chem.* **1984**, *88* (23), 5526-5530.

156. Timoshenko, J.; Cuenya, B. R.; In Situ/Operando Electrocatalyst Characterization by X-ray Absorption Spectroscopy, *Chem. Rev.* **2021**, *121* (2), 882-961.

157. Newville, M.; Fundamentals of XAFS, *Spectroscopic Methods in Mineralology and Materials Sciences* **2014**, *78*, 33-74.

158. Herzog, A.; Bergmann, A.; Jeon, H. S.; Timoshenko, J.; Kühl, S.; Rettenmaier, C.; Lopez Luna, M.; Haase, F. T.; Roldan Cuenya, B.; Operando Investigation of Ag-Decorated Cu2O Nanocube Catalysts with Enhanced CO2 Electroreduction toward Liquid Products, *Angew. Chem. Int. Ed.* **2021**, *60* (13), 7426-7435.

159. Schnohr, C. S.; Ridgway, M. C.; *X-Ray Absorption Spectroscopy of Semiconductors*, Springer Series in Optical Sciences **2015**, First edition, 1-26.

160. Mino, L.; Agostini, G.; Borfecchia, E.; Gianolio, D.; Piovano, A.; Gallo, E.; Lamberti, C.; Low-dimensional systems investigated by X-ray absorption spectroscopy: a selection of 2D, 1D and 0D cases, *J. Phys. D* **2013**, *46* (42), 423001.

161. Benfatto, M.; Meneghini, C.; *A Close Look into the Low Energy Region of the XAS Spectra: The XANES Region*, Springer Berlin, Heidelberg **2015**, First edition, 213-240.

162. Bunker, G.; *Introduction to XAFS: A Practical Guide to X-ray Absorption Fine Structure Spectroscopy*, Cambridge University Press **2010**, First edition.

163. Rehr, J. J.; Albers, R. C.; Theoretical approaches to x-ray absorption fine structure, *Rev. Mod. Phys.* **2000**, *72* (3), 621-654.

164. Rehr, J. J.; Kas, J. J.; Vila, F. D.; Prange, M. P.; Jorissen, K.; Parameter-free calculations of X-ray spectra with FEFF9, *Phys. Chem. Chem. Phys.* **2010**, *12* (21), 5503-5513.

165. Timoshenko, J.; Wrasman, C. J.; Luneau, M.; Shirman, T.; Cargnello, M.; Bare, S. R.; Aizenberg, J.; Friend, C. M.; Frenkel, A. I.; Probing Atomic Distributions in Mono- and Bimetallic Nanoparticles by Supervised Machine Learning, *Nano Lett.* **2019**, *19* (1), 520-529.

166. Uruga, T.; *Quick XAFS in XAFS Techniques for Catalysts, Nanomaterials, and Surfaces*, Springer International Publishing **2017**, First edition, 93-108.

167. Degerman, D.; Amann, P.; Goodwin, C. M.; Lömker, P.; Wang, H.-Y.; Soldemo, M.; Shipilin, M.; Schlueter, C.; Nilsson, A.; Operando X-ray Photoelectron Spectroscopy for High-Pressure Catalysis Research Using the POLARIS Endstation, *Synchrotron Radiation News* **2022**, *35* (3), 11-18.

168. Van der Heide, P.; *X-Ray Photoelectron Spectroscopy: An Introduction to Principles and Practices*, **2011**, First edition, 27-60.

169. Biesinger, M. C.; Advanced analysis of copper X-ray photoelectron spectra, *Surf. Interface Anal.* **2017**, *49* (13), 1325-1334.

170. Holland, D.; *Surface Structure of Sol–Gel-Derived Materials Using X-ray Photoelectron Spectroscopy (XPS) in Handbook of Sol-Gel Science and Technology*, Springer International Publishing **2017**, Second edition, 1-23.

171. Waseda, Y.; Matsubara, E.; Shinoda, K.; *Scattering and Diffraction in X-Ray Diffraction Crystallography: Introduction, Examples and Solved Problems*, Springer Berlin, Heidelberg **2011**, First edition, 67-106.

172. Flewitt, P. E. J.; Wild, R. K.; *Physical Methods for Materials Characterisation*, CRC Press **2017**, Third edition.

173. Scherrer, P.; Bestimmung der Größe und der inneren Struktur von Kolloidteilchen mittels Röntgenstrahlen, *Nachrichten von der Gesellschaft der Wissenschaften zu Göttingen, Mathematisch-Physikalische Klasse* **1918**, 98-100.

174. He, B. B.; *Two-dimensional X-ray Diffraction*, Wiley **2018**, Second edition.

175. Rietveld, H.; A profile refinement method for nuclear and magnetic structures, *J. Appl. Crystallogr.* **1969**, *2* (2), 65-71.

176. Rietveld, H. M.; The Rietveld Method: A Retrospection, **2010**, *225* (12), 545-547.

177. Sakata, O.; Nakamura, M.; *Grazing Incidence X-Ray Diffraction in Surface Science Techniques*, Springer Berlin, Heidelberg **2013**, First edition, 165-190.

178. Ashiotis, G.; Deschildre, A.; Nawaz, Z.; Wright, J. P.; Karkoulis, D.; Picca, F. E.; Kieffer, J.; The fast azimuthal integration Python library: pyFAI, *J. Appl. Crystallogr.* **2015**, *48* (2), 510-519.

179. Dattila, F.; García-Muelas, R.; López, N.; Active and Selective Ensembles in Oxide-Derived Copper Catalysts for CO2 Reduction, *ACS Energy Lett.* **2020**, *5* (10), 3176-3184.

180. Liu, X. W.; Wang, F. Y.; Zhen, F.; Huang, J. R.; In situ growth of Au nanoparticles on the surfaces of Cu2O nanocubes for chemical sensors with enhanced performance, *RSC Adv.* **2012**, *2* (20), 7647-7651.

181. Ke, W.-H.; Hsia, C.-F.; Chen, Y.-J.; Huang, M. H.; Synthesis of Ultrasmall Cu2O Nanocubes and Octahedra with Tunable Sizes for Facet-Dependent Optical Property Examination, *Small* **2016**, *12* (26), 3530-3534.

182. Wang, Z.; Wang, H.; Wang, L.; Pan, L.; One-pot synthesis of single-crystalline Cu2O hollow nanocubes, *J. Phys. Chem. Solids* **2009**, *70* (3), 719-722.

183. Wang, Q.; Kuang, Q.; Wang, K.; Wang, X.; Xie, Z.; A surfactant free synthesis and formation mechanism of hollow Cu2O nanocubes using Cl- ions as the morphology regulator, *RSC Adv.* **2015**, *5* (75), 61421-61425.

184. Sayson, L. V. A.; Regulacio, M. D.; Rational Design and Synthesis of Ag−Cu2O Nanocomposites for SERS Detection, Catalysis, and Antibacterial Applications, *ChemNanoMat* **2022**, *8* (5), e202200052.

185. Wang, Y.; Gao, T.; Wang, K.; Wu, X.; Shi, X.; Liu, Y.; Lou, S.; Zhou, S.; Template-assisted synthesis of uniform nanosheet-assembled silver hollow microcubes, *Nanoscale* **2012**, *4* (22), 7121-7126.

186. Widrinna, S.; Study of the structure- and size-sensitivity of mono- and bimetallic catalysts for the CO2 hydrogenation reaction to methanol, *Masterthesis*, Ruhr University Bochum, **2019**.

187. Chu, S.; Cui, Y.; Liu, N.; The path towards sustainable energy, *Nat. Mater.* **2017**, *16* (1), 16-22.

188. De Luna, P.; Hahn, C.; Higgins, D.; Jaffer, S. A.; Jaramillo, T. F.; Sargent, E. H.; What would it take for renewably powered electrosynthesis to displace petrochemical processes?, *Science* **2019**, *364* (6438), 350-+.

189. Jouny, M.; Luc, W.; Jiao, F.; General Techno-Economic Analysis of CO2 Electrolysis Systems, *Ind. Eng. Chem. Res.* **2018**, *57* (6), 2165-2177.

190. Mussatto, S. I.; Dragone, G.; Guimarães, P. M. R.; Silva, J. P. A.; Carneiro, L. M.; Roberto, I. C.; Vicente, A.; Domingues, L.; Teixeira, J. A.; Technological trends, global market, and challenges of bio-ethanol production, *Biotechnol. Adv.* **2010**, *28* (6), 817-830.

191. Mistry, H.; Varela, A. S.; Kühl, S.; Strasser, P.; Roldan Cuenya, B.; Nanostructured electrocatalysts with tunable activity and selectivity, *Nat. Rev. Mater.* **2016**, *1* (4), 16009-16022.

192. Mistry, H.; Reske, R.; Zeng, Z.; Zhao, Z.-J.; Greeley, J.; Strasser, P.; Roldan Cuenya, B.; Exceptional Size-Dependent Activity Enhancement in the Electroreduction of CO2 over Au Nanoparticles, *J. Am. Chem. Soc.* **2014**, *136* (47), 16473-16476.

193. Wang, Z.; Yang, G.; Zhang, Z.; Jin, M.; Yin, Y.; Selectivity on Etching: Creation of High-Energy Facets on Copper Nanocrystals for CO2 Electrochemical Reduction, *ACS Nano* **2016**, *10* (4), 4559-4564.

194. Varela, A. S.; Kroschel, M.; Reier, T.; Strasser, P.; Controlling the selectivity of CO2 electroreduction on copper: The effect of the electrolyte concentration and the importance of the local pH, *Catal. Today* **2016**, *260*, 8-13.

195. Ren, D.; Fong, J.; Yeo, B. S.; The effects of currents and potentials on the selectivities of copper toward carbon dioxide electroreduction, *Nat. Commun.* **2018**, *9* (1), 925-932.

196. Lum, Y.; Yue, B.; Lobaccaro, P.; Bell, A. T.; Ager, J. W.; Optimizing C–C Coupling on Oxide-Derived Copper Catalysts for Electrochemical CO2 Reduction, *J. Phys. Chem. C* **2017**, *121* (26), 14191-14203.

197. Gao, D.; Scholten, F.; Roldan Cuenya, B.; Improved CO2 Electroreduction Performance on Plasma-Activated Cu Catalysts via Electrolyte Design: Halide Effect, *ACS Catal.* **2017**, *7* (8), 5112-5120.

198. Resasco, J.; Chen, L. D.; Clark, E.; Tsai, C.; Hahn, C.; Jaramillo, T. F.; Chan, K.; Bell, A. T.; Promoter Effects of Alkali Metal Cations on the Electrochemical Reduction of Carbon Dioxide, *J. Am. Chem. Soc.* **2017**, *139* (32), 11277-11287.

199. Velasco-Vélez, J.-J.; Jones, T.; Gao, D.; Carbonio, E.; Arrigo, R.; Hsu, C.-J.; Huang, Y.-C.; Dong, C.-L.; Chen, J.-M.; Lee, J.-F.; Strasser, P.; Roldan Cuenya, B.; Schlögl, R.; Knop-Gericke, A.; Chuang, C.-H.; The Role of the Copper Oxidation State in the Electrocatalytic Reduction of CO2 into Valuable Hydrocarbons, *ACS Sustain. Chem. Eng.* **2019**, *7* (1), 1485-1492.

200. Liu, C.; Lourenço, M. P.; Hedström, S.; Cavalca, F.; Diaz-Morales, O.; Duarte, H. A.; Nilsson, A.; Pettersson, L. G. M.; Stability and Effects of Subsurface Oxygen in Oxide-Derived Cu Catalyst for CO2 Reduction, *J. Phys. Chem. C* **2017**, *121* (45), 25010-25017.

201. Ma, S.; Sadakiyo, M.; Heima, M.; Luo, R.; Haasch, R. T.; Gold, J. I.; Yamauchi, M.; Kenis, P. J. A.; Electroreduction of Carbon Dioxide to Hydrocarbons Using Bimetallic Cu–Pd Catalysts with Different Mixing Patterns, *J. Am. Chem. Soc.* **2017**, *139* (1), 47-50.

202. Bernal, M.; Bagger, A.; Scholten, F.; Sinev, I.; Bergmann, A.; Ahmadi, M.; Rossmeisl, J.; Roldan Cuenya, B.; CO2 electroreduction on copper-cobalt nanoparticles: Size and composition effect, *Nano Energy* **2018**, *53*, 27-36.

203. Hoang, T. T. H.; Verma, S.; Ma, S.; Fister, T. T.; Timoshenko, J.; Frenkel, A. I.; Kenis, P. J. A.; Gewirth, A. A.; Nanoporous Copper–Silver Alloys by Additive-Controlled Electrodeposition for the Selective Electroreduction of CO2 to Ethylene and Ethanol, *J. Am. Chem. Soc.* **2018**, *140* (17), 5791-5797.

204. Ravel, B.; Newville, M.; ATHENA, ARTEMIS, HEPHAESTUS: data analysis for X-ray absorption spectroscopy using IFEFFIT, *J. Synchrotron Radiat.* **2005**, *12* (4), 537-541.

205. Ankudinov, A. L.; Ravel, B.; Rehr, J. J.; Conradson, S. D.; Real-space multiple-scattering calculation and interpretation of x-ray-absorption near-edge structure, *Phys. Rev. B* **1998**, *58* (12), 7565-7576.

206. Dutta, A.; Montiel, I. Z.; Erni, R.; Kiran, K.; Rahaman, M.; Drnec, J.; Broekmann, P.; Activation of bimetallic AgCu foam electrocatalysts for ethanol formation from CO2 by selective Cu oxidation/reduction, *Nano Energy* **2020**, *68*, 104331.

207. Kottakkat, T.; Klingan, K.; Jiang, S.; Jovanov, Z. P.; Davies, V. H.; El-Nagar, G. A. M.; Dau, H.; Roth, C.; Electrodeposited AgCu Foam Catalysts for Enhanced Reduction of CO2 to CO, *ACS Appl. Mater. Interfaces* **2019**, *11* (16), 14734-14744.

208. Timoshenko, J.; Roese, S.; Hövel, H.; Frenkel, A. I.; Silver clusters shape determination from in-situ XANES data, *Radiat. Phys. Chem.* **2020**, *175*, 108049-108052.

209. Deng, Y.; Handoko, A. D.; Du, Y.; Xi, S.; Yeo, B. S.; In Situ Raman Spectroscopy of Copper and Copper Oxide Surfaces during Electrochemical Oxygen Evolution Reaction: Identification of CuIII Oxides as Catalytically Active Species, *ACS Catal.* **2016**, *6* (4), 2473-2481.

210. Niaura, G.; Surface-enhanced Raman spectroscopic observation of two kinds of adsorbed OH- ions at copper electrode, *Electrochim. Acta* **2000**, *45* (21), 3507-3519.

211. Singhal, A.; Pai, M. R.; Rao, R.; Pillai, K. T.; Lieberwirth, I.; Tyagi, A. K.; Copper(I) Oxide Nanocrystals – One Step Synthesis, Characterization, Formation Mechanism, and Photocatalytic Properties, *Eur. J. Inorg. Chem.* **2013**, *2013* (14), 2640-2651.

212. Li, Y. C.; Wang, Z.; Yuan, T.; Nam, D.-H.; Luo, M.; Wicks, J.; Chen, B.; Li, J.; Li, F.; de Arquer, F. P. G.; Wang, Y.; Dinh, C.-T.; Voznyy, O.; Sinton, D.; Sargent, E. H.; Binding Site Diversity Promotes CO2 Electroreduction to Ethanol, *J. Am. Chem. Soc.* **2019**, *141* (21), 8584-8591.

213. Oda, I.; Ogasawara, H.; Ito, M.; Carbon Monoxide Adsorption on Copper and Silver Electrodes during Carbon Dioxide Electroreduction Studied by Infrared Reflection Absorption Spectroscopy and Surface-Enhanced Raman Spectroscopy, *Langmuir* **1996**, *12* (4), 1094-1097.

214. Gao, D. F.; McCrum, I. T.; Deo, S.; Choi, Y. W.; Scholten, F.; Wan, W. M.; Chen, J. G. G.; Janik, M. J.; Roldan Cuenya, B.; Activity and Selectivity Control in CO2 Electroreduction to Multicarbon Products over CuOx Catalysts via Electrolyte Design, *ACS Catal.* **2018**, *8* (11), 10012-10020.

215. Ting, L. R. L.; Piqué, O.; Lim, S. Y.; Tanhaei, M.; Calle-Vallejo, F.; Yeo, B. S.; Enhancing CO2 Electroreduction to Ethanol on Copper–Silver Composites by Opening an Alternative Catalytic Pathway, *ACS Catal.* **2020**, *10* (7), 4059-4069.

216. Wang, L.; Higgins, D. C.; Ji, Y.; Morales-Guio, C. G.; Chan, K.; Hahn, C.; Jaramillo, T. F.; Selective reduction of CO to acetaldehyde with CuAg electrocatalysts, *Proc. Natl. Acad. Sci. U.S.A.* **2020**, *117* (23), 12572-12575.

217. Jeon, H. S.; Kunze, S.; Scholten, F.; Roldan Cuenya, B.; Prism-Shaped Cu Nanocatalysts for Electrochemical CO2 Reduction to Ethylene, *ACS Catal.* **2018**, *8* (1), 531-535.

218. De Luna, P.; Quintero-Bermudez, R.; Dinh, C.-T.; Ross, M. B.; Bushuyev, O. S.; Todorović, P.; Regier, T.; Kelley, S. O.; Yang, P.; Sargent, E. H.; Catalyst electro-redeposition controls morphology and oxidation state for selective carbon dioxide reduction, *Nat. Catal.* **2018**, *1* (2), 103-110.

219. Gunathunge, C. M.; Ovalle, V. J.; Li, Y.; Janik, M. J.; Waegele, M. M.; Existence of an Electrochemically Inert CO Population on Cu Electrodes in Alkaline pH, *ACS Catal.* **2018**, *8* (8), 7507-7516.

220. Li, J.; Chang, X.; Zhang, H.; Malkani, A. S.; Cheng, M.-j.; Xu, B.; Lu, Q.; Electrokinetic and in situ spectroscopic investigations of CO electrochemical reduction on copper, *Nat. Commun.* **2021**, *12* (1), 3264-3274.

221. Bodappa, N.; Su, M.; Zhao, Y.; Le, J.-B.; Yang, W.-M.; Radjenovic, P.; Dong, J.-C.; Cheng, J.; Tian, Z.-Q.; Li, J.-F.; Early Stages of Electrochemical Oxidation of Cu(111) and Polycrystalline Cu Surfaces Revealed by in Situ Raman Spectroscopy, *J. Am. Chem. Soc.* **2019**, *141* (31), 12192-12196.

222. Zhao, Y.; Chang, X.; Malkani, A. S.; Yang, X.; Thompson, L.; Jiao, F.; Xu, B.; Speciation of Cu Surfaces During the Electrochemical CO Reduction Reaction, *J. Am. Chem. Soc.* **2020**, *142* (21), 9735-9743.

223. Zhang, Q.; Ren, D.; Gao, J.; Wang, Z.; Wang, J.; Pan, S.; Wang, M.; Luo, J.; Zhao, Y.; Grätzel, M.; Zhang, X.; Regulated CO adsorption by the electrode with OH-repulsive property for enhancing C–C coupling, *GreenChE* **2022**.

224. Jiang, K.; Huang, Y.; Zeng, G.; Toma, F. M.; Goddard, W. A., III; Bell, A. T.; Effects of Surface Roughness on the Electrochemical Reduction of CO2 over Cu, *ACS Energy Lett.* **2020**, *5* (4), 1206-1214.

225. Akemann, W.; Otto, A.; Vibrational modes of CO adsorbed on disordered copper films, *J. Raman Spectrosc.* **1991**, *22* (12), 797-803.

226. Sullivan, I.; Goryachev, A.; Digdaya, I. A.; Li, X. Q.; Atwater, H. A.; Vermaas, D. A.; Xiang, C. X.; Coupling electrochemical CO2 conversion with CO2 capture, *Nature Catalysis* **2021**, *4* (11), 952-958.

227. Yin, C.; Li, Q.; Zheng, J.; Ni, Y.; Wu, H.; Kjøniksen, A.-L.; Liu, C.; Lei, Y.; Zhang, Y.; Progress in regulating electronic structure strategies on Cu-based bimetallic catalysts for CO2 reduction reaction, *Adv. Powder Technol.* **2022**, *1* (4), 100055.

228. Ren, D.; Ang, B. S.-H.; Yeo, B. S.; Tuning the Selectivity of Carbon Dioxide Electroreduction toward Ethanol on Oxide-Derived CuxZn Catalysts, *ACS Catal.* **2016**, *6* (12), 8239-8247.

229. Wan, L.; Zhang, X.; Cheng, J.; Chen, R.; Wu, L.; Shi, J.; Luo, J.; Bimetallic Cu–Zn Catalysts for Electrochemical CO2 Reduction: Phase-Separated versus Core–Shell Distribution, *ACS Catal.* **2022**, *12* (5), 2741-2748.

230. Speck, F. D.; Cherevko, S.; Electrochemical copper dissolution: A benchmark for stable CO2 reduction on copper electrocatalysts, *Electrochem. commun.* **2020**, *115*, 106739-106742.

231. Kieffer, J.; Valls, V.; Blanc, N.; Hennig, C.; New tools for calibrating diffraction setups, *J. Synchrotron Radiat.* **2020**, *27* (2), 558-566.

232. Rajiv, P.; Dinnebier, R. E.; Jansen, M.; "Powder 3D Parametric"- A program for Automated Sequential and Parametric Rietveld Refinement Using Topas, *Materials Science Forum* **2010**, *651*, 97-104.

233. Schmitt, K. G.; Gewirth, A. A.; In Situ Surface-Enhanced Raman Spectroscopy of the Electrochemical Reduction of Carbon Dioxide on Silver with 3,5-Diamino-1,2,4-Triazole, *J. Phys. Chem. C* **2014**, *118* (31), 17567-17576.

234. Chan, H. Y. H.; Takoudis, C. G.; Weaver, M. J.; Oxide Film Formation and Oxygen Adsorption on Copper in Aqueous Media As Probed by Surface-Enhanced Raman Spectroscopy, *J. Phys. Chem. B* **1999**, *103* (2), 357-365.

235. Wang, M.; Jiang, L.; Kim, E. J.; Hahn, S. H.; Electronic structure and optical properties of Zn(OH)2: LDA+U calculations and intense yellow luminescence, *RSC Adv.* **2015**, *5* (106), 87496-87503.

236. Wang, J.; Zhu, Z.; Wei, X.; Li, Z.; Chen, J. S.; Wu, R.; Wei, Z.; Hydrogen-Mediated Synthesis of 3D Hierarchical Porous Zinc Catalyst for CO2 Electroreduction with High Current Density, *J. Phys. Chem. C* **2021**, *125* (43), 23784-23790.

237. Werner, A.; Hochheimer, H. D.; High-pressure x-ray study of Cu2O and Ag2O, *Phys. Rev. B* **1982**, *25* (9), 5929-5934.

238. Davey, W. P.; Precision Measurements of the Lattice Constants of Twelve Common Metals, *Phys. Rev.* **1925**, *25* (6), 753-761.

239. Velasco-Vélez, J.-J.; Chuang, C.-H.; Gao, D.; Zhu, Q.; Ivanov, D.; Jeon, H. S.; Arrigo, R.; Mom, R. V.; Stotz, E.; Wu, H.-L.; Jones, T. E.; Roldan Cuenya, B.; Knop-Gericke, A.; Schlögl, R.; On the Activity/Selectivity and Phase Stability of Thermally Grown Copper Oxides during the Electrocatalytic Reduction of CO2, *ACS Catal.* **2020**, *10* (19), 11510-11518.

240. Yoon, Y.; Yan, B.; Surendranath, Y.; Suppressing Ion Transfer Enables Versatile Measurements of Electrochemical Surface Area for Intrinsic Activity Comparisons, *J. Am. Chem. Soc.* **2018**, *140* (7), 2397-2400.